Composite

Structural Program

Rensselaer Polytechnic Institute
Troy, N.Y. 12181

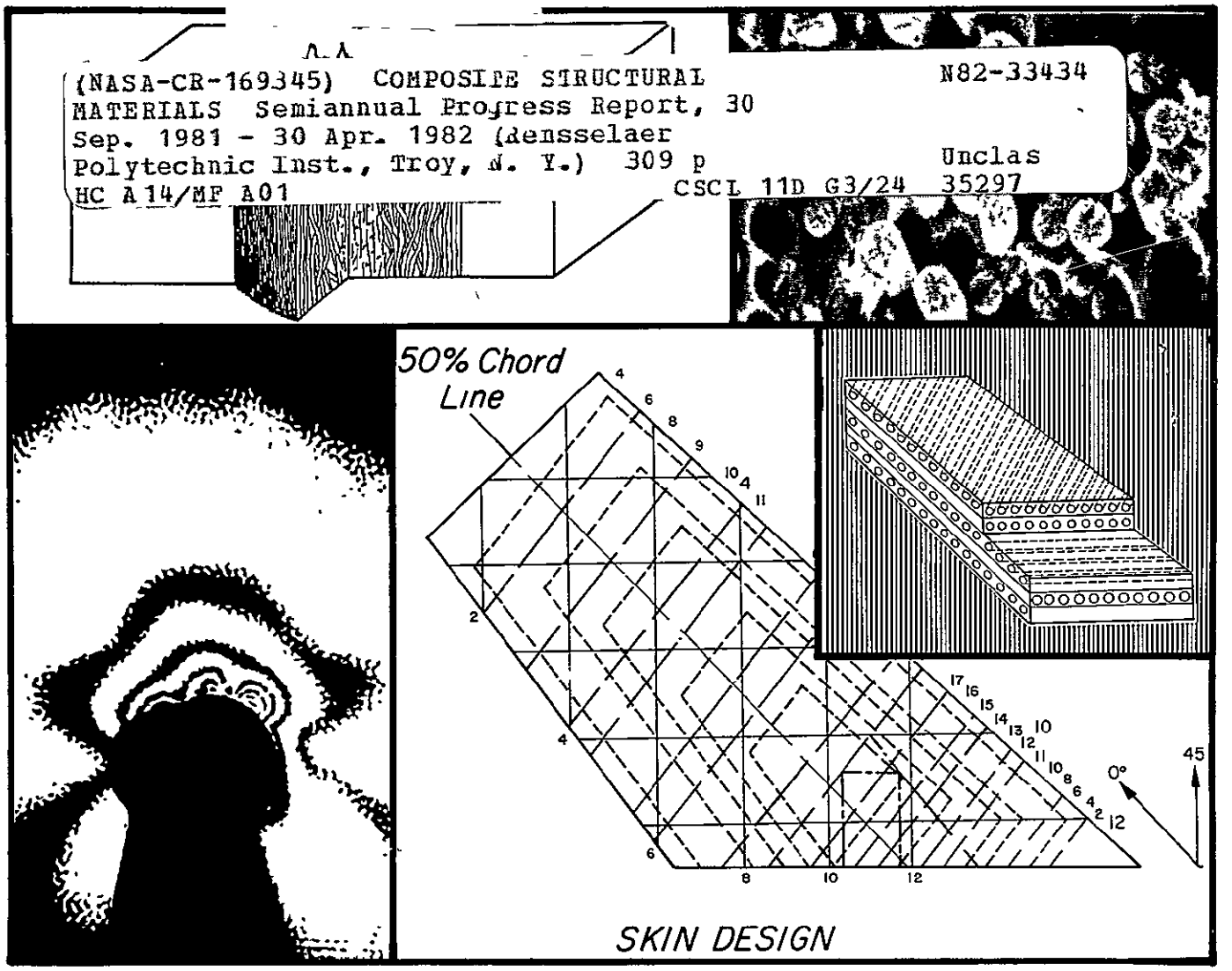

Sponsored by

NASA/AFOSR

Composite

Structural Program

Rensselaer Polytechnic Institute
Troy, N.Y. 12181

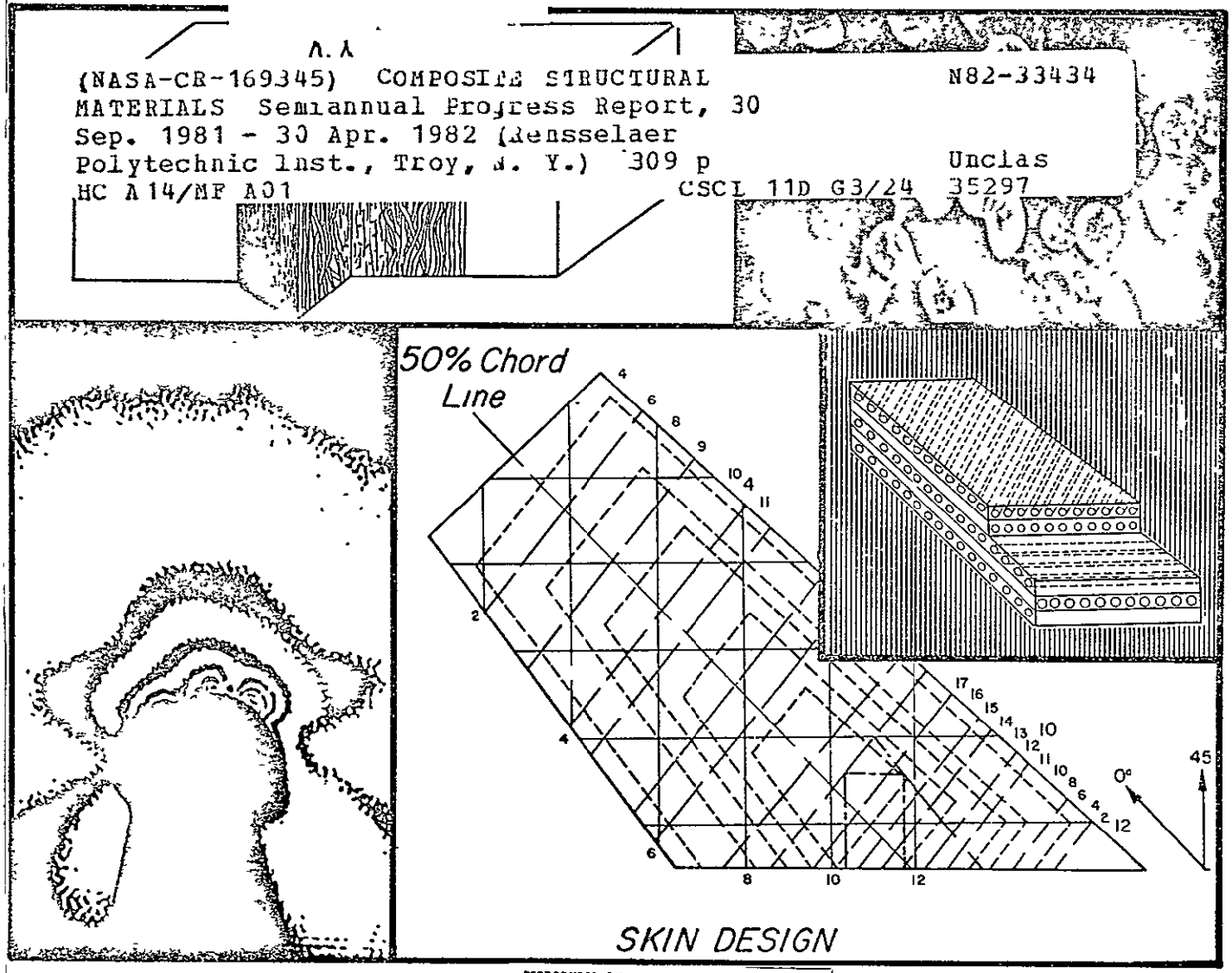

Sponsored by
NASA/AFOSR

Semi-Annual Progress Report

September 30, 1981 through April 30, 1982

COMPOSITE STRUCTURAL MATERIALS

Air Force Office of Scientific Research
and
National Aeronautics and Space Administration
Grant No. NGL 33-018-003

Co-Principal Investigators:

George S. Ansell
Dean, School of Engineering

Robert G. Loewy
Institute Professor

and

Stephen E. Wiberley
Professor of Chemistry

Rensselaer Polytechnic Institute
Troy, New York 12181

NASA Technical Officer

Michael A. Greenfield
Materials and Structures Division
NASA Headquarters

CONTENTS

Page

Page

LIST OF TABLES

LIST OF FIGURES

PART I
INTRODUCTION

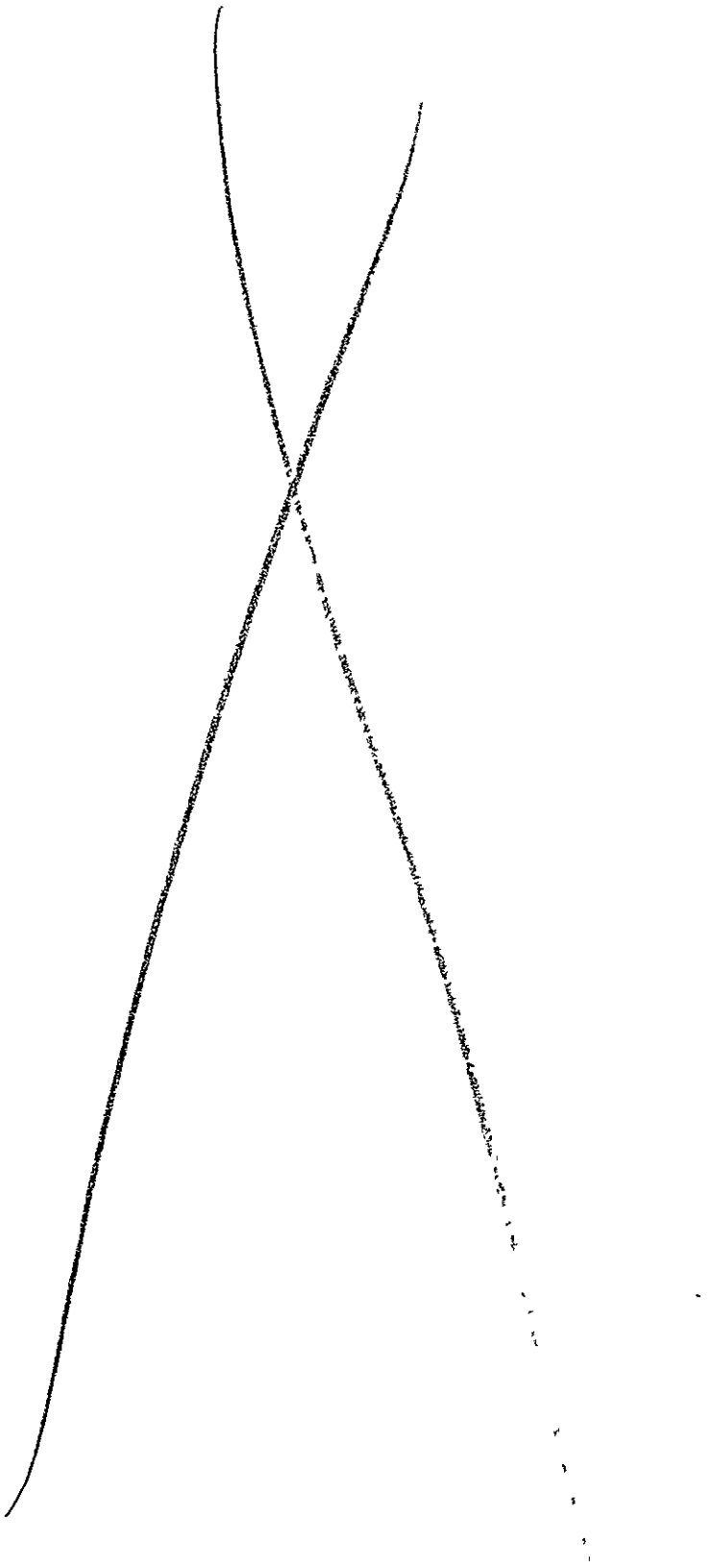

PAGE 2 INTENTIONALLY BLANK

INTRODUCTION

The promise of filamentary composite materials, whose development may be considered as entering its second generation, continues to generate intense interest and applications activity. Such interest and activity are well founded, since they are based on the possibility of using relatively brittle materials with high modulus, high strength, but low density in composites with good durability and high tolerance to damage and which, when they do fail, do so in a non-catastrophic manner. Fiber reinforced composite materials of this kind offer substantially improved performance and potentially lower costs for aerospace hardware.

Much progress has been achieved since the initial developments in the mid 1960's. Rather limited applications to primary aircraft structure have been made, however, mainly in a material-substitution mode on military aircraft, except for a few experiments now being conducted on large passenger airplanes.

To fulfill the promise of composite materials completely requires a strong technology base. NASA and AFOSR recognize the present state of the art to be such that to fully exploit composites in sophisticated aerospace structures, the technology base must be improved. This, in turn, calls for expanding fundamental knowledge and the means by which it can be sucessfully applied in design and manufacture.

As technology of composite materials and structures moves toward fuller adoption into aerospace structures, some of the problems of an earlier era are being solved, others which seemed important are being put into perspective as relatively minor, and still others unanticipated or put aside are emerging as of high priority. The purpose of the RPI program as funded by NASA and AFOSR has been to develop critical advanced technology in the areas of physical properties, structural concepts and analysis, manufacturing, reliability and life prediction.

Our approach to accomplishing these goals is through an interdisciplinary program, unusual in at least two important aspects for a university. First, the nature of the research is comprehensive - from fiber and matrix constituent properties research, through the integration of constituents into composite materials and their characterization, the behavior of composites as they are used in generic structural components, their non-destructive and proof testing, to the logical conclusion of such activities; namely research into the composite structure's long term integrity under conditions pertinent to service use. Inherent in the RPI program is the motivation which basic research into the structural aspects provides for research at the materials level, and vice versa.

Second, interactions among faculty contributing to program objectives - which is a group wider than that supported under the project - is on a day to day basis, regardless of

organizational lines. Program management is largely at the working level, and administrative, scientific and technical decisions are made, for the most part, independent of considerations normally associated with academic departments. Involvement of this kind includes - depending on the flow of the research - faculty, staff and students from chemistry, chemical engineering, civil engineering, materials engineering, and the department of mechanical engineering, aeronautical engineering and mechanics.

Both of these characteristics of the NASA/AFOSR program of research in composite materials and structures foster the kinds of fundamental advances which are triggered by insights into aspects beyond the narrow confines of an individual discipline. This is a program characteristic often sought in many fields at a university, but seldom achieved.

Overall program emphasis, is on basic, long-term research in the following categories: (a) constituent materials, (b) composite materials, (c) generic structural elements, (d) processing science technology and (e) maintaining long-term structural integrity. Progress in the program will be reported in the following pages under these headings. Those computer software developments are also undertaken which both support Rensselaer projects in composite materials and structures research in the areas listed above and which also represent research with the potential of widely useful results in their own right.

In short, the NASA/AFOSR Composites Aircraft Program is a multi-faceted program planned and managed so that scientists and engineers in a number of pertinent disciplines will interact to achieve its goals. Research in the basic composition, characteristics and processing science of composite materials and their constituents is balanced against the mechanics, conceptual design, fabrication and testing of generic structural elements typical of aerospace vehicles so as to encourage the discovery of unusual solutions to present and future problems. In the following sections, more detailed descriptions of the progress achieved in the various component parts of this comprehensive program are presented.

PART II

CONSTITUENT MATERIALS

II-A TRANSVERSE PROPERTIES OF ANISOTROPIC FIBER REINFORCED EPOXY MATRIX COMPOSITES (A step in determining the transverse properties of anisotropic fibers)

II-A TRANSVERSE PROPERTIES OF ANISOTROPIC FIBER REINFORCED EPOXY MATRIX COMPOSITES (A step in determining the transverse properties of anisotropic fibers)

Senior Investigator: R. J. Diefendorf

1. Introduction

Unlike the longitudinal properties, the transverse properties of composites are a function of packing and homogeneity. If, as is often the case, the transverse properties dictate or limit composite utilization, then homogeneity and packing take on added importance. Inhomogeneity produces critical resin areas which may induce crack propagation (see Figure II-A-1). Therefore, a measure of packing uniformity is essential for describing transverse properties.

Several researchers have attempted to make provisions for homogeneity and packing. Jones[1]* and Chamis and Sendeckyj[2] use a semi-empirical method and introduce a term called a contiguity factor, C, where C = 0 for areas where one fiber is isolated from others, and C = 1 for areas where matrix material is surrounded by fibers (see Figure II-A-2). Values between 0 and 1 are determined by comparison of the composite cross-section to experimental results (i.e., properties) and interpolating. For either the case of C = 1 or C = 0, there is no provision for distinguishing between the effects of a square or hexagonal array. Tsai[3] includes

*Numbers in brackets in this section refer to the references which are listed on page 64.

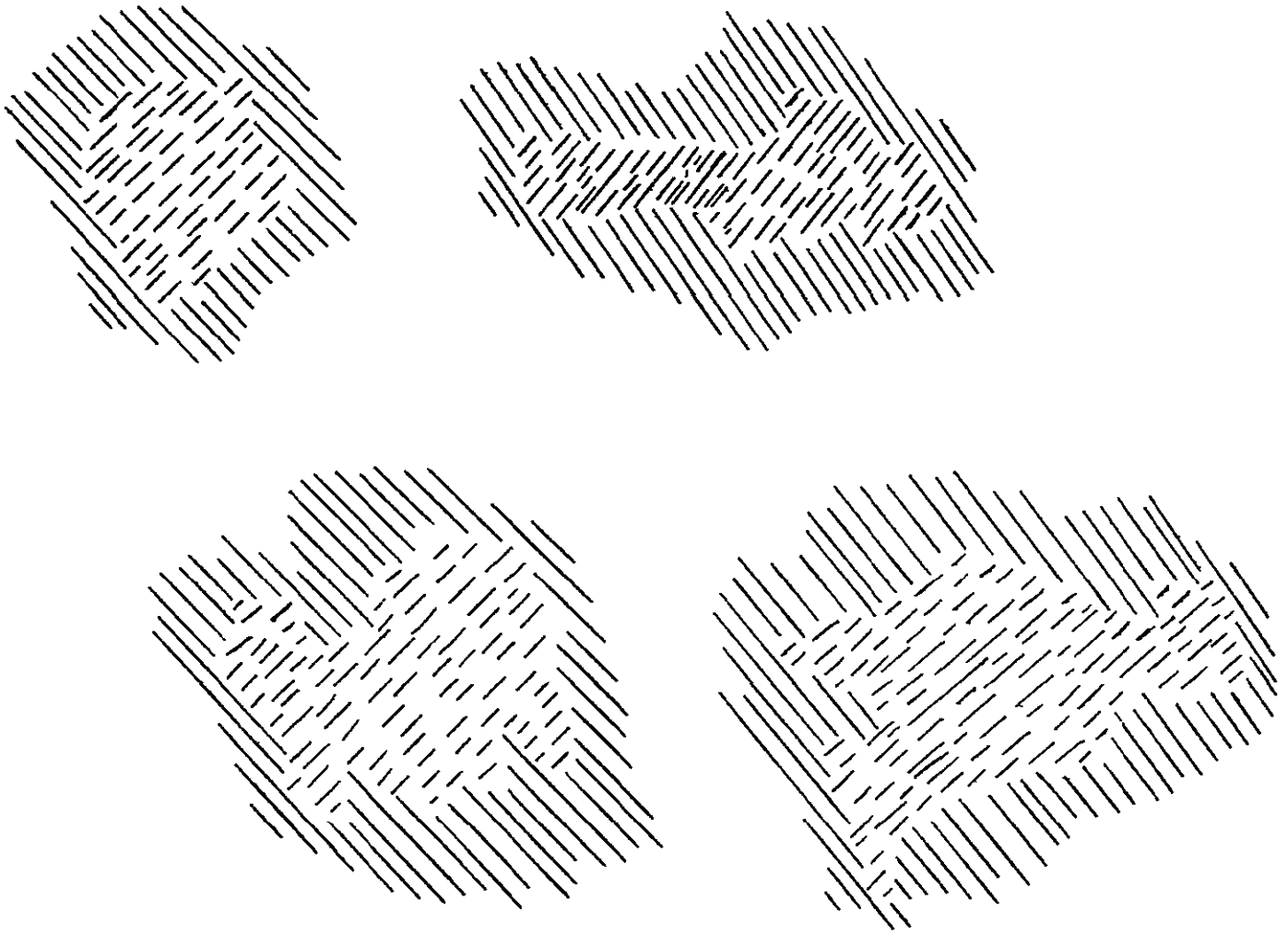

Figure II-A-1. Schematic Diagram Depicting Various Resin Rich Geometries

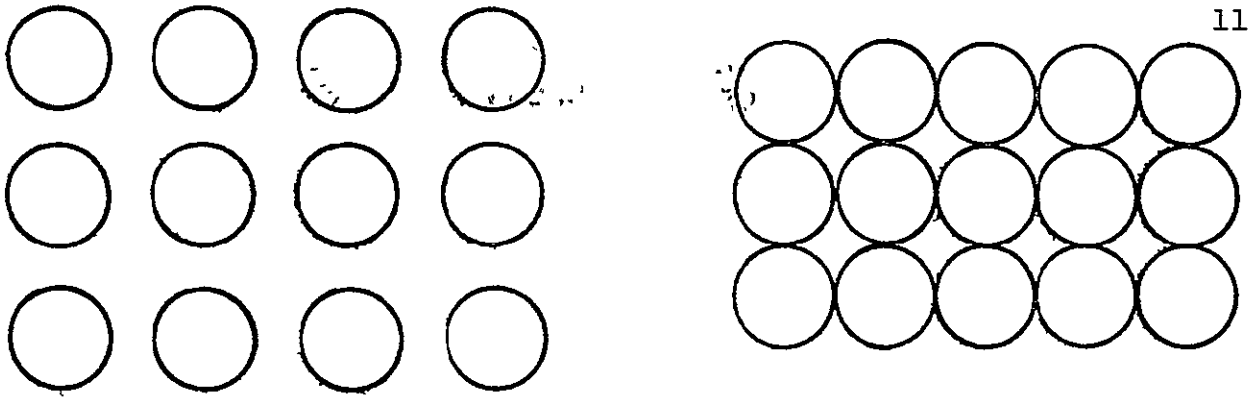

SQUARE

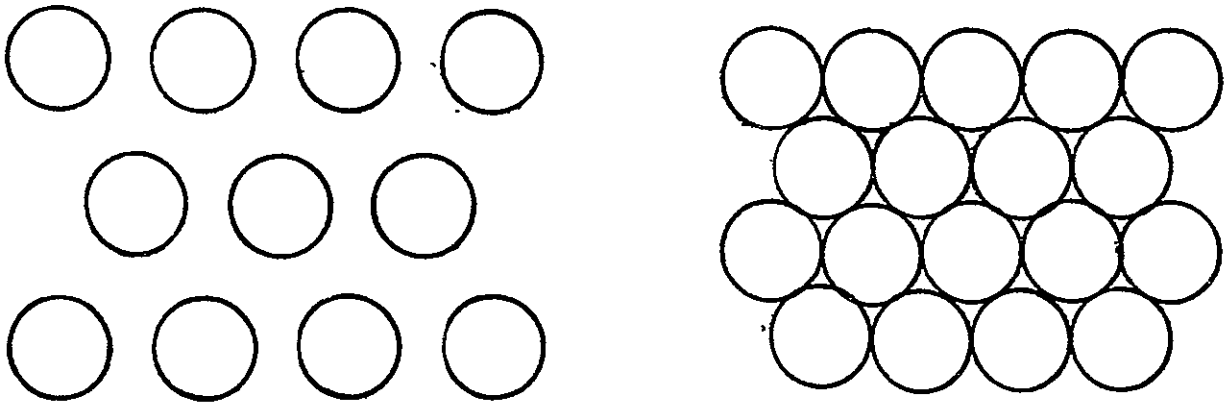

HEXAGONAL

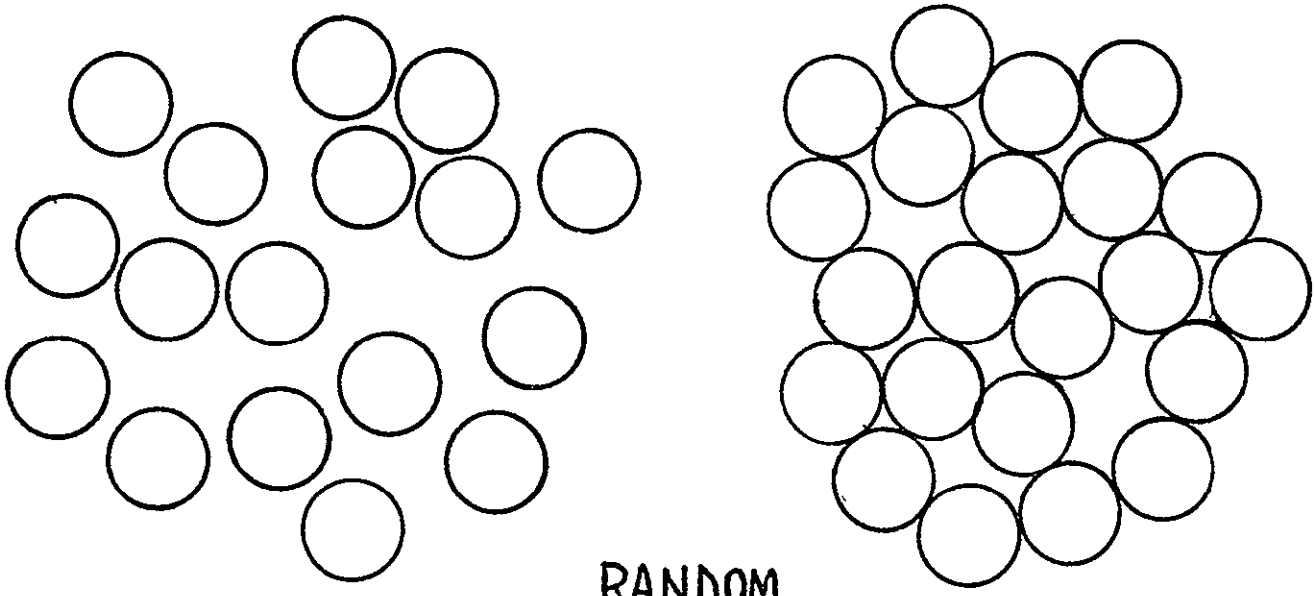

RANDOM

C = 0

C = 1

Figure II-A-2. Schematic Diagram Depicting Various Packing Geometries for Continuity Factor, C = 0 and C = 1

contiguity in an elasticity approach in order to obtain a value for the composite modulus transverse to the fiber axis. As can be seen from Equations (1) through (5), the formulation is somewhat cumbersome.

$$E_2 = 2[1 - \nu_f + (\nu_f - \nu_m)V_n]\left[(1-C)\frac{K_f(2K_m + G_m) - G_m(K_f - K_m)V_m}{(2K_m + G_m) + 2(K_f - K_m)V_m} + C\,\frac{K_f(2K_m + G_f) + G_f(K_m - K_f)V_m}{(2K_m + G_f) - 2(K_m - K_f)V_m}\right] \tag{1}$$

where

$$K_f = \frac{E_f}{2(1 - \nu_f)} \tag{2}$$

$$K_m = \frac{E_m}{2(1 - \nu_m)} \tag{3}$$

$$G_f = \frac{E_f}{2(1 + \nu_f)} \tag{4}$$

$$G_m = \frac{E_m}{2(1 + \nu_m)} \tag{5}$$

For C = 1 the first term in brackets drops out, while the same is true for the second term when C = 0. Intermediate values were determined by comparing curves of E_2 versus volume fraction. A shortcoming of the formulation is that it makes the assumption of isotropic constituents.

Another formulation that considers geometric configuration, to a somewhat limited degree, is the Halpin-Tsai equations[4]. These equations are based on Herman's[5]

generalized solutions of Hill's model[6] and can be reduced to the approximate forms given below.

$$\frac{E_2}{E_m} = \frac{1 + \varepsilon\eta V_f}{1 - \eta V_f} \tag{6}$$

$$\eta = \frac{(E_f/E_m) - 1}{(E_f/E_m) + \varepsilon} \tag{7}$$

where ε is related to fiber geometry, packing geometry and load conditions. For circular fibers in a square array, $\varepsilon = 2$ and $\eta = 1$, and a value of $\eta = 0$ indicates a homogeneous material. Difficulties arise in determining appropriate values for ε, since ε can vary from zero to infinity. Values are usually determined via curve fitting and by comparing Equations (6) and (7) to exact elasticity solutions. However, Halpin and Tsai were able to predict with high accuracy the properties of a composite with 55% reinforcing (see Figure II-A-3). This theory also assumes isotropic constituents and does not account for fiber anisotropies. An interesting concept is the theory of fiber spacing, δ/r. However, the model only considers regularly spaced (i.e., non-random) arrays, since δ in the X direction is always equal to δ in the Y direction. A modification which would allow analysis of random geometries may be possible and would be highly beneficial in including geometry in composite properties calculations.

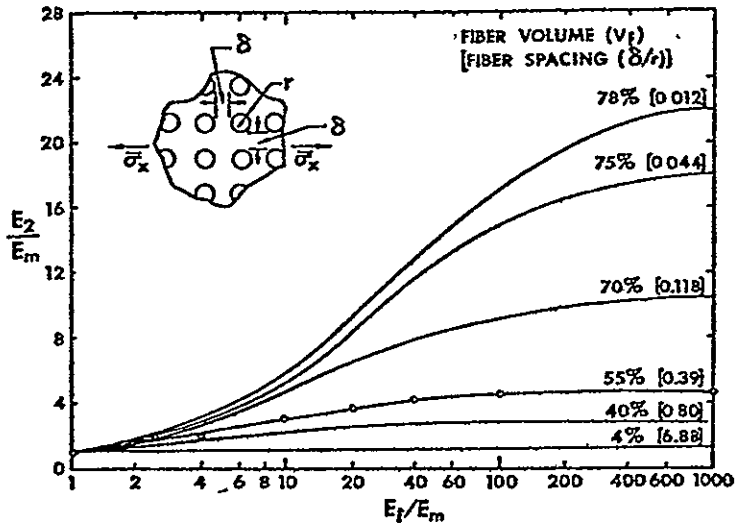

Figure II-A-3. Comparison of Halpin-Tsai Calculations (circles) with Adams and Doner's Calculations for E_2 of Circular Fibers in a Square Array
(after Halpin and Tsai, Ref. 4)

An example of packing effect is given by Piggot[7]. In this work, packing is related to shear modulus G_m with the result being:

$$U_R - U_f = \frac{e^r}{G_m} \ell n(R/r) \tag{8}$$

where U_R is the nearest neighbor fiber displacement under load, U_f is the fiber displacement under load and the quantity R/r is the argument dependent upon packing.

The respective expressions for a square and hexagonal array are:

$$\ell n(R/r)_s = \tfrac{1}{2} \ell n(\pi/V_f) \tag{9}$$

$$\ell n(R/r)_h = \tfrac{1}{2} \ell n(2\pi/\sqrt{3V_f}) \tag{10}$$

For a volume fraction of 50%, Equation (9) yields a value of $\ell n(R/r)$ equal to .92 for the square array and Equation (10) a value of .99 for the hexagonal array. These equations can be generalized to yield the following results:

$$\ell n(R/r) = \tfrac{1}{2} \ell n(P_f/V_f) \tag{11}$$*

where

P_f = geometrical packing factor.

The difference in packing factor between square and hexagonal arrays is .07. While this may not be significant for the

*NOTE: For a more detailed account, the reader is referred to the material in Reference [7].

shear modulus, two points must be mentioned. First, packing may have an important effect on failure. Second, the effect of random geometry has not been fully described and quantified.

2. Status

In order to measure homogeneity in a laminate, a specimen was cut from a plate which was fabricated from 27 layers of graphite prepreg using a standard 250°F cure at a pressure of 200 psi with 8 bleeders. The specimen was prepared as a metallographic sample, and photomicrographs were taken. These pictures were analyzed with the ASTM's grid technique and the Bausch & Lomb image analysis system, to determine the sample's fiber volume fraction.

As a first step towards describing homogeneity, the image analysis system was used to perform subfield analysis on the sample. That is, the area of scan was subsequently subdivided from whole field to halves, quarters, eighths, sixteenths and finally thirty-seconds. Values of volume fraction were obtained for each set of subfields so as to gain some insight into the variation of volume fraction across the sample and, therefore, the "variation of homogeneity". From this data a plot of volume fraction versus area^{-1} was obtained. A plot of variance versus reciprocal area was also constructed so as to determine the machine's effect in subfield analysis.

The variance versus volume fraction was determined, using data from theoretical arrays of hexagonal (48.0%) packing and square (34.9% and 66.1%) packing. A parabolic relationship should exist between variance and volume fraction, with a minima occuring around 50% fibers. The reason for the 50% minima was attributable to the fact that even amounts of fiber and matrix material are spaced uniformly, thus resulting in a drop in variance. Experimental data, as seen in Figure II-A-4, validated the hypothesis.

3. Progress During Report Period

The work reported here is largely that of graduate student J. F. Helmer.

a. Transverse Composite Homogeneity

Theoretical arrays of hexagonal and square geometries were constructed, and volume fraction versus area was measured. The purpose was twofold. First, the data from the arrays was needed to understand the "best case" limit of fiber packing. Second, the information was useful in evaluating actual composite performance via comparisons. The next step was to characterize a real composite by means of comparison to the square and hexagonal arrays.

The volume fractions of the square and hexagonal arrays were 66.1% and 48.0%, respectively. As was the case for the composite specimen, the two theoretical arrays were analyzed for volume fraction at full, half, quarter, eighth, sixteenth

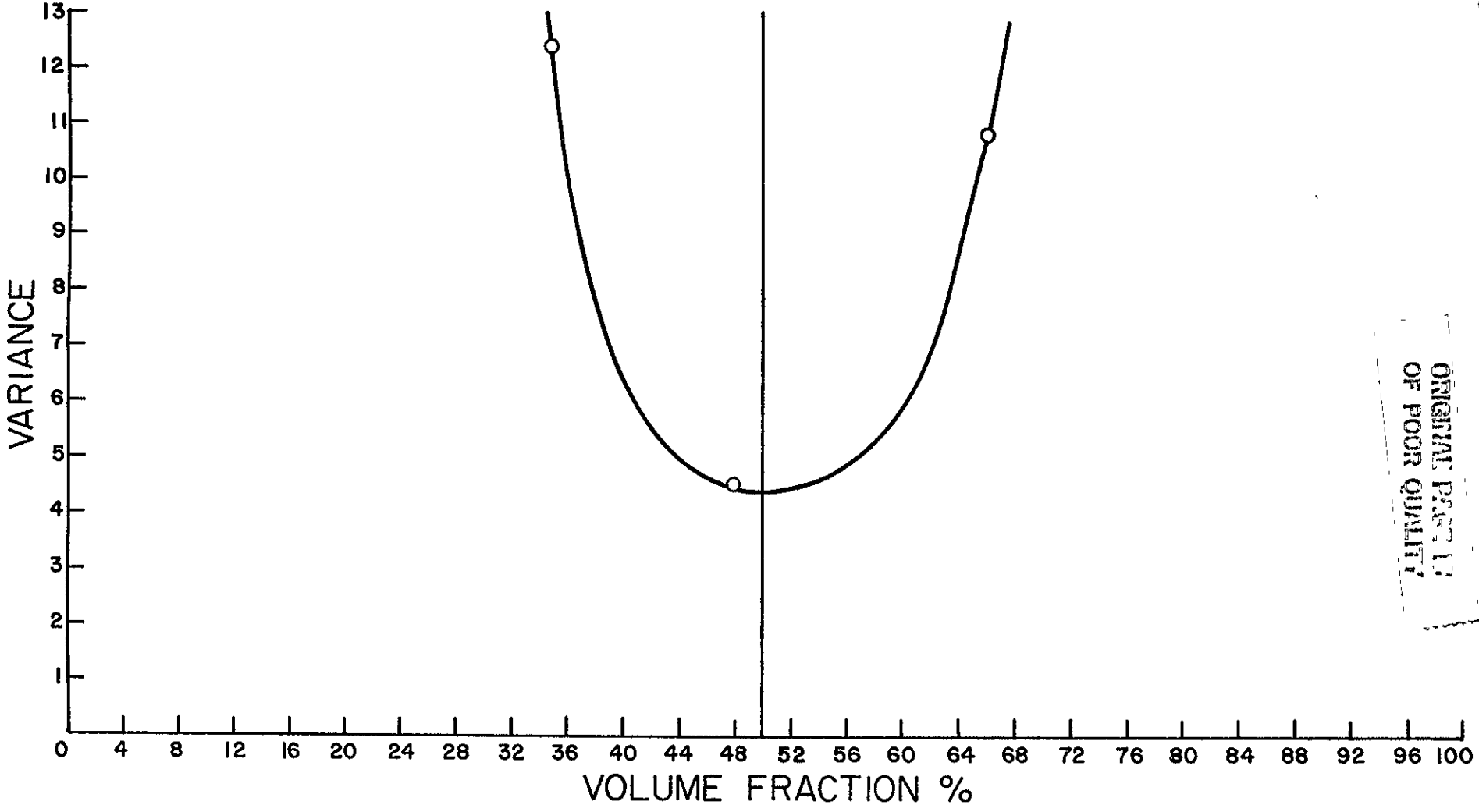

Figure II-A-4. Variance versus Volume Fraction - Theoretical Array

and thirty-second divisions. Averaged data for groups of ten measurements is presented for the square array in Table II-A-1. Table II-A-2 is a comparison of the results for a square array and the composite sample. It can be seen that the dispersion, as expected, is far less for the regular, square array than it is for the composite. This is also evident in Figures II-A-5 and -6, which are plots of volume fraction versus area for the square array and for the composite and square array, respectively. Even in the case of the hexagonal array (shown in Figure II-A-7) the theoretical dispersion is less than that of the composite, so that the composite dispersion may be used as a measure of the degree of overall inhomogeneity.

Plots of standard deviation of volume fraction versus average volume fraction were constructed for the composite and for the square array (see Figures II-A-8a and -8b). Since the slopes have different signs and the scattering of a few of the data points determines the slope, it was concluded that the standard deviation was independent of volume fraction over the range studied. An estimate of technique error can be obtained by constructing a plot of frequency versus deviation from mean including all 320 data points for the 1/32nd subfield analysis. That is, taking the average of each individual data set and subtracting each of the ten data points in the set to obtain the individualized data points. Figure II-A-9a is a plot of this data for the

TABLE II-A-1

VOLUME FRACTION DATA FROM SUBFIELD ANALYSIS

Subfield Divisions	32nds		16ths	8ths	4ths	Halves	Full
	68.1	67.7	68.6	66.3	68.6	67.6	68.3
	66.7	68.4	68.2	68.3	68.7	86.8	----
	68.6	68.8	70.3	68.5	67.2	----	
	67.5	68.1	69.6	67.0	68.7		
	67.2	67.7	68.3	67.1	----		
	68.3	68.1	71.0	69.2			
Volume Fraction in Percent	67.9	67.4	66.3	67.6			
	67.9	68.8	70.1	67.8			
	66.2	68.1	65.6	----			
	65.8	66.3	65.5				
	69.2	69.6	67.4				
	66.9	69.3	69.3				
	68.4	70.1	67.0				
	67.4	67.9	70.0				
	67.0	74.0	68.6				
	66.3	71.7	70.2				
Mean	68.2		68.5	67.7	68.3	66.7	68.3
Standard Deviation	1.612		1.730	0.932	0.735	1.273	----
Variance	2.518		2.806	0.759	0.405	0.81	----

TABLE II-A-2

COMPARISON OF SUBFIELD DATA FOR COMPOSITE AND SQUARE ARRAY

Subfield Divisions	32^{nds}	16^{ths}	8^{ths}	4^{ths}	Halves	Full
Composite						
Mean	64.2	63.9	64.1	66.4	66.8	66.0
Standard Deviation	6.325	5.003	1.842	1.771	2.616	----
Variance	38.754	23.465	2.970	2.353	3.423	----
Square Array						
Mean	68.2	68.5	67.7	68.3	66.7	68.3
Standard Deviation	1.612	1.730	0.932	0.735	1.273	----
Variance	2.518	2.896	0.759	0.405	0.81	----

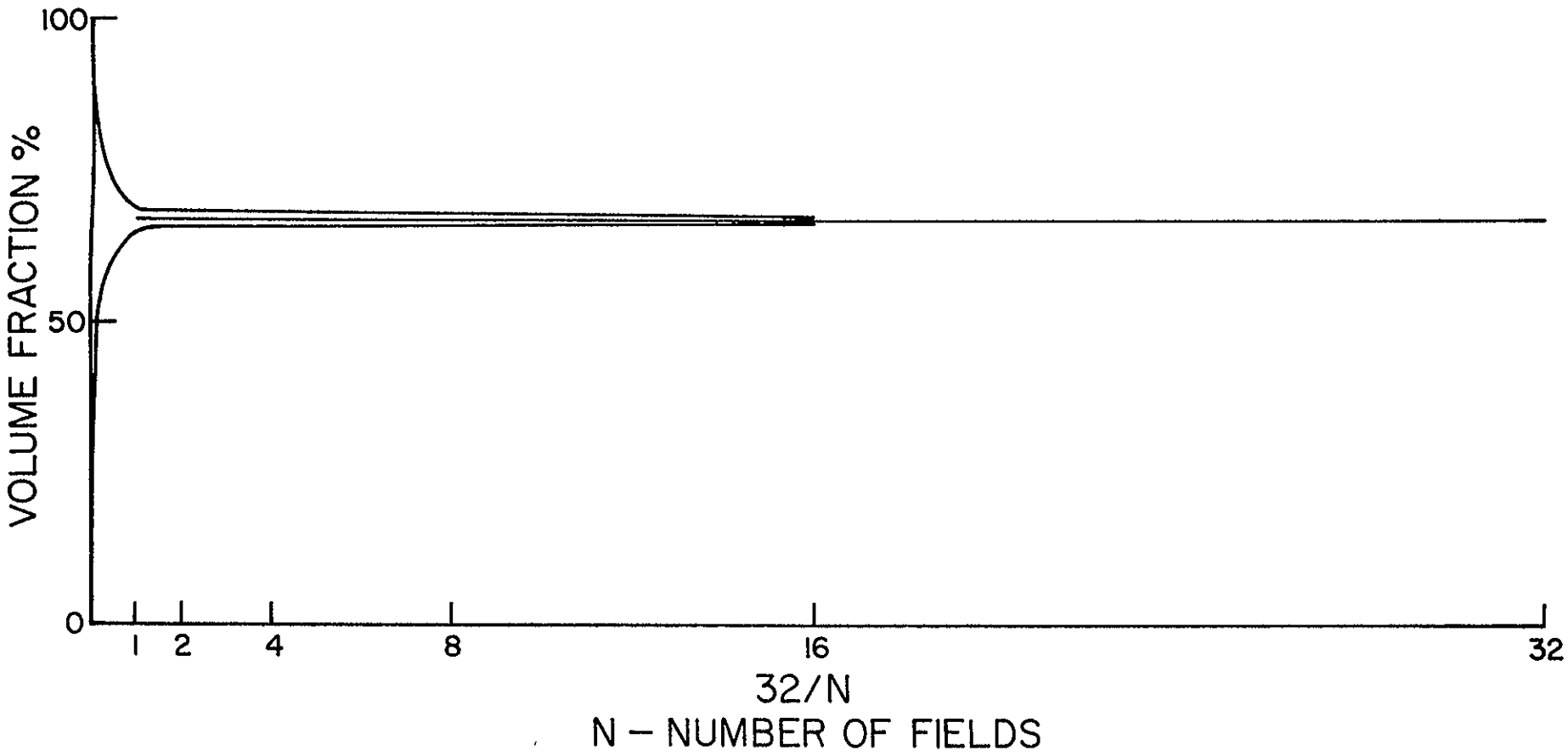

Figure II-A-5. Volume Fraction of Fibers versus Area for Theoretical Square Array

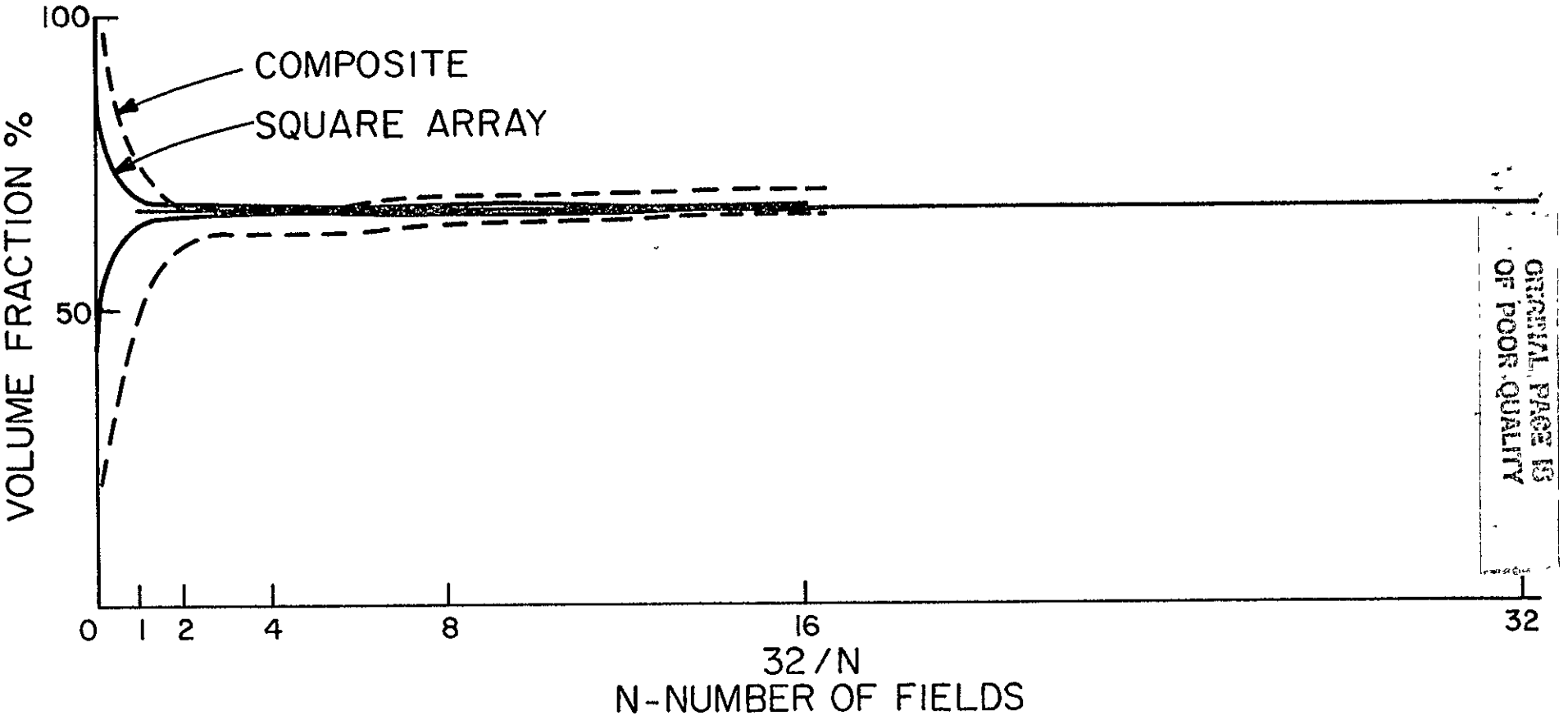

Figure II-A-6. Volume Fraction of Fibers versus Area (number of fields)

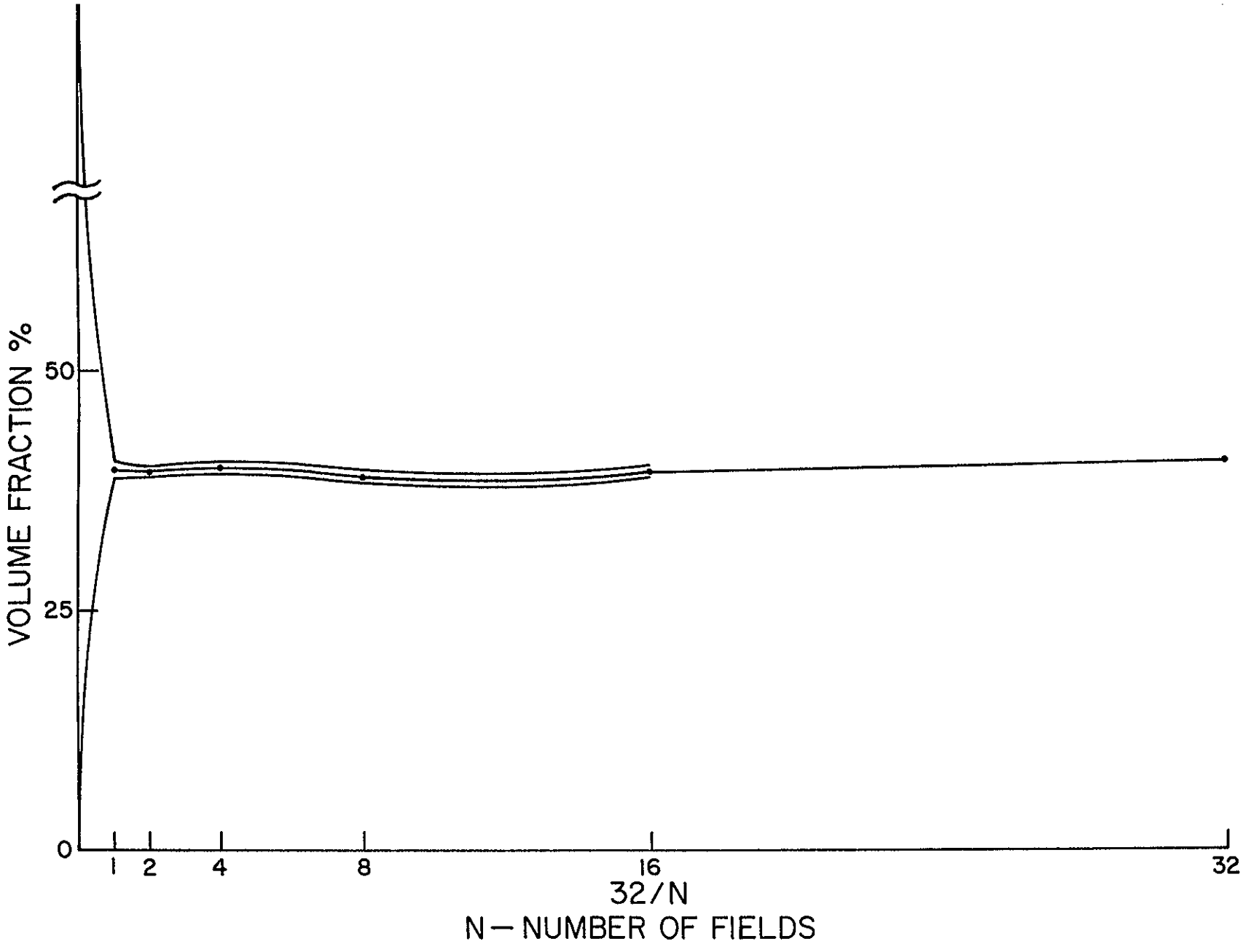

Figure IV-A-7. Volume Fraction of Fibers versus Area for Theoretical Hexagonal Array

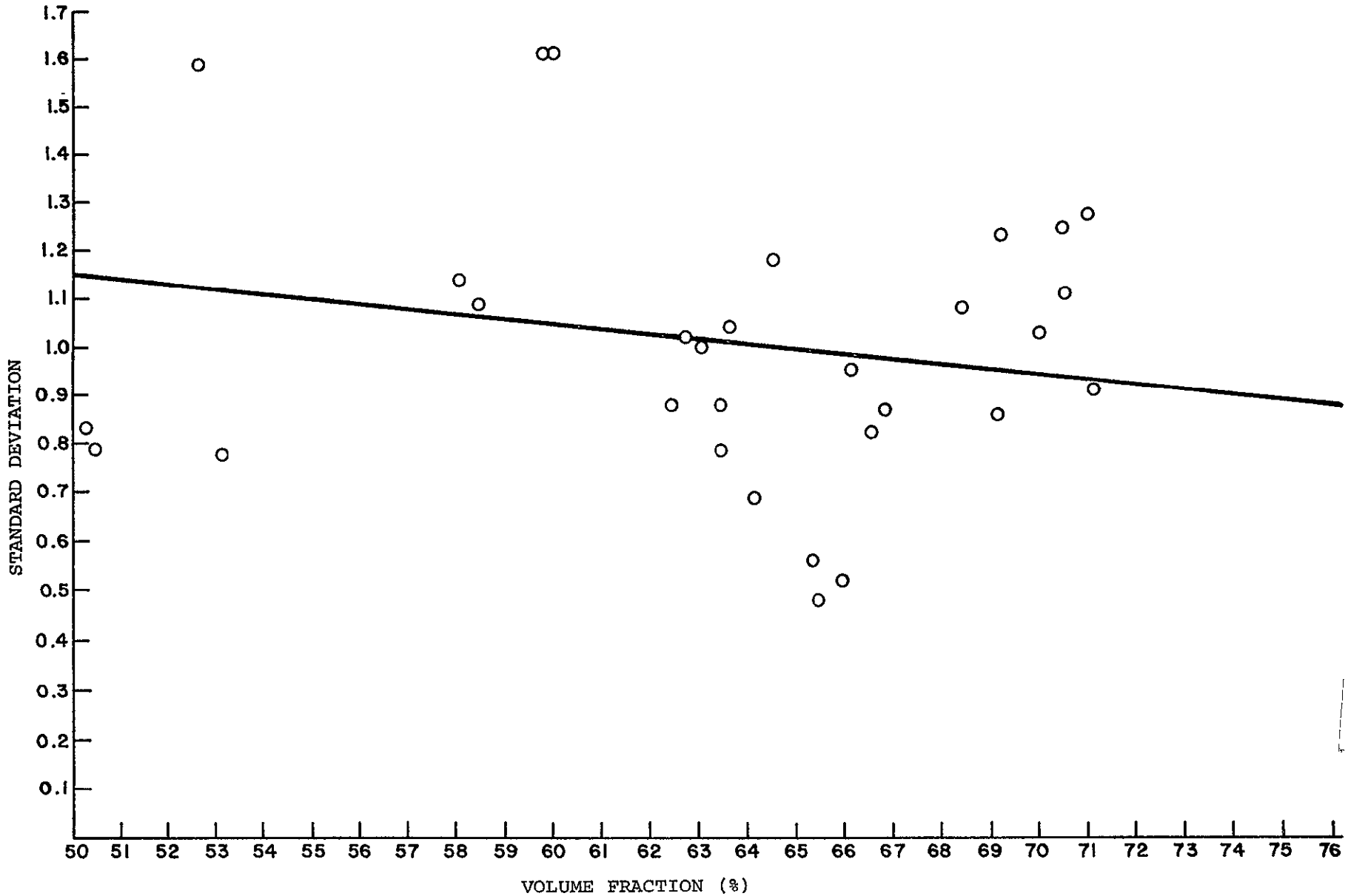

Figure II-A-8a. Standard Deviation versus Volume Fraction. 32nd Subfield Analysis - Composite

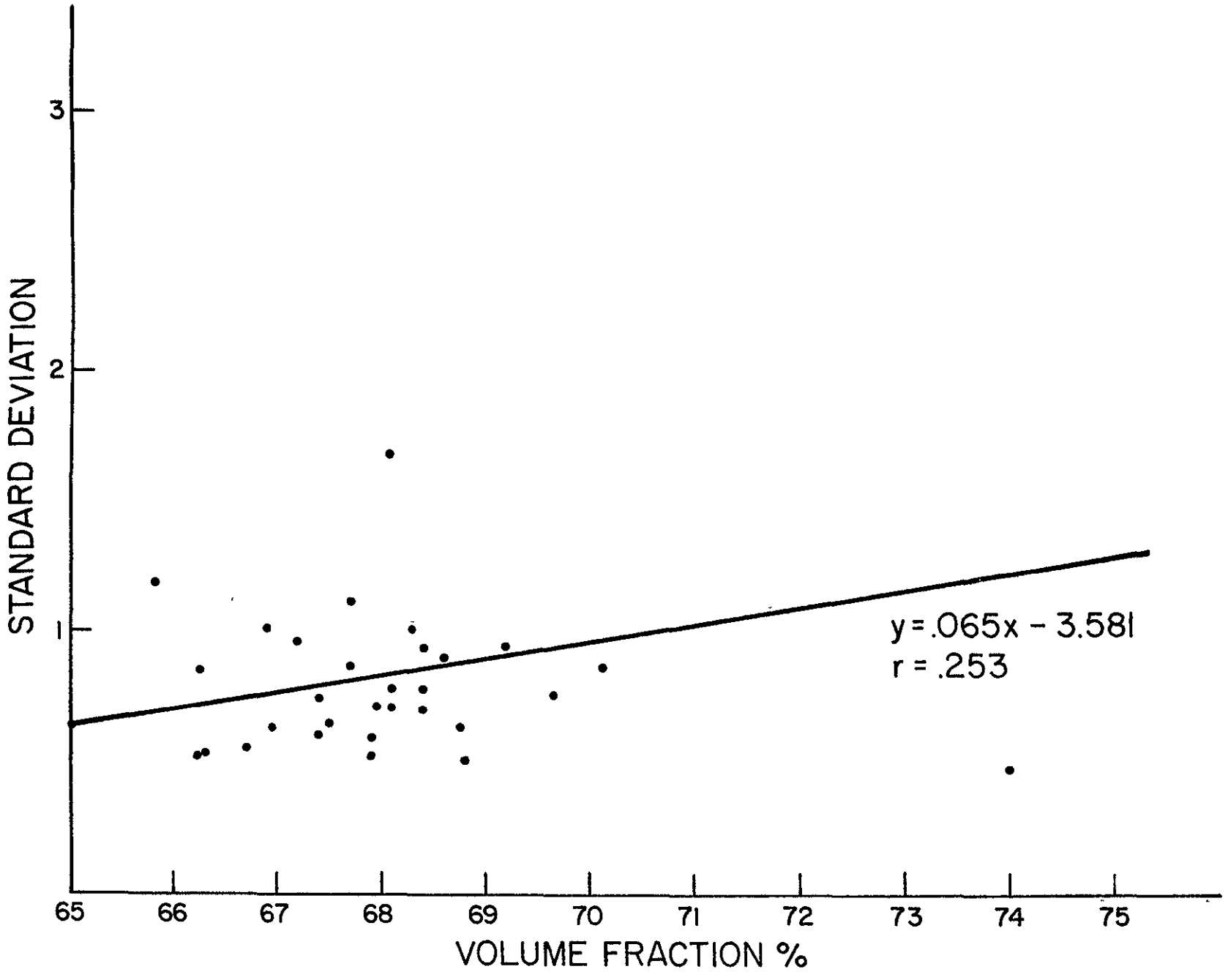

Figure II-A-8b. Standard Deviation versus Volume Fraction: 32nd Subfield Analysis - Square Array

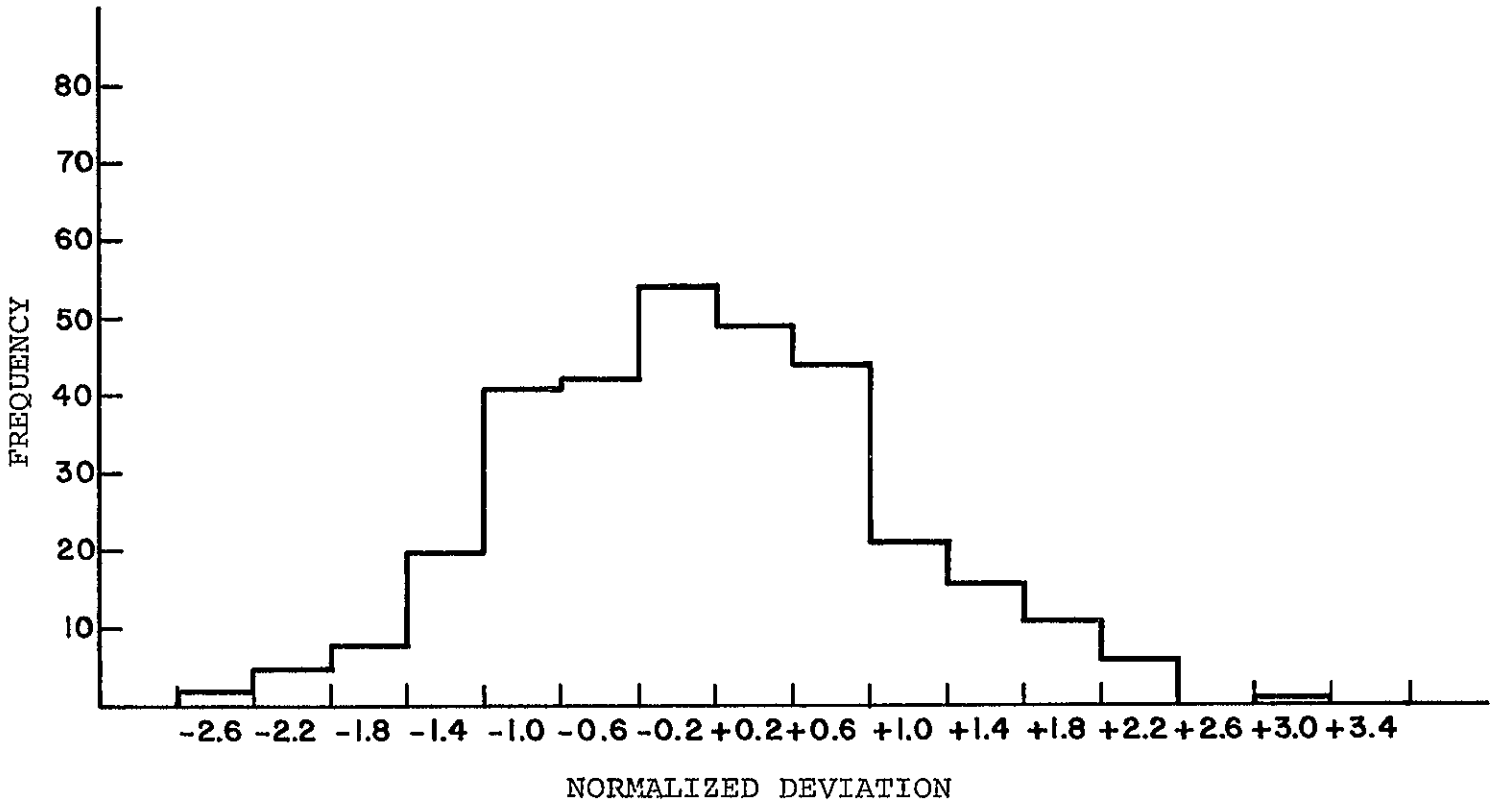

Figure II-A-9a. Frequency versus Normalized Deviation, 320 Points: 32nd Subfield Analysis - Square Array

composite, while Figures II-A-9b and -9c are similar plots for the square array. Again, both data sets appear to be normally distributed, but in this case, the breadths should be the same. The breadth is a measure of the standard deviation in the technique.

Further insight can be gained by constructing a plot of frequency versus volume fraction for the thirty-second subfield analysis for both the composite and the square array. Such are shown in Figures II-A-10a and -10b. As can be ascertained by inspection, the distribution of data for both the square array and composites are quite Gaussian. The distribution for the composite, however, while fairly normal, is skewed towards low volume fraction or resin rich areas (see Figure II-A-10c).

It is possible to plot volume fraction dispersion versus area for a periodic array, in terms of volume fraction versus length in unit cell dimensions. Such a curve, in theory, takes the shape of Figure II-A-11, assuming no instrumental error. The dispersion of the measured volume fractions is shown to decrease with increasing number of unit cell areas, since the relative importance of that part of the subfield area which is not an integer multiple of a unit cell decreases with increasing viewing area. In fact, as the number of unit cells gets very large, the dispersion bands will asymptotically approach zero, since the fractional unit cells are negligible in comparison to the area

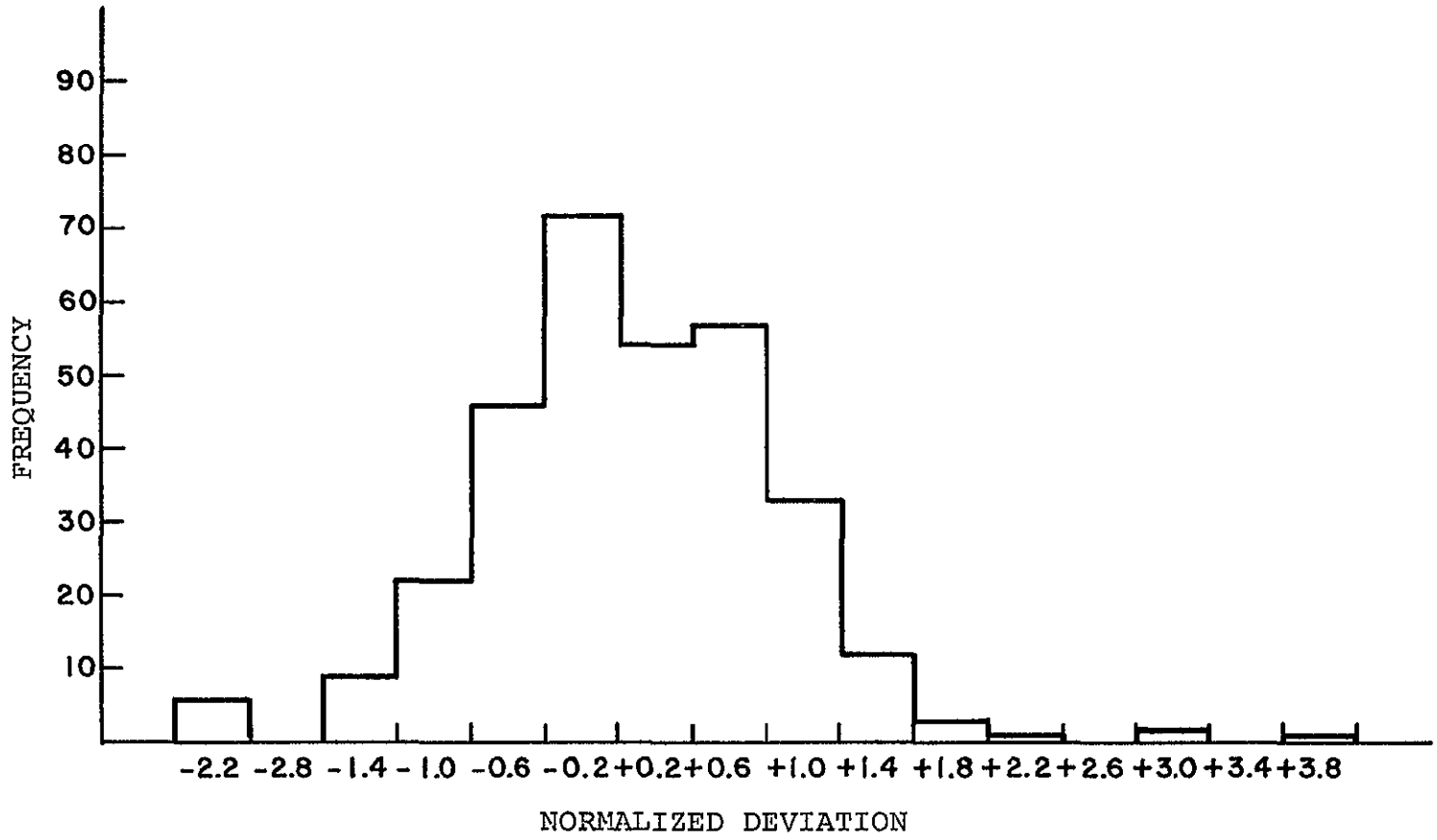

Figure II-A-9b. Frequency versus Normalized Deviation, 320 Points: 32nd Subfield Analysis - Square Array

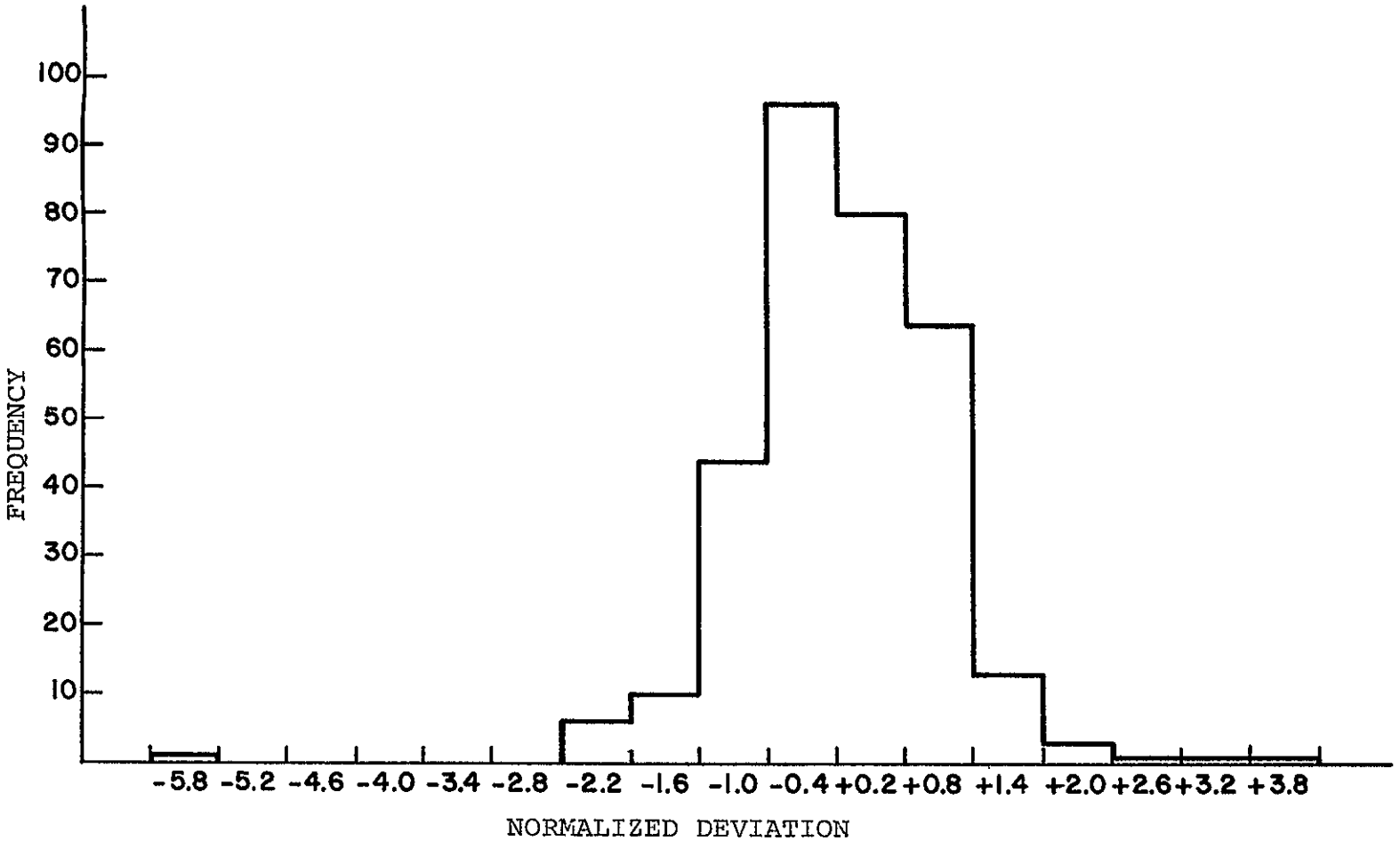

Figure II-A-9c. Frequency versus Normalized Deviation, 320 Points: 32nd Subfield Analysis - Square Array

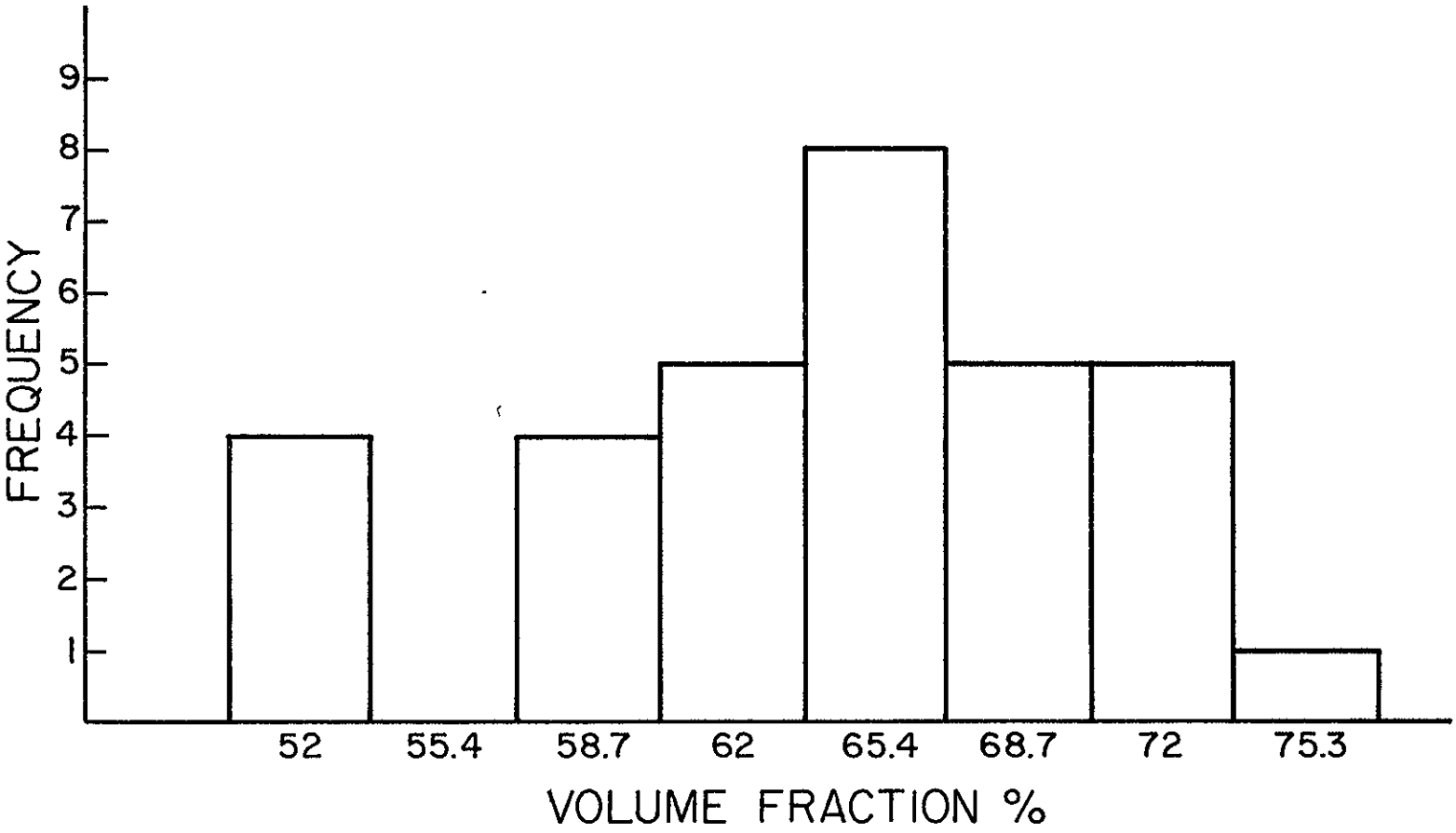

Figure II-A-10a. Frequency versus Volume Fraction: 32nd Subfield Analysis - Composite Data

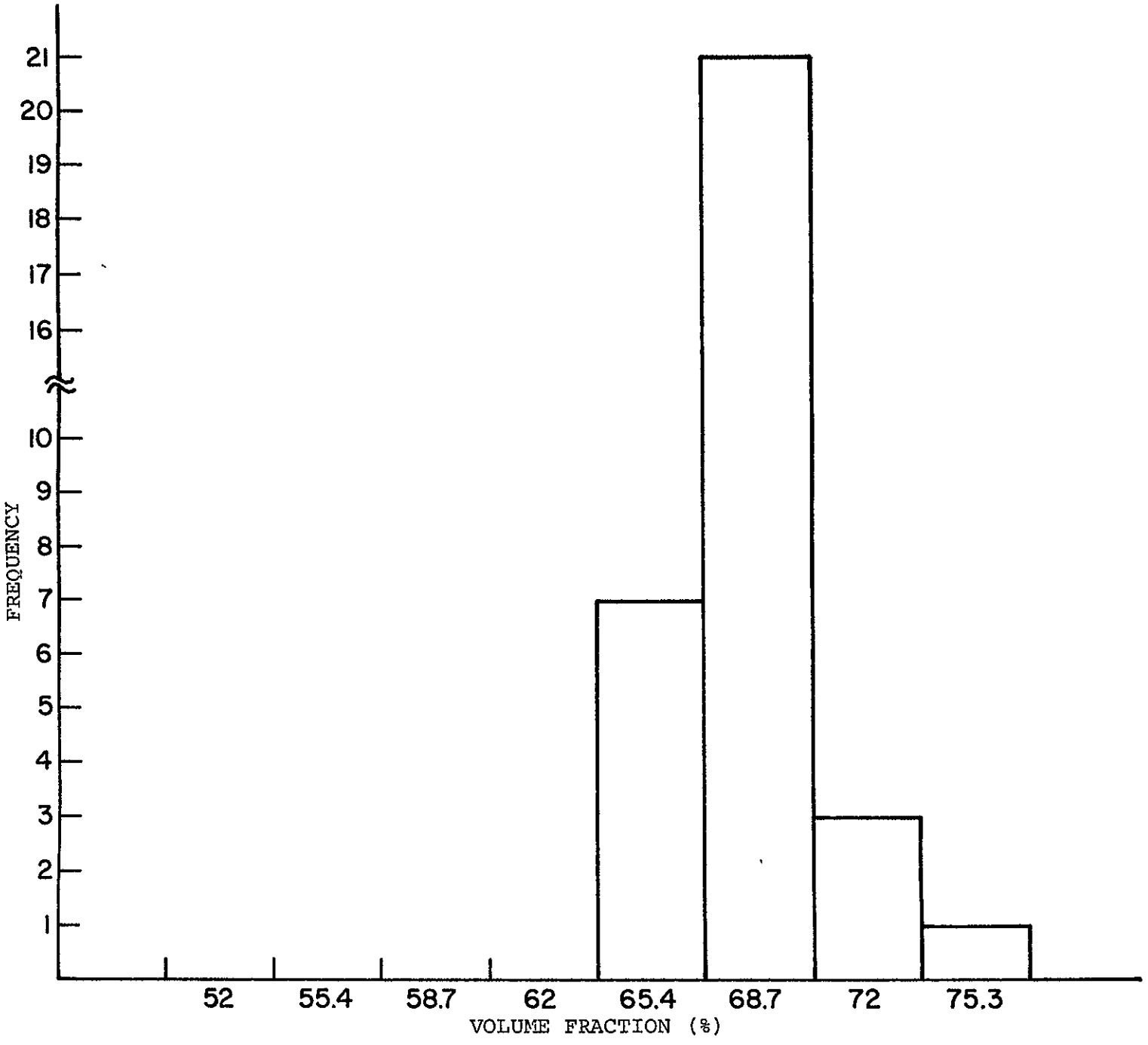

Figure II-A-10b. Frequency vs. Volume Fraction: 32nd Subfield Analysis - Square Array Data

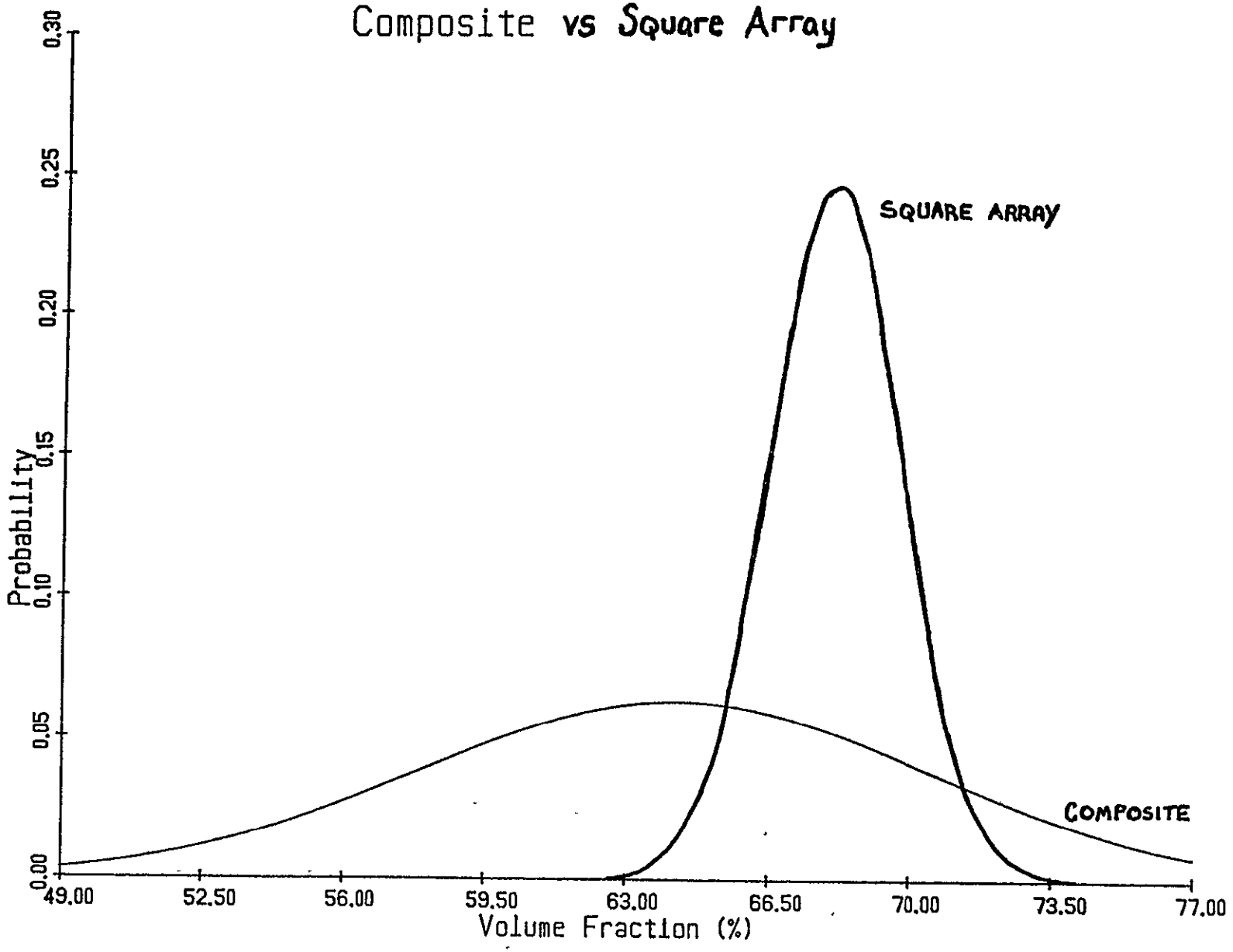

Figure II-A-10c. Normal Curves (based on data for frequency in terms of probability, 32 points each curve) versus Volume Fraction for the 32nd Subfield Analysis Comparison of Composite versus Square Array

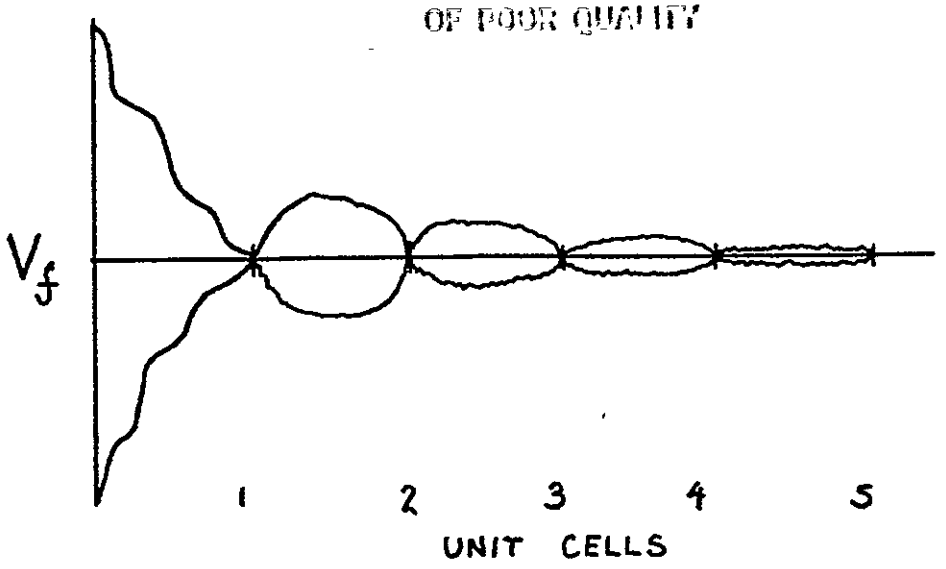

Figure II-A-11. Volume Fraction Dispersion versus Area for a Periodic Array

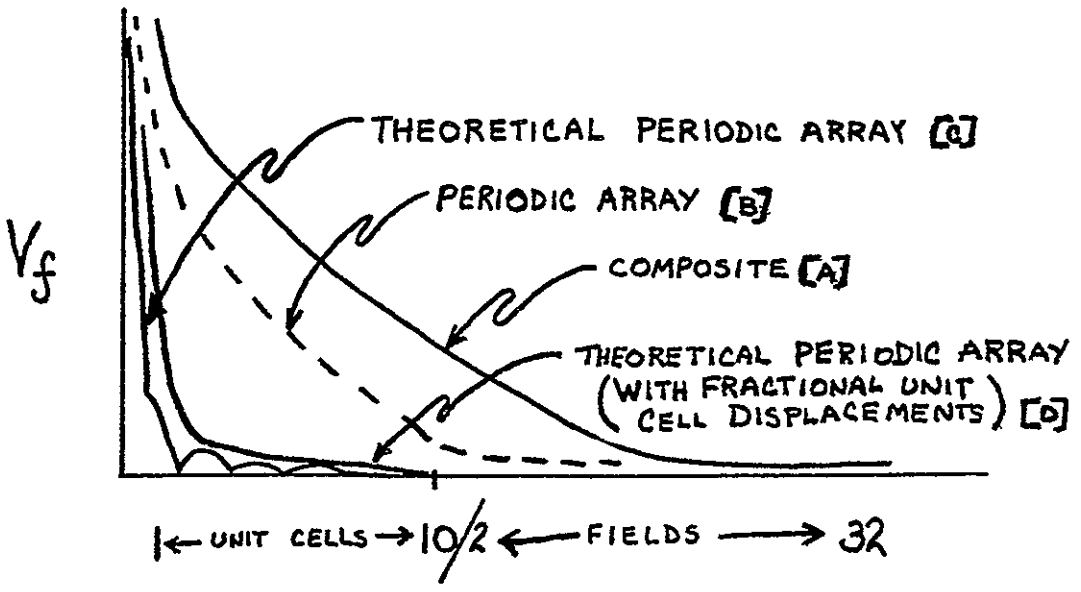

Figure II-A-12. Comparison of Volume Fraction versus Number of Unit Cells for Various Arrays

of view. When the field of view is exactly an integer multiple of a unit cell, the dispersion bands should also be zero.

Figure II-A-12 is a schematic close-up of the composite ([A]), periodic square array ([B]) and theoretical square array ([C]) curves. The experimental square array curve is observed to be broader than the corresponding theoretical curve due to machine broadening. This is similar in nature to the effect encountered in crystallography and x-ray studies. In particular, errors are attributable to the pixel count of the machine. In the case of the composite curve, assuming no machine error, inhomogeneity would increase the dispersion at the nodal points and smooth out the modulation. If the inhomogeneity were at the level of a fraction of a unit cell ([D]), the modulation of the dispersion in V_f would smooth, but not drastically increase. For large inhomogeneities, the disperson increases, as well as smoothing to monotonic behavior.

b. Resin Characterization

Since the overall major goal of the project is the prediction of transverse fiber properties via derivation from the transverse composite properties, the properties of the matrix are a major consideration. To this end, and for the purpose of determining the aging effects in resins used in the ultralight glider, the RP-1 (see Part V-A of this

report), several resin systems were tested for glass transition as well as strength data.

The resin systems were chosen for their properties and their widespread usage in the composites laboratory and the composites structural program. The systems picked were Ciba Giegy epoxies 508 and 509 mixed with Ciba Giegy hardeners XU-224 and XU-225 and a Shell system consisting of epon 828 resin mixed with epon V-40 curing agent. For the case of the Ciba Giegy resin, one of the epoxies was mixed with varying amounts of hardeners. The hardener itself was a mixture of XU-224 and XU-225 which varied in the range from 3-to-1 to 12-to-1, while the ratio of epoxy to hardeners was varied from 3-to-1 to 4-to-1. In the Shell system, the percentage of the V-40 curing agent ranged from 40% to 60%, in steps of 5%. The rationale behind varying the ratio of mixtures is to determine the best matrix system for transverse properties research as well as supplying data for the processing science experiments described in Part V-B. The cure time for the V-40 was approximately 24 hours, but samples were not tested until three days had passed. The 509-based system required approximately three weeks to cure, while the 508 system did not totally cure. Even after three months, the 508 system was still tacky and could easily be plastically deformed. All cures were made at room temperature in an open environment without vacuum. Samples, in disc shape, were not stored in a dessicator so as to reflect with

greater accuracy the actual operating conditions encountered by the components of the RP-1 sailplane. Some of the partially cured 508 system samples were postcured at 212°F for between one to five days in a furnace. The result in each case was still a rubber-like material with the only obvious effect of differing postcure times being a deepening of color with increasing time. Due to these characteristics, the 508 system was dropped from further study.

While it was apparent that the glass transition temperatures for the 508 systems were at or below room temperature, it was felt that the T_g information for the other systems would be useful in characterizing them. The results of work performed using several samples on a differential scanning calorimeter (DSC) indicated that the T_g for the 508 system also occurred at or below room temperature. A verification run of one postcured sample validated the "room temperature or below" T_g hypothesis for the 508 system.

In addition to thermal testing, the discs were measured for diameter and thickness at the center and then mechanically tested to further determine the optimal system. In these tests, edges of the specimens rested around their complete circumferences on a ledge 1/8 inch wide and the load was applied to their centers by means of a blunt rod. The various specimen data and test results are listed in Table II-A-3. In an attempt to estimate the long-term behavior of the matrix material used in the structure of the RP-1

TABLE II-A-3

MODIFIED SHORTBEAM SHEAR TEST RESULTS FOR SEVERAL COMPOSITE RESIN SYSTEMS

Sample Number	Resin Systems 509	224	225	Dia. (in.)	Thick. (in.)	Scale (load)	$P_{yld.}$ (lb.)	$P_{ult.}$ (lb.)	δ and P_y (in.)	$S_{max} = K_1 w/t^2$ (psi)	$E = \frac{Kwa^2}{Y_{max} t^3}$ (psi)
1	24	9	1	1.508	.103	.25	122	126	.0394	11,822	474,643
2	36	9	1	1.487	.168	.25	161	NA	.0787	5,864	72,267
3	36	12	1	∿1.516	.141	.25	98	371	.0197	5,067	297,247
4	36	9	1	1.504	.189	.25	217	NA	.0344	6,245	156,506
5	32	8	1	1.500	----	.25	153	472	.0394	------	-------
6	32	8	1	1.498	.181	.25	294	634	.0492	9,225	168,796
7	30	10	1	1.517	∿.242	.25	444	0.5	.0443	7,794	118,454
8	27	9	1	1.511	∿.185	.5	273	616	.0443	8,200	163,027
9	33	11	1	1.515	∿.188	.5	224	560	.0443	6,525	127,463
10*	24	8	1	1.506	.198	.5	No Curve		No Curve	------	-------
11*	30	10	1	1.511	.213	.5	308	336	.0344	6,979	155,192
12*	32	8	1	1.499	.203	.5	175	259	.0197	4,366	177,868
13*	33	11	1	1.502	.169	.5	147	---	.0148	5,291	344,675
14*	36	12	1	1.499	.195	.25	266	---	.0344	7,191	174,676
15*	24	8	1	1.510	.260	.25	294	500	.0148	4,471	189,313
16*	24	9	1	1.508	.185	.25	140	262	.0148	4,205	250,245
17*	27	9	1	1,508	.205	.25	318	343	.0295	7,779	209,584
18*	30	10	1	1.502	.152	.25	No Curve		No Curve	------	-------
19*	32	8	1	1.503	.198	.25	224	---	.0197	5,874	245,358
20*	33	11	1	1.506	.185	.25	140	---	.0148	4,205	250,245
21*	36	12	1	1.506	.173	.25	147	168	.0246	4,415	193,312
22	24	8	1	1.516	.266	.25	595	1,071	.0443	8,645	119,532
23*	24	8	1	1.508	.246	.5	385	770	.0246	6,540	176,090
24	24	9	1	1.511	.166	.5	217	602	.0394	8,095	201,676
25	24	9	1	1.512	.212	.5	378	770	.0442	8,646	150,001

[Continued]

*post-cured or treated

TABLE II-A-3 (Continued)

Sample Number	Resin Systems 509	224	225	Dia. (in.)	Thick. (in.)	Scale (load)	$P_{yld.}$ (lb.)	$P_{ult.}$ (lb.)	δ and P_y (in.)	$S_{max} = K_1 w/t^2$ (psi)	$E = \frac{Kwa^2}{Y_{max} t^3}$ (psi)
26	24	10	1	1.513	.202	.5	322	791	.0394	8,112	166,081
27	24	10	1	1.515	.194	.5	329	714	.0492	8,986	153,405
28	27	9	1	1.511	.207	.5	266	595	.0443	6,382	133,392
29	27	9	1	1.506	.200	.5	245	574	.0394	6,296	130.195
30	30	10	1	1.506	.182	.5	182	441	.0443	5,648	114,148
31	30	10	1	1.511	.210	.5	259	588	..0443	6,037	105,743
32	32	8	1	1.506	.187	.5	210	504	.0541	6,173	99,429
33	32	8	1	1.504	.173	.5	189	497	.0541	6,492	113,016
34	33	11	1	1.510	.193	.5	217	511	.0443	5,989	114,130
35	33	11	1	1.507	.196	.5	161	427	.0492	4,308	72,796
36	36	9	1	1.507	.096	.5	---	301	------	33,575	-------
37	36	9	1	1.498	.158	.5	---	329	-----	13,548	-------
38	36	12	1	1.512	.224	.5	196	497	.0394	4,016	74,136
39	36	12	1	1.507	.136	.5	126	392	.0492	7,003	170,531
40*	36	12	1	1.512	.183	.5	328	679	.0492	10,068	182,209
41*	30	10	1	1.513	.202	.5	No Curve		No Curve	------	-------
42*	24	9	1	1.513	.223	.5	252	---	.0246	5,209	154,727

*post-cured or treated

TABLE II-A-3 (Continued)

Sample Number	Resin Systems V-40	828	Dia. (in.)	Thick. (in.)	Scale (load)	$P_{yld.}$ (lb.)	$P_{ult.}$ (lb.)	δ and P_y (in.)	$S_{max} = K_1 w/t^2$ (psi)	$E = \frac{Kwa^2}{Y_{max} t^3}$ (psi)
43*	40	60	1.515	.140	.1	126	---	.0344	6,609	223,585
44	40	60	1.515	.137	.5	105	217	.0246	5,751	278,040
45	40	60	1.512	.120	.25	112	---	.0345	7,996	314,681
46*()	40	60	1.513	.109	.1	193	---	.0984	16,699	253,687
47*	40	60	1.515	.148	.1	141	---	.0246	6,617	296,151
48	45	55	1.510	.098	.25	56	63	.0344	5,994	289,712
49	45	55	1.513	.096	.25	112	---	.0738	12,493	287,318
50*-	45	55	1.507	.078	.1	71	---	.0738	11,997	339,573
51*()	45	55	1.508	.105	.1	132	370	.0738	12,308	258,800
52	50	50	1.509	.132	.1	161	---	.0443	9,499	264,676
53	50	50	1.514	.181	.1	396	---	.0640	12,426	174,781
54*()	50	50	1.512	.141	.1	217	430	.0640	11,220	202,599
55*()	50	50	1.514	.163	.1	286	441	.0590	11,066	187,485
56*^	50	50	1.514	.162	.1	209	288	.0492	8,187	167,360
57	55	45	1.512	.104	.1	104	---	.0886	9,885	174,789
58	55	45	1.510	.122	.1	428	451	.3297	29,561	119,746
59*^	55	45	1.511	.109	.1	374	444	.2756	32,360	175,520
60*-	55	45	1.511	.115	.1	272	378	.3199	21,143	93,643
61	60	40	1.511	.095	.1	81	---	.0443	9,226	357,211
62	60	40	1.511	.160	.1	153	---	.0246	6,144	254,338
63*()	60	40	1.513	.103	.1	168	---	.0935	16,279	275,423
64*^	60	40	1.505	.076	.1	94	---	.0886	16,730	404,826

*post-cured

() no change in thickness

^ 1 mil change in thickness

- 2 mil change in thickness

sailplane, several of the samples were postcured and/or submerged in water prior to testing. The purpose was to gain added insight into just how brittle the matrix would become after prolonged exposure (postcuring).

A schematic of the apparatus used in testing the samples is shown in Figure II-A-13. Since the discs are supported at their edges over a radial distance of only an eighth of an inch and centrally loaded, the test is actually a modified three-point bend test. Further, because of the dimensions of the specimens, failure will occur in shear. Maximum shear stress and modulus were calculated for a circular plate with this kind of loading[8]. It was assumed that the blunt rod applied a uniform load over a circular area. The radius of the blunt piston, r_c, was measured and used as the radius of the circular load area. The fact that the rod end was not perfectly flat was ignored, since the disc need only deform a little before the entire radius of the rod was in contact with the specimen.

The values of K and K_1, geometric shape factors, for this specific case were determined. Using interpolation for an a/r_o value of 2.478 ('a' is radius from center of sample to support) yielded values of 1.440 and 1.028 for K and K_1, respectively. The equations used in the calculations are given as follows:

$$S_{max} = K_1 w/t^2 \qquad (12)$$

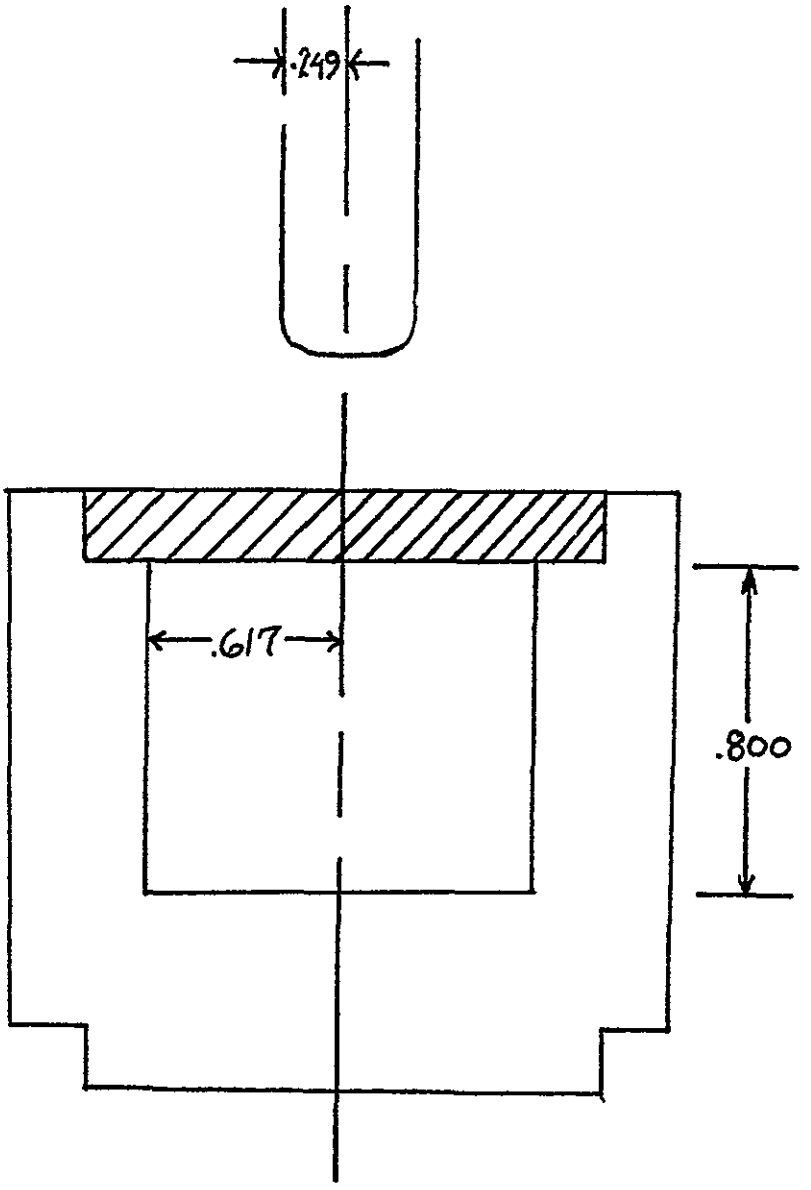

Figure II-A-13. Schematic Diagram of Modified SBS Test Apparatus

$$Y_{max} = Kwa^2/Et^3 \quad (13)$$

where

S_{max} = maximum shear stress

Y_{max} = maximum deflection

E = isotropic Young's modulus

w = load

a = one-half support distance (constant)

t = specimen thickness.

Rearranging Equation (13) to solve for modulus yields:

$$E = Kwa^2/Y_{max}t^3 \quad (14)$$

Table II-A-3 lists the test results and the calculated values for S_{max} and E. Table II-A-4 lists special conditions, if any, for the discs listed in Table II-A-3. Tables II-A-5 to -7 illustrate some of the effects on dimensional stability of heat-treatment and moisture absorbance encountered with some of the resin systems.

c. Short Beam Shear Strength/Homogeneity

The effect of homogeneity on the properties of different samples is to be determined using shear strength as a measure. This choice was based on the fact that it is easier to pick up packing differences in the short beam shear (SBS) test than in a tensile test. Two different fabrication techniques for the test specimens were employed. The first was a typical lay-up (Specimen #20), consisting of 27 layers

TABLE II-A-4

ENVIRONMENTAL CONDITIONS ON TEST DISCS

Specimen Number	Heat-Treatment Time (hrs.)	Heat-Treatment Temp. (°C)	Other
10	48.5	100	----------
11	48.5	100	----------
12	48.5	100	----------
13	48.5	100	----------
14	48.5	100	----------
15	73	100	----------
16	73	100	----------
17	73	100	----------
18	73	100	----------
19	73	100	----------
20	73	100	----------
21	73	100	----------
23	18	100	----------
40	6	100	----------
41	15	100	----------
42	12	100	----------
43	9	60	----------
46	12	60	----------
50	9	70	----------
51	12	60	----------
54	12	60	----------
55	----	---	60 hrs. submerged in H_2O.
56	21	60-75	Submerged in H_2O bath for duration.
59	12	60	----------
60	----	---	60 hrs. submerged in H_2O.
63	12	60	----------
64	36	60	----------

TABLE II-A-5

WEIGHT GAIN CHARACTERISTICS OF RESIN EMERSED IN WATER

Sample Number	Time (hrs.)	Temp. (°C)	Weight (g)		Δ wt. (g)	Δ (%)
			Before	After		
55	60	Room	5.570	5.602	.032	.57
56	60	Room	5.5851	5.7179	.1328	2.38
60	36	60-75	3.9132	4.0512	.1380	3.53

TABLE II-A-6

SHRINKAGE DATA FOR TYPICALLY POST-CURED RESIN MATERIALS

Sample Number	Initial Diameter (in.)	Diameter After Post-Curing at 60°C for 12 Hrs.	Δ (%)	Initial Thickness (in.)	Thickness After Post-Curing at 60°C for 12 Hrs.	Δ (%)
46	1.513	1.510	-.20	.109	.109	0
51	1.508	1.509	.07	.105	.105	0
54	1.512	1.513	.07	.141	.141	0
59	1.511	1.510	-.07	.109	.110	0.92
63	1.513	1.512	-.07	.103	.103	0
64	1.505	1.510*	.33*	.075	.076*	1.33*

*Data is for post-curing at 100°C for 36 hours.

TABLE II-A-7

PERIODIC SHRINKAGE DATA FOR RESIN SAMPLE NUMBER 23

t (hrs. at 100°C)	Diameter (in.)	Thickness in.(m)
0	1.508	.228 (5.800)
2	1.516	.231 (5.874)
4	1.512	.244 (6.206)
6	1.514	.246 (6.264)
18	1.513	.246 (6.256)
1 hour after	1.512	.246 (6.250)

	Initial (in.)	Final (in.)	1 Hr. Cool Off (in.)	Δ (in.)	Δ (%)
Diameter*	1.508	1.513	1.512	.004	.26
Thickness	.228	.246	.246	.018	7.89

*in inches

of graphite prepreg cured in a Dake 75-ton press. The temperature was increased to 174°F in approximately 40 minutes at which time 300 psi pressure was applied. The temperature was then further increased to 250°F in approximately twenty minutes. Temperature and pressure were held constant for two hours. The part was then cooled to 75°F, the pressure removed and the cure process considered complete. Twelve layers of bleeders were used to absorb the excess resin and to increase the volume fraction of the fibers. The second technique was to make composites by using fiber bundles and a room temperature-curing resin. The idea was to attempt to characterize the two ends of the fabrication spectrum; i.e., well-made and poorly-made composites.

Specimen #20 was chosen for investigating the prepreg fabrication technique. Three test samples were cut for each fiber orientation, longitudinal and transverse. The samples were then tested in an Instron 1333 mechanical tester. Specifications, test results and calculated values for maximum shear stress are presented for the specimens in Table II-A-8. The equation utilized for the calculation is $S_{max} = 3P/4bd$ and is given in the ASTM Book of Standards, Part 36[9], where P = applied load, and b and d are the width and depth of the cross section, respectively.

Results to date are available only for the 250°F, 300 psi cured prepreg. Sideviews of the failures in the longitudinal specimens are given in Figure II-A-14. Parts (A) and

TABLE II-A-8

SHORTBEAM STRESS DATA

Sample	Length (in.)	d Thickness at Midspan (in.)	b Width at Midspan (in.)	Load (lbs.)	Shear Stress (psi)
20-XTA	.921	.129 + .003	$.267\ \frac{-.004}{+.001}$	116	2526
20-XTB	.982	.129 + .001	$.273\ \frac{-.008}{+.002}$	84	1789
20-XTC	.911	.131 + .002	$.284\ \frac{-.005}{-----}$	143	2883

Sample	Load (lbs.)	bd ($in.^2$)	Shear Stress (psi)
20-XLα	468	.0826	4249
20-XLβ	431	.0782	4134
20-XLγ	456	.0772	4430

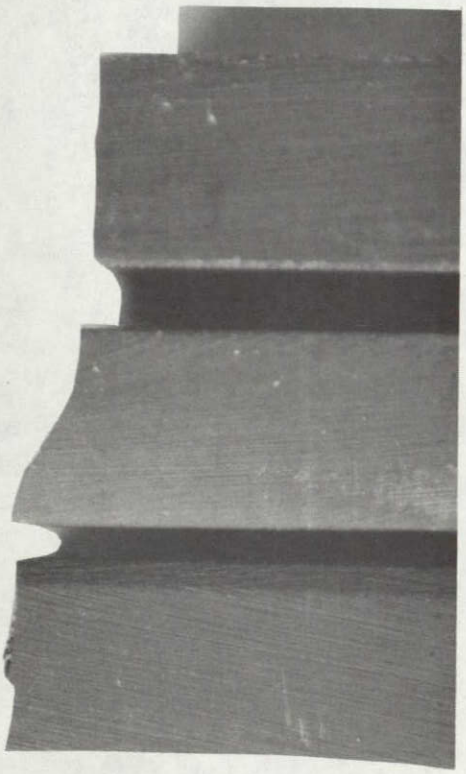

(A) (B) (C)

Figure II-A-14. Sideviews of Failed Short Beam Shear Specimens

and (C) show planar failure surfaces, while part (B) exhibits a beveled type of surface failure. A head-on look at the failure surface is provided in Figure II-A-15. As can be seen, the specimens failed in a brittle manner. High variability of results often is associated with brittle fracture, and, in these cases, failure stress cannot be described with a single number but as a probability of failure at a given stress.

One problem encountered in using a three-point bending test is in choosing the appropriate span-to-depth ratio which insures that the specimen will fail in shear. If the span-to-depth ratio is too large, then the specimen fails in bending on the tension side, while a bearing-compressive type failure, under the loading point, results if the span-to-depth ratio is not high enough. The longitudinal specimen #20 samples are suspected of failing in a compressive mode, although some shear cracks are visible. This is substantiated by the pictures in Figures II-A-16a and -16b and -17 for γ, α and β, respectively. This type of microstructure is indicative of a compressive failure in a bend test. Figure II-A-18 is an exploded view of the β specimen. A side experiment that would add insight into the phenomenon of failure via compression would be a photographic examination of a specimen with a single fiber failed in a buckling mode. Future experiments will be conducted with further steps taken to insure failure in the desired mode.

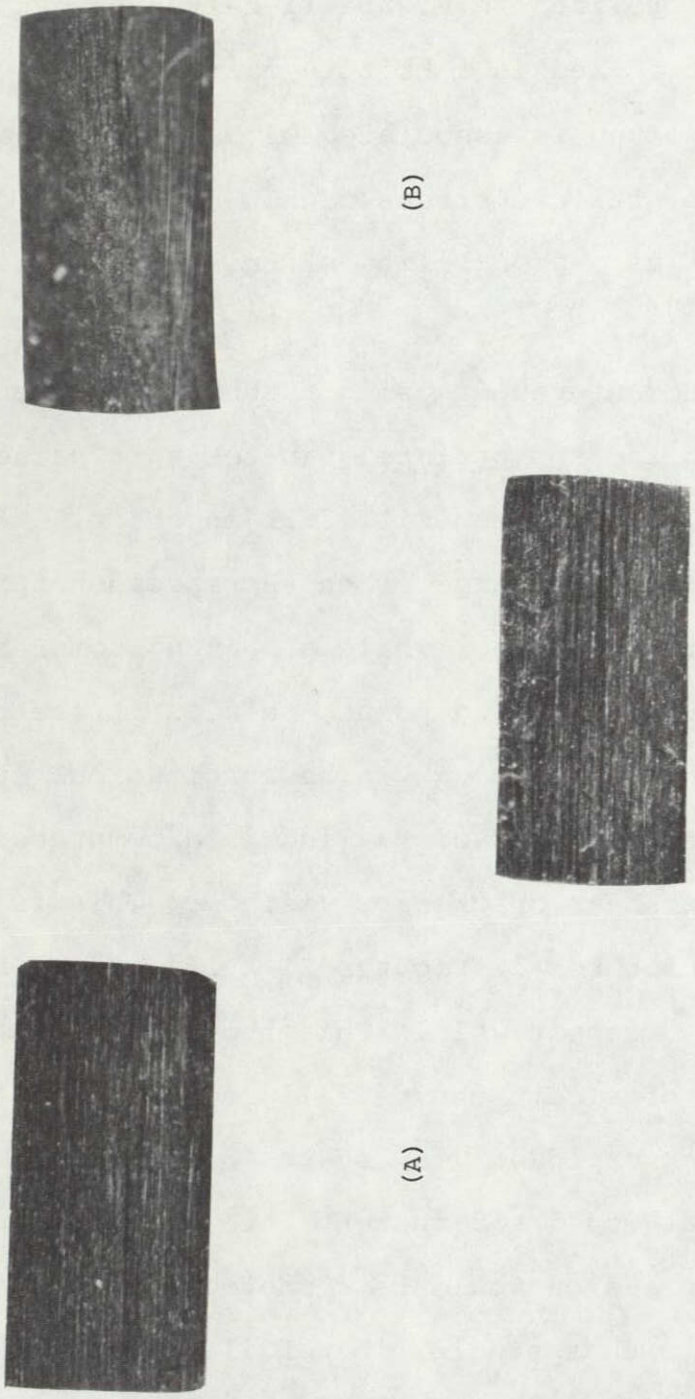

(A) (B) (C)

Figure II-A-15. Photographs of Failed Cross-Sections Short Beam Shear Specimens

(A) Specimen 20-XL γ (100X)

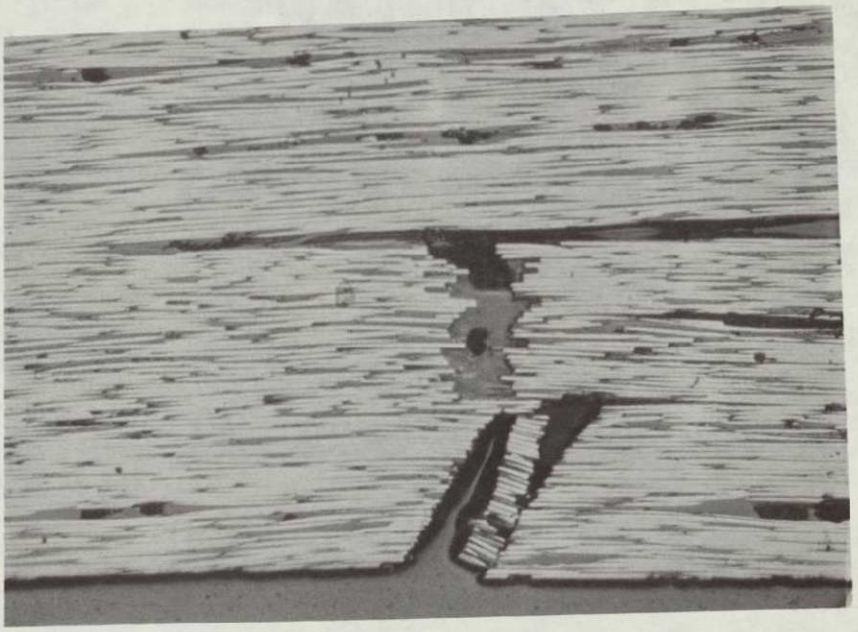

(B) Specimen 20-XL α (100X)

Figure II-A-16. Evidence of Compressive Failure in Short Beam Shear Specimen 20-XL

Specimen 20-XL β (100X)

Figure II-A-17. Evidence of Compressive Failure in Short Beam Shear Specimen 20-XL

Figure II-A-18. Exploded Views of Specimen 20-XL β (500X) (showing compressive failure and laminar cracking and misalignment; note the moisture spot)

The materials used in the specimen molding were Hercules' HMS fiber strands and the Miller-Stephenson resin system. The V-40 and 828 compositions were varied and are given along with specimen and test dimensions in Table II-A-9. In many cases post-test examination showed that the interior fibers were not completely wet, thus explaining the low shear failure stress results. Future work will emphasize refining fabrication techniques to prevent this phenomenon from reoccurring.

d. Thermal Expansion Coefficients

The thermal coefficient of expansion, CTE, is an important quantity in the process of determining composite and fiber constituent data. Further, transverse CTE may also provide another way to evaluate property variations with homogeneity.

Specimens for these kinds of tests have already been fabricated[10]. To date, a number of samples have been tested for CTE. The first, a practice run, was tested at a rate of 5°C/min. This rate was found to be too fast to achieve thermal equilibrium in the sample. One means available to achieve equilibrium is long thermal stabilization times. However, there are advantages to finding a heating rate that facilitates a constant heating mode, thereby alleviating the need to reach complete thermal equilibrium. The problem then translates into one of compensating for the poor thermal conductivity of the material.

TABLE II-A-9

SHORTBEAM SHEAR TEST RESULTS OF VARIOUS COMPOSITIONS OF V-40/828*

Specimen	Composition	Length (in.)	b Width (in.)	d Thickness (in.)	Span (in.)	Span/Depth	S_{max}** (psi)
A	50% V-40	1.751	.245	.112	.750	6.70	2400
B	50% V-40	1.751	.243	.129	.750	5.81	5275
C	40% V-40	1.654	.185	.095	.750	7.89	3875
D	50% V-40	1.546	.245	.102	.750	7.35	4200
E	50% V-40	1.739	.248	.049	.750	15.62	2400
F	50% V-40	1.732	.245	.082	.250	3.05	5500

*V-40/828 - reinforced with Hercules As-4 Fiber

**$S_{max} = 3P/4bd$

In order to estimate the thermal transmittance of the samples, a sample was placed between two blocks of copper, and one of the blocks was placed on a hot plate heating source. One would expect that a uniform temperature would be obtained in the copper block. Even with the large heat sink provided by the second copper block, the temperature difference never exceeded 6½°C. The temperature difference in a specimen undergoing CTE testing at a heating rate of 1°C/min. is, therefore, estimated to be less than one-half this value for the composites that are to be studied. The effect of not reaching equilibrium with a constant heating rate seems likely to be just a lag effect on the sample. It may, therefore be a reasonable approximation to consider that the effective terminus of the testing temperature range is shifted 2 to 4°C lower. To test this hypothesis, a sample will be run at a rate of 1°C/min., and then the same sample will be allowed to stabilize and the two results compared to determine how close the CTE measured with the 1°C/min. constant rate is to that measured using stepped equilibrium conditions.

Specimens for which results have been obtained thus far were tested on a Dilatronic brand dilatometer manufactured by Theta Industries. The furnace used, a 1600C, is capable of temperatures over 1500°C. The process is regulated and controlled by a transducer signal conditioner, and the apparatus is monitored by built-in programming capabilities.

Data is recorded automatically at desired intervals by a Fluke data logger, model 2200B. Three critical parameters are monitored every two minutes: 1) furnace temperature, 2) sample temperature and 3) dilatometer millivolt output. The change in millivolts can be easily calibrated in terms of expansion by a micrometer included in the test apparatus. The machine can accommodate specimens of any length up to two inches and any width up to one-half inch. Any geometry can be handled, but the most accurate results are obtained with a flat plate of length approximately one inch and width one-half inch.

Several such samples have already been tested. The specimens and their dimensions, weights (before and after testing) and drying times at 150°C before testing were recorded. Neglible change in weight indicates that no moisture gain or loss occurred during testing. Since the sample holder is made of alumina, a fused quartz cylinder was run as a standard in order to determine and subtract out the expansion of the alumina. The quartz also serves as a check on the accuracy of the system and as a means of calibrating it or enabling a correction factor to be calculated. The expansion of the quartz, the temperature range and the heating rate are given in Table II-A-10. This table also presents values for some of the samples already tested. The curve of the expansion of the quartz must be subtracted from (or, as the case may be, added to) the expansion curve of

TABLE II-A-10

COEFFICIENT OF THERMAL EXPANSION FOR COMPOSITE MATERIALS AND QUARTZ

Specimen	Lower Temp °C	Upper Temp °C	CTE ($x10^{-6}$) Range in./in./°C
1-3TA	30.3	107.9	65.0
1-3TB	28.0	107.0	61.1
2-3TA	25.3	107.0	64.0
2-3TB	27.8	107.0	64.6
3-XTA	23.4	107.5	64.2
3-XTB	31.3	106.9	62.1
4-1TA*	29.7	107.7	62.3
4-1TA	28.0	107.2	60.3
4-1TB	31.3	106.6	60.7
5-XTA*	27.9	107.7	69.9
5-XTA	26.3	107.0	61.6
5-XTB	30.3	106.8	62.7
5-51a	26.4	106.4	-8.4
6-3TA	26.6	107.1	63.1
6-3TB	30.6	106.9	58.7
6-31a	28.9	107.9	-9.4
8-4TA	30.8	107.1	33.3
8-5TA	30.7	106.5	40.2
†8-XT	22.1	151.8	47.3
8-x1a	29.9	106.8	-4.9
9-XTA	21.7	107.4	34.9
9-XTB	29.4	107.4	34.5
10-5TA	29.0	107.1	33.1
10-5TB	31.8	107.6	29.7
10-51a	26.6	107.4	-6.3
11-3TA	30.3	107.2	40.5
11-3TB	30.1	106.6	37.0
11-51a	27.1	106.5	-6.7
12-1TA	28.7	107.0	31.8
12-1TB	29.6	107.7	31.7
12-41a	30.2	108.0	-5.7
13-XTA	23.8	107.8	36.9
13-3TA	30.5	106.9	38.1
13-51a	29.1	106.9	-5.8
14-4TA	29.5	106.4	28.1
14-4TC	31.4	106.8	26.5
15-TA	25.7	107.0	28.7
15-TB	20.3	106.9	22.4
15-LA	24.8	108.1	-6.2
16-1TA	30.8	107.2	29.3
16-1TB	29.6	106.6	26.9
16-31a	27.0	107.4	-5.9
17-2TC	21.6	107.9	26.2
17-5TA	26.7	107.7	29.4
17-31a	21.3	106.4	-5.2

[Cont'd.]

TABLE II-A-10 (Continued)

Specimen	Lower Temp °C	Upper Temp °C	CTE ($x10^{-6}$) Range in./in./°C
18-4TA	29.7	107.8	23.3
18-XTA	30.5	107.0	31.3
18-11a	28.1	107.4	-6.6
19-XTA	28.4	107.7	24.8
19-XTB	30.5	106.5	23.5
20-4TC	30.3	106.9	24.9
20-5TA	17.5	107.3	25.4
20-51a	28.9	107.3	-5.9
21-1TA	19.8	106.6	30.3
21-1TC	29.4	107.6	28.1
21-41a	29.7	107.6	-5.2
22-4TA	23.4	107.2	26.3
22-4TB	30.4	107.1	25.6
23-5TA	19.6	107.4	24.1
23-5TB	31.4	106.8	21.1
24-3TA	28.0	108.0	29.7
24-3TB	27.4	107.8	27.3
24-51a	29.1	107.7	-3.0
25-XTB	33.4	106.0	27.6
25-XTC	31.1	107.9	27.4
26-1TA	29.1	106.4	26.3
26-1TB	29.6	107.1	24.7
26-41a	29.6	106.4	-5.6
27-XTA	29.6	106.8	24.0
27-XTB	30.1	107.4	21.5
27-x1a	27.5	106.8	-6.1
28-XTA	24.9	106.9	40.6
28-XTB	29.3	107.3	44.9
29-5TA	19.6	106.4	29.9
29-5TC	31.3	108.3	24.5
30-4TA	28.1	106.5	38.0
30-XT	44.7	106.0	50.5
30-x1a	30.5	108.0	-1.5
31-XTA	23.7	106.7	26.5
31-XTB	29.6	106.5	25.5
32-1TA	28.4	107.6	43.9
32-1TC	30.6	106.8	43.3
32-11a	28.9	107.3	-6.3
33-4TA	28.6	107.6	30.2
33-4TC	31.1	107.3	25.1
33-11a	23.1	107.4	-3.8
34-1TC	18.5	106.5	34.9
34-1TA	28.7	106.3	36.8
35-2TA	26.2	106.7	42.7
35-2TB	30.9	106.9	39.0
36-XTB	17.4	106.5	28.0
36-XTC	24.2	105.5	24.6

[Cont'd.]

TABLE II-A-10 (Continued)

Specimen	Lower Temp °C	Upper Temp °C	CTE ($x10^{-6}$) Range in./in./°C
37-4TA	26.9	106.4	49.7
37-4TC	27.3	107.0	50.0
38-1TA	26.7	106.5	30.4
38-1TC	29.6	107.2	26.1
39-XTA	20.5	106.5	23.6
39-1TB	27.4	106.8	24.7
QUARTZ	35.9	106.8	3.6
quartz	22.8	142.1	3.6
1908 2*	28.1	107.0	69.9
1908 2	25.8	107.3	67.7
1908 3	25.7	107.0	63.8
979-A1*	24.6	106.9	63.2
979-A1	25.9	107.8	56.2
979-B1	24.6	106.7	56.6

† All samples were run at a programmed heating rate of 1 °C/min. Sample 8-XT was run at a rate of 5 °C/min.

* All samples were postcured unless denoted by a "*". In this case the sample was tested prior to postcuring. [Subsequently postcured and tested.]

NOTE: Items 1-6 --- Kevlar
Items 8-39 -- Graphite
Items 979 & 1908 --- Neat Resin

the samples to eliminate the expansion of the alumina, since the recorded data reflects the differential expansion between the alumina boat and the sample. This can be facilitated by using a Bascom-Turner 800 smart recorder. After running a significant number of CTE experiments, the next phase will be to determine the volume fraction for each sample after they have all been mechanically tested for elastic constants and - because of its importance to homogeneity aspects - short-beam shear. Two things are then possible. First, a plot of CTE versus volume fraction can be constructed, and the transverse CTE value of the fiber determined by extrapolating to a volume fraction of 100 percent. Second, the test data can be correlated and the concept of homogeneity included in property assessment.

4. Plans for Upcoming Period

Future work will continue in several major areas, one of which is the effect of unit cell periodicity on homogeneity of the composite. As reported here, the preliminary work performed in this area tends to support the hypothesis that if the view space is n (i.e., an integer multiple) unit cells, the only variance is machine error and that dispersion is at a minimum. Future work will attempt to model this problem via theoretical calculations and compare it to actual experimental results. Once this phenomenon is more fully understood, the shape of the curve in Figure II-A-12 can be

described and perhaps the previously mentioned "machine broadening" can be accurately predicted.

Work has also started on the concept of fiber dimensions and agglomerated fiber dimension distributions and their relationship to packing. As can be seen from Figure II-A-19, such items as distribution of fiber diameter, maximum horizontal length to the longest dimension and maximum width to area are being investigated as potential shape factors. The concept may also be applicable to resin rich areas and warrants further experimentation.

Further work will also proceed in the area of resin characterization. Mechanical testing will also continue. As mentioned in the report, appropriate steps will be taken to make sure all fibers are wet, that the composite is not too densely packed and that the necessary span-to-depth ratio will be incorporated in SBS specimens so that they fail in the desired shear mode. Thermal expansion runs and analysis will continue. Eventually, the work will be assembled in such a way as to enable the accurate prediction of transverse properties.

5. References

1. Jones, R. M., "Mechanics of Composite Materials", Scripta Book Co., 1975, 110-115.

2. Chamis, C. C. and G. P. Sendeckyj, "Critique on Theories Predicting Thermoelastic Properties of Fibrous Composites", Journal of Composite Materials, July 1969, 332-358.

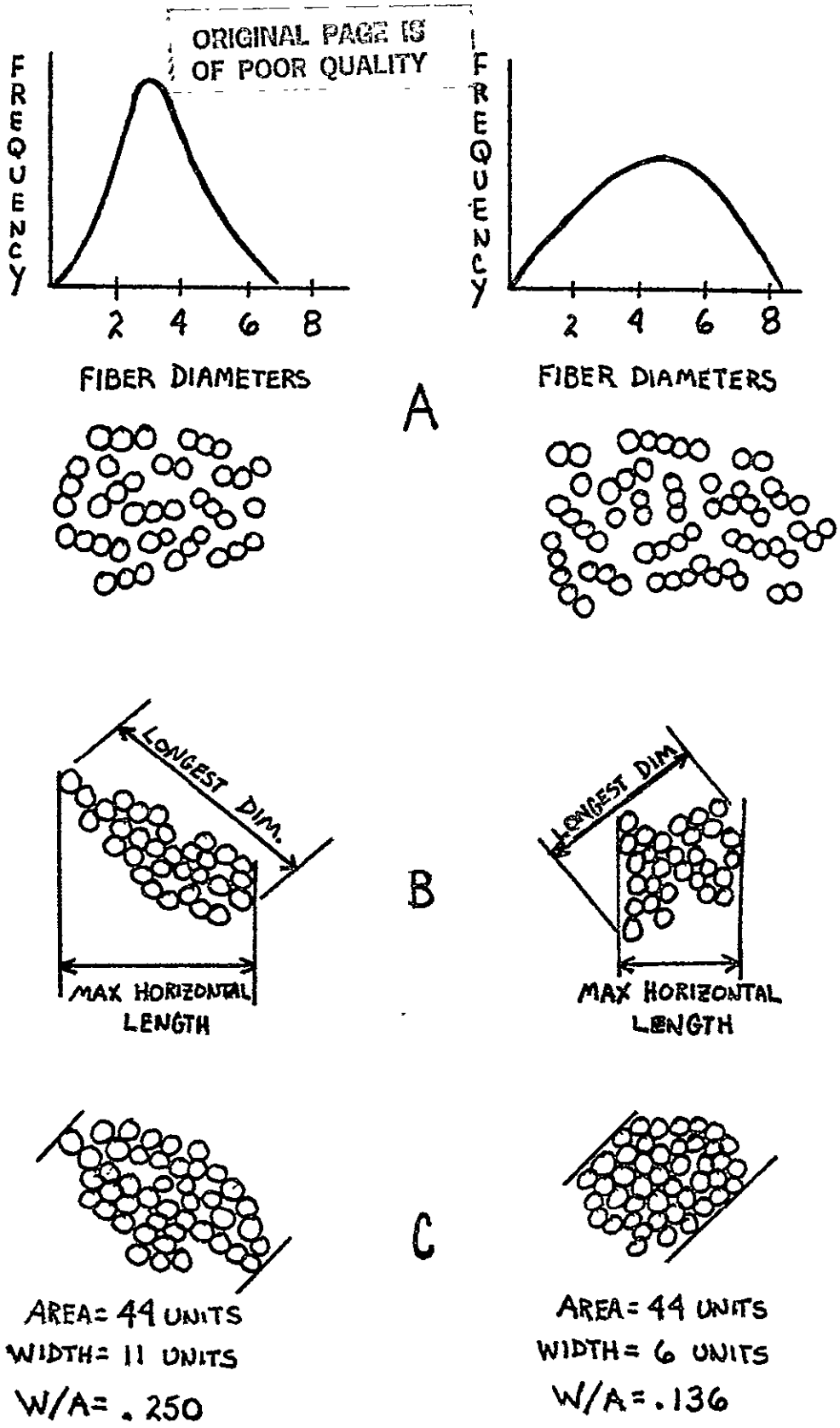

Figure II-A-19. Schematic Diagrams Depicting Fiber Packing
A - Agglomerated Fiber Dimension Distribution
B - Max. Horizontal Length and Longest Dimension
C - Width to Area

3. Tsai, S. W., "Structural Behavior of Composite Materials', NASA CR-71, July 1964.

4. Halpin, J. C. and S. W. Tsai, "Effects of Environmental Factors on Composite Materials", AFML-TR 67-423, June 1969.

5. Hermans, J. S., "The Elastic Properties of Fiber Reinforced Materials When the Fibers are Aligned", Proc. Kon. Ned, Akad Wentensch Amsterdam, Ser B, Vol. 70, No. 1, pp. 1-9.

6. Hill, R., "Theory of Mechanical Properties of Fiber Strengthened Materials - (1) Self Consistent Model", Journal of Mechanics and Physics of Solids, August 1965, 189-198.

7. Piggot, M. R., "Load Bearing Fiber Composites", Pergamon Press, Oxford, 1980, 84-85.

8. Griffel, W., "Plate Formulas", Frederick Ungar Publishing Co., New York, 1968, 21.

9. 1978 Annual Book of ASTM Standards, Part 36, "Plastics-Materials, Film, Reinforced and Cellular Plastics; High Modulus Fibers and Their Composites", American Society for Testing and Materials, Philadelphia, 1978, 361-364 (D2344).

10. Diefendorf, R. J. and J. F. Helmer, "40th Semi-Annual Progress Report, Composites Structural Program", NASA/AFOSR, May 1981.

11. Van Vlack, L., "Elements of Materials Science", Addison-Wesley, London, 1975, 470.

6. Current Publications or Presentations by Professor Diefendorf on this Subject

"Principles and Potential of Composites in High Temperature and Ceramic Matrix Composites for Oxidizing Atmosphere Applications"

Published in NMAB - 376, October 1981, 47-96.

"Ceramic Composites"

Presented at the Norton Company, Worchester, MA, October 22, 1981.

"Composite Materials"

Presented at the General Electric Company, Saratoga, NY, October 28, 1981.

"The Structure of Carbon Fibers and the Consequences on Performance"

Presented at the DuPont Pioneering Research Lab., Wilmington, DE, November 3, 1981.

"The Strength of Carbon Fibers"

Presented at Exxon Enterprises, Fountain Inn, South Carolina, November 4-5, 1981.

"Aerospace Applications of Composite Materials"

Presented at the ACS and Society of Plastics Engimeers Meeting, Albany, NY, January 6, 1982.

"Structure of Carbon Fibers and Consequences on Performance"

Presented at the Aerospace Corporation, El Segundo, CA, January 14, 1982.

"Residual Stresses in Carbon Fibers"

Presented at the Gordon Conference on Composite Materials, Ventura, CA, January 18-22, 1982.

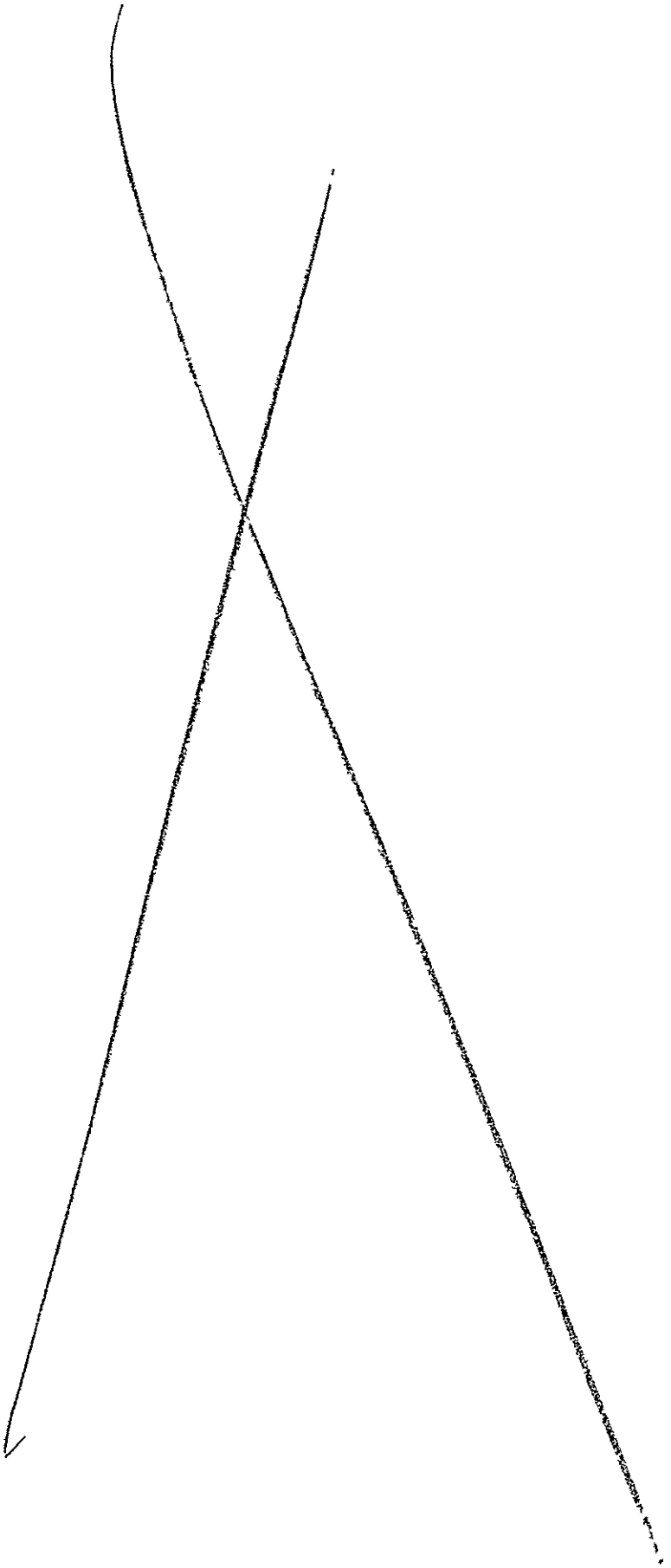

PART III
COMPOSITE MATERIALS

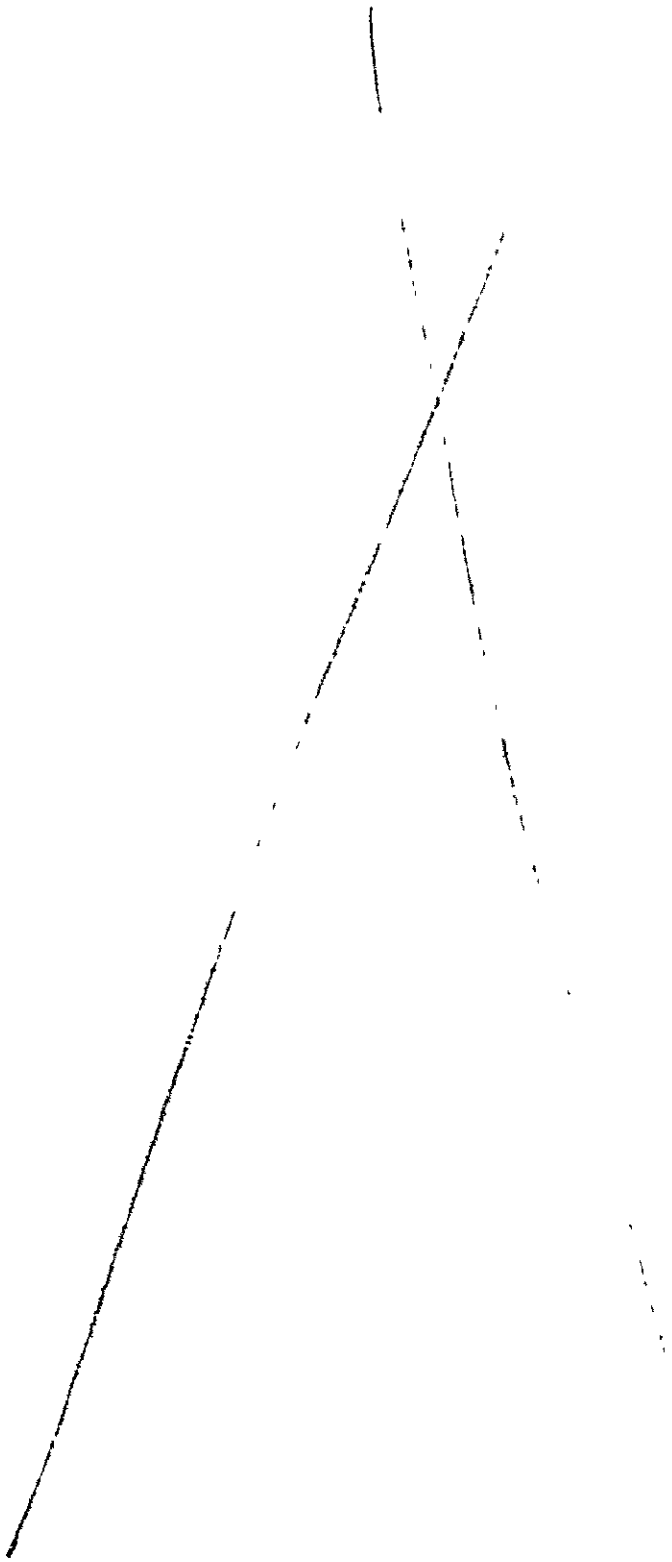

III-A ADVANCED ANALYSIS METHODS

Senior Investigator: E. J. Brunelle

1. Introduction

The ultimate purpose of this research effort is to understand exactly how each parameter changes the solution of any composite plate problem. Standard methods provide answers to specific analysis problems, but they do not address the above statement of intent.

Recognizing that a primary difficulty is that of a multiplicity of variables, solutions for orthotropic plates have been sought in terms of generalized variables. These efforts have produced many solutions for individual lamina and they are expected to form a basis for solving general composite plate problems. The first such solutions (by the present investigator) for a composite plate are one of the topics reported on in this progress report.

2. Status

The principal results of the last period are summarized as follows:

a) The generally orthotropic plate equation (which has the same form as the symmetric angle-ply plate) was found to depend on only two parameters in its affine plane representation. Thus, the coefficients of the operator

$$\frac{\partial^4 w}{\partial \bar{x}_o^4} + \bar{L}\frac{\partial^4 w}{\partial \bar{x}_o \partial \bar{y}_o^3} + 2\bar{D}\frac{\partial^4 w}{\partial \bar{x}_o^2 \partial \bar{y}_o^2} + \bar{R}\frac{\partial^4 w}{\partial \bar{x}_o^3 \partial \bar{y}_o} + \frac{\partial^4 w}{\partial \bar{y}_o^4}$$

depend only on the values of D_{11}/D_{22} and D^* in principal directions. Furthermore, $\bar{L}(D^*, D_{11}/D_{22}, \theta) = \bar{R}(D^*, D_{11}/D_{22}, 90 - \theta)$ and vice versa.

b) A very efficient numerical procedure was found for factoring the quartic associated with the above operator.

c) Exact solution bounds were found for the specially orthotropic plate.

d) The incremental behavior of D^* with respect to the plate coefficients was delineated.

e) The similarity rules for free vibration of a specially orthotropic plate were presented.

3. Progress During Report Period

Progress in the last reporting period has been made principally in the three areas described below [(a) - (c)].

a) The existence of double frequencies for other than square (a/b = 1) isotropic plates has been questioned and hotly debated in the literature. Assuming a simply-supported plate, an explicit relation is now presented for a_o/b_o values at which $\Omega_{mn} \equiv \Omega_{m^*n^*}$ with a parametric dependence on D^*.

$$\left(\frac{a_o}{b_o}\right)^2 = \frac{D^*[(m^*n^*)^2 - (mn)^2] \pm \sqrt{(D^{*2} - 1)[(m^*n^*)^2 - (mn)^2]^2 + [(m^*n)^2 - (mn^*)^2]^2}}{n^4 - n^{*4}}$$

where the positive square root is chosen. The values of $(a_o/b_o)^2$ for the limiting values of D* = 1 and 0 are:

$$\left(\frac{a_o}{b_o}\right)^2_{D^*=1} = \frac{m^{*2} - m^2}{n^2 - n^{*2}}$$

$$\left(\frac{a_o}{b_o}\right)^2_{D^*=0} = \sqrt{\frac{m^{*4} - m^4}{n^4 - n^{*4}}}$$

and, finally, if $(m^*n^*)^2 - (mn)^2 = 0$, one determines values of $\frac{a_o}{b_o}$ that are independent of D*,

$$\left(\frac{a_o}{b_o}\right)^2_{\text{INDEP. OF } D^*} = \left(\frac{m}{n^*}\right)^2 .$$

From the expression

$$\Omega^2_{mn} = m^4\left(\frac{b_o}{a_o}\right)^4 + n^4 + 2D^*(mn)^2\left(\frac{b_o}{a_o}\right)^2$$

it is seen that the frequencies corresponding to the above special values of a_o/b_o are not independent of the value of D*.

b) During the last dozen years many solutions have been presented for a wide variety of laminated rectangular composite plate problems. Unfortunately, all of these solutions are specific (a specific material and a specific aspect ratio must be given in order to present numerical results) rather than generic. Thus, the general behavior of these

solutions as various parameters change is not well understood. Employing techniques used by the present investigator on orthotropic plate problems, both the static deformation problem and the eigenvalue problems (vibration and buckling) are solved for S2 antisymmetric cross-ply plates with all sides simply supported. These solutions are in terms of the similarity variable $T = \frac{an}{mb}$ which presents the results in a highly understandable and intuitively appealing form.

For example, the frequency spectrum is represented by

$$\frac{\Omega^2 mn}{n^4} = f_1(T,D^*) - F_1(T,A,A^*)\frac{(B_{11})^2}{A_{11}D_{11}}$$

The function $f_1(T,D^*)$ is the orthotropic plate solution so that the function $F_1(T,A,A^*)$ determines the coefficient of the bending-extension parameter $(B_{11})^2/A_{11}D_{11}$. In expanded form,

$$F_1(T,A,A^*) = \frac{2A^*T^{-4} + (AT^{-2} + 1)T^{-3} + A + T^{-2}}{(A + T^{-2})(1 + AT^{-2}) - (A^*T^{-1})^2}$$

$$A = A_{66}/A_{11}$$

and

$$A^* = \frac{A_{12} + A_{66}}{A_{11}} = A + \frac{A_{12}}{A_{11}}$$

Note that the bending extension matrix element B_{11} appears only in the combination $(B_{11})^2/A_{11}D_{11}$ shown above, i.e., it does not appear in the F_1 (or f_1) function.

c) Many advanced composites have large values of Q_{11} and Q_{22} such that $Q_{11}, Q_{22} >> Q_{12}, Q_{66}$. One consequence of this is that the parameter D* is in the .1 to .2 range. It has been demonstrated many times (exclusively at RPI) that the "D* = 0 solution" is always in the neighborhood of low D* (.1 to .2) solutions. Therefore, the "D* = 0 solution" (which also really means that the ratios of $A_{66}/\sqrt{A_{11}A_{22}}$ and $(A_{12} + A_{66})/\sqrt{A_{11}A_{22}}$ are neglected) is a very convenient and very useful extremum† solution. For example, when considering S2 antisymmetric cross-ply plates, the "D* = 0 solution" is physically interpreted as neglecting the Poisson coupling and the twist-curvature coupling but retaining fully the bending-extension composite plate couplings. Thus, the three u, v, and w coupled equations of motion take on the simple form

$$u_{,xx} = \frac{B_{11}}{A_{11}} w_{,yyy}$$

$$v_{,yy} = \frac{B_{11}}{A_{11}} w_{,yyy}$$

$$D_{11}(w_{,xxxx} + w_{,yyyy}) - B_{11}(u_{,xxx} - v_{,yyy}) + Pw_{,ww} + \ldots + \rho w_{,tt} = q(x,y,t)$$

It is easily verified that the uncoupled w equation is given as

$$w_{,xxxx} + w_{,yyyy} + \frac{P}{(1 - J)D_{11}} w_{,xx} + \frac{\rho}{(1 - J)D_{11}} w_{,tt} = \frac{q(x,y,t)}{(1 - J)D_{11}}$$

---

†Upper bounds for deflection problems and lower bounds for eigenvalue problems

where $J = (B_{11})^2/A_{11}D_{11}$. This equation yields extremum solutions for the cross-ply antisymmetric plate. Notice that it is a separable equation, so that arbitrary boundary conditions may be imposed on all four sides. For example, defining the buckling coefficient at $k_o = Pb^2/\pi^2(1 - J)D_{11}$ the k_o versus a_o/b_o buckling curve for all sides clamped is shown in Figure III-A-1. This is an exact solution, which has as one of its most important features the fact that J (the effect of the bending-extension coupling) appears only in the denominator of the k_x definition.

4. Plans for Upcoming Period

Research on this project will be suspended temporarily this summer, but will resume with the beginning of the Fall '82 Semester. At that time the work on similarity solutions will be extended to S3 angle-ply antisymmetric plates, and earlier work on the material parameter $B = \frac{U_2}{4U_3}$ will be suitably generalized and presented in what is hoped to be a final form.

5. Current Publications or Presentations by Professor Brunelle on this Subject

"Thermal Buckling of Initially Stressed Thick Plates"
To be published in the ASME Journal.

"Generic Buckling Curves for Specially Orthotropic Rectangular Plates", with G. Oyibo.
Accepted for publication by the AIAA Journal, June 4, 1982.

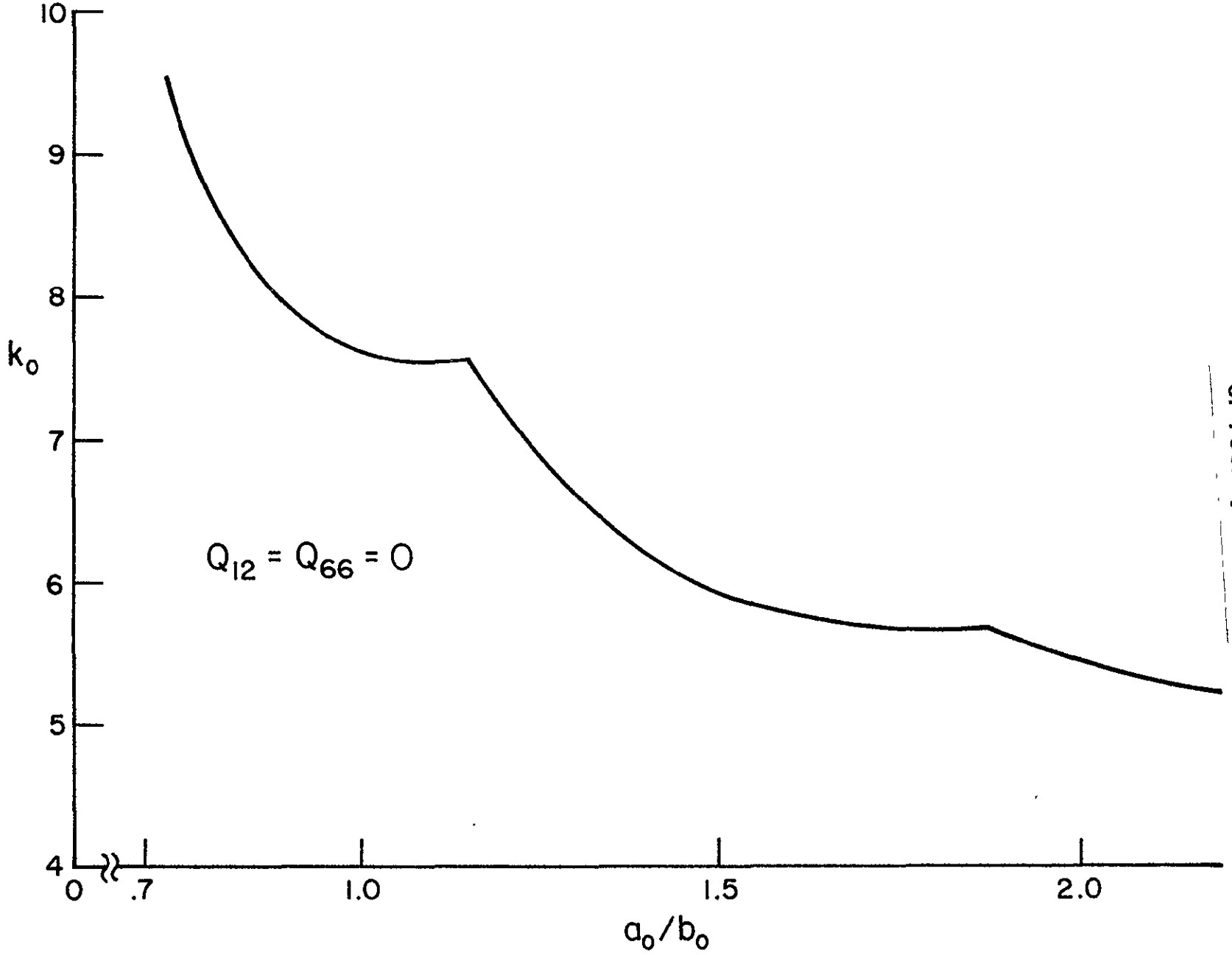

Figure III-A-1. Critical Buckling Coefficient vs. Plate Aspect Ratio (all sides clamped)

"Eigenvalue Similarity Rules for a Class of Rectangular Specially Orthotropic Laminated Plates"

To be presented at the Ninth U. S. National Congress of Applied Mechanics, Ithaca, NY, June 21-25, 1982.

"Similarity Solutions for the Eigenvalue Problems of S2 Antisymmetric Cross-Ply Composite Plates"

To be presented at the SIAM 30th Anniversary Meeting, Stanford, CA, July 19-23, 1982.

III-B FATIGUE IN COMPOSITE MATERIALS

Senior Investigator: E. Krempl

1. Introduction

The deformation and failure behavior of graphite-epoxy tubes under biaxial (tension, torsion) loading is investigated with the assistance of Ph.D. candidate T.-M. Niu. The aim of this research is to provide basic understanding and design information on the biaxial response of graphite-epoxy composites.

2. Status

Using graphite-epoxy $[\pm 45]_s$ thin-walled tubes, the static axial and torsional strength were determined together with the elastic moduli. Fatigue tests under completely reversed, load-controlled axial loading showed comparatively poor axial fatigue strength; furthermore, fatigue life was affected by frequency. A paper on this subject will appear in the Journal of Composite Materials[1]*.

3. Progress During Report Period

During the report period, static combined loading tests as well as combined tension-torsion, completely reversed, load-controlled fatigue tests were performed with the loads in-phase and out-of-phase. A total of 58 tubes were tested.

---

*Numbers in brackets in this section refer to the references which are listed on page 85.

Publications are in preparation and only highlights are given here.

a. Combined Static Tests

Test results are shown in Figure III-B-1 where σ and τ represent the axial and shear stress components, respectively. Previously only pure axial and torsion tests were reported[1]. It is seen that the combined tests complement the previously reported data very well.

It was noted in our earlier publication[1] that the low negative torsional strength of the tubes is due to local buckling. The combined loading results suggest that local buckling reduces the strength in cases where negative torque (the fibers of the outer layer are tensed) is applied compared to the cases where positive torque (the fibers of the outer layer are compressed) is involved. The failure envelope can be represented by two half ellipses with the same "axial half axis" as shown. One represents the local buckling failure mode; the other can be thought of as representing fiber breakage.

b. Combined Fatigue Tests

All tests were run in the completely reversed, load-controlled mode using a 1 Hz sine wave. If the variations in applied axial and shear stress are in phase with each other ($\phi = 0$), the image of this loading in the $\sigma - \tau$ plane is a straight line which passes through the first

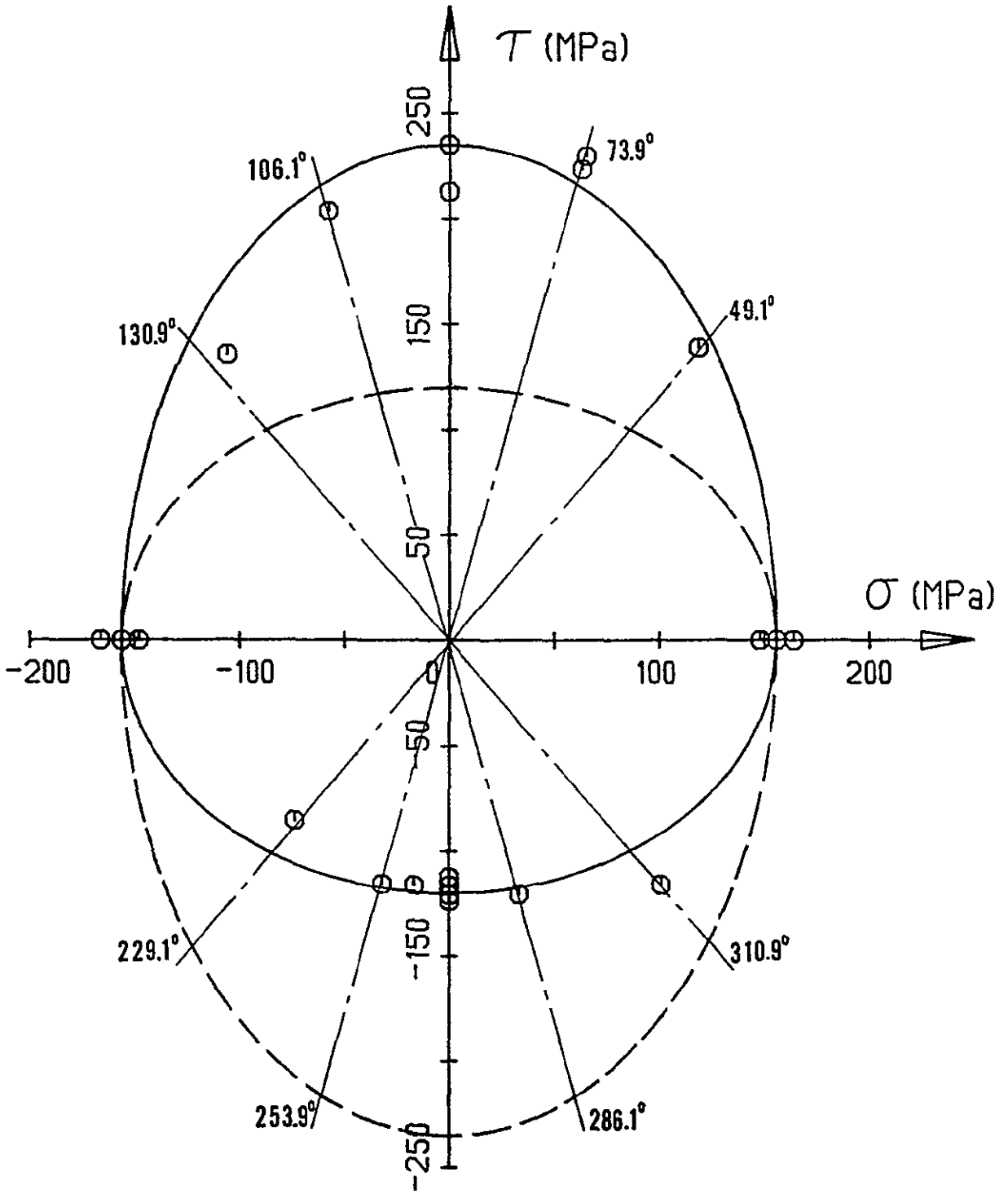

⊙—STRESSES AT FAILURE

Figure III-B-1. Biaxial Failure Locus for Static Tests
(Two failure mechanisms - buckling and fiber breakage - are operative and result in two distinct surfaces.)

and third quadrant (see Figure III-B-2). For a phase shift $\phi = \pi$ (ϕ denotes the phase shift) between the axial and the shear stress, a straight line in the second and fourth quadrant is obtained. For phase shifts of $\pi/2$ and $3\pi/2$, an ellipse is obtained in the $\sigma - \tau$ plane, with clockwise and counterclockwise rotation for $\pi/2$ and $3\pi/2$, respectively.

Since $\phi = 0$ and $\phi = \pi$ result in straight line images on the $\sigma - \tau$ plane, they will be referred to as in-phase loadings.

The ratio between the axial and shear stress amplitude is characterized by the angle θ such that

$$\tan \theta = \frac{\tau_a}{\sigma_a}$$

where the subscript 'a' designates the amplitude. Values of $\theta > \pi/2$ designate the tests with images in the second and fourth quadrants.

Figures III-B-3 and -4 show the results of the combined load fatigue testing. In this figure relative axial stress amplitude is plotted versus cycles to failure. Figure III-B-4 shows the results on the basis of the relative shear stress amplitude. (The data are normalized by $\sigma_u = 156$ MPa and by $\tau_u = 120$ MPa.)

As expected, the pure torsional fatigue performance is very good. No fatigue failure was obtained at 95% stress amplitude in 10^6 cycles (the failure recorded at 10^5 cycles was obtained on a specimen with an initial flaw; an arrow next to a symbol designates a run-out).

FATIGUE TEST CONDITIONS FOR COMPOSITE TUBES

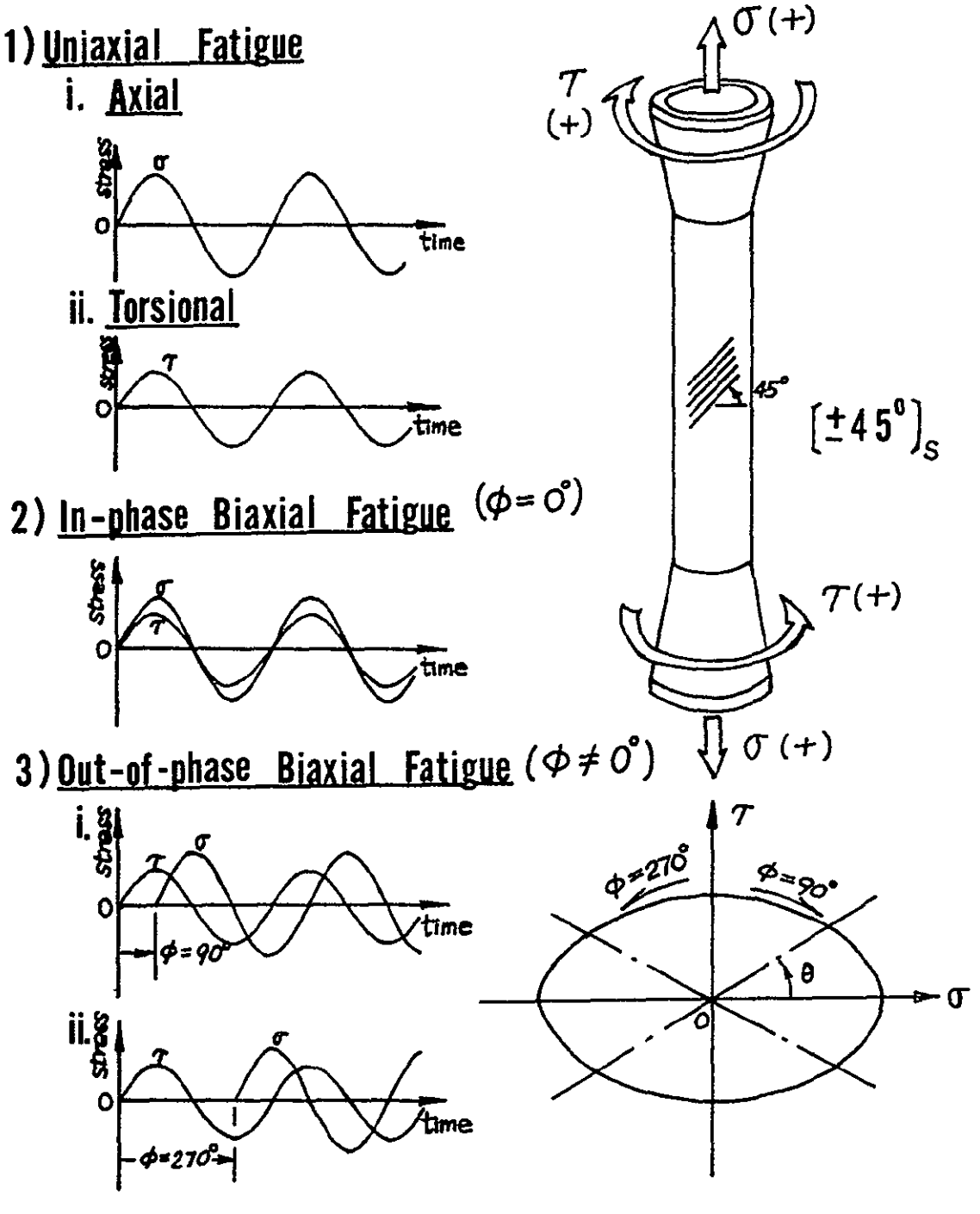

Figure III-B-2. Fatigue Test Conditions

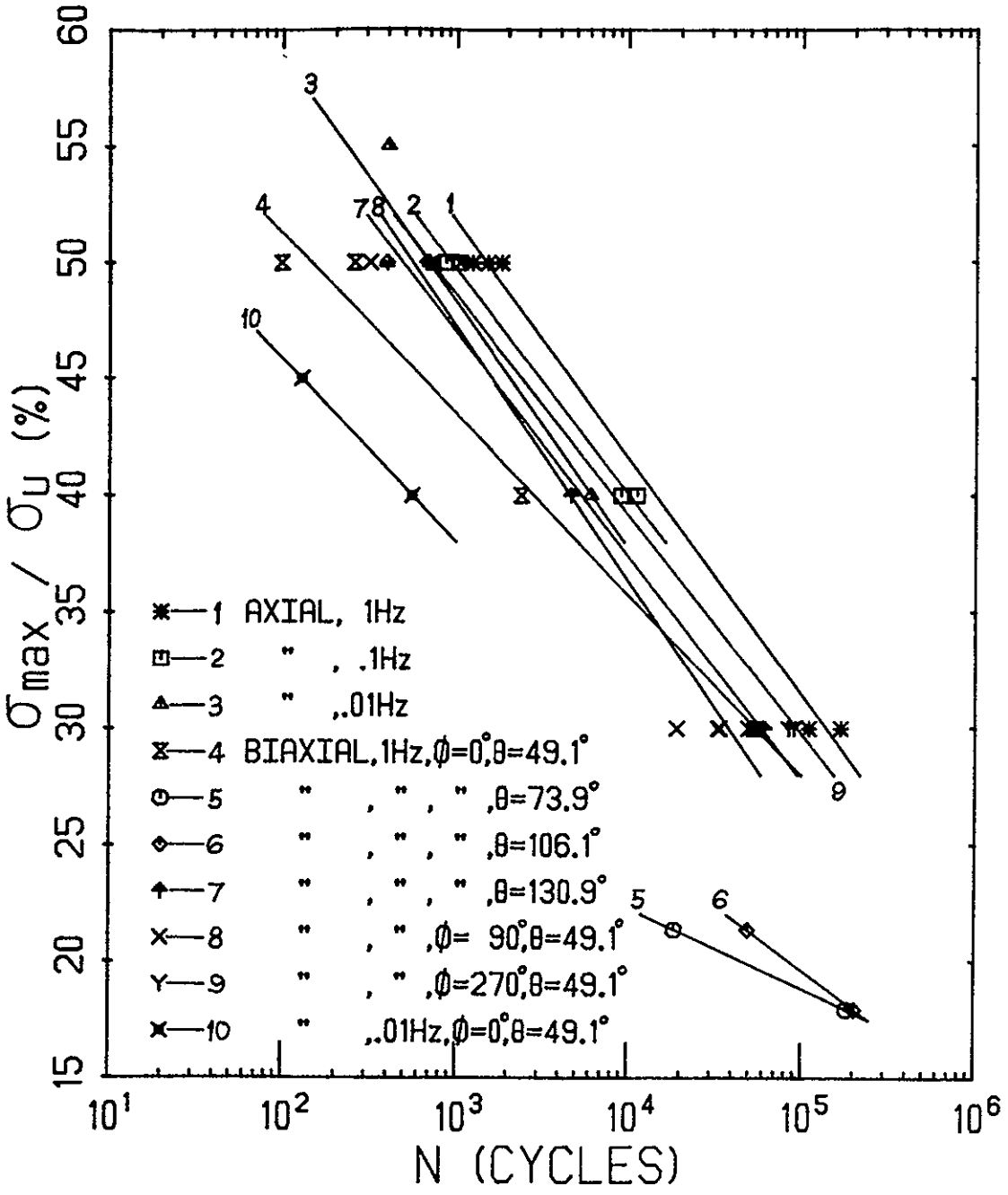

Figure III-B-3. Fatigue Test Results Plotting σ_{max}/σ_u versus Cycles-to-Failure (σ_u = 156 MPa)

Although the uniaxial case - where deformation is strongly matrix dominated - was expected to be the worst case in fatigue performance, the data in Figures III-B-3 and -4 show that the biaxial loading case with θ = 49.1 degrees exhibits the worst fatigue performance of all the combinations tested.

From the static test results shown in Figure III-B-1, two failure mechanisms are apparent. Buckling was shown to be limiting for negative twist. It appears that buckling is also limiting in the fatigue case. At amplitudes just below the torsional buckling strength, no fatigue failure is observed in pure torsion. This behavior is made evident in Figure III-B-5 which shows a cross-plot of the (sometimes extrapolated) data in Figures III-B-3 and -4. (Only in-phase test results can be plotted in Figure III-B-5.) All points are inside the small ellipse which represents the buckling mode of failure in static loading.

4. Plans for Upcoming Period

The fatigue test results will be analyzed and manuscripts for publication will be prepared.

5. References

1. Krempl, E. and T.-M. Niu, Journal of Composite Materials, Vol. 16, 1982, pp. 172-187.

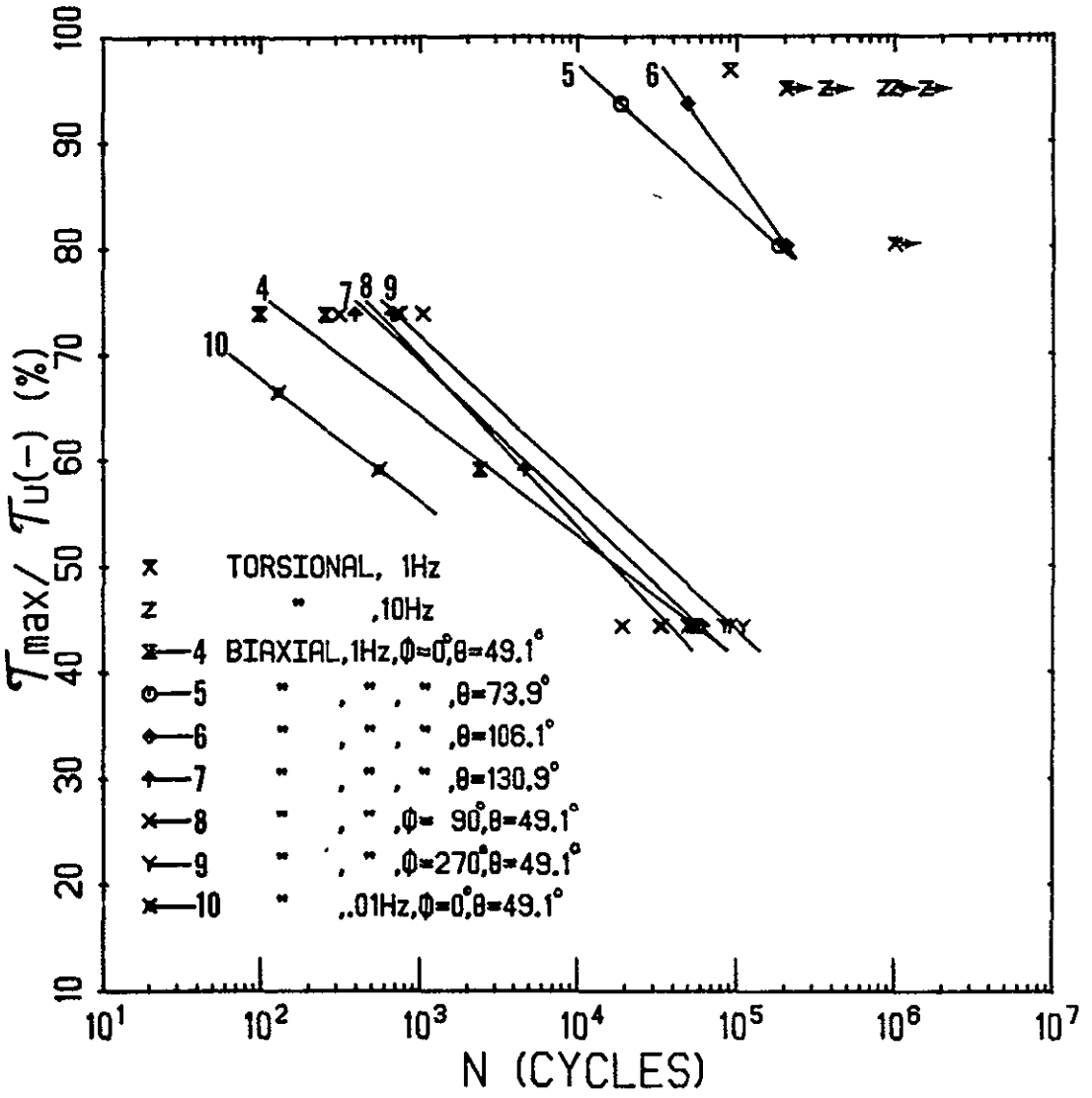

Figure III-B-4. Same Test Results as in Figure III-B-3 (τ_{max}/τ_u is used as ordinate τ_u = 120 MPa)

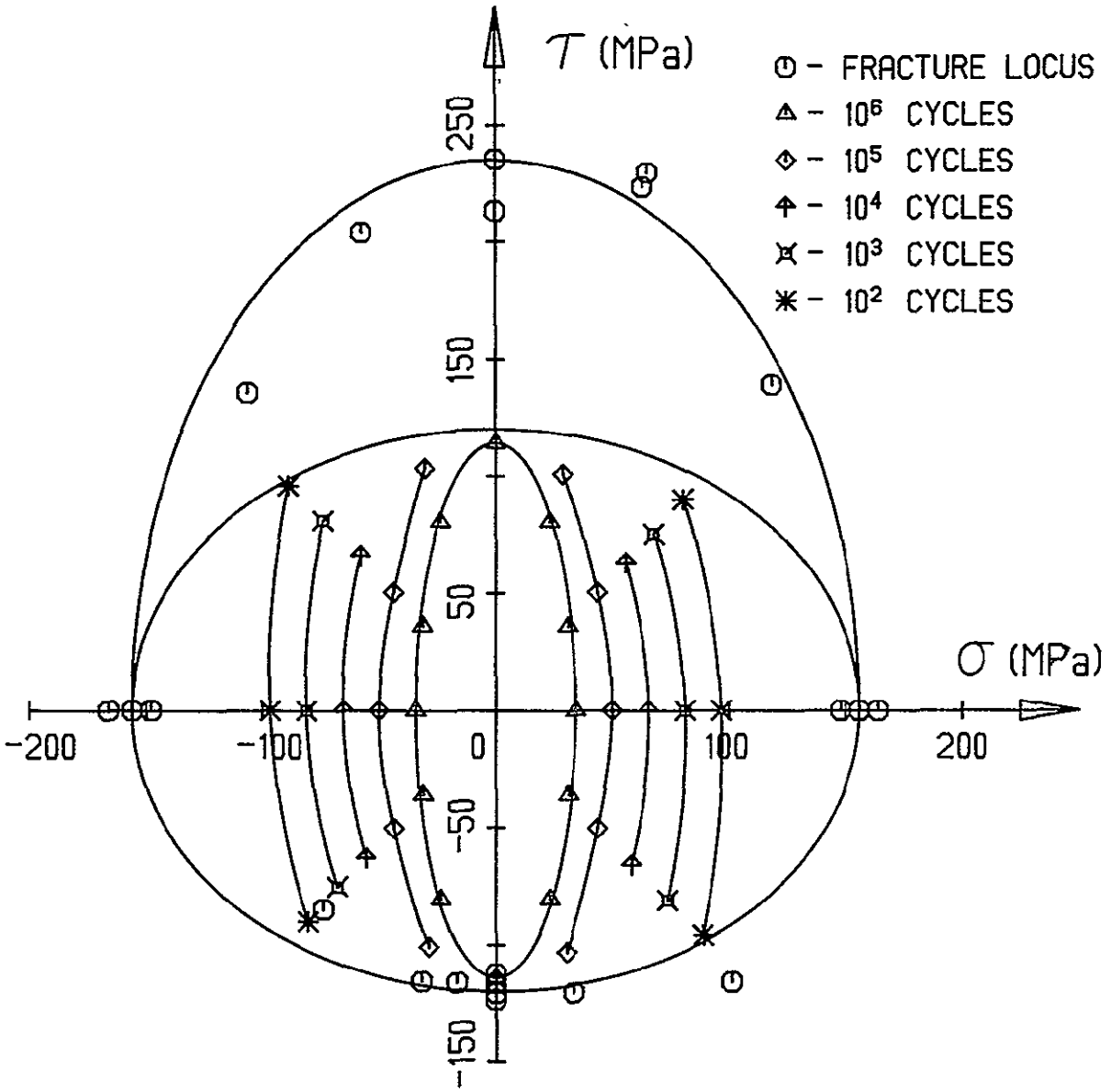

Figure III-B-5. Surfaces of Constant Fatigue Lives (obtained using Figures III-B-3 and -4)

C-2

6. Current Publications or Presentations by Professor Krempl on this Subject

"Graphite-Epoxy $[\pm 45]_S$ Tubes. Their Static Axial and Shear Properties and Their Fatigue Behavior under Completely Reversed Load Controlled Loading", with T.-M. Niu.

Published in the Journal of Composite Materials, Vol. 16, 1982, 172-187.

"Biaxial In-Phase and Out-of-Phase Behavior of Graphite-Epoxy Tubes"

To be presented at the ASTM Conference on Biaxial/Multiaxial Fatigue, San Francisco, CA, December 15-17, 1982.

III-C MOISTURE AND TEMPERATURE EFFECTS ON THE MECHANICAL PROPERTIES OF LAMINATES

Senior Investigator: S. Sternstein

1. Introduction

This project is concerned with those properties of high performance composites which are strongly dependent on the physical properties of the matrix resin. To date, the research has involved the precise viscoelastic characterization of epoxy neat resins, interlaminar failure of composites and the inhomogeneous swelling of and the effects of moisture on composites.

2. Status

It has been shown that the dispersion characteristics of neat resin and in situ resin are equivalent and that time-temperature superposition is obeyed in the glass transition region of the epoxy. Using the centro-symmetric deformation (CSD) testing method, it was found that when a postcured laminate sample is subjected to moisture its glass transition temperature varies directly with moisture content as measured by weight gain. Further, that a sample which is dried will recover its original glass transition temperature. To the contrary, laminate samples which have not been previously post-cured, when initially exposed to moisture, experience a decrease of glass transition temperature which is not recovered after drying. Typically, the decrease in T_g is five to ten degrees, depending on the moisture treatment.

Mechanical tests to determine dynamic modulus variations versus time, at constant temperature on wet samples, indicate that moisture interacts strongly with the postcure kinetics. It appears that even after the sample has dried there is still a residual effect on postcure kinetics.

A broad out-of-phase modulus peak in the dynamic behavior of wet neat resin samples of Narmco 5208, extending from 160°C to 240°C, contrasted with a 20°C to 30°C wide peak for a dry sample. This broadness of the wet glass transition peak may be direct rheological evidence for the presence of structure in the resin. Previously, other investigators have suggested that an amorphous structure exists in thermosets, based on electron microscopy of fracture surfaces. In the work reported here, the results represent bulk behavior, not surface behavior. These results may be of considerable utility in probing the structural features of epoxy resins.

3. Progress During Report Period

The characterization of matrix dominated mechanical properties of carbon-epoxy laminates using dynamic mechanical techniques is being continued. The sample test geometry involving centro-symmetric deformation (CSD) of a circular disc has been described previously and some of the early results with this technique reported. We are now using dynamic techniques to probe the damage induced by water absorption

and desorption. The CSD test geometry was used in earlier project periods to measure the delamination strengths of laminates of various stacking sequences and the results reported. In that study, it was found that the delamination strength and load drop at the first failure event were both markedly altered by the presence of moisture uptake-produced, delamination cracking, even prior to sample loading.

As a result of this previous study, we felt it necessary to examine in some detail the development of damage in laminates as a result of the moisture uptake process itself and without the influence of externally applied loads on the sample. Dynamic mechanical techniques appear to be a good method for characterizing the damage, per se, since this method utilizes sample loads which are about a factor of 30 lower than the first delamination event load level, and consequently, is not likely by itself to promote additional damage.

In order to isolate the damage caused by the uptake of water from the possible additional damage caused by subsequent drying of the sample, we felt that it would be best to obtain the dynamic data at 30°C and not at elevated temperatures. Thus, we would be able to control the drying conditions in a separate experiment.

The question which remains to be answered is whether or not dynamic mechanical measurements are reflective of the

damage process and if so, how sensitive are they? The preliminary results are most encouraging.

The storage (in-phase) and loss (out-of-phase) moduli of a 12-ply carbon-epoxy laminate which has been kept dry are shown versus frequency for 30°C in Figure III-C-1. After boiling the sample for 210 hours in a water bath, the results (again at 30°C) are shown in Figure III-C-2. There is a small but appreciable decrease in the storage modulus as a result of the water treatment. The loss modulus, however, is increased significantly (a factor of two at 0.1 Hz). The sample was then partially dried until its residual water weight gain reached one percent and the data in Figure III-C-3 were obtained. Note that the storage modulus is significantly lower than in Figure III-C-2, even though the sample has been partially dried. Finally, the sample was dried to a residual weight gain of 0.25% and the results in Figure III-C-4 were obtained. There is a slight increase in the storage modulus relative to Figure III-C-3 but the loss modulus remains high (compare Figures III-C-1 and -4).

The storage moduli results are summarized in Figure III-C-5. Note that the values shown (actually stiffnesses) have been normalized to the thickness of the dry sample by correcting for the thickness-cubed effect of out-of-plane deformation. Clearly, the effect of moisture absorption followed by drying results in a permanent reduction of flexural stiffness.

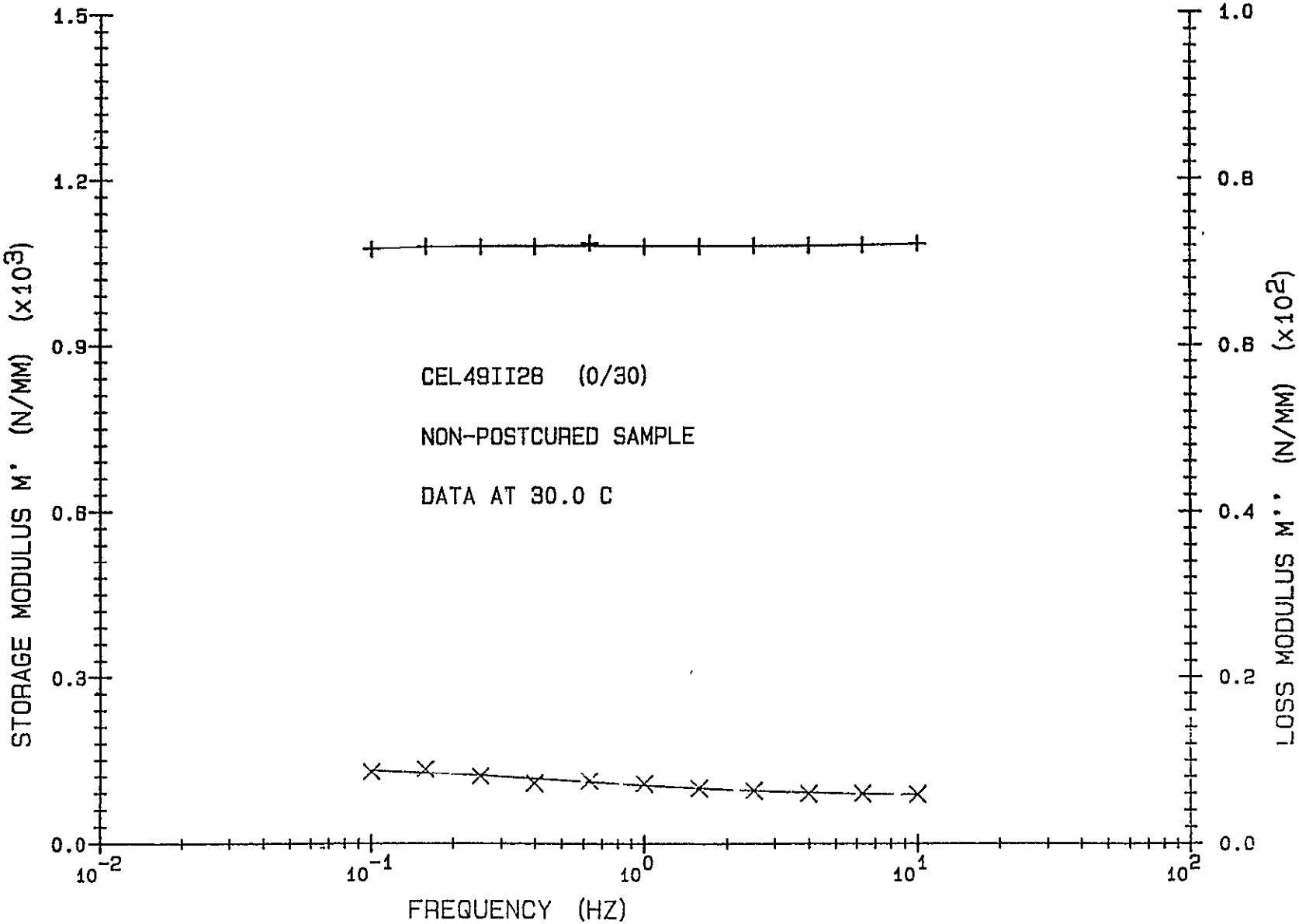

Figure III-C-1. Storage and Loss Moduli of a Dry Carbon/Epoxy Laminate (30°C)

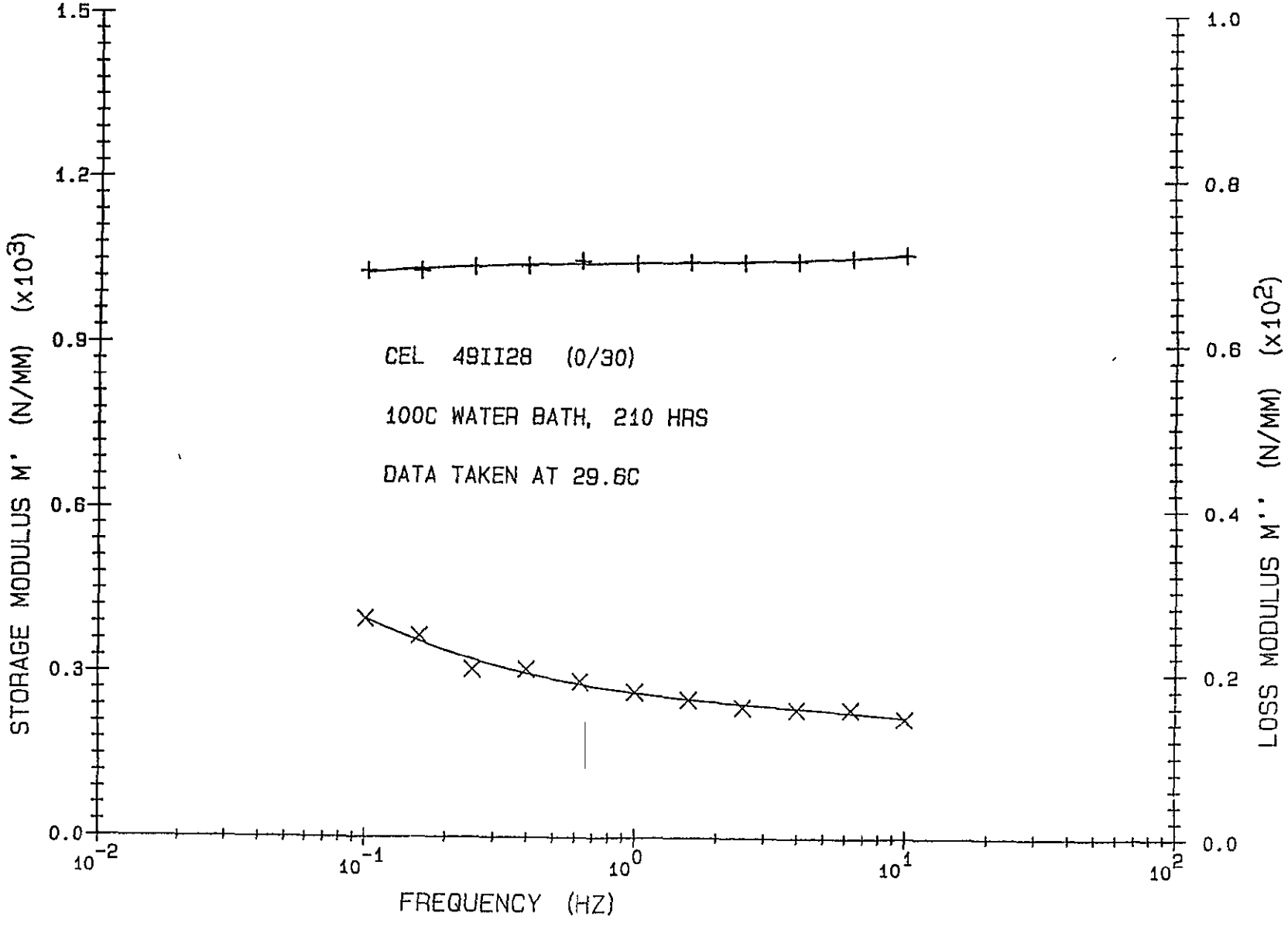

Figure III-C-2. Storage and Loss Moduli of a Wet Carbon/Epoxy Laminate (30°C; after boiling the Figure III-C-1 specimen in water)

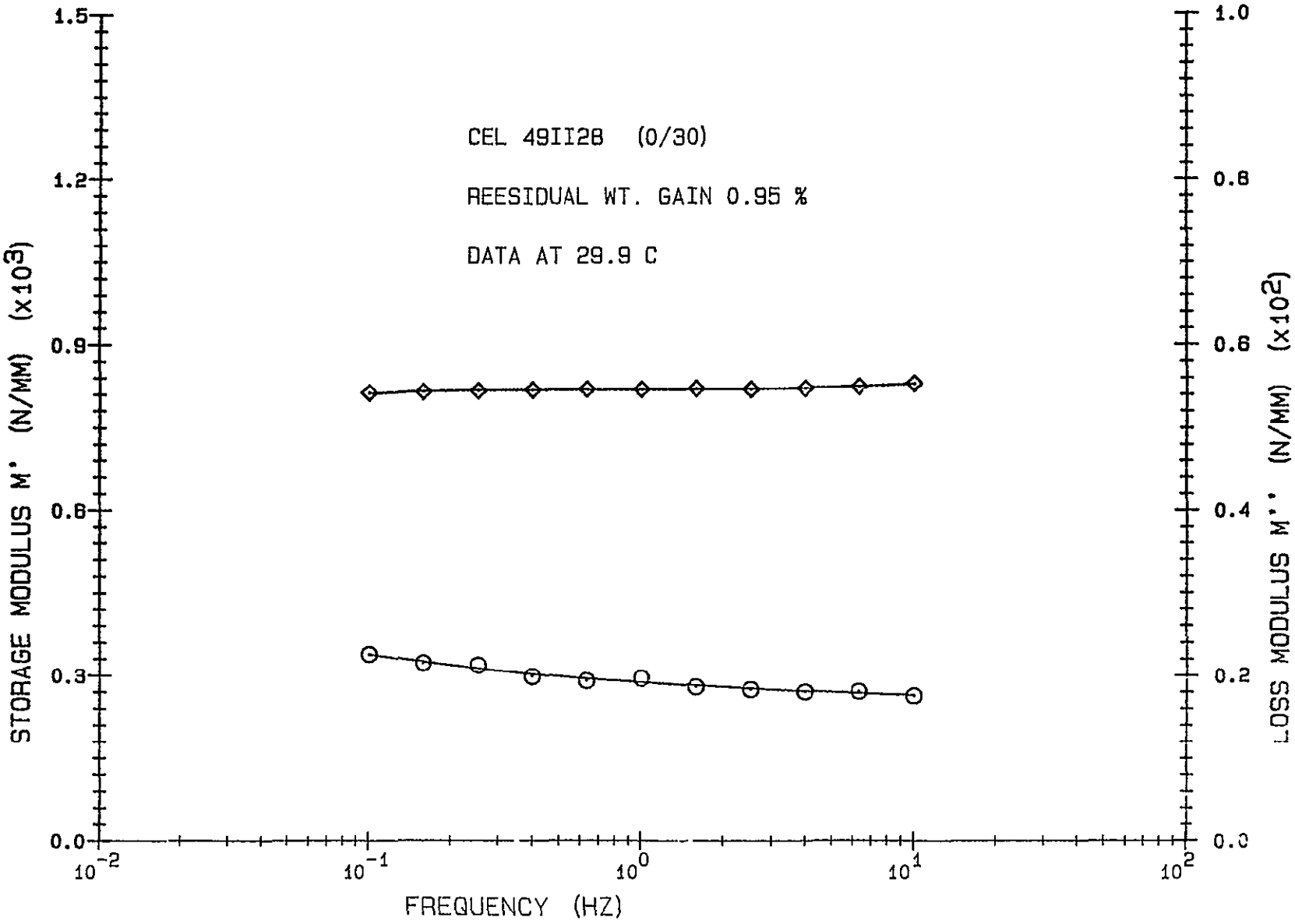

Figure III-C-3. Storage and Loss Moduli of a Partially Dried Carbon/Epoxy Laminate (30°C; after drying the Figure III-C-2 specimen to 1% weight gain)

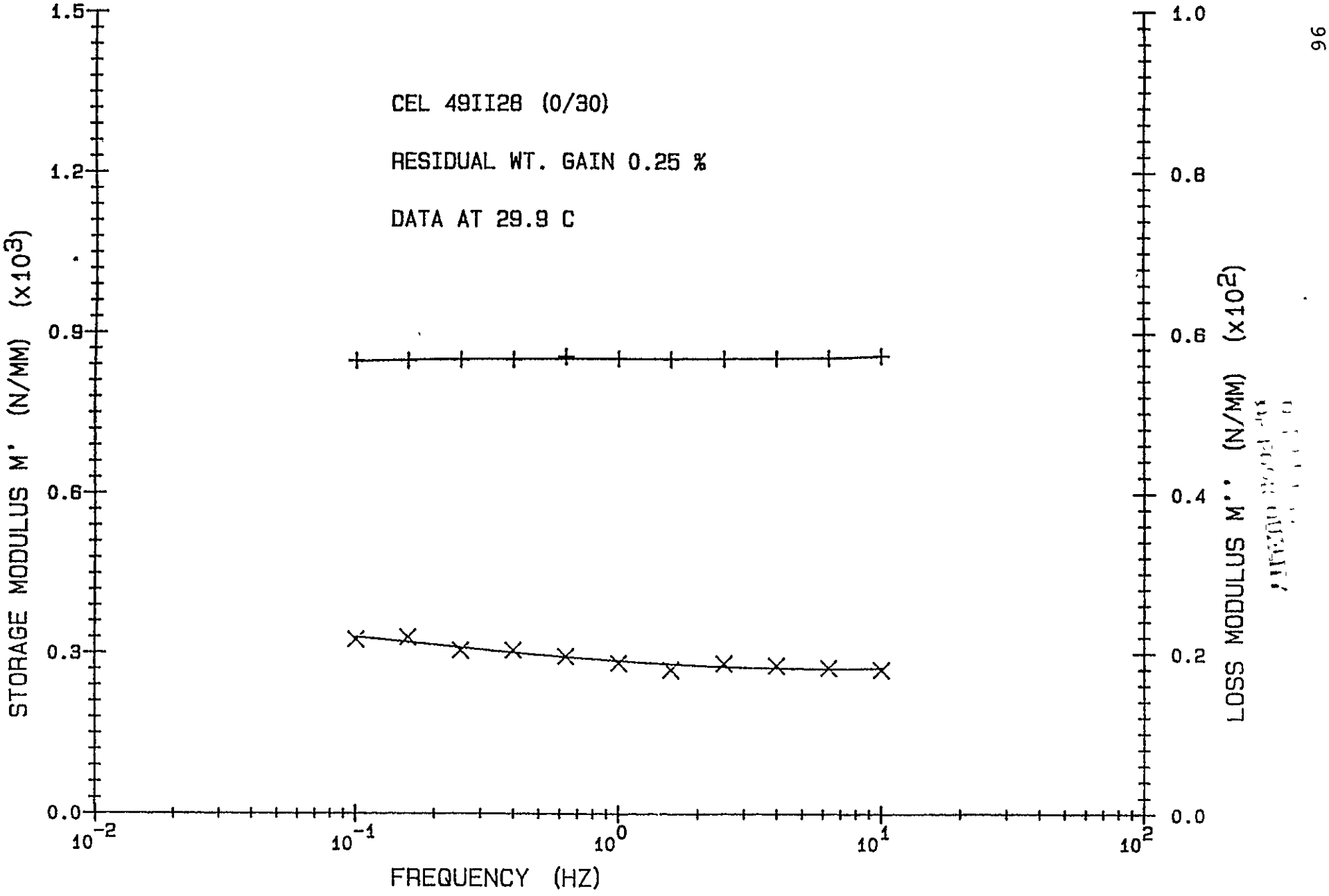

Figure III-C-4. Storage and Loss Moduli of a Dried Carbon/Epoxy Laminate (30°C; after drying the Figure III-C-2 specimen to 0.25% weight gain)

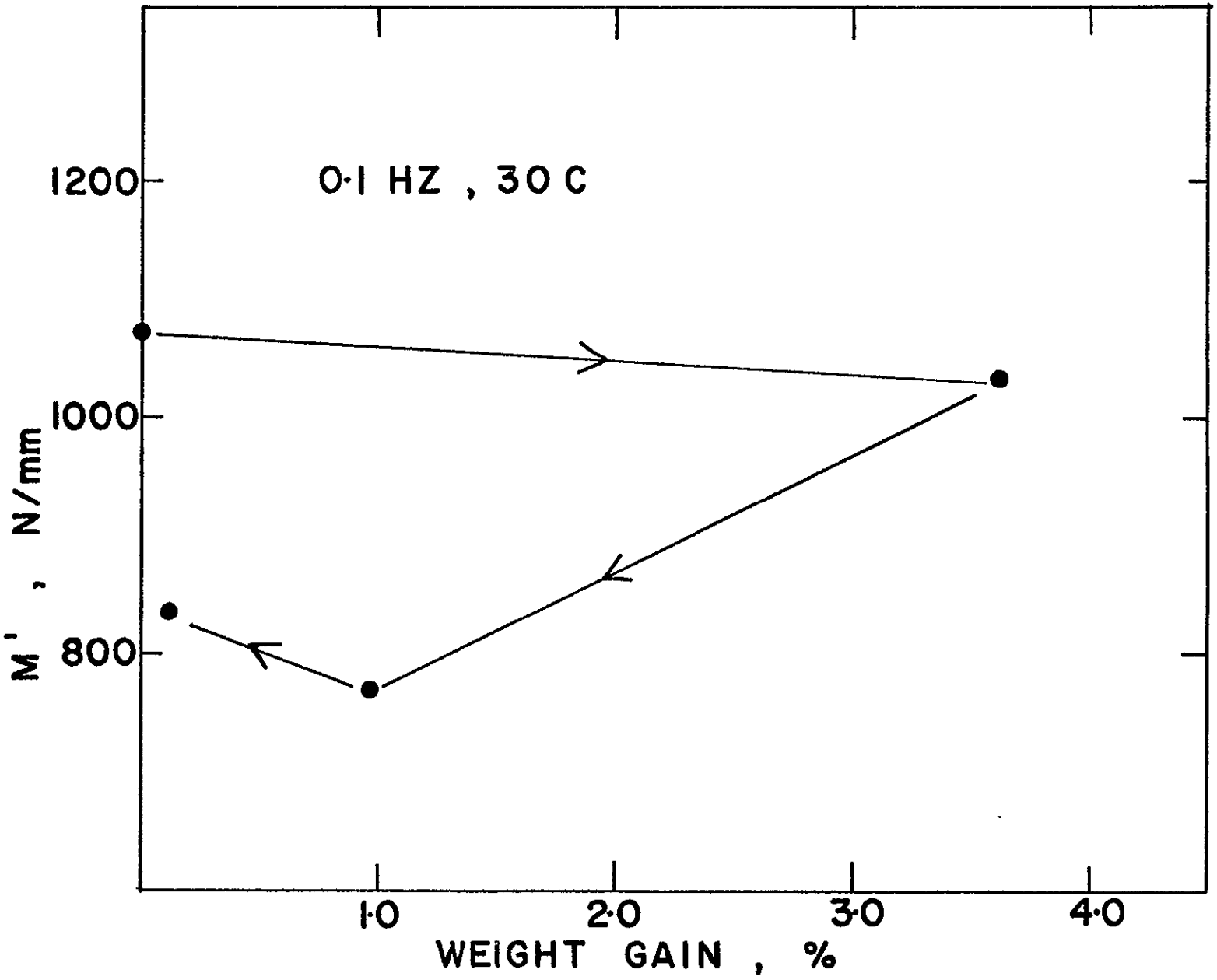

Figure III-C-5. Summary Comparison of Carbon/Epoxy Specimen Stiffness (normalized to dry sample thickness)

The loss modulii data are summarized in Figure III-C-6 where the loss factor ($\tan \delta$, the ratio of M''/M') relative to the dry state is shown versus moisture level. Several experiments and samples are summarized on this graph. If moisture level is increased only (no drying), all samples indicate a linear increase of $\tan \delta$ with moisture level. If the sample is dried beginning with any level of moisture, then a permanent residual increase in $\tan \delta$ is observed. What is somewhat suprising is that even the sample which has only been subjected to a weight gain of ca. 1% shows a hysteresis effect on drying

The results of Figure III-C-6 strongly suggest that dynamic mechanical loss factor can be used as a measure of moisture induced residual damage in carbon-epoxy laminates. This work is being continued.

4. Current Publications or Presentations by Professor Sternstein on this Subject

"Matrix Dominated Mechanical Properties of Composites"

Presented at an S.P.E. Short Course, Louisville, KY, November 4, 1981.

"Composites"

Presented at the CIBA-Geigy Research Center, Tarrytown, NY, November 19, 1981.

"Viscoelastic Characterization of Composites"

Presented at the Naval Research Labs., December 1, 1981.

"Matrix Dominated Mechanical Properties of High Performance Composites"

Presented at the International Conference on Deformation, Yield and Fracture of Polymers, Churchill College, Cambridge, England, March 29, 1982.

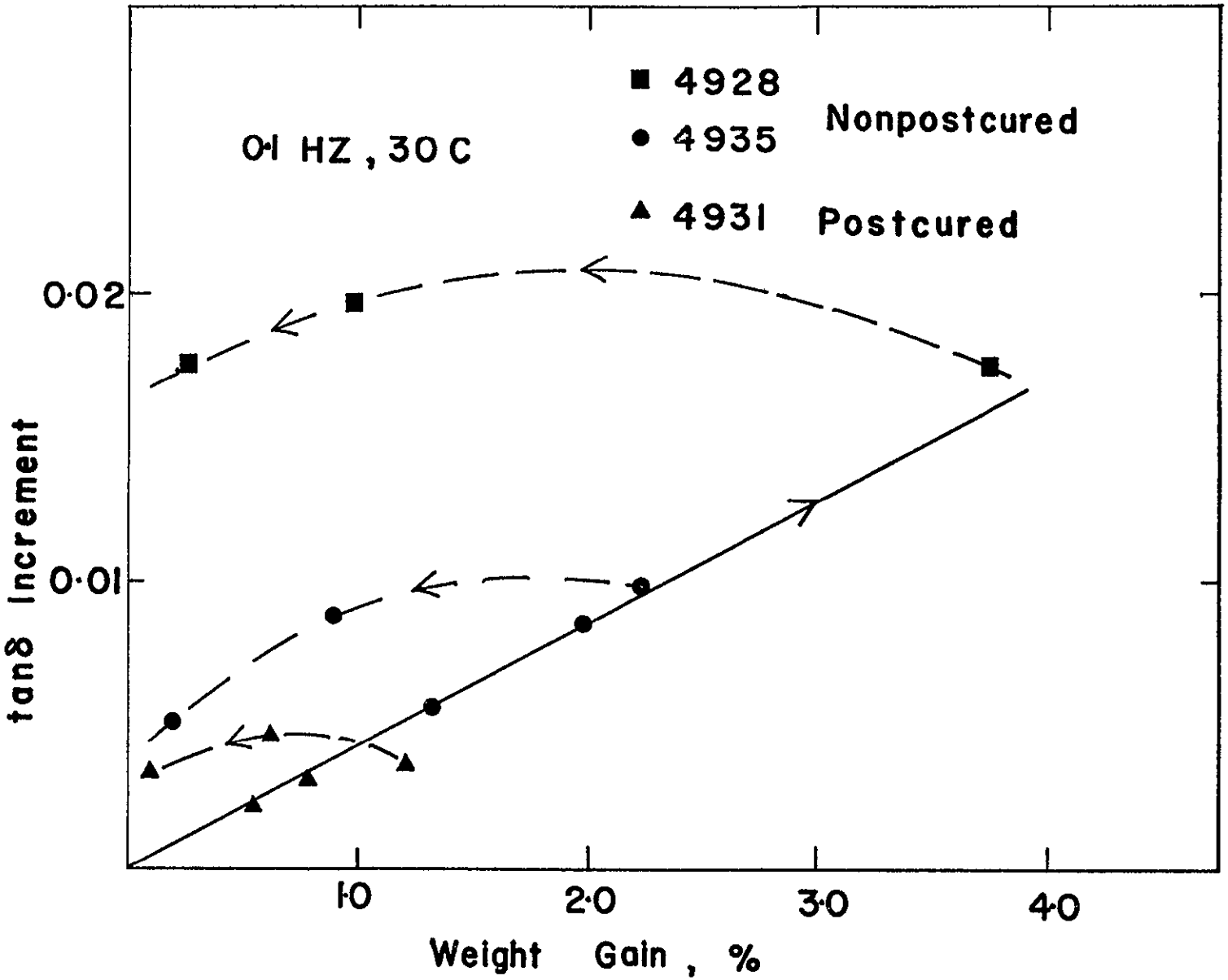

Figure III-C-6. Summary Comparison of Carbon/Epoxy Specimen Loss Moduli (with moisture level and history as a parameter)

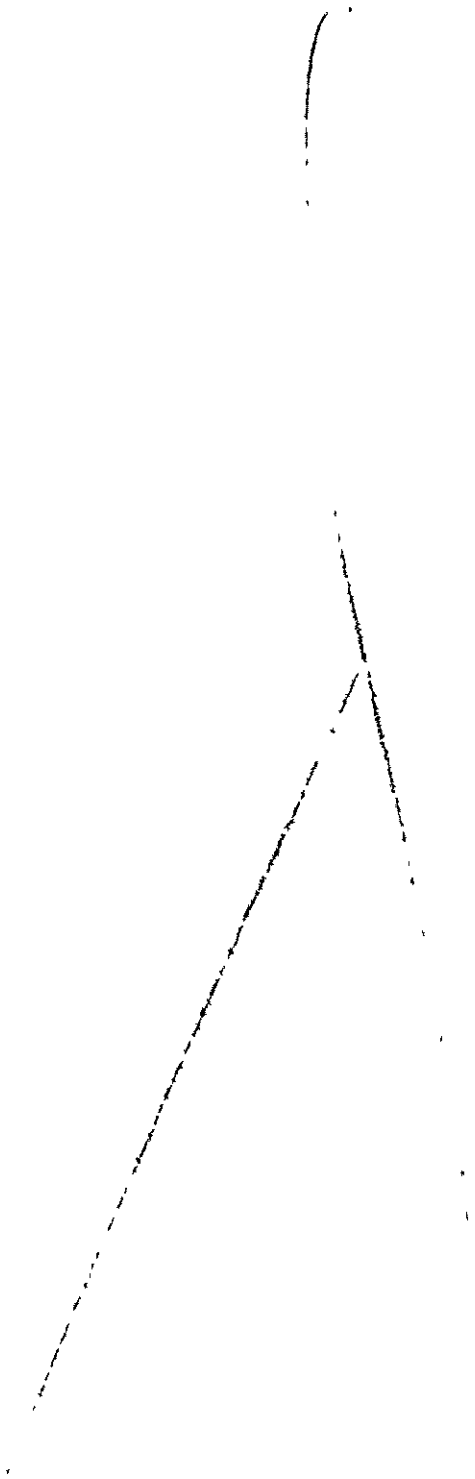

III-D NUMERICAL INVESTIGATION OF MOISTURE EFFECTS

Senior Investigator: M. S. Shephard

1. Introduction

This analysis builds on the theoretical developments of Professor S. Sternstein (reported in progress reports dated December '79 and June '80) in which the fully-coupled, nonlinear thermomechanical equations of inhomogeneous swelling of composites in the presence of moisture and temperature are analyzed. Here the one-dimensional case of a single fiber in an infinite matrix is being extended to two-dimensional, multiple fiber cases.

2. Status

As discussed in earlier progress reports, moisture effects were introduced into the problem through a nonlinear constitutive relation, the principle of virtual displacements was employed to develop a nonlinear matrix equation using displacement-based finite elements and these nonlinear equations were solved using quasi-Newton methods. Subsequently, the constitutive equation was built into the finite element analysis. The results of a single fiber comparison analysis were also given.

3. Progress During Report Period

Graduate student Frida Lumban-Tobing has continued, during the last reporting period, testing the program with sample problems and establishing additional features in it.

The areas of major analysis improvement are in the quasi-Newton solution. Improvements have also been made in the two-dimensional postprocessor, allowing the user to plot additional information. These additions include contours of the liquid volume fraction, principle strains, strain components and additional stress components. The following two sections, extracted from Reference [1]*, discuss the numerical solution procedure and the results of a two-fiber problem.

a. Numerical Solution

a.1) Quasi-Newton Method. Newton's method could be used to solve the nonlinear algebraic equations resulting from the application of the principal of virtual work. For a large system of equations, however, this method is expensive, because the Jacobian matrix has to be inverted at every iteration. To avoid this, the quasi-Newton method was applied to update the inverse of the stiffness matrix at every iteration. Of the several quasi-Newton methods available[2,3], the Davidon update, which is a rank one correction, was selected here for two major reasons. First, this is a symmetric update, i.e., the updated stiffness matrix remains symmetric. Second, it is less costly per iteration than rank two correction methods and appears to be less expensive overall.

*Numbers in brackets in this section refer to the references which are listed on page 118.

In the quasi-Newton method, the Jacobian matrix is approximated by evaluating the residual at two successive points, that is

$$\underset{\sim}{G}(\underset{\sim}{\Delta})(\underset{\sim}{\Delta} - \overline{\underset{\sim}{\Delta}}) = \underset{\sim}{r}(\underset{\sim}{\Delta}) - \underset{\sim}{r}(\overline{\underset{\sim}{\Delta}})$$

or

$$\underset{\sim}{G}(\underset{\sim}{\Delta})\underset{\sim}{d} = \underset{\sim}{y} \tag{1}$$

where

$\underset{\sim}{G}(\underset{\sim}{\Delta})$ is an approximation of the Jacobian matrix

$\underset{\sim}{\Delta}$ and $\overline{\underset{\sim}{\Delta}}$ are the column matrices of displacements for two steps

$\underset{\sim}{r}(\underset{\sim}{\Delta})$ and $\underset{\sim}{r}(\overline{\underset{\sim}{\Delta}})$ are the column matrices of residuals for the same two steps

$\underset{\sim}{d} = \underset{\sim}{\Delta} - \overline{\underset{\sim}{\Delta}}$

$\underset{\sim}{y} = \underset{\sim}{r}(\underset{\sim}{\Delta}) - \underset{\sim}{r}(\overline{\underset{\sim}{\Delta}})$

For the Davidon update, the matrix $\underset{\sim}{G}$ for the $(k+1)^{th}$ iteration is updated in the following form

$$\underset{\sim}{G}_{k+1} = \underset{\sim}{G}_k + \frac{(\underset{\sim}{y}_k - \underset{\sim}{G}_k\underset{\sim}{d}_k)(\underset{\sim}{y}_k - \underset{\sim}{G}_k\underset{\sim}{d}_k)^T}{(\underset{\sim}{y}_k - \underset{\sim}{G}_k\underset{\sim}{d}_k)^T\underset{\sim}{d}_k} \tag{2}$$

The superscript T indicates the transpose of the matrix. To avoid inverting the matrix $\underset{\sim}{G}$ at every iteration, it must be possible to directly update the inverse of the matrix $\underset{\sim}{G}$ for the $(k+1)^{th}$ iteration. This can be done by inverting equation (2) using Householder's formula

$$(\underset{\sim}{A} + q\underset{\sim}{c}\underset{\sim}{b}^T)^{-1} = \underset{\sim}{A}^{-1} - \gamma\underset{\sim}{x}\underset{\sim}{z}^T$$

where

q = a scalar,

$\underset{\sim}{b}$ and $\underset{\sim}{c}$ are column matrices

and

$$\underset{\sim}{x} = \underset{\sim}{A}^{-1}\underset{\sim}{c}$$

$$\underset{\sim}{z} = \underset{\sim}{A}^{-1}\underset{\sim}{b}$$

$$\gamma = q(1 + q\underset{\sim}{b}^{T}\underset{\sim}{A}^{-1}\underset{\sim}{c})^{-1}$$

which for equation (2) gives

$$\underset{\sim}{G}_{k+1}^{-1} = \underset{\sim}{G}_{k}^{-1} + \frac{(\underset{\sim}{d}_k - \underset{\sim}{G}_k^{-1}\underset{\sim}{y}_k)(\underset{\sim}{d}_k - \underset{\sim}{G}_k^{-1}\underset{\sim}{y}_k)^{T}}{(\underset{\sim}{d}_k - \underset{\sim}{G}_k^{-1}\underset{\sim}{y}_k)^{T}\underset{\sim}{y}_k} \tag{3}$$

For a given set of initial values $\underset{\sim}{\Delta}_0$ and $\underset{\sim}{G}_0$, the inverse update in equation (3) can be written as

$$\underset{\sim}{G}_{k+1}^{-1} = \underset{\sim}{G}_{0}^{-1} + \sum_{i=0}^{k} \underset{\sim}{s}_i\underset{\sim}{s}_i^{T}/\beta_i \tag{4.a}$$

where

$$\underset{\sim}{s}_i = \hat{\underset{\sim}{d}}_1 - \underset{\sim}{G}_i^{-1}\underset{\sim}{y}_i \tag{4.b}$$

$$\beta_i = \underset{\sim}{s}_i^{T}\underset{\sim}{y}_i \tag{4.c}$$

$$\underset{\sim}{y}_i = \underset{\sim}{r}_{i+1} - \underset{\sim}{r}_i \tag{4.d}$$

$$\hat{\underset{\sim}{d}}_i = t_i\underset{\sim}{d}_1 \tag{4.e}$$

$$\underset{\sim}{d}_i = -\underset{\sim}{G}_i^{-1}\underset{\sim}{r}_i \tag{4.f}$$

$$\underset{\sim}{r}_i = \underset{\sim}{r}(\underset{\sim}{\Delta}_1)$$

and t_i is a scalar obtained using a line search which will be discussed in the next section.

a.2) Devices to Insure and Speed Convergence. To insure and speed up convergence, it is important that the approximate Jacobian be as accurate as possible. In this study, two devices were used to insure that. One is the use of a line search to select reasonable step sizes. The other is a domain check which will force any unacceptable solution step back into the feasible domain.

a.2.1) Domain of the problem: All of Rivlin's strain invariants have to be positive because they are squares of functions of the extension ratios. In addition, the Flory-Huggins equation requires the volume fraction of polymer in the swollen body, v_2, to be less than 1. This restriction can be stated as

$$v_2 = V_2^*/\sqrt{I_3} < 1 \tag{5.a}$$

or

$$I_3 > (V_2^*)^2 \tag{5.b}$$

Thus, the following conditions must be met to insure that the domain of the problem is not violated

$$\begin{aligned} I_1 &\geq 0 \\ I_2 &\geq 0 \\ I_3 &> (V_2^*)^2 \end{aligned} \tag{6}$$

If at any point during the analysis, these domain

requirements are not met, the line search technique is used to bring the analysis back inside the domain.

a.2.2) Line search: Bathe and Matthies[4,5] suggested the use of line search techniques to improve convergence of the quasi-Newton method. The suggested line search requires the use of step length t_k in the direction of d_k such that

$$| \underset{\sim}{d}_k^T \underset{\sim}{r}(\underset{\sim}{\Delta}_k + t_k \underset{\sim}{d}_k) | \leq \eta | \underset{\sim}{d}_k^T \underset{\sim}{r}(\underset{\sim}{\Delta}_k) |$$

where η is convergence tolerance. They suggested the value of η to be 0.5. Geradin et al.[3] concluded that this line search did not give substantial improvement to the convergence rate, and Bathe[4] indicated that, for some problems, a still larger value of η yields good convergence rates.

For the problem reported here, the line search is needed in some steps to insure that the solution remains in the domain of the problem. Comparing the convergence rate for values of $\eta = 0.5$ and $\eta = 0.9$ indicated that the convergence rate for $\eta = 0.5$ is not better than the convergence rate for $\eta = 0.9$. Since the line search is an expensive operation it is only conducted while

$$| \underset{\sim}{d}_k^T \underset{\sim}{r}(\underset{\sim}{\Delta}_k + t_k \underset{\sim}{d}_k) | > 0.9 | \underset{\sim}{d}_k^T \underset{\sim}{r}(\underset{\sim}{\Delta}_k) |$$

Ocasionally, the value of t_k is negative. This is not surprising since Bard and Broyden[6,7] mentioned that negative steps are sometimes necessary.

a.3) Solution Algorithm. For small problems, where the number of independent variables is reasonably low, the $\underset{\sim}{s}_i\underset{\sim}{s}_i^T/\beta_i$ term from equation (4.a) can be stored in a matrix form. In this case, the summation process of the updating matrix $\underset{\sim}{s}_i\underset{\sim}{s}_i^T/\beta_i$ is simple. The new $\underset{\sim}{s}_i\underset{\sim}{s}_i^T/\beta_i$ can be added into the matrix that is obtained in the previous iteration.

For large problems, it is not convenient to store $\underset{\sim}{s}_i\underset{\sim}{s}_i^T/\beta_i$ in matrix form. In this case, the β_i's and the vectors $\underset{\sim}{s}_i$'s must be stored, and the summation process has to be done at every iteration. The algorithm shown below indicates how to avoid this summation every time $\underset{\sim}{G}^{-1}$ is encountered at each iteration. In this way, only one summation of $\underset{\sim}{s}_i\underset{\sim}{s}_i^T/\beta_i$ per iteration needs to be performed.

Step 1: read $\underset{\sim}{\Delta}_0$

Step 2: $k = 0$

$$\underset{\sim}{r}_0 = \underset{\sim}{r}(\underset{\sim}{\Delta}_0)$$

$$\underset{\sim}{G}_0 = \underset{\sim}{G}(\underset{\sim}{\Delta}_0)$$

$$\underset{\sim}{b}_0 = \underset{\sim}{G}_0^{-1}\underset{\sim}{r}_0$$

$$\underset{\sim}{d}_0 = -\underset{\sim}{b}_0$$

Step 3: $k = k + 1$

$t_{k-1} = 1$

$\underset{\sim}{\Delta}_k = \underset{\sim}{\Delta}_{k-1} + t_{k-1}\underset{\sim}{d}_{k-1}$

(find t_{k-1} using line search if the solution is outside the domain or if $|\underset{\sim}{d}_{k-1}^T \underset{\sim}{r}(\underset{\sim}{\Delta}_{k-1} + t_{k-1}\underset{\sim}{d}_{k-1})| / |\underset{\sim}{d}_{k-1}^T \underset{\sim}{r}(\underset{\sim}{\Delta}_{k-1})| > 0.9$)

$\underset{\sim}{r}_k = \underset{\sim}{r}(\underset{\sim}{\Delta}_k)$

Step 4: check convergence: $||\underset{\sim}{r}_k|| \leq$ a specified value. If satisfied, $\underset{\sim}{\Delta}$ is solved, stop. Otherwise, continue to Step 5.

Step 5: $\underset{\sim}{y}_k = \underset{\sim}{r}_k - \underset{\sim}{r}_{k-1}$

$\underset{\sim}{b}_k = \underset{\sim}{G}_0^{-1}\underset{\sim}{r}_k$

$\underset{\sim}{c}_k = (\sum_{i=0}^{k-1} \underset{\sim}{s}_i\underset{\sim}{s}_i/\beta_1)\underset{\sim}{r}_k$

$\underset{\sim}{g}_k = -\underset{\sim}{b}_k - \underset{\sim}{c}_k$

$\underset{\sim}{s}_k = (t_{k-1} - 1)\underset{\sim}{d}_{k-1} + \underset{\sim}{g}_k$

$\beta_k = \underset{\sim}{s}_k^T\underset{\sim}{y}_k$

store $\underset{\sim}{s}_k$ and β_k

$\underset{\sim}{d}_k = \underset{\sim}{g}_k - (\underset{\sim}{s}_k\underset{\sim}{s}_k/\beta_k)\underset{\sim}{r}_k$

Step 6: go back to step 3.

In this algorithm, the only matrix to be inverted is $\underset{\sim}{G}_0$. By factoring $\underset{\sim}{G}_0$ into upper and lower triangular matrices, the

forward reduction and backward substitution can be done later when the vector $\underset{\sim}{b}$ needs to be calculated.

For the problem under consideration, two methods can be used to start the iteration. The first method is to guess a starting v_2 value, apply this to the entire region and use it to estimate $\underset{\sim}{\Delta}_0$ and $\underset{\sim}{G}_0$. This does not work well for a problem with a large range of v_2 values, which is usually the case when high tensile load is applied. The second method is to use the displacements due to zero load or lower load level as the initial displacements.

b. Example Problems

b.1) A Pair of Fibers in an Epoxy Matrix Without Applied Load. In this example, the interaction between the two fibers at a given humidity is studied by varying the distance between those fibers. The basic model of this problem is shown in Figure III-D-1. It is analyzed using six-nodal isoparametric elements. Figure III-D-2 summarizes the results for the case of 100% humidity. The values used in this figure are for the maximum value anywhere on the interface, for point A on the interface (see Figure III-D-1) and at the center of the model (point B in Figure III-D-1). Figure III-D-2 indicates a strong dependence of fiber spacing with the peak values occurring in the one radius case. For spacings of less than five radii, the interaction between the fibers is significant and thus differs appreciably from the case of a single fiber in an infinite matrix. The results

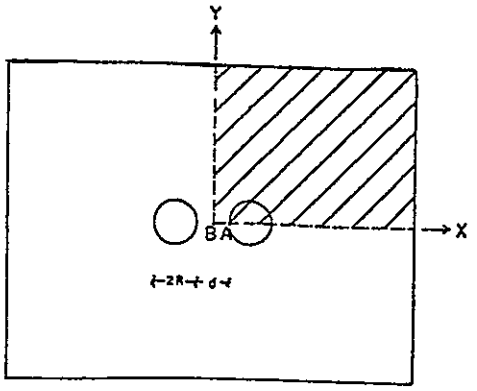

Figure III-D-1. Basic Model of Two Fiber Problem

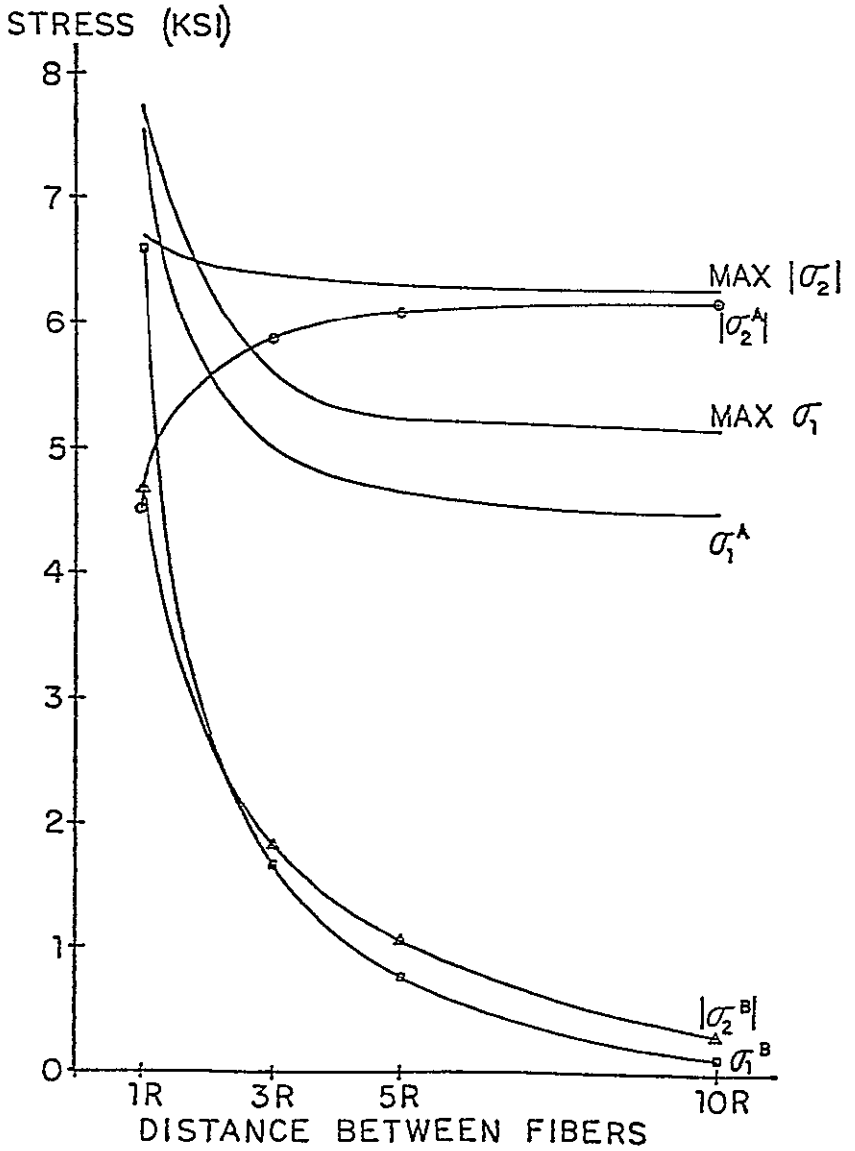

Figure III-D-2. Effect of Fiber Spacing on Stress in Unloaded Problem

also indicate that at reasonable fiber distances the magnitude of the principal stress σ_2 is larger than σ_1. As the distance becomes smaller, the interaction becomes stronger, and at a certain distance the magnitude of the principal stress σ_2 becomes less than σ_1. The maximum value of the liquid volume fraction increases with decreasing fiber spacing and at a certain distance it becomes larger than the saturated value for epoxy under no load.

The interaction between the fibers is also affected by the level of humidity. Figure III-D-3 shows this interaction as a function of humidity for the case where the distance between the fibers is one fiber radius. This figure shows that the interaction becomes weaker as the level of humidity is reduced.

b.2) A Pair of Fibers in an Epoxy Matrix Under Applied Load. Here, three groups of problems are presented. The particular groupings are selected because the results are similar for all the cases within a group. The first group consists of cases where the applied load is either uniform tension in the x-direction, uniform compression in the y-direction, or both tension in x and compression in y-directions. The second group consists of cases where the applied uniform load is either compression in the x-direction, tension in the y-direction, or both compression in x and tension in y-directions. The cases in the third group include those

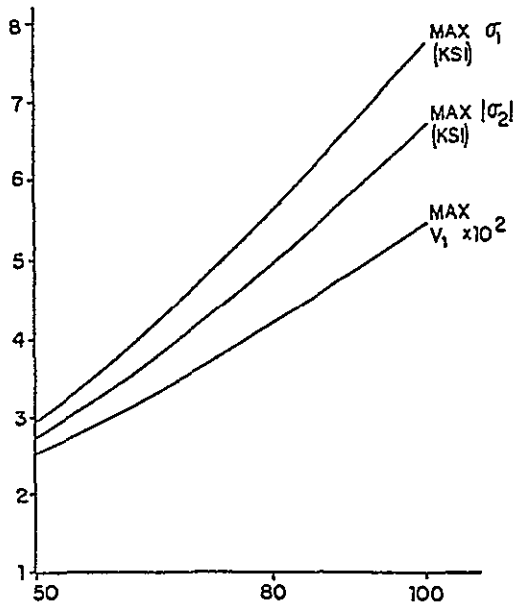

Figure III-D-3. Maximum Principal Stress and Liquid Volume Fraction Values as a Function of Humidity for One Radius Fiber Spacing

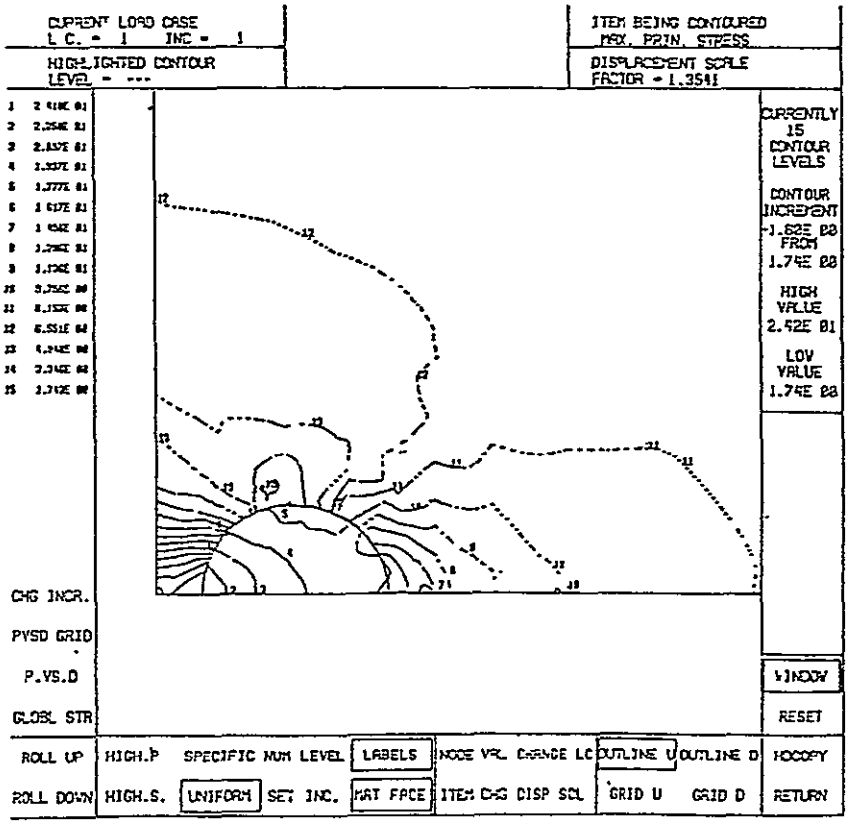

Figure III-D-4. σ_1 Contours for Uniform Load in X-Direction

where the applied load is one of the following: either in both x and y-directions, tension in both x and y-directions or the no-load condition.

The shapes of the contours of the principal stresses and volume fraction of liquid in the swollen body within each group have similar shapes but with different values associated with those contours. Figures III-D-4 to 9 show the shapes of the σ_1 and σ_2 contours for all three groups under 100% humidity, where the fiber spacing is one radius. More specifically, Figures III-D-4 and -5 are σ_1 and σ_2 contours when load is applied in the positive x-direction; Figures III-D-6 and -7 are σ_1 and σ_2 when the load is applied in the positive y-direction; and Figures III-D-8 and -9 are σ_1 and σ_2 when the load is applied in both x and y-directions. As might have been expected, these results show that the difference between the cases in each group cannot be eliminated by simple addition or subtraction of one case with another, as can be done in linear problems where the superposition principle holds.

Figure III-D-10 shows the maximum of σ_1 (anywhere on the interface) versus applied uniform load, for the problem with 100% humidity and with fiber spacing of one fiber radius. The trends in the maximum value of the liquid volume fraction are similar to the trends in the maximum value of the principal stress σ_1. The maximum values of the stress and the liquid volume fraction always occur at a point on the interface which depends on the applied load.

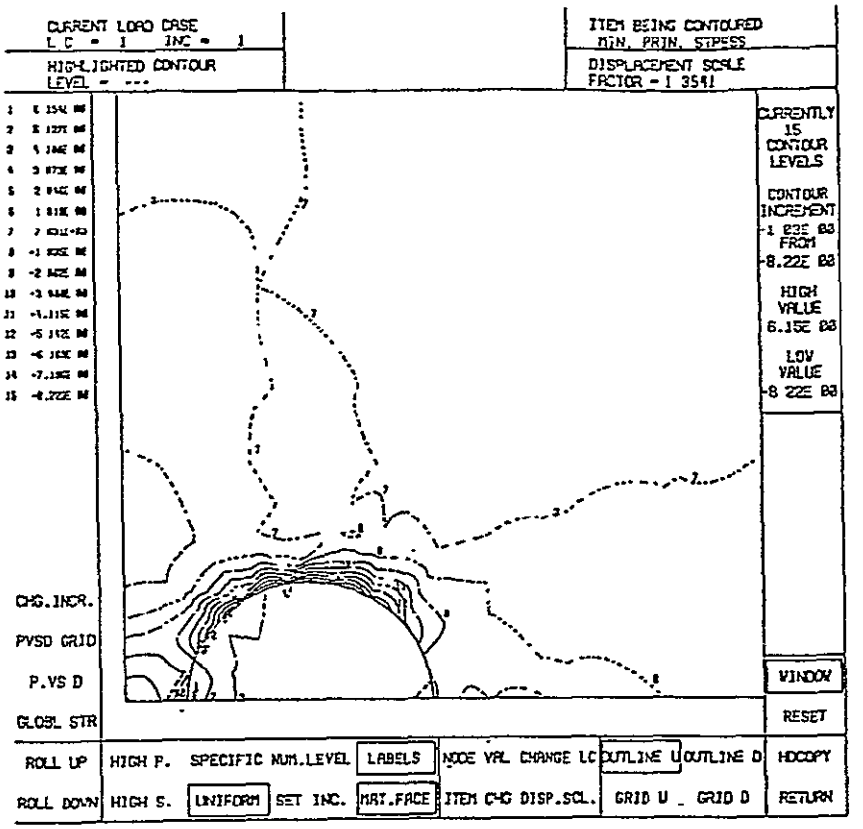

Figure III-D-5. σ_2 Contours for Uniform Load in X-Direction

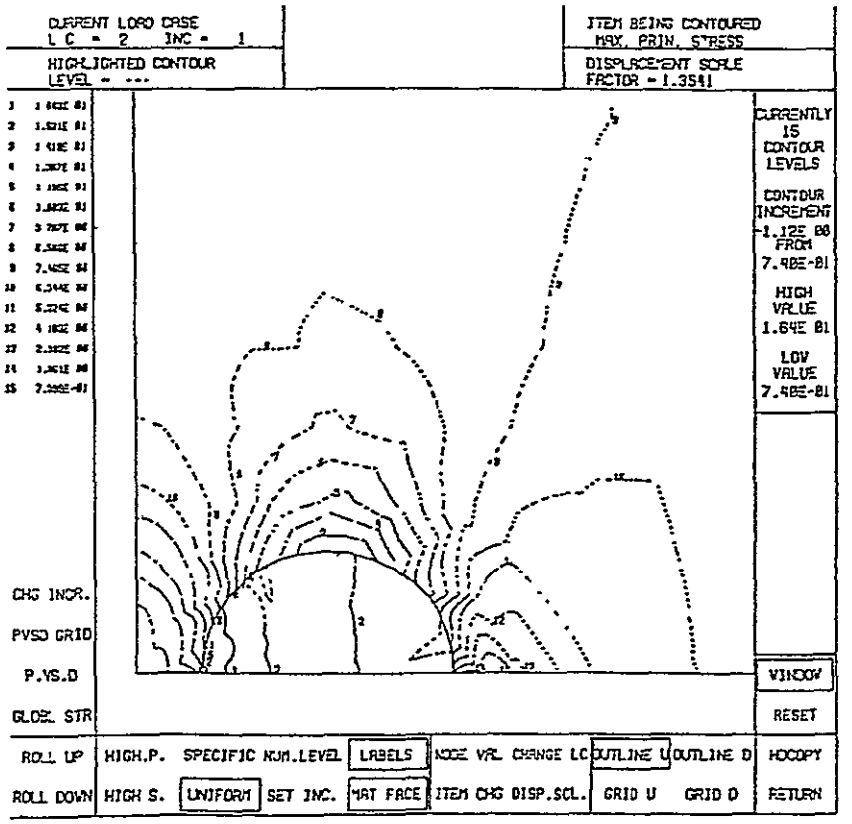

Figure III-D-6. σ_1 Contours for Uniform Load in Y-Direction

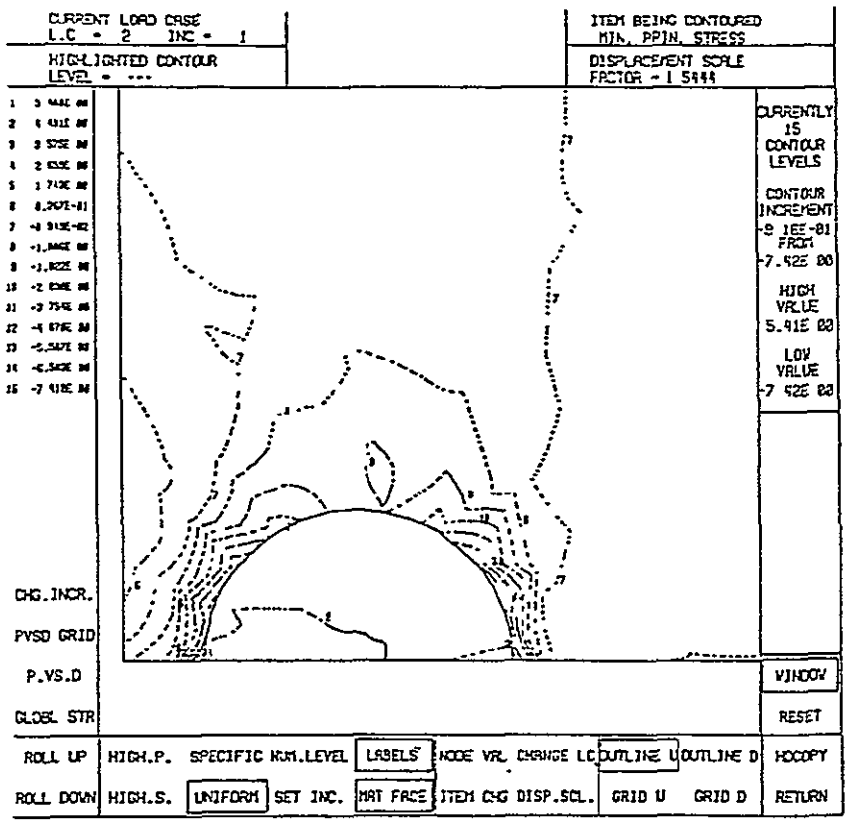

Figure III-D-7. σ_2 Contours for Uniform Load in Y-Direction

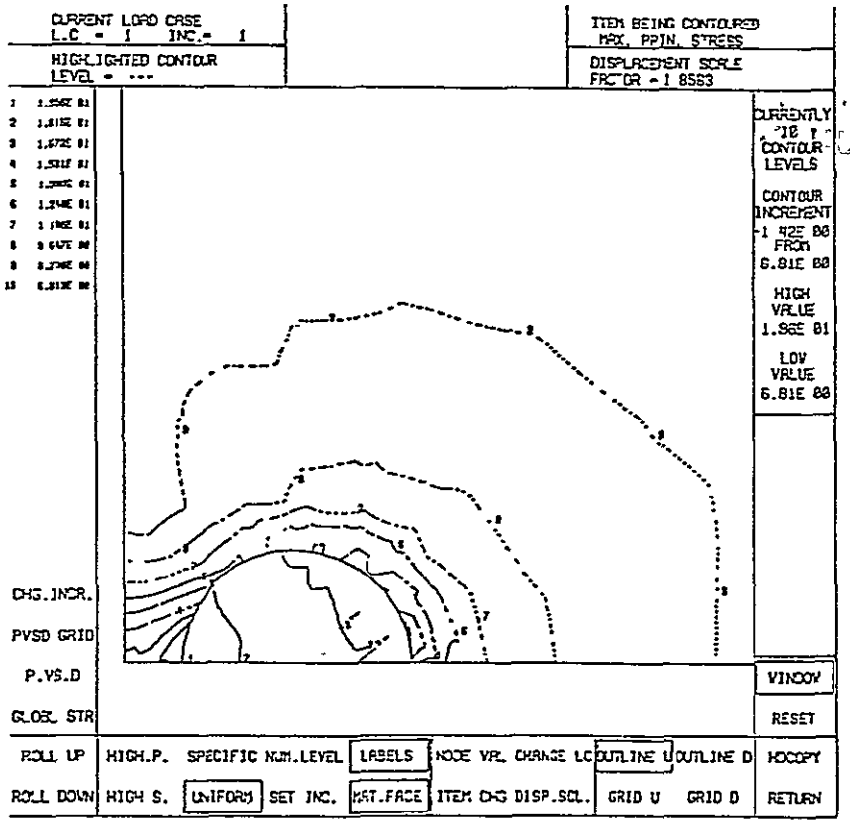

Figure III-D-8. σ_1 Contours for Uniform Load in Both X and Y-Directions

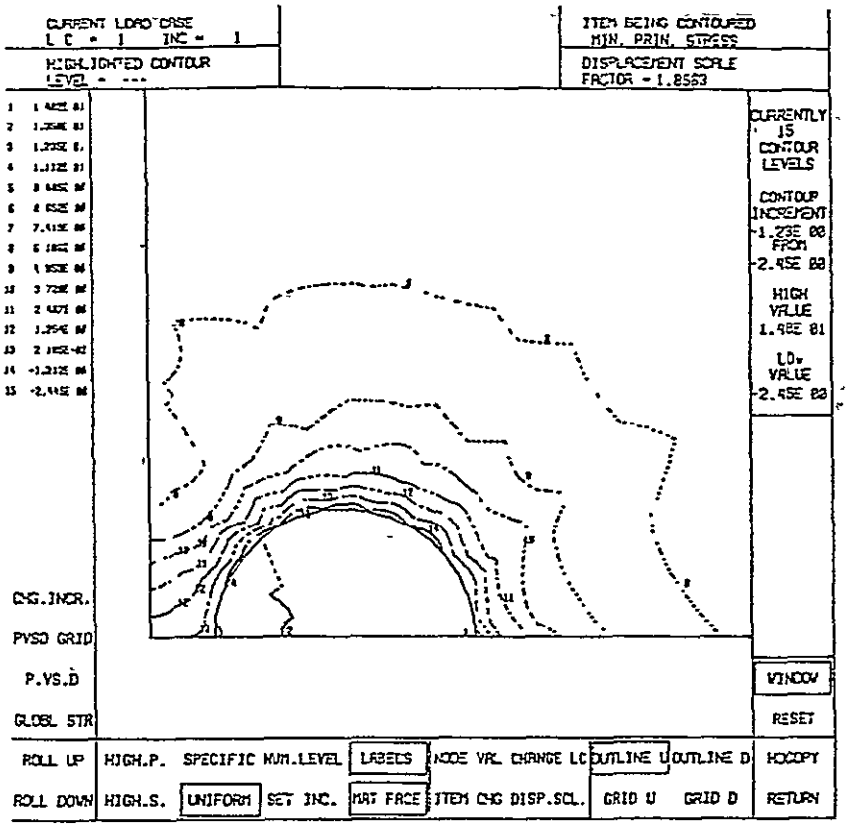

Figure III-D-9. σ_2 Contours for Uniform Load in Both X and Y-Directions

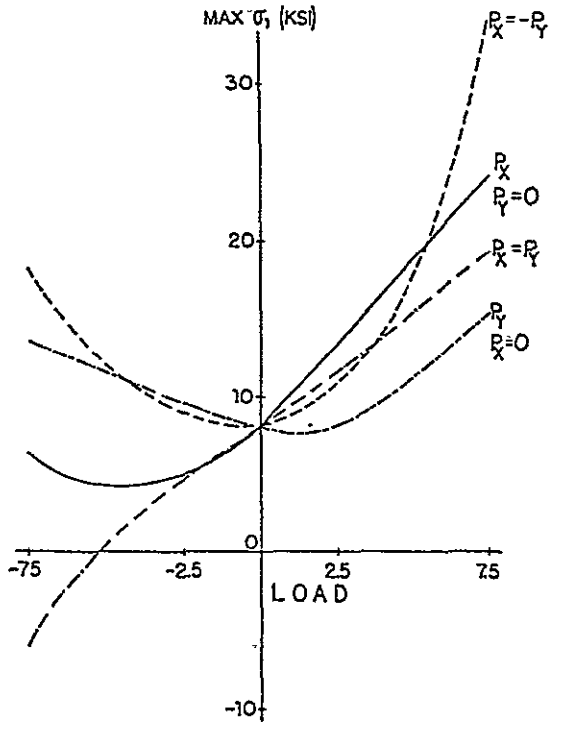

Figure III-D-10. Values of Maximum σ_1 as a Function of Load for Various Load Combinations

b.3) Discussion of Results. The first example indicates that the stress level is affected by the distance between the fibers. When this distance is less than five fiber radii, the combination cannot be approximated by a single fiber in an infinite medium. As the distance becomes smaller, the stress magnitude becomes larger and at a certain distance σ_1 becomes larger than the magnitude of σ_2. The liquid volume fraction also increases with the decrease in distance between the fibers. The lower the humidity level the less important is fiber interaction.

When there is applied load, the effects of nonlinearity become more pronounced and the superposition principle cannot be used. The trends in the maximum values of the liquid volume fraction and those of σ_1 are found to be similar.

In all two-fiber analyses, the stresses developed are quite high for cases with both high humidity and small fiber spacing, even when there is no applied load. It seems from these studies that permanent damage at the interface between fiber and epoxy could occur for combinations of these parameters as they are found in practice.

4. Plans for Upcoming Period

During the next reporting period, effort will be expended on additional analyses to gain more insight into load-humidity interactions. A different form of the constitutive relation may also be investigated.

5. References

1. Lumban-Tobing, F. E., M. S. Shephard and S. S. Sternstein, "Finite Element Analysis of Moisture Effects in Graphite-Epoxy Composites", to appear Proc. Symposium on Advances and Trends in Structural and Solid Mechanics, October, 1982.

2. Dennis, J. E., Jr. and J. J. More, "Quasi-Newton Methods, Motivation and Theory", SIAM Rev. 19 (1), 1977, 46-89.

3. Geradin, M., S. Idelsohn and M. Hogge, "Computational Strategies for the Solution of Large Nonlinear Problem via Quasi-Newton Methods", Comput. & Structures 13, 1981, 73-81.

4. Bathe, K. J. and A. Cimento, "Some Practical Procedures for the Solution of Nonlinear Finite Element Applications", Comp. Meth. Appl. Mech. Engng. 22, 1980, 59-85.

5. Matthies H. and G. Strang, "The Solution of Nonlinear Finite Element Applications", Int. J. Num. Meth. Engng. 14, 1979, 1613-1626.

6. Bard, Y., "On a Numerical Instability of Davidon-like Methods", Math. Comp. 22, 1968, 665-666.

7. Broyden, C. G., "Quasi-Newton Methods and Their Application to Function Minimization", Math. Comp. 21, 1967, 368-381.

III-E NUMERICAL INVESTIGATION OF THE MICROMECHANICS OF COMPOSITE FRACTURE

Senior Investigator: M. S. Shephard

1. Introduction

To understand the mechanisms of failure in composites it is necessary to develop insight into the micromechanical behavior, including interactions between matrix and fibers as the load is increased from zero to that corresponding to failure. Investigations of these phenomena, either experimental or numerical, are difficult. The purpose of this project, being carried out by graduate student Nabil Yehia, is to develop a nonlinear finite element analysis capability for performing numerical investigations of the micromechanical failure of composites.

2. Status

A survey of the applicable literature has been conducted, the conclusion drawn that crack modeling ability is not available in existing programs and a decision was made to design and develop a special nonlinear code. The basic structure of the required FEM program has been designed and many of the procedures to be included started. Coding of the first set of features was begun.

3. Progress During Report Period

Since the last progress report, effort has been concentrated on designing and implementing the program data base

and initial program features. Work has also been done on the process of piecing together a consistent set of numerical fracture mechanics procedures to track the entire fracture problem from crack initiation through crack propagation to identifying the point of unstable crack growth.

The program data structure has been designed and the linear elastic portions of the program implemented and tested. The major components of the linear elastic static portions are:

a. Six different 2-D element types and a variable-node, 3-D brick element.

b. An equation solver based on the frontal solution algorithm for single and multiple load cases.

c. A generalized stress recovery algorithm.

Geometric nonlinearities in terms of Green's strain tensor and nonlinear elastic material properties based on the polynominal strain energy function have been implemented but not yet checked. Portions of the material yield criteria have been coded and are currently being tested.

The major challenges of the cracking/fracture problem include the predicting of crack initiation, the direction of crack propagation, the rate of crack growth, debonding at the matrix-fiber interface and the point at which crack growth becomes unstable. Based on an examination of all available information, the most promising methods for

attacking the cracking/fracture problem have been selected and are listed as follows:

a. Crack initiation and propagation:

   i) For predicting crack initiation, the maximum tangential stress criterion will be used.

   ii) For crack propagation and for pre-cracked problems, the minimum strain energy (S) criterion will be employed[1,2]*.

b. The use of the minimum strain energy criterion will facilitate the process of predicting the direction and the rate of crack propagation[3].

c. Stress intensity factors will be evaluated using the displacement method, through the use of crack tip singular elements[4] with a layer of transition elements to improve the results[5].

d. At bimaterial interfaces, the problem will be solved partially by introducing material discontinuity effects in evaluating the stress intensity factors determined from the numerical results on the crack flanks.

e. To determine crack growth stability, two criteria are proposed and listed as follows:

---

*Numbers in brackets in this section refer to the references which are listed on page 122.

i) Compare the size of the crack with some typical (global) dimensions of the problem.

ii) Compare the crack growth increment (given for a stable crack as $\frac{\Delta a(n+1)}{\Delta a_n}$ where Δa_n is the crack growth increment in step n) with a stability constant.

A summary of possible crack problem algorithms and the reasons for selecting those listed above is given in [6].

4. Plans for Upcoming Period

During the next reporting period we will concentrate our efforts on implementing the various computational modules of the crack problem. One such module, not yet solved, is the remeshing of the finite elements as cracks move through a region. This aspect will be considered. We expect the automatic mesh generation capability, discussed in Section IV-D of this report, to play a central role in the solution to this problem.

5. References

1. Sih, G. C., "Strain-Energy Density Factor Applied to Mixed Mode Crack Problems", Int. J. Fracture, Vol. 10, No. 3, September 1974, 305-321.

2. Sih, G. C. and B. MacDonald, "Fracture Mechanics Applied to Engineering Problems - Strain Energy Density Fracture Criterion", Eng. Fract. Mech., Vol. 6, 1974, 361-386.

3. Sih, G. C., "Mechanics of Ductile Fracture", Fract. Mechanics and Technology, Eds.: G. C. Sih and C. L. Chos, Vol. II, 1977, 767-784.

4. Ingraffea, R. A. and C. Manu, "Stress-Intensity Factor Computation in Three Dimensions with Quarter-Point Elements", Int. J. Num. Meth. Engng., Vol. 15, 1980, 1426-1445.

5. Lynn, P. P. and R. A. Ingraffea, "Transition Elements to be used with Quarter-Point Crack-Tip Elements", Int. J. Num. Meth. Engng., Vol. 12, 1978, 1031-1036.

6. Yehia, N., "Micromechanical Failure of Composites", Ph.D. Thesis project proposal, RPI, April 1982.

6. Current Publications or Presentations by Professor Shephard on this Subject

"The Finite Element Modeling Process - Will it be Automated"

Published in New and Future Developments in Commercial Finite Element Methods, J. Robinson, Ed., October, 1981, 451-468.

"Adaptive Finite Element Analysis Accounting for Material Interfaces"

Presented at the ASCE Conference, St. Louis, MO, October 1981.

"Automatic Finite Element Mesh Generation"

Presented at a Program for Computer Graphics, Cornell University, March 19, 1982.

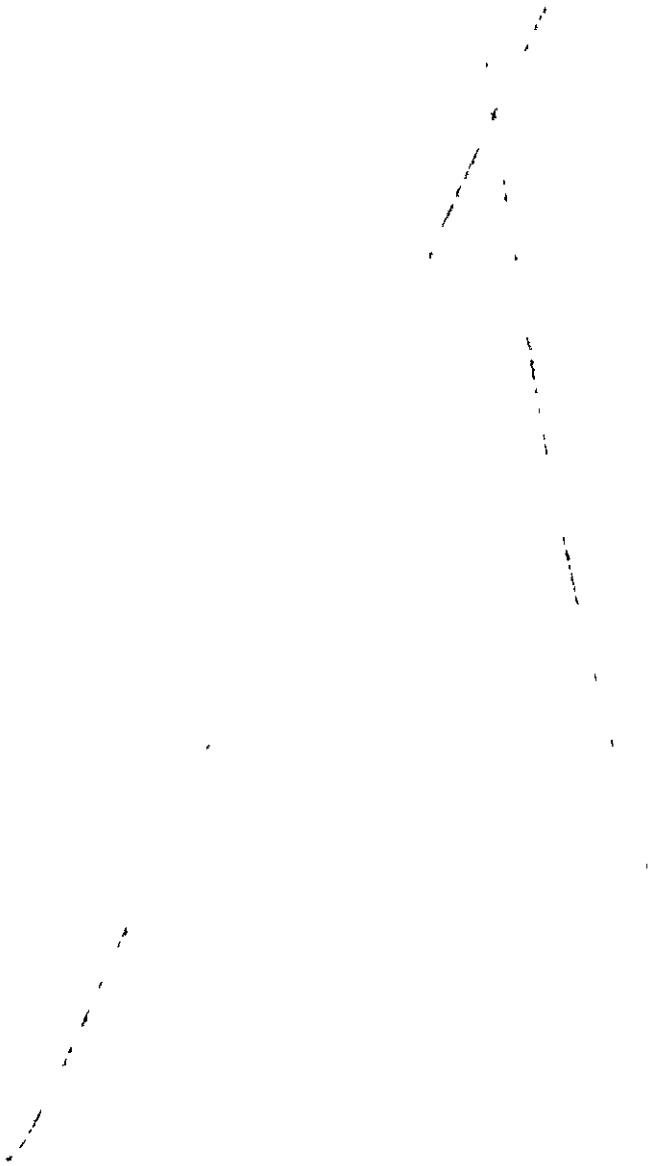

PART IV
GENERIC STRUCTURAL ELEMENTS

INTRODUCTION

The redesign of flight-critical structural components currently in service as metal parts on existing aircraft was included as part of RPI's composite materials and structures program to assure relevance and realism to the project's direction and to contribute to the nation's pool of innovative structural design concepts. Two such components were selected in cooperation with major commercial airframe manufacturers, Boeing Commercial Airplane Co. and Lockheed California Company, and with advice from NASA. The first, the 727 airplane's elevator actuator attachment rib, has completed the cycle planned at the project's inception. That is, several alternate redesigns were attempted; one was selected, analyzed and finalized; and two specimens were fabricated and successfully tested to ultimate load. The second, a redesign of the wing-mounted engine drag strut for the L-1011 airplane, has been carried to the point where (a) the usefulness of certain basic research performed earlier at RPI under the NASA/AFOSR program was made very clear and was called on in the design process, and (b) several areas of research in which results are needed for such a redesign - but are not now available - have been identified.

As a matter of fact, a number of basic research projects motivated by the early work on the 727 elevator rib, have been reported in these project reports for some time. Some

of these have been completed, others are reported here and still others were planned based on challenges encountered in the 727 elevator problem. Both these research projects and those arising out of the L-1011 engine drag strut redesign were selected for study because they were seen as having the potential to contribute significantly to classes of generic composite aerospace structures. It was decided in November 1981 to suspend any further conceptual design research on actual aircraft components, in favor of pursuing basic studies of such generic structural elements. Progress on these projects during the current program period is reported in the sections that follow.

IV-A MECHANICAL JOINTS IN COMPOSITES

The 727 elevator actuator attachment rib redesign in composites at RPI, reported in earlier progress reports, led to separate research projects. One deals with heavily loaded holes in composites such as are encountered at the actuator attachment; the second deals with lightly loaded mechanical joints, such as occur, for example, in a row of small bolts or rivets, typified by the more or less continuous joint between rib flange and the elevator skin. Both of these problems have required the development of new analysis and/or test methods.

More recently, the importance of optimizing the strength of compact lugs has become clear. All three of these projects are described in the paragraphs to follow.

1. Analysis of Heavily Loaded Mechanical Joints

Senior Investigator: C. Muser

a. Introduction

Discontinuities such as mechanical joints and openings are always going to be found in structures independent of the materials used. Although fiber reinforced materials have the potential to yield efficient designs for such discontinuities, these materials are used in only a very few cases for heavily loaded mechanical joints. It is believed that this is due to a lack of knowledge of how to use composites efficiently for

such discontinuities and, therefore, a detailed investigation is justified.

b. Status

It had been decided to focus on cylindrically orthotropic materials rather than on materials orthotropic with respect to cartesian coordinates. A closed form solution for the stress distribution in a circular plate with a circular hole at its center was found by Dr. N. J. Hoff for the case when its material is cylindrically orthotropic. The geometry of that plate can be seen in Figure IV-C-1-a of the previous report[1]*. Later, this analysis was extended to treat a similar plate whose elastic properties, however, were a function of the distance from the hole. The constitutive equations used were:

$$E_i = S^*_{ij}(1 + Q_{(i)(j)} r^h)\sigma_i$$

$$\gamma_{r\theta} = S^*_{66}(1 + Q_{66} r^h) T_{r\theta}$$

where i, j = r,θ and () indicates no sum on indices.

The constants S^*_{ij} and Q_{ij} are a function of the dimension of the plate and the parameter h, which describes the rate of change of material properties along the radius r. The compliances, S_{ij}, can be prescribed at both boundaries independent of the choice of the parameter h, so long as the convergence criteria are observed.

---

*Numbers in brackets in this section refer to the references which are listed on page 133.

It was shown that cylindrical orthotropy can reduce the stress concentrations along the edge of the hole substantially, especially when the stiffness of the fibers is much higher than that of the matrix. The same behavior can be observed for the case with varying material properties. In the latter case, however, it is possible to link the properties yielding low stress concentrations with those normally encountered in designing a plate as a structural element.

c. Progress During Report Period

Substantial effort was devoted to reporting the results obtained, as described in the previous section. One paper has been accepted for publication and a second is going to be presented at an international composites conference (see Section e. Current Publications or Presentations, etc., page 133).

Progress was also made in applying the same analytical methods to the problem of a circular plate pulled at one end in one direction, with that load reacted by a bolt inserted in the centrally located hole (see Figure IV-A-1-b of the previous report [1]). The material properties of that plate were allowed to vary along the radius.

As mentioned in the previous report, this work does not attempt to find the exact boundary conditions at the edge of the hole. The goal is rather to develop an algorithm which is capable of handling, to a satisfactory degree of approximation, any conditions at both boundaries of the plate.

Therefore, the assumptions commonly used, i.e., there is no friction between the bolt and the plate and there is no gap between the bolt and the plate, were considered to apply. The boundary conditions were expanded in Fourier series. This implies that there are n sets of boundary conditions, if for every stress acting on the boundaries, n terms are considered. For every such set, a solution can be found. The total of all n solutions found in such a manner yield the solution for the bolt-loaded plate.

A typical form of the stress function, $\underline{\phi}$, used is:

$$\underline{\phi} = \sum_{n=1}^{\infty} \sum_{p=1}^{4} A_p^n \sum_{m=0}^{\infty} K_p^m r^{t_p + hm} \cos n\theta$$

The coefficients K_p^m can be determined with a recursion formula which emerges from the process of satisfying the compatibility equations. (There is one compatibility equation for every n, where n is the index of terms considered in the expansion of the boundary conditions.) The constants A_p^n can be determined with the aid of the n-th set of boundary conditions. The roots, t_p are those obtained from the case of homogeneous materials, for which a closed form solution had been found, as mentioned earlier. These roots, t_p, are also a function of n.

A computer program, which is in the process of being tested, will be used to calculate the stresses in a circular bolt-loaded plate whose elastic properties vary radially.

d. Plans for Upcoming Period

The investigation of stress distributions in circular, bolt-loaded plates, the materials of which are cylindrically orthotropic and vary radially, is planned for completion in the next reporting period.

e. References

1. 41st Semi-Annual Report, Composite Structural Materials, AFOSR and NASA Grant No. NGL 33-018-003, Rensselaer Polytechnic Institute, Troy, NY, December 1981, 117 and 120.

f. Current Publications or Presentations by C. Muser on this Subject

"Stress Concentration Factors for Cylindrically Orthotropic Plates, with N. J. Hoff.

To be published in the Journal of Composite Materials, May 1982.

"Stress Concentrations in Cylindrically Orthotropic Plates with Radial Variation of the Compliances", with N. J. Hoff.

To be presented at the Fourth International Conference on Composite Materials (IV-ICCM), Tokyo, Japan, October 25-28, 1982.

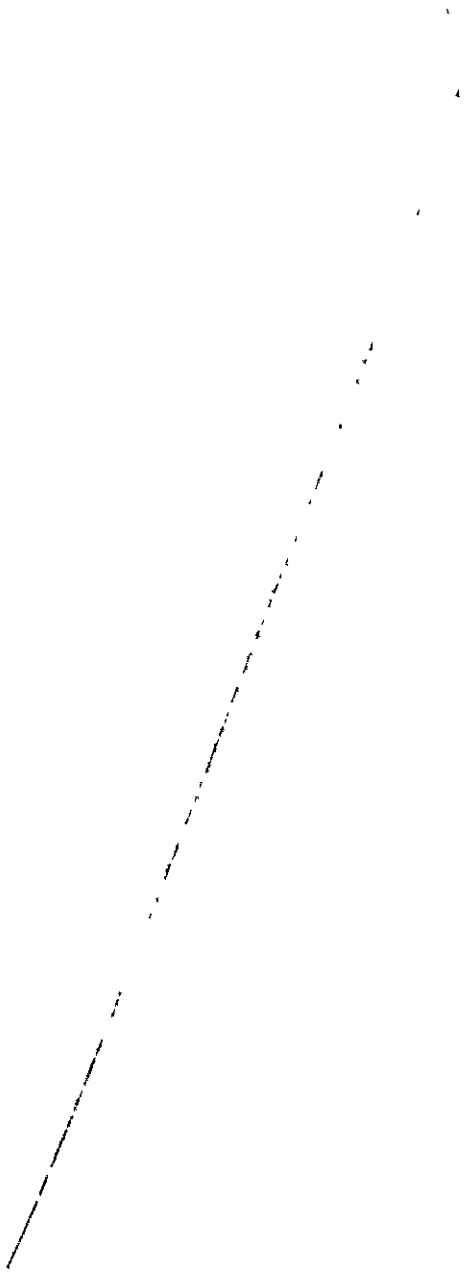

2. Pin-Loaded Holes in Uniform Composite Plates

Senior Investigator: R. G. Loewy

a. Introduction

Stress analysis is a key step in the design of an optimum mechanical joint in composites as it is in the design of any other structural member. To study this problem, an idealized model of a single fastener joint has been postulated (see Figure IV-A-2-1). Note the existence of pin-hole clearance, δ. This gives rise to uncertain boundary conditions, particularly as to the amount of the contact along the pin hole boundary under load, as explained in previous reports. These unprescribed boundary conditions preclude application of ordinary stress solution methods to this problem.

b. Status

The work reported in this section is that of graduate student Wonsub Kim.

A linear constraint equation has been introduced in the finite element method (FEM) analysis of this problem to describe the motion of pin-hole contact points as the hole boundary deflects under load. These constraint equations were constructed on the basis that any boundary point within the region of pin-hole contact must remain on the surface of the pin (assumed rigid and frictionless) for a given applied load level. Thus, the only remaining unknown regarding

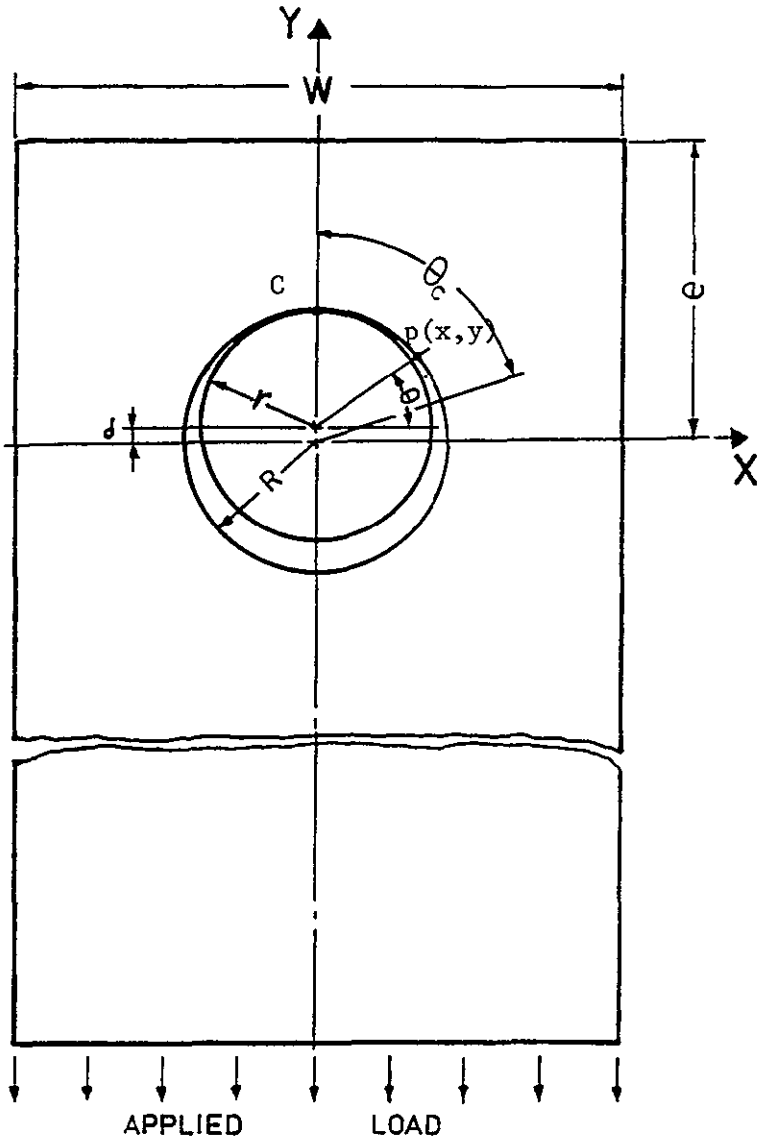

Figure IV-A-2-1. Idealized Model of Single Fastener Joint

boundary conditions is the extent of the pin-hole contact. Next, a "mixed method" was introduced, consisting of the finite element analysis (FEM) as an analytic part and photoelastic experiments as an empirical counterpart. In the mixed method, the unknown extent of the contact region θ_c is assumed and FEM analyses iterated until a value of θ_c can be deduced which produces a distribution of maximum shear strain which matches that produced by the photoelastic experiments. This contact angle is assumed to be close to the actual one, and the numerical method (FEM) is then available for all aspects of a solution.

Two advantages of the mixed method over more conventional methods are evident. First, it is a self-checking method, since experimentally determined results are reflected in the analysis and some confidence can be gained as to the mathematic modeling and the theory used in the analysis. Second, extrapolated analyses can be conducted at failure load levels, and reliable failure prediction studies are, therefore, possible.

In the previous reporting periods, analyses were performed at several load levels for the so-called B-type specimen ($[\pm 45°/0°]_{ns}$) to produce the curve relating applied force versus assumed contact angle, which is shown again in Figure IV-A-2-2, for convenience. Also, results were obtained in photoelastic experiments for laminate specimens type B, $[\pm 45°/0°]_{ns}$ and type F, $[\pm 30°/0°]_{ns}$.

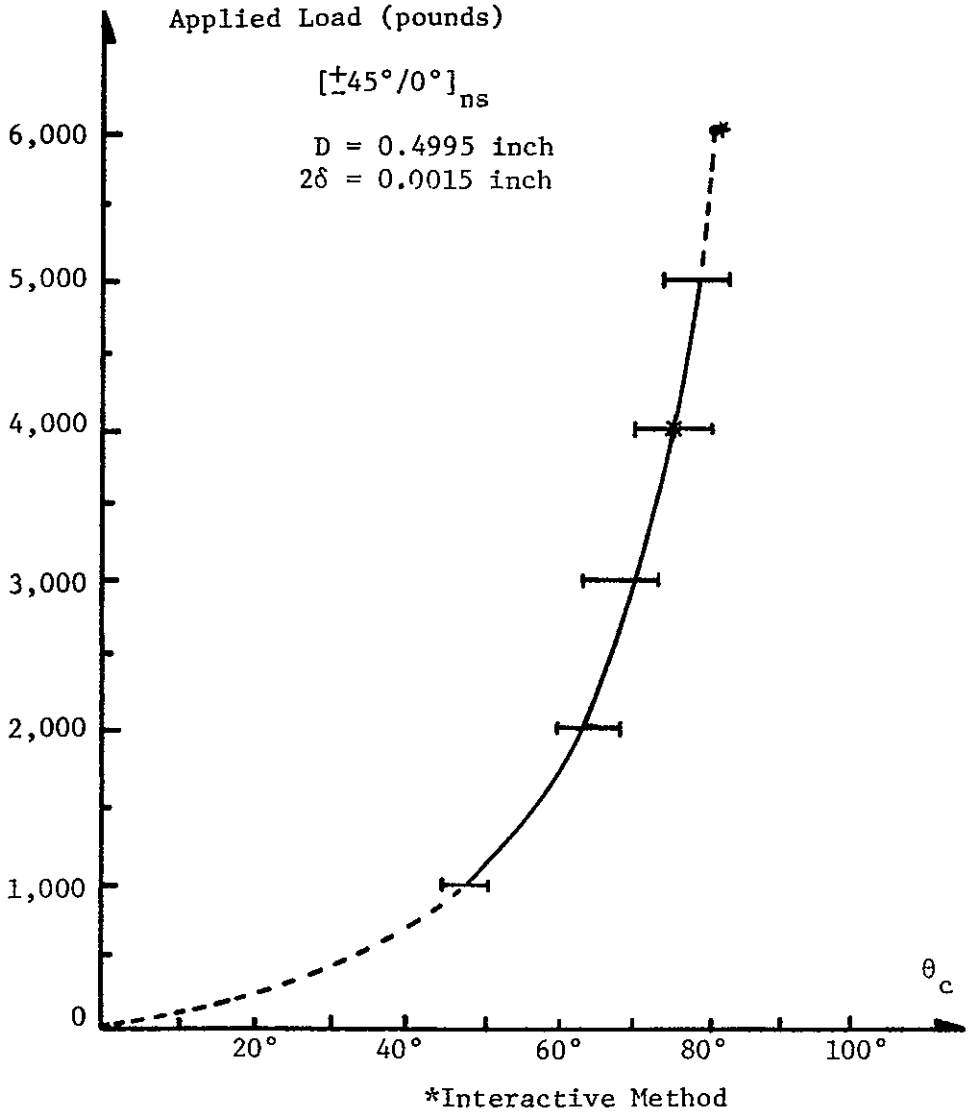

Figure IV-A-2-2. Relationship Between Applied Load and Half-Contact Angle (θ_c) -- Semi-Empirical Method

c. Progress During Report Period

Analyses for the types B and F laminate specimens were completed at a number of additional load levels in this reporting period. In addition, two new analysis approaches to the pin-hole contact problem were devised, each of which has its own distinct advantages.

An attempt was also made to predict failure loads by introducing two distinct existing failure criteria, using the FEM stress computation results. These criteria are O. Hoffman's failure criterion[1]* and the so-called "maximum stress criterion"[2]. Correlation attempts showed that both criteria predicted correct failure modes but were too conservative in predicting joint strength.

In the following paragraphs, the two new analysis methods will be explained, the results of the analyses summarized and failure prediction attempts described.

1) Interactive Method and Energy Criteria

Figures IV-A-2-3a, b and c show deformed shapes of the fastener hole as dotted curved lines for cases in which the assumed contact angles are correct, too small and too big, respectively. In the same figures, the shape of the pin as recognized by the FEM through the linear constraint equations (which is the only way the FEM can recognize the existence

*Numbers in brackets in this section refer to the references which are listed on page 171.

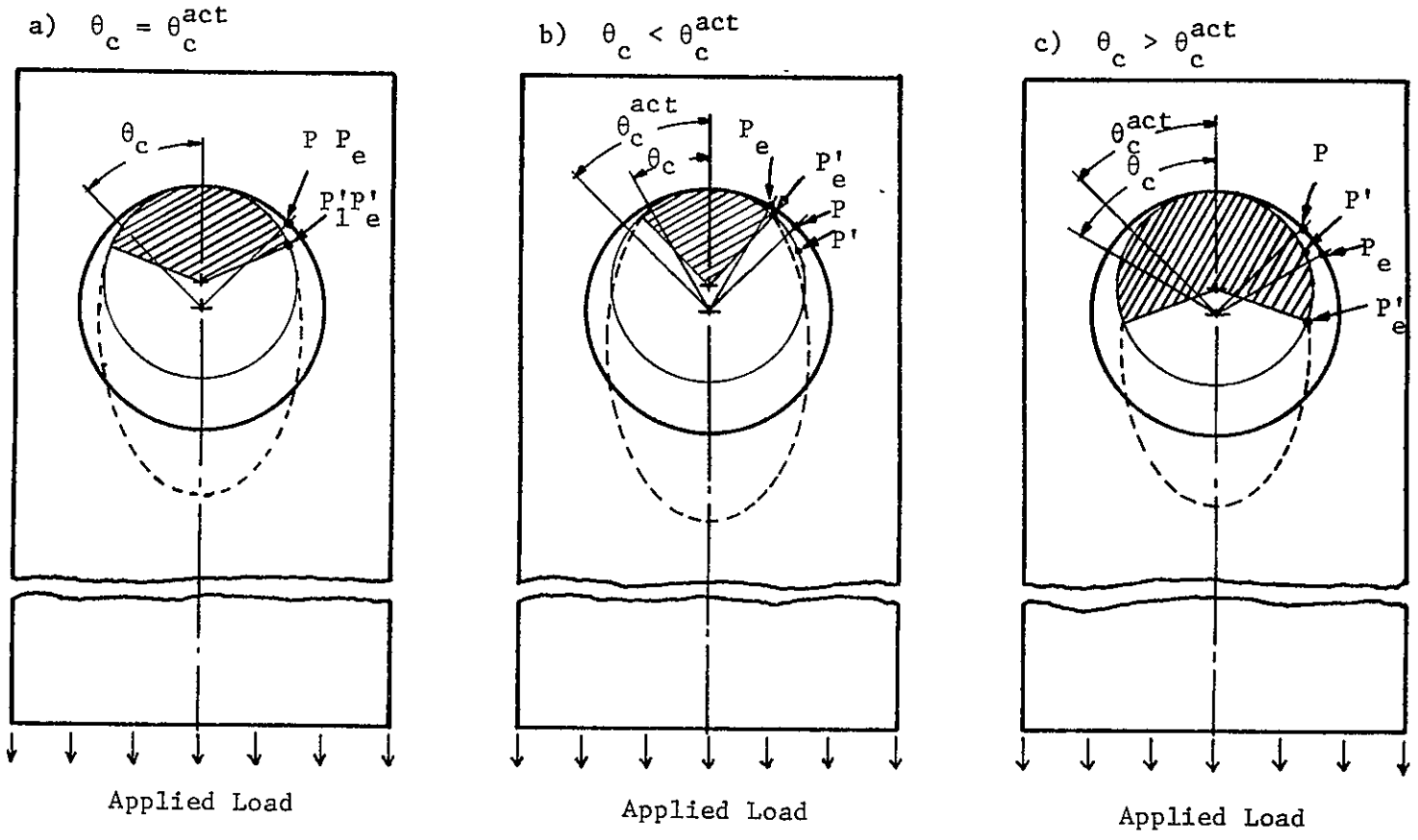

Figure IV-A-2-3. Deformation of Hole Due to Assumed Contact Angle (θ_c)

of the pin) are also depicted. Comparing Figures IV-A-2-3a and -3b, one can see that the Figure 3b case lost some support (between points P_e, assumed end of contact, and P, the actual end of contact) nominally provided by the pin, which is fixed in space. In fact, there is an inadmissable interference between the pin and the deformed hole edge configuration. If the pin were not shown, however, there is still an identifiable kink in the deformed boundary near point P'_e. From the lost support there results a bigger displacement, compared to Figure IV-A-2-3a, at the end of the plate where the external tensile load is applied, although this doesn't show in Figures IV-A-2-3. Thus, more work is done by the applied force, and it can be expected, in a conservative system, that this will result in more strain energy stored in the plate.

On the other hand, by comparing Figures IV-A-2-3a and -3c, it can be seen that the effect of assuming θ_c to be bigger than the actual contact angle, θ_c^{act}, some hole boundary points located between points P and P_e, are forced unrealistically to the surface of the pin. This produces the inward hump on the deformed boundary shown in Figure IV-A-2-3c. If one imagines that forces on the hole boundary between P and P_e have done work in forcing these points to the pin contour, then, in this case too, the total external work and the strain energy stored in the plate would be bigger than that in Figure IV-A-2-3a.

This leads to the conclusions that:

i) a smooth hole edge deformation shape is possible only when $\theta_c = \theta_c^{act}$ and

ii) the strain energy stored in the body and the potential of (in linear elasticity, two times the work done by) applied forces both have a relative minimum when $\theta_c = \theta_c^{act}$.

if $\theta_c < \frac{\pi}{2}$.

Either of these two facts can be used as a criterion to determine the correct value for θ_c in clearance-fit joint analysis. One such example may be seen in Figure IV-A-2-4. This shows the deformed shape of a FEM mesh plotted over the original, undeformed mesh for cases in which the assumed θ_c's are equal to (a) 50°, (b) 65° and (c) 70° when a load of 2,000 pounds is uniformly applied to a B-type specimen. The original mesh is shown as solid lines and the deformed mesh as dashed lines. The original, undeformed hole boundaries are shown as dashed lines and the deformed hole boundaries by dot-dashed lines. In these plots, displacements are exaggerated by factors of 50, 100 and 100 times the actual computed amounts for figure parts (a), (b) and (c), respectively. As indicated by arrows in the figures, the deformed shape of the hole edge boundary of case (a) has a kink ($\theta_c < \theta_c^{act}$) and case (c) has a kink ($\theta_c > \theta_c^{act}$) while case (b) shows none. This indicates that the actual contact angle is close to 65° in this example. Indeed, this is confirmed in the applied load versus assumed contact angle

(a) $\theta_c = 50^0$ (b) $\theta_c = 65^0$ (c) $\theta_c = 70^0$

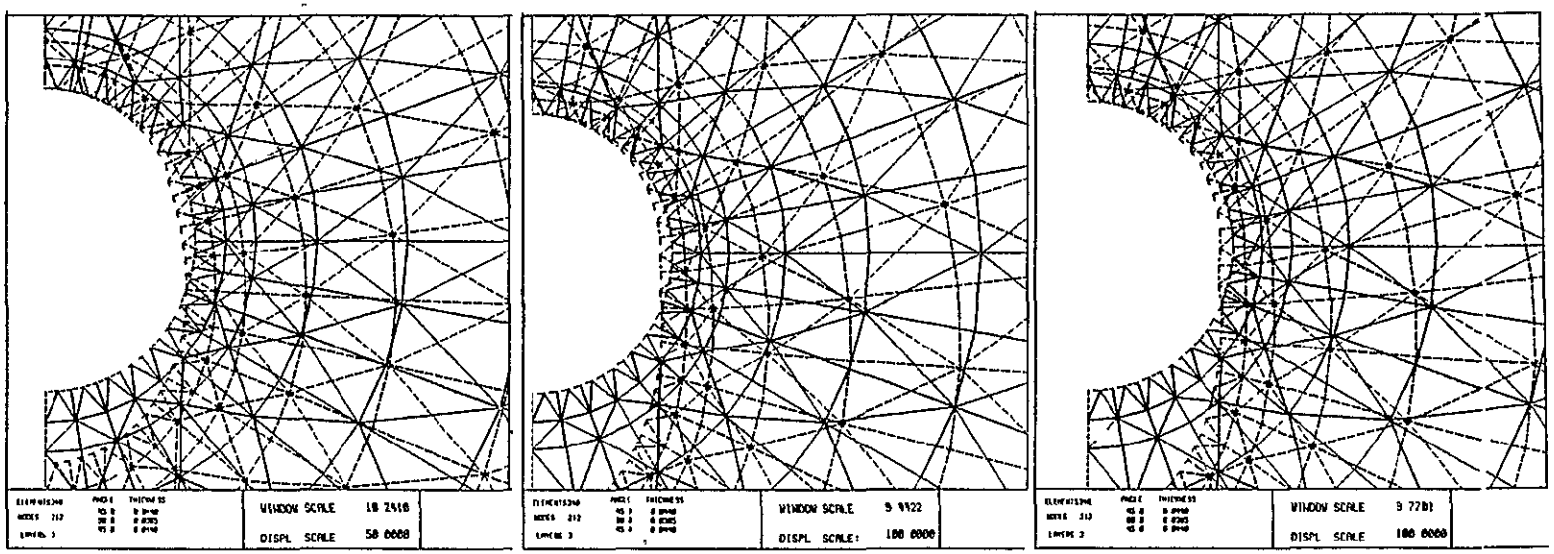

Figure IV-A-2-4. Deformed Shape of the Hole Boundary (dot-dash lines) as a Function of Assumed Half-Contact Angle (θ_c). (B-type $[\pm 45°/0°]_{ns}$ laminate; applied load 2,000 lbs.)

curve of Figure IV-A-2-2, where θ_c is found to be about 63° for an applied load level of 2,000 pounds.

The second approach to a purely analytical determination of θ_c is shown in Figure IV-A-2-5, which presents the potential of the applied force as a function of assumed contact angle. In this figure, potential variation in terms of assumed contact angle can be seen for four cases of load and lamination combinations. The existence of a relative minimum of potential variation is clearly indicated. Moreover, the minima for the cases B4000 and B6000 in Figure IV-A-2-5 fall at values of θ_c almost identical to those which Figure IV-A-2-2 gives for the corresponding loads.

The above discussion leads to the conclusion that both the smoothness of the hole edge deformation and the minimum property of potential can be used to determine θ_c.

2) Some Results of Analysis

Both the semi-empirical and the interactive methods described in the previous sections were applied to a single-fastener joint model (Figure IV-A-2-1) for two different types of graphite-epoxy laminate. These laminates were $[\pm 30°/0°]_{ns}$ or F-type (24 layers) and $[\pm 45°/0°]_{ns}$ or B-type (23 layers). The elastic properties of the material are shown in Table IV-A-2-1, and the strength data is given in Table IV-A-2-2.

In the finite element idealizations, the layers of F-type laminates were rearranged as follows: $[(+30°)_8/(0°)_8/(-30°)_8]$, whereas, the layers of B-type laminate were

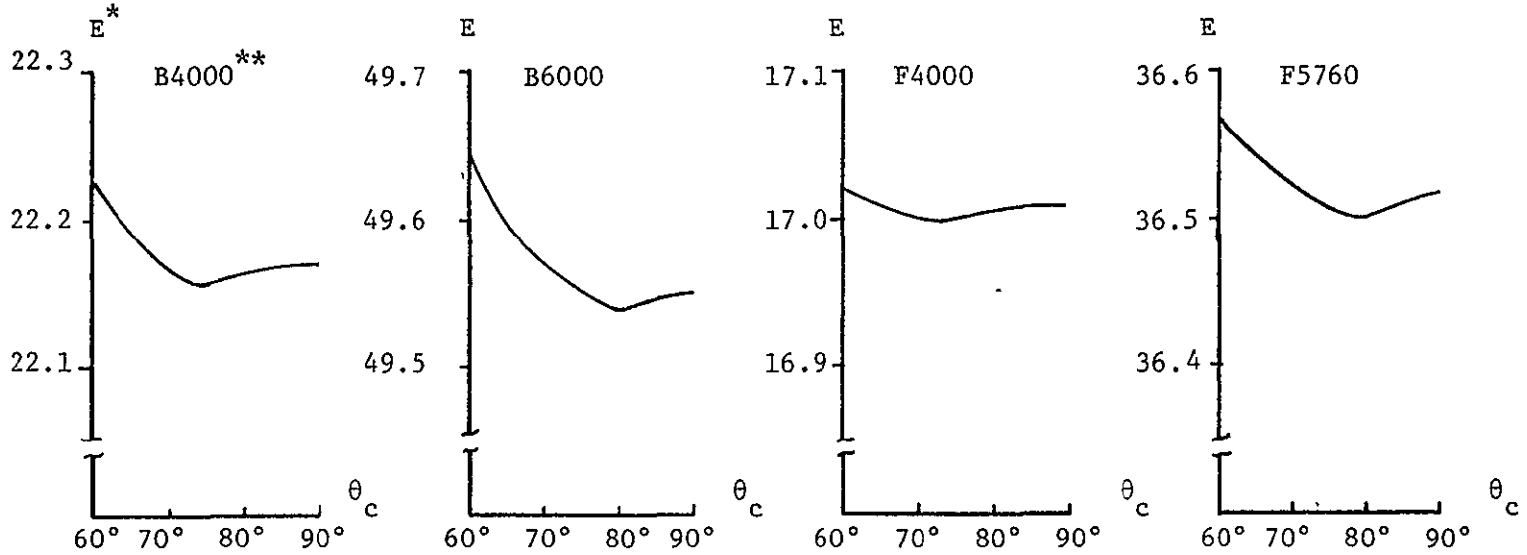

Figure IV-A-2-5. Energy Potentials of Applied Loads as a Funtion of Assumed Half-Contact Angle (θ_c)

*E: Energy potential of applied loads undergoing displacements (lbs./in.)

**B and F indicate the type of lamination (B: $[\pm 45°/0°]_{ns}$, F: $[\pm 30°/0°]_{ns}$). The associated numbers indicate the levels of applied load.

TABLE IV-A-2-1

PROPERTIES OF GRAPHITE/EPOXY TAPE

(Fiberite Hy-E 1048AlE)

Properties*	Symbols	Values
Modulus in Fiber Direction (10^6 psi)	E_L	21.306
Modulus Transverse Direction (10^6 psi)	E_T	1.4
Shear Modulus (10^6 psi)	G_{LT}	0.93
Poisson's Ratio	ν_{LT}	0.32

*For a fiber volume fraction of 60%.

TABLE IV-A-2-2

STRENGTH PROPERTIES OF GRAPHITE/EPOXY* COMPOSITES

Property	Explanation	Value (ksi)
X	Tensile strength in fiber direction	200.0
X'	Compression strength in fiber direction	207.0**
Y	Tensile strength transverse direction	8.0
Y'	Compression strength transverse to fiber	18.0
S	Shear strength (interlaminar)	19.0**

*Hy-E 1048 AiE prepreg tapes (60% fiber volume fraction), Fiberite Co.

**These values were suggested by Prof. Diefendorf of the Dept. of Materials Engineering, RPI, based on his experiences with similar fiber-resin systems. The rest of the properties were given by Dr. J. Allen of Fiberite Co., the manufacturer of the materials, through telephone communication with Wonsub Kim on January 12, 1982.

represented as $[(+45°)_8/(0°)_7/(-45°)_8]$. This was possible without loss of accuracy, since laminate plate theory for in-plane tension problems recognizes only average values through the thickness.

The isochromatic fringes of Figures IV-A-2-6a, b and c showed maximum shear strains which were well-matched with the distribution of the corresponding contours generated by the FEM analysis (see Figures IV-A-2-7a, b and c, respectively). The isochromatic fringe of Figure IV-A-2-6c, for the B-type laminate at 6,000 pounds applied load, was obtained immediately before failure occurred. Isochromatic pictures of the F-type laminate at failure load, 5,760 pounds, however, which would have corresponded to Figure IV-A-2-7d, could not be taken, since failure took place suddenly (the usual case) and before a fringe picture could be taken.

It can be seen in Figure IV-A-2-6b that the symmetry of the fringe pattern of the F-type specimen was disturbed, due to small twisting moments which came about because of the rotation of the spindle of the Instron testing machine. These rotations were not controllable. As a result, ring-type isochromatic fringes appeared just above the hole in the figure, in which the pin pushes upward. Accordingly, the analysis for the F-type laminate was done purely by the interactive method. Analyses for the B-type laminate, however, were done using both the semi-empirical and interactive approaches. Results from both methods for this type of

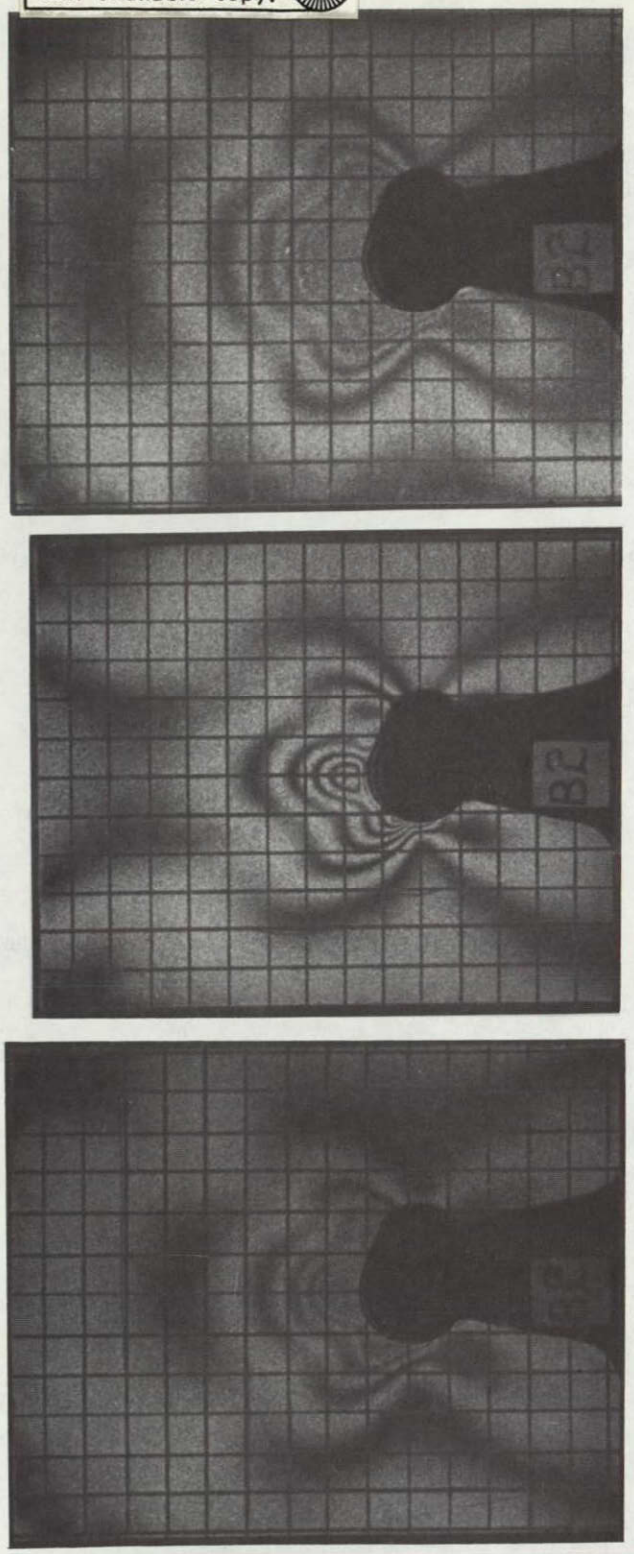

(a) B4000 (b) F4000 (c) B6000

Figure IV-A-2-6. Isochromatic Fringes: (a) B4000, (b) F4000 and (c) B6000
(one fringe value γ_{max} = 0.0018917 in./in.)

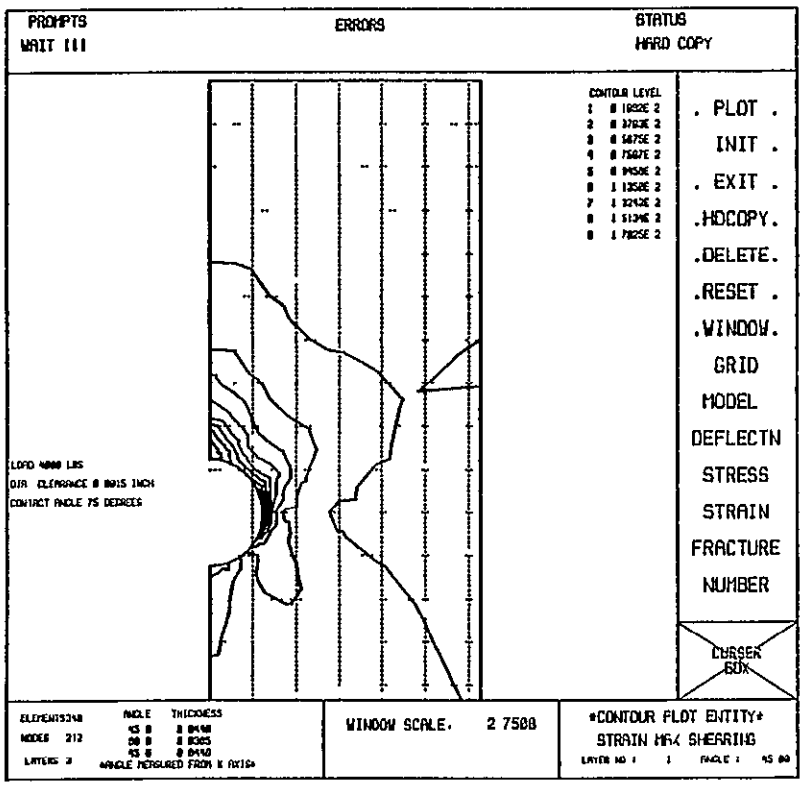

(a) B4000 - (+45°) - γ_{max}

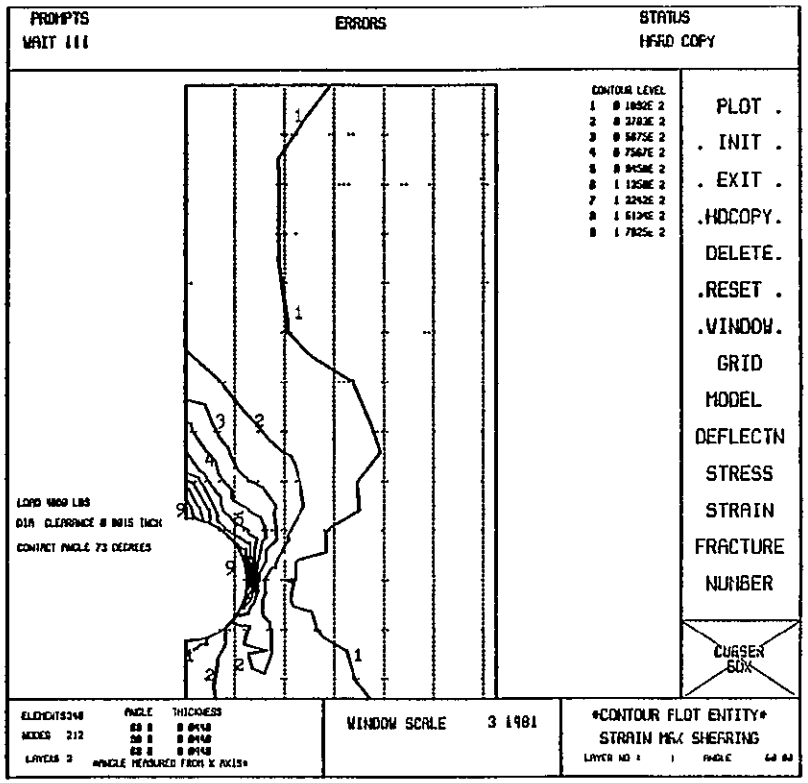

(b) F4000 - (+30°) - γ_{max}

Figure IV-A-2-7. Maximum Shear Strain Distribution Contours from FEM Analysis (a) B4000 & (b) F4000 (one fringe value γ_{max} = 0.0018917 in./in.)

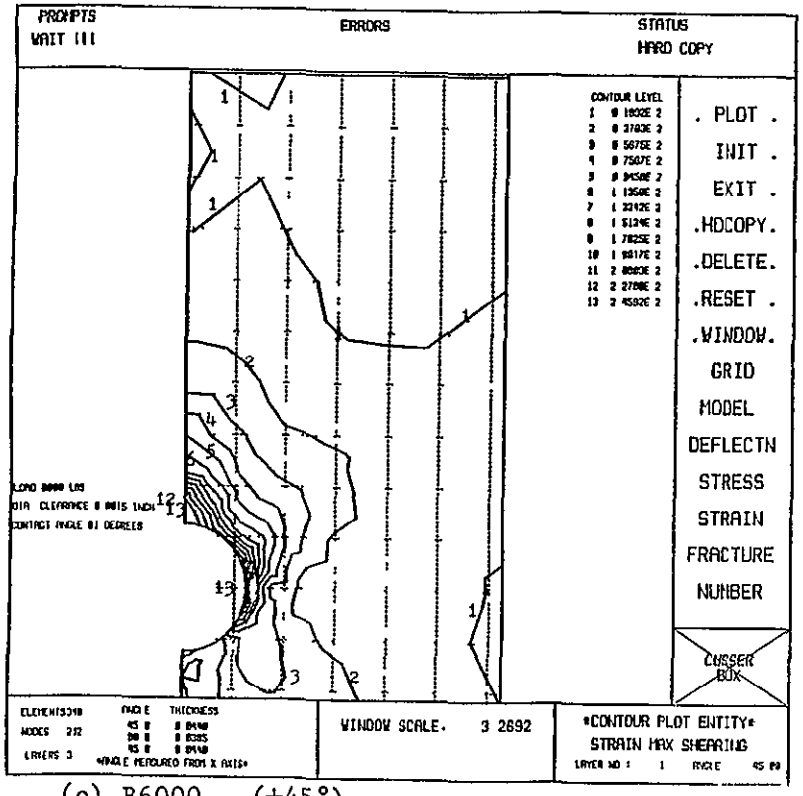

(c) B6000 - (+45°) - γ_{max}

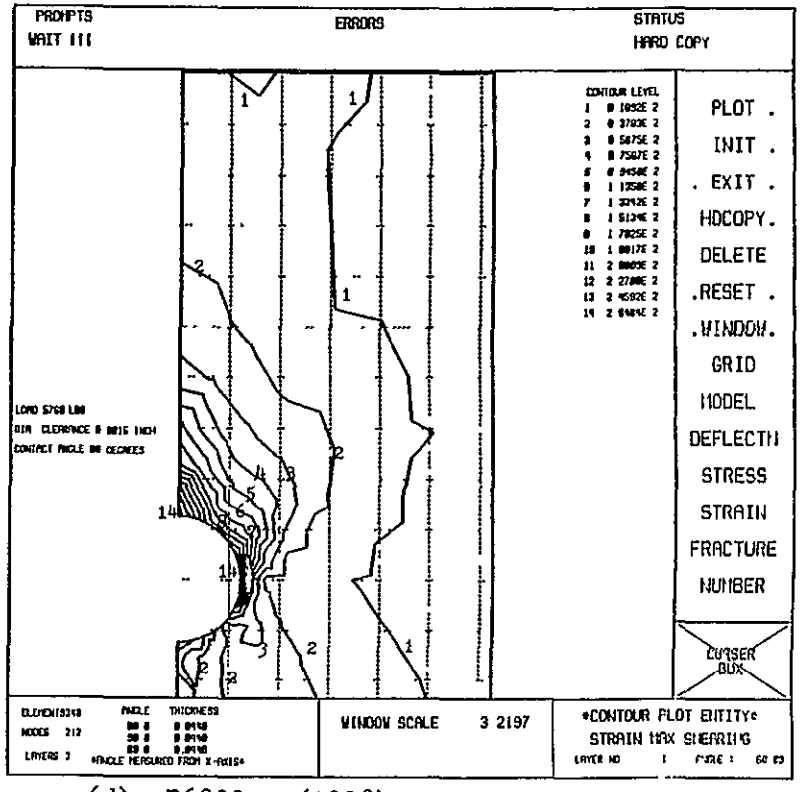

(d) B6000 - (+30°) - γ_{max}

Figure IV-A-2-7. (Continued), (c) B4000 - [+45°] & (d) B6000 - [+30°]
(one fringe value γ_{max} = 0.0018917 in./in.)

laminate were almost identical. The results from the interactive method were not included here to avoid duplication.

It should be noted that the semi-empirical method does not require an iterative approach to the failure load condition, as regards pin contact angle θ_c, when the analysis has been performed at several other load levels, as explained in the previous report and indicated in Figure IV-A-2-2. Calculations for the failure load level with several different assumed contact angles were performed, however, to check the smoothness of the deformed contours of the hole edge and the level variation of potential with assumed contact angle, a necessary procedure for the interactive and minimum potential methods, respectively.

The nomenclature used in Figures IV-A-2-8a through -8d is explained in Table IV-A-2-3. These figures show the radial and circumferential stresses in each layer of the laminate as well as the average values across the thickness of the plate along the edge of the hole. Comparing Figures IV-A-2-8a and -8b, one observes clearly the nonlinear nature of the problem in its various aspects, even though pin-hole clearance is as small as 0.0015 inch. For example, when the applied load level on the B-type laminate increased from 4,000 pounds (see Figure IV-A-2-8a) to 6,000 pounds (see Figure IV-A-2-8b), the maximum circumferential stresses more than doubled, while the peak values of radial stress increased by only relatively small amounts. Furthermore, the rate at which stress

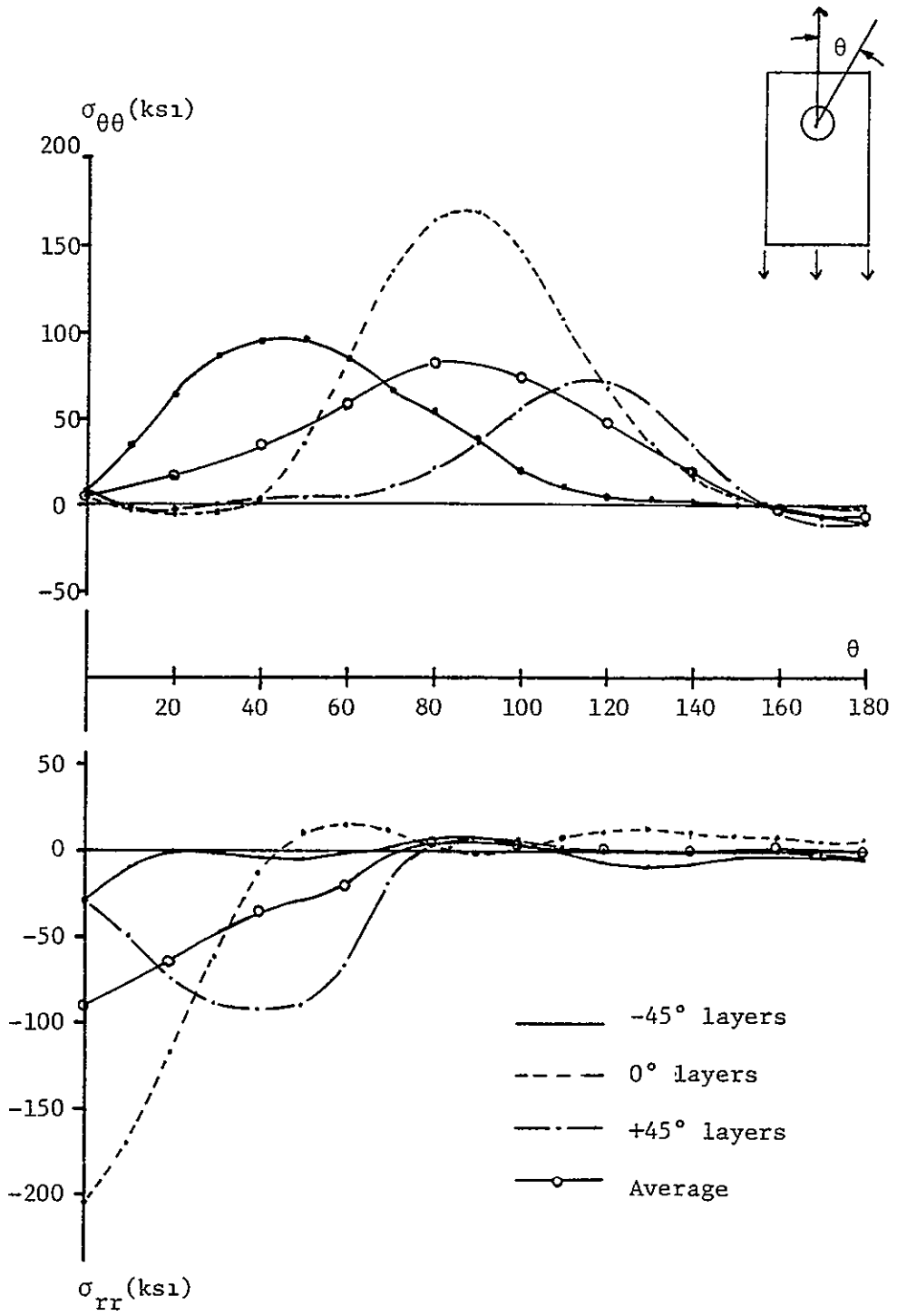

Figure IV-A-2-8a. Circumferential and Radial Stresses on Hole Boundary, B4000 (All)

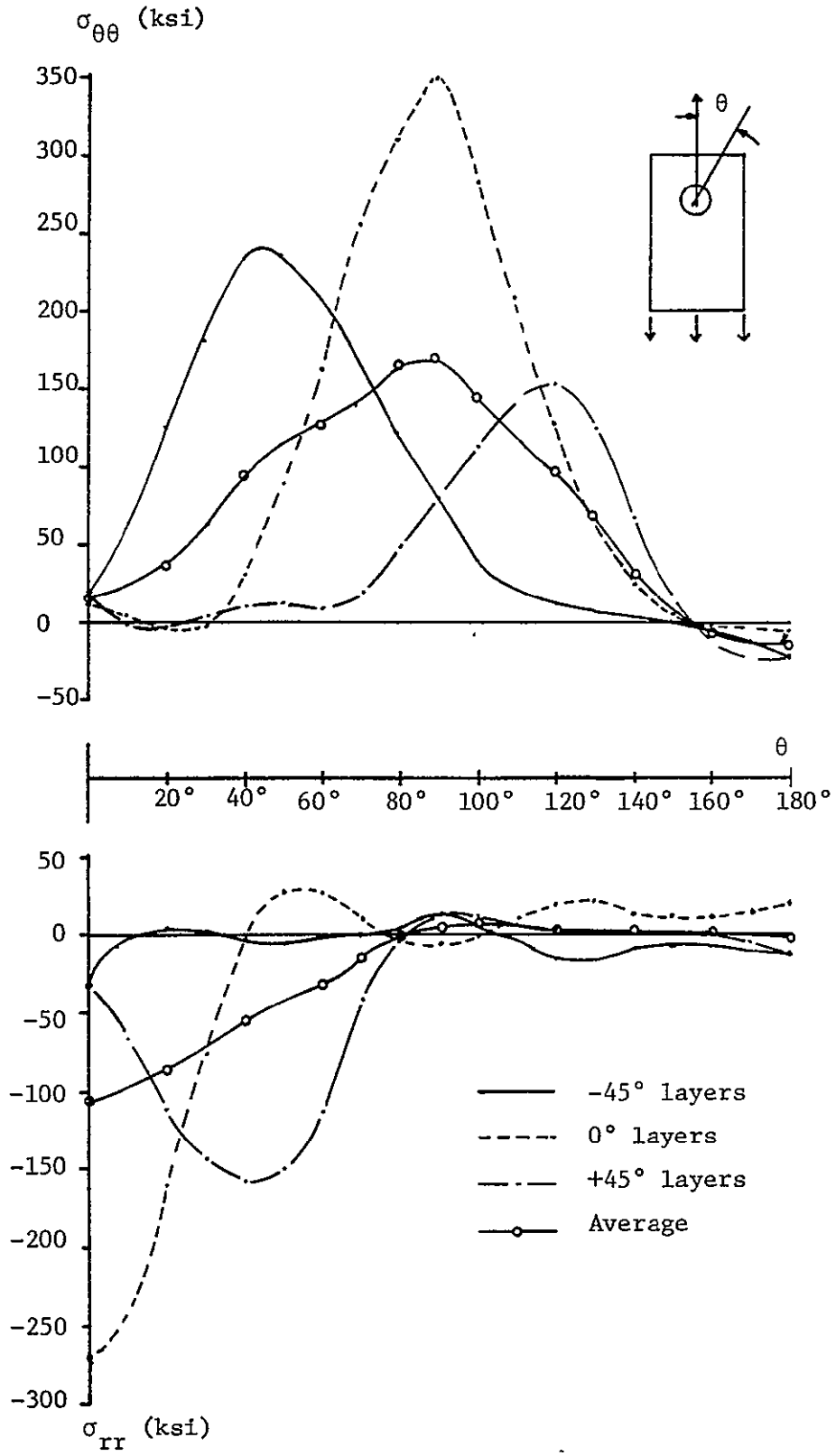

Figure IV-A-2-8b. Circumferential and Radial Stress on Hole Boundary, B6000 (All)

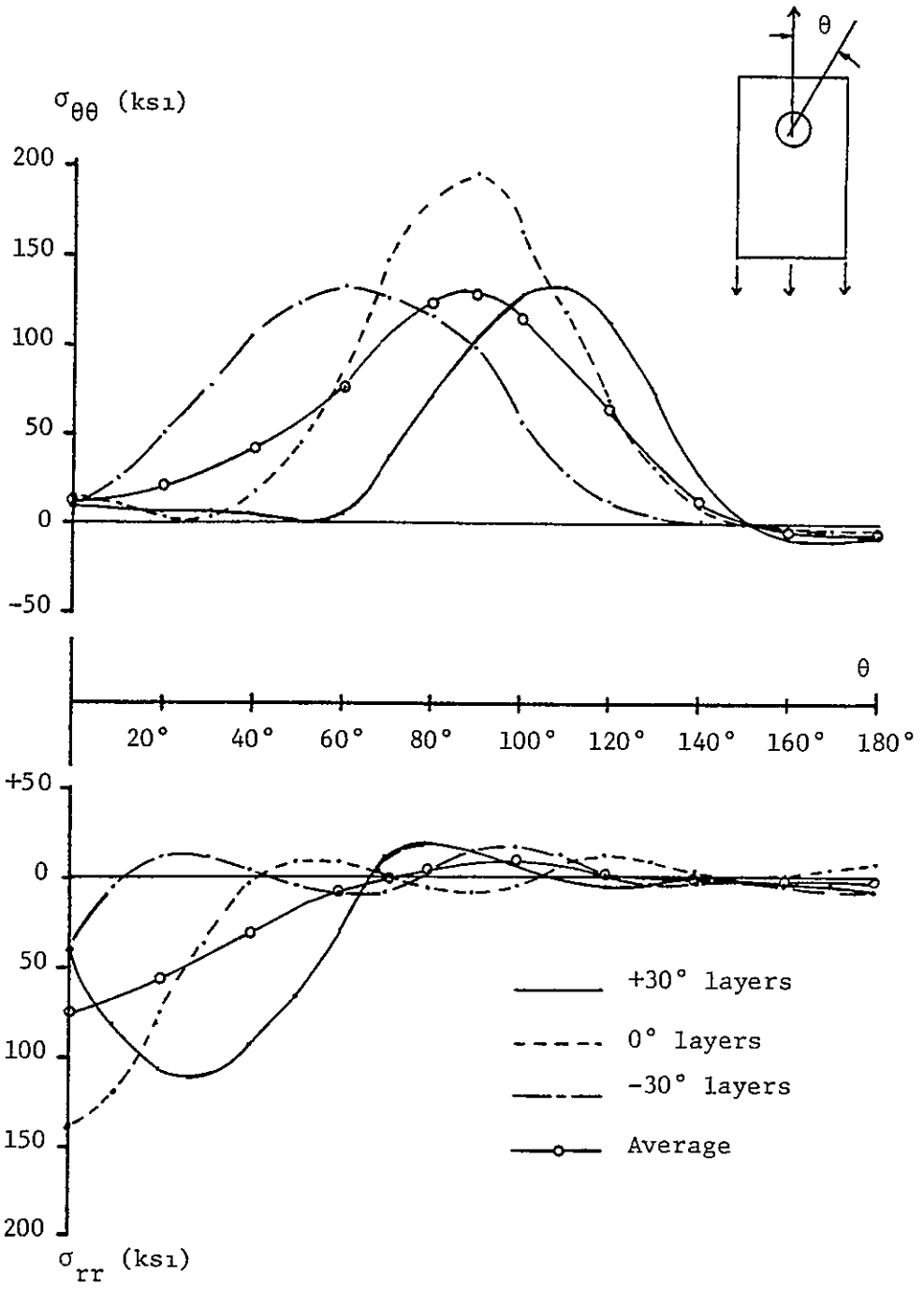

Figure IV-A-2-8c. Circumferential and Radial Stresses on Hole Boundary, F4000 (All)

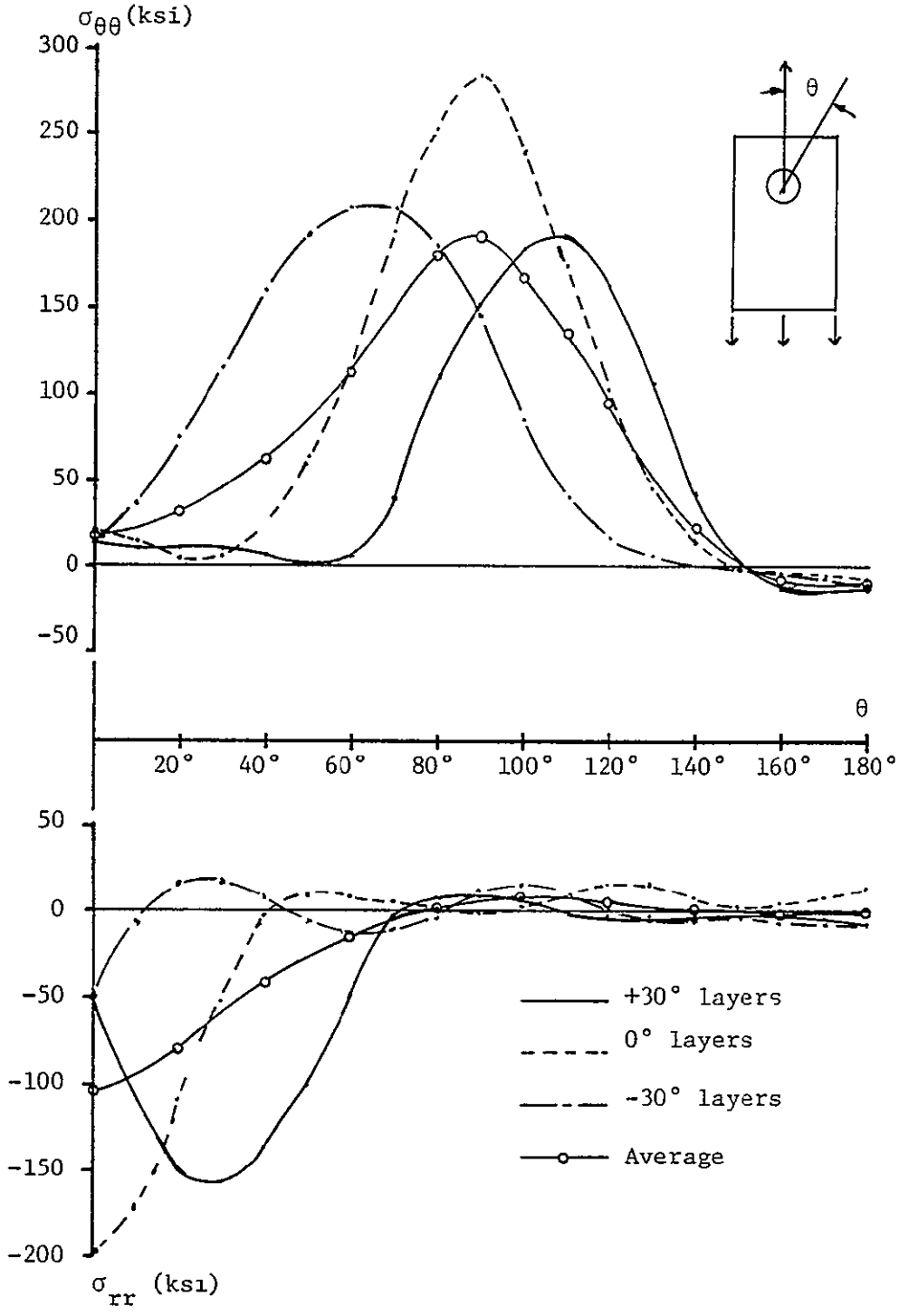

Figure IV-A-2-8d. Circumferential and Radial Stresses on Hole Boundary, F5760 (All)

TABLE IV-A-2-3

NOMENCLATURE EXPLANATION FOR FIGURES 8 THROUGH 10

Symbol	Explanation
σ_{net} (ksi):	Average net tension stress = Applied load (P)/net cross-sectional area
σ_b (ksi):	Average pin-bearing stress = Applied load (P)/pin-bearing area (2rt)
σ_{rr} (ksi):	Radial stress on the hole-edge boundary
$\sigma_{\theta\theta}$ (ksi):	Circumferential stress on the hole-edge boundary
σ_{max} (psi):	Maximum principal stress
σ_{min} (psi):	Minimum principal stress
τ_{max} (psi):	Maximum shear stress
σ_L (psi):	Stress in material (fiber) direction
σ_T (psi):	Stress in transverse fiber direction
τ_{LT} (psi):	Shear stress in material coordinates
γ_{max} (in./in/):	Maximum shear strain
B, F:	Lamination type: B: $[\pm 45°/0°]_{ns}$, F: $[\pm 30°/0°]_{ns}$
r (inch):	Radius of pin
t (inch):	Thickness of the laminate

Picture Identification Title

Example: B4000 - (-45°) - σ_{max}

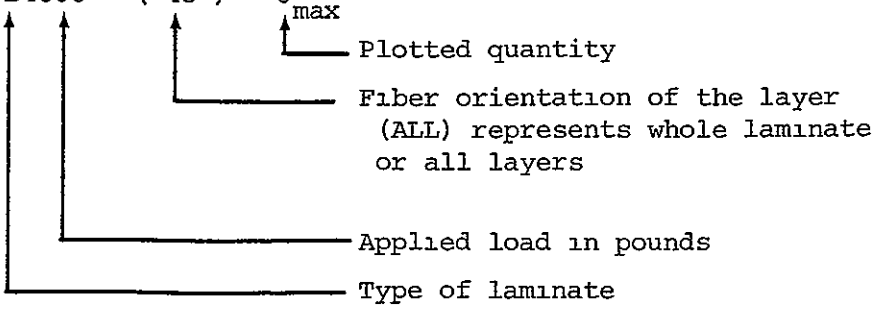

increases with applied load differs from layer to layer. Similar trends occur with F-type laminates (see Figures IV-A-2-8c and -8d).

Comparing Figures IV-A-2-8a and -8c shows that the peak value of circumferential stresses in each layer, as well as the averaged value through the thickness of the whole plate, is higher for the F-type laminate than those for the B-type laminate at an applied load of 4,000 pounds. This trend, however, is reversed for radial stresses. Both the circumferential and radial stresses occurring in the F-type laminate are spread more evenly among its layers than those of the B-type, except for radial stresses in angle-ply layers. On the other hand, comparisons between Figure IV-A-2-8b for the B-type laminate under an applied load of 6,000 pounds and Figure IV-A-2-8d for the F-type with 5,760 pounds load applied, show that the peak circumferential stress in the B-type's zero degree layers is higher than that of the F-type laminate; this despite the fact that the peak of the average circumferential stress in the F-type remains higher than that of the B-type. Radial stresses display basically the same trends for higher load levels as at lower level loads comparing the two laminates. The average stresses, however, are again exceptions. The maximum value of the average radial stress in the F-type plate is about the same as that of the B-type laminate; namely, about 103,000 psi in compression, while those at lower load levels differ between the two

types of laminates. This is particularly interesting, in view of the fact that the maximum average radial stresses at failure were about the same for both types of laminates, and both specimens failed in the same failure mode, i.e., bearing.

Figures IV-A-2-9a through -9d are plots of stresses in the direction of load application, i.e., normal stresses on the net tension cross-section. Data for both types of laminate are shown at two levels of applied load. In these figures, average tensile stress across the section (calculated by dividing the applied load by the net cross-section area) is indicated for each case, to allow rapid estimation of stress concentration factors, rather than show separate plots of stress concentration factor. Surprisingly, tension stress concentration factors in both laminates increased with load increases, in spite of increasing contact angles. Furthermore, the growth in stress concentration for B-type laminates is bigger than for the F-type.

Similar plots were made for compression stresses in the direction of applied load along the line of symmetry, as shown in Figures IV-A-2-10a through -10d. In these figures, the average pin-bearing stress, which was obtained by dividing the applied load by the pin-bearing area (diameter of the pin multiplied by the plate thickness), is included for each case. It is noteworthy, as may be seen in Figures IV-A-2-10c and -10d, that the maximum compression stress value in the

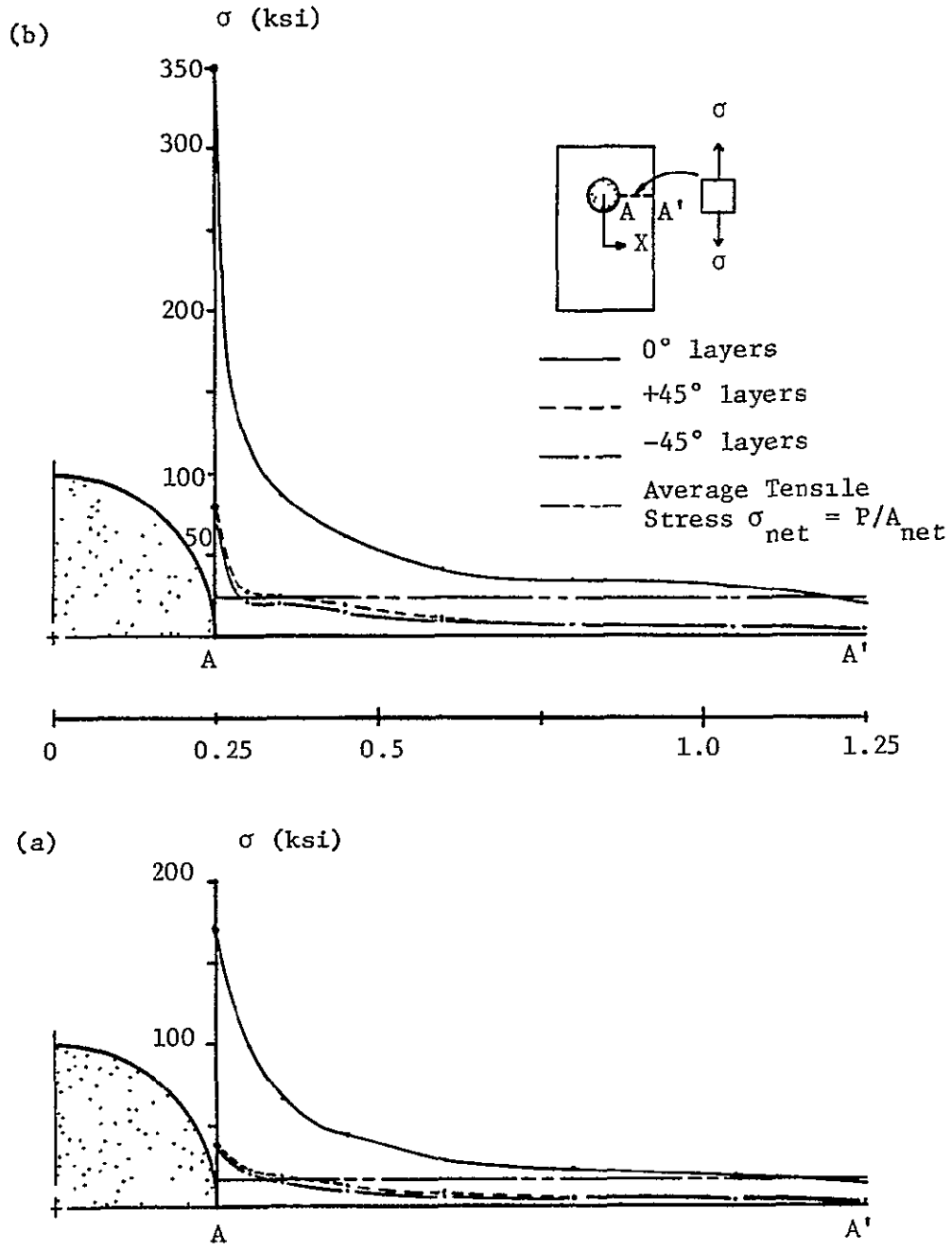

Figure IV-A-2-9. Tensile Stresses Along Net Tension Cross-Section (a) B4000 (A11), (b) B6000 (A11)

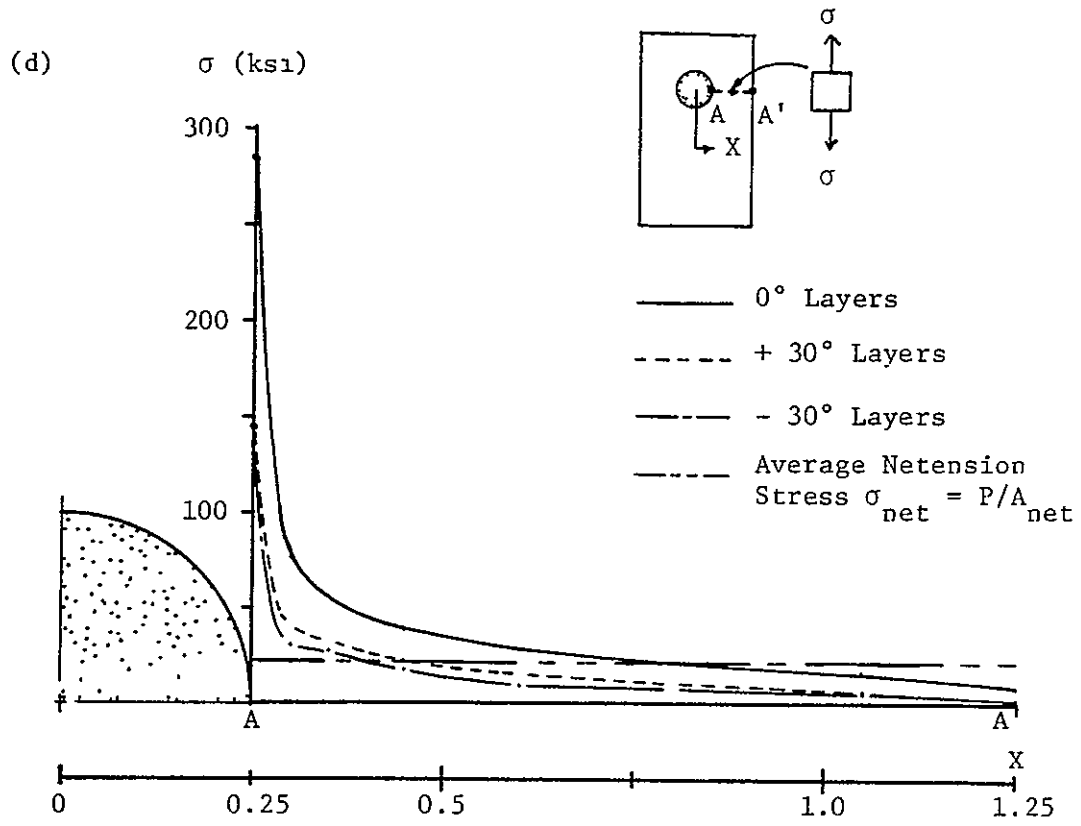

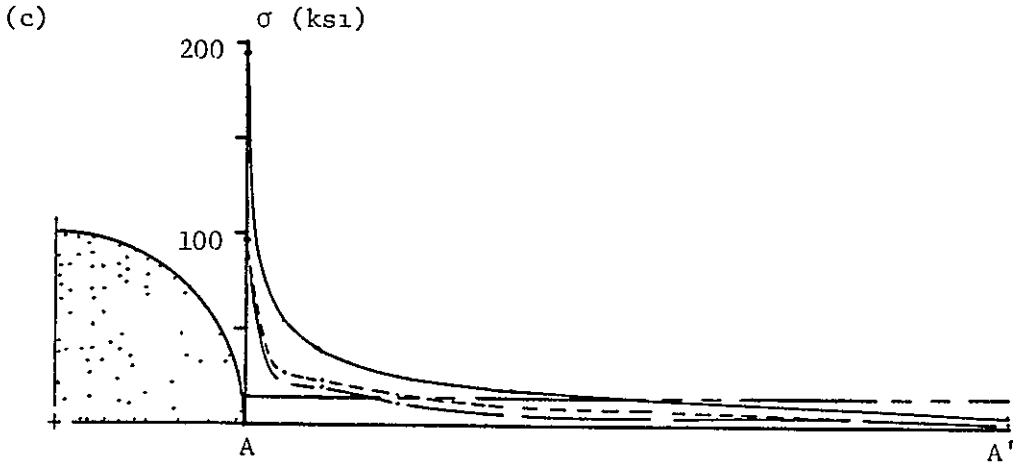

Figure IV-A-2-9. (Continued)
(c) F4000 (All), (d) F5760 (All)

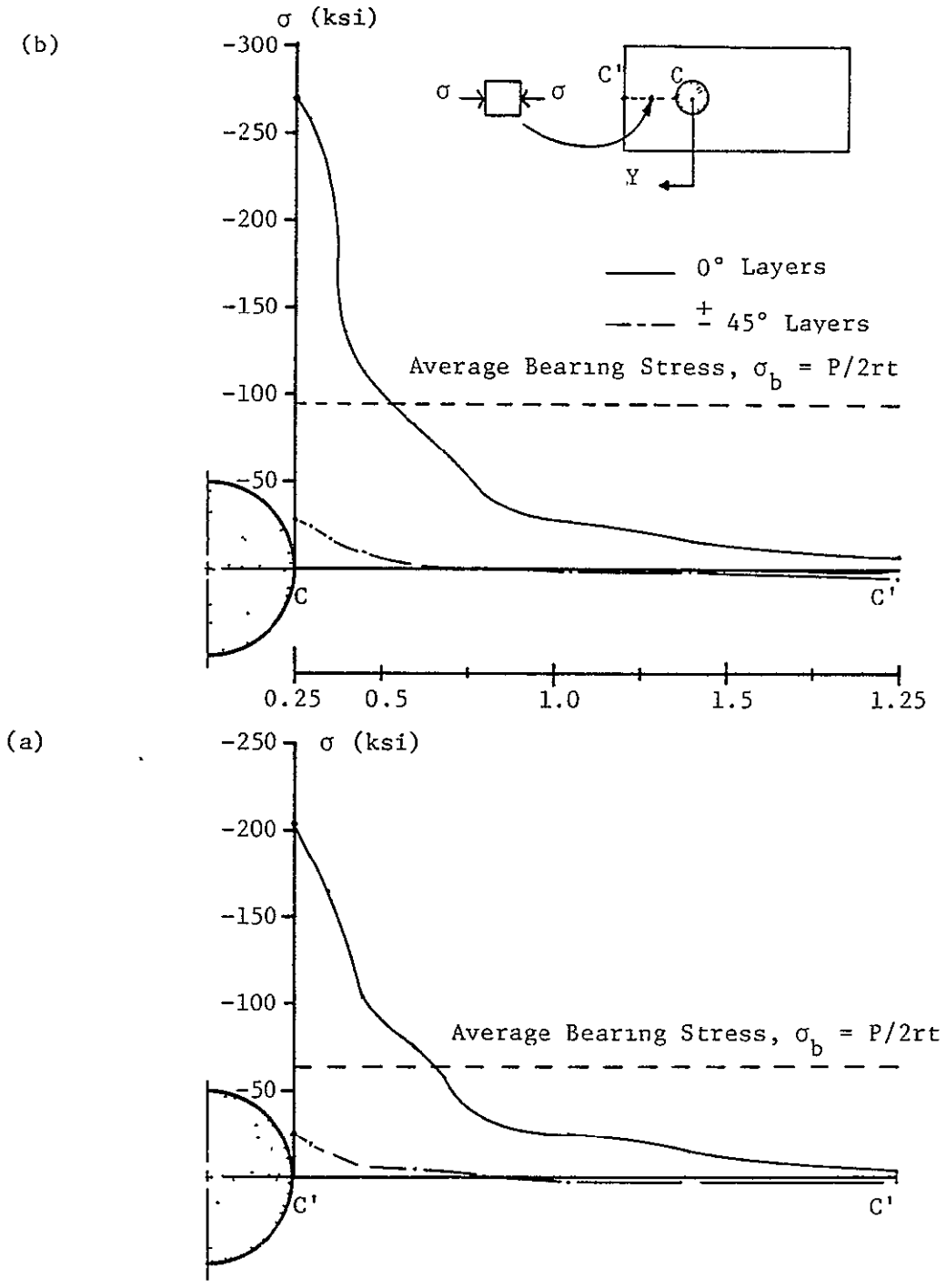

Figure IV-A-2-10. Compression Stresses Along the Line of Symmetry (a) B4000 (All), (b) B6000 (All)

(d)

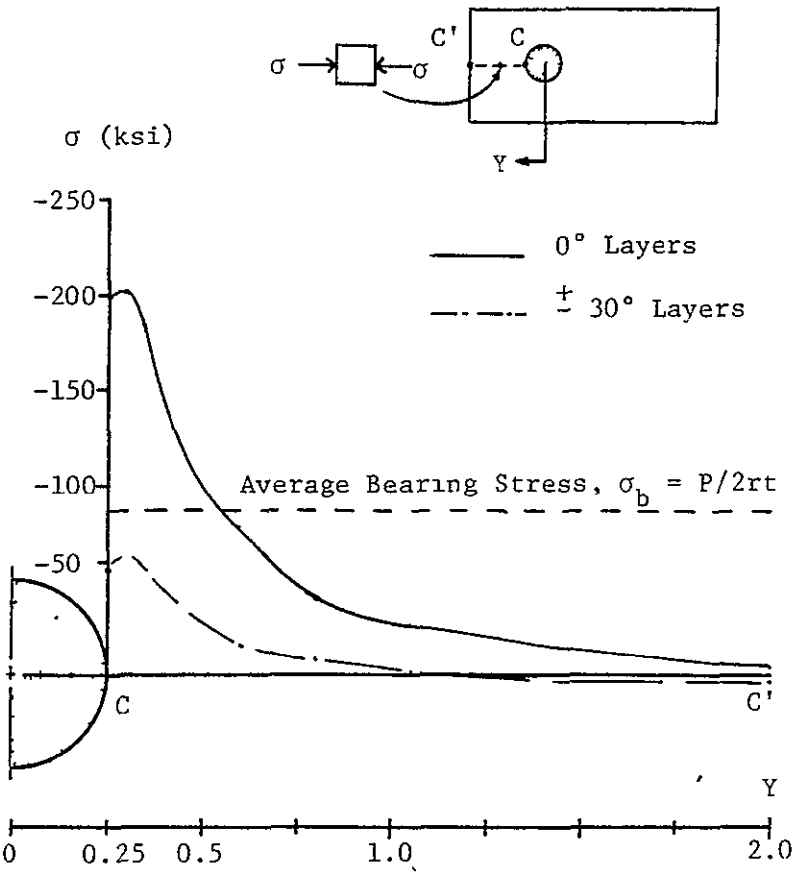

(c)

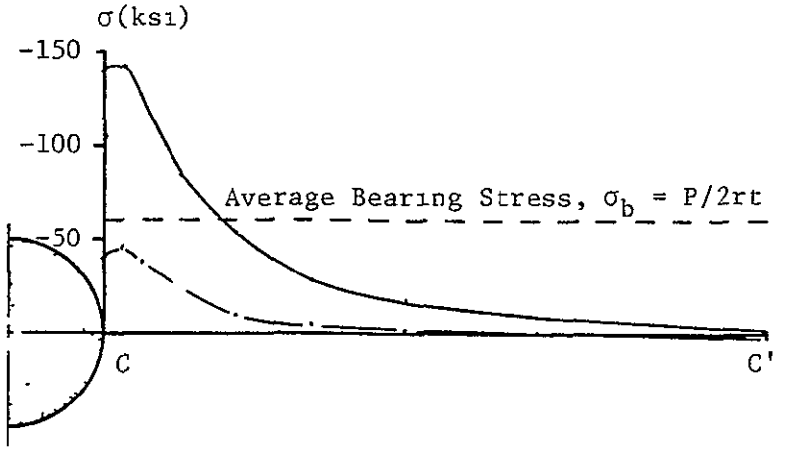

Figure IV-A-2-10. (Continued)
(c) F4000 (All), (d) F5760 (All)

loading direction along the line of symmetry occurred a small distance away from the edge of the hole for the F-type specimen. This phenomena had also been observed in the photoelastic experiments with several types of laminates.

According to Figure IV-A-2-10a, the compression stress for the B-type laminate in zero degree layers at the edge of the hole (204,000 psi) has almost reached the compression strength limit of the material as given in Table IV-A-2-2 (207,000 psi), at a load level of only 4,000 pounds. At 6,000 pounds applied load (see Figure IV-A-2-10b), zero-degree layer compression stress exceeds by far the stress allowable of this component. The actual failure, however, occurred at 6,000 pounds. Figures IV-A-2-10c and -10d for the F-type laminate, on the other hand, show compression stresses at the failure load which check reasonably with the material allowable data given in Table IV-A-2-2.

Similar disagreement between calculated tensile stresses at failure load and the material tensile strength data is even more severe, as seen in Figures IV-A-2-8 and -9.

Examination of Figure IV-A-2-8 reveals that the absolute maxima of circumferential stress along the edge of the hole take place roughly at the points where fibers are tangent to the hole boundary. In contrast, the absolute maxima of radial stress occur close to the points where fibers are perpendicular to this boundary.

The small non-zero value of average radial stress seen in Figures IV-A-2-9 on the free edge of the hole, at points which are beyond the contact region defined by θ_c, requires some discussion. Radial stresses should be zero along the traction free portion of the hole edge. Therefore, these non-zero radial stresses must be regarded as computational inaccuracies. The reason for their existence is as follows: These stress plots were based on the nodal values along the hole boundary. The nodal stresses on this boundary were calculated from the element centroidal values of each stress component in material coordinates by the smoothing technique explained in previous reports. The nodal values were then transformed into the polar coordinate system which would provide radial and circumferential components of stress for each layer. This interpolation (actually closer to extrapolation for the hole boundary) causes small errors for each component of stress in each layer. These errors accumulate through coordinate transformations and averaging processes. Thus, the non-zero values of the stress resultants at these hole-edge nodes, in deviating from traction free boundary conditions, may provide an indication of the upper bound for the kind of numerical errors likely to be found in the FEM analysis results.

3) Fracture Prediction

Attempts, which must be considered preliminary, were made to examine the ability of two distinct criteria, i.e., the O.Hoffman and the maximum stress criteria, to predict ultimate joint strength based on the computed stresses.

Stresses at each node and at each element centroid were transformed into material coordinate systems for each layer, and stress components, σ_L, σ_T and τ_{LT}, were put into the selected failure criteria. For Hoffman's criterion, the value of η, as given by the following equation, was calculated at each node and element centroid.

$$\eta = (\frac{1}{X} - \frac{1}{X'})\sigma_L + (\frac{1}{Y} - \frac{1}{Y'})\sigma_T + \frac{1}{XX'}\sigma_L^2 + \frac{1}{YY'}\sigma_T^2 + \frac{1}{S^2}\tau_{LT}^2 - \frac{1}{XX'}\tau_L\tau_T$$

where, material strength properties are, as also shown in Table IV-A-2-2,

X = tensile strength in the fiber direction

X' = compression strength in the fiber direction

Y = tensile strength transverse to the fibers

Y' = compression strength transverse to the fibers

S = inplane shear strength.

After this, every node and centroid of every element where

$$\eta \geq 1$$

was marked on the FEM mesh model, which was displayed on the screen of the graphics computer terminal. These points indicate where failures are predicted to occur according to the Hoffman criterion.

A similar process was followed using the maximum stress criterion. In this case, the failure marks were put on the points where one of the following conditions were met:

i) $\sigma_L \geq X$

ii) $\sigma_L < o$ and $|\sigma_L| \geq X'$

iii) $\sigma_T \geq Y$

iv) $\sigma_T < o$ and $|\sigma_T| \geq Y'$

v) $|\tau_{LT}| \geq S$

Some of the results of such failure prediction routines are shown in Figures IV-A-2-11a through -11g, in which the laminate type, applied load level, and the failure criterion used are indicated. Failure plots for the B-type specimen at 4,000 pounds applied load, based on the maximum stress criterion were not included, because the prediction indicated no failure in this case.

Judging from these plots, both failure criteria were too conservative in predicting ultimate strength allowables for the joints, but they were correct in predicting the modes of failure.

d. Plans for Upcoming Period

In the next reporting period, we will concentrate our efforts in extending the methods reported here to the analysis of multi-hole fastener joints. Consideration will also be given to similar analysis of pin-hole joints with interference fits.

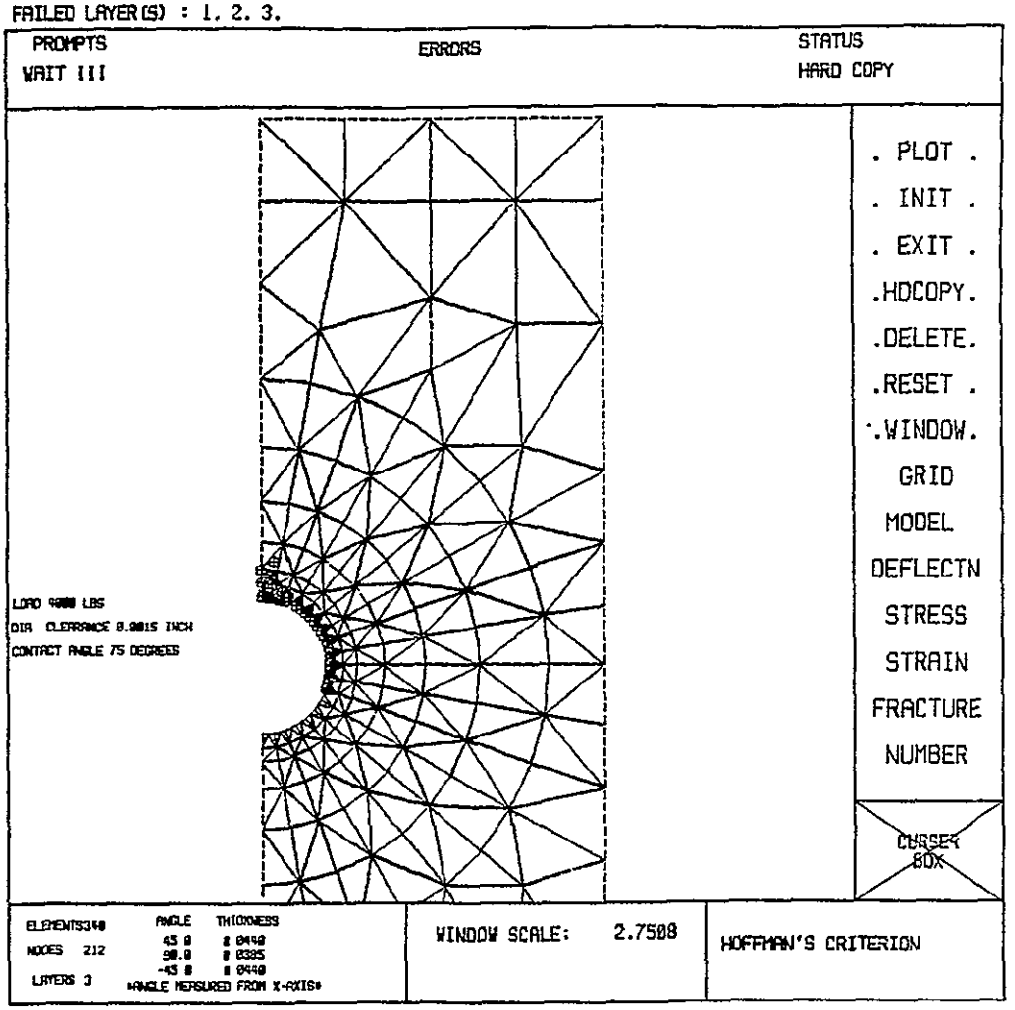

(a) B4000 - (A11)

Figure IV-A-2-11. Failure Prediction: (a) B4000 (A11) (Small circular marks on nodes and elements indicate failure occurred on those points.)

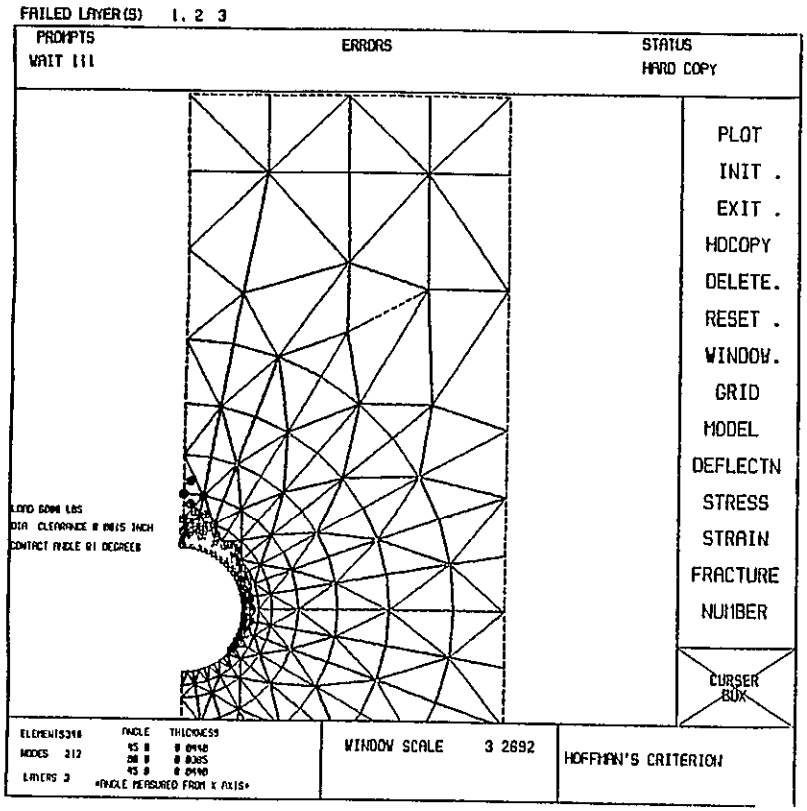

(b) B6000 - (A11)

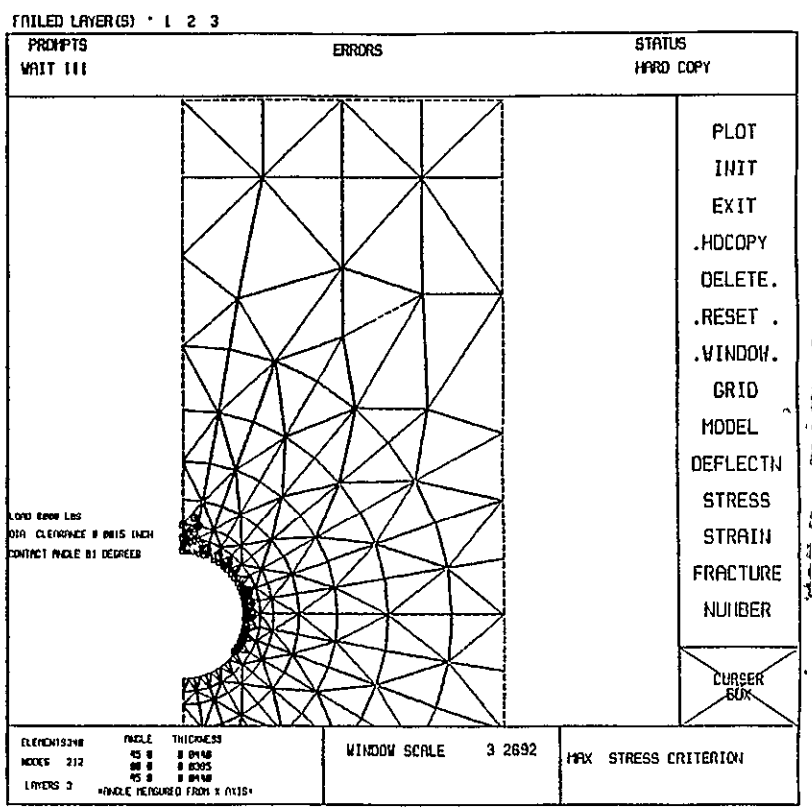

(c) B6000 - (A11)

Figure IV-A-2-11. (Continued)
(b) B6000 (A11), (c) B6000 (A11)

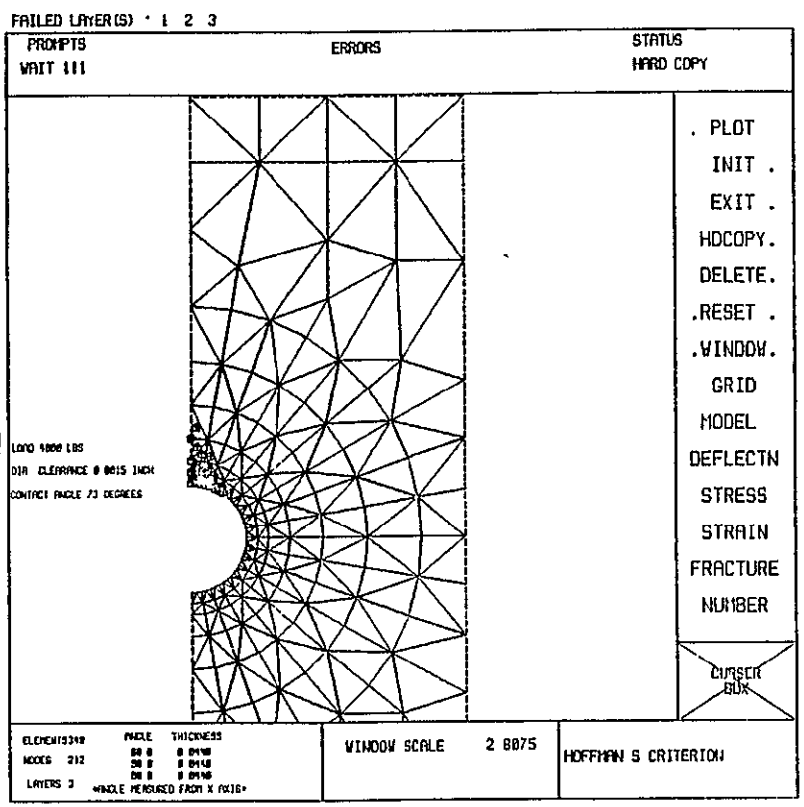

(d) F4000 - (A11)

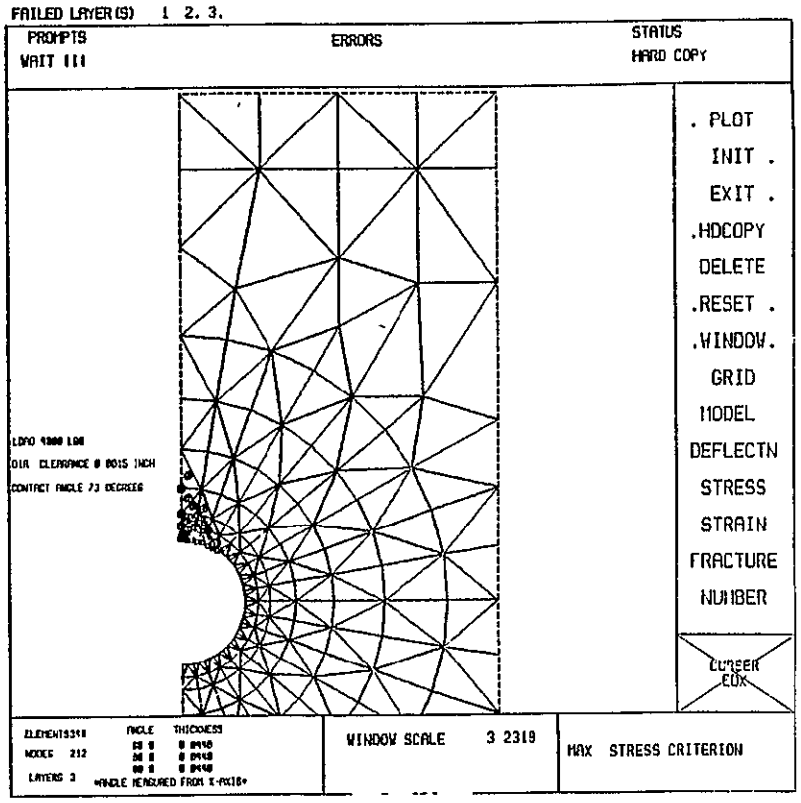

(e) F4000 - (A11)

Figure IV-A-2-11. (Continued)
(d) F4000 (A11), (e) F4000 (A11)

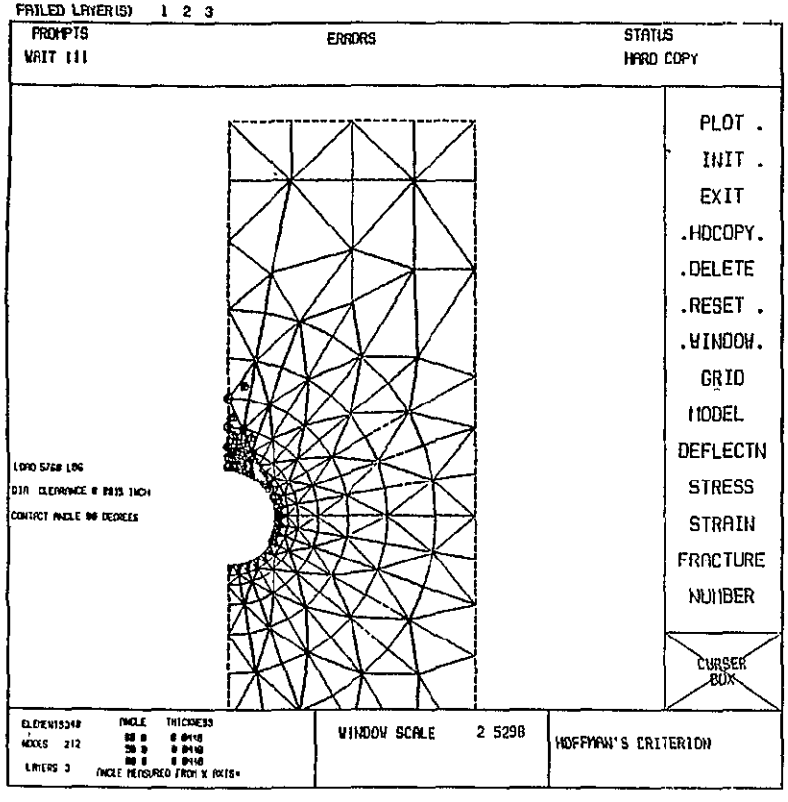

(f) F5760 - (A11)

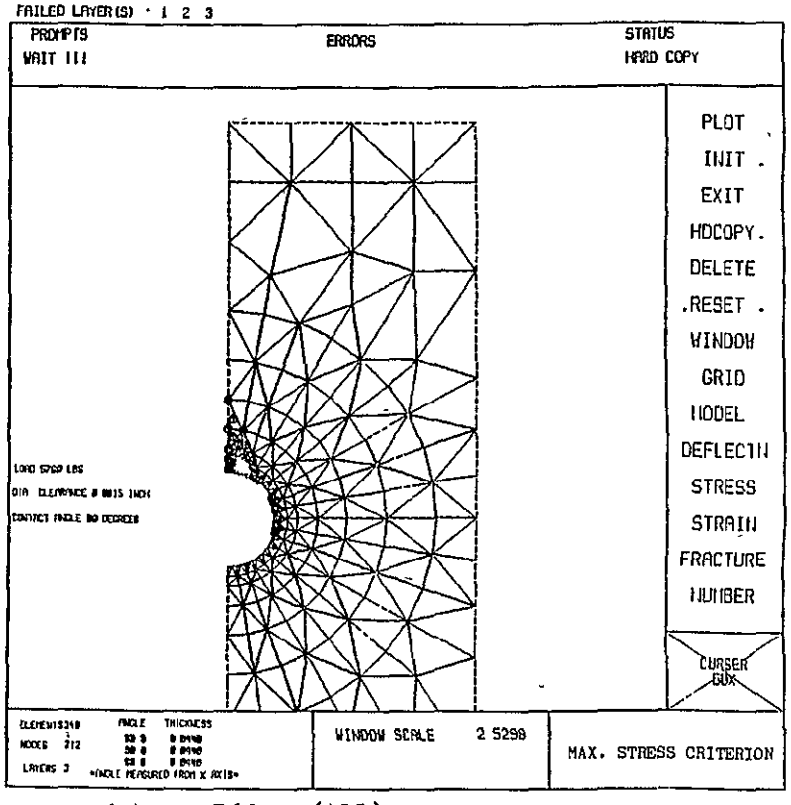

(g) F5760 - (A11)

Figure IV-A-2-11. (Continued)
(f) F5760 (A11), (g) F5760 (A11)

e. References

1. Hoffman, O., "The Brittle Strength of Orthotropic Materials", Journal of Composite Materials, Vol. 1, 1967.

2. Tsai, S. W. and H. T. Hahn, "Composite Materials Workbook", AFML-TR-78-33, Air Force Materials Laboratory, Wright-Patterson Air Force Base, 1978.

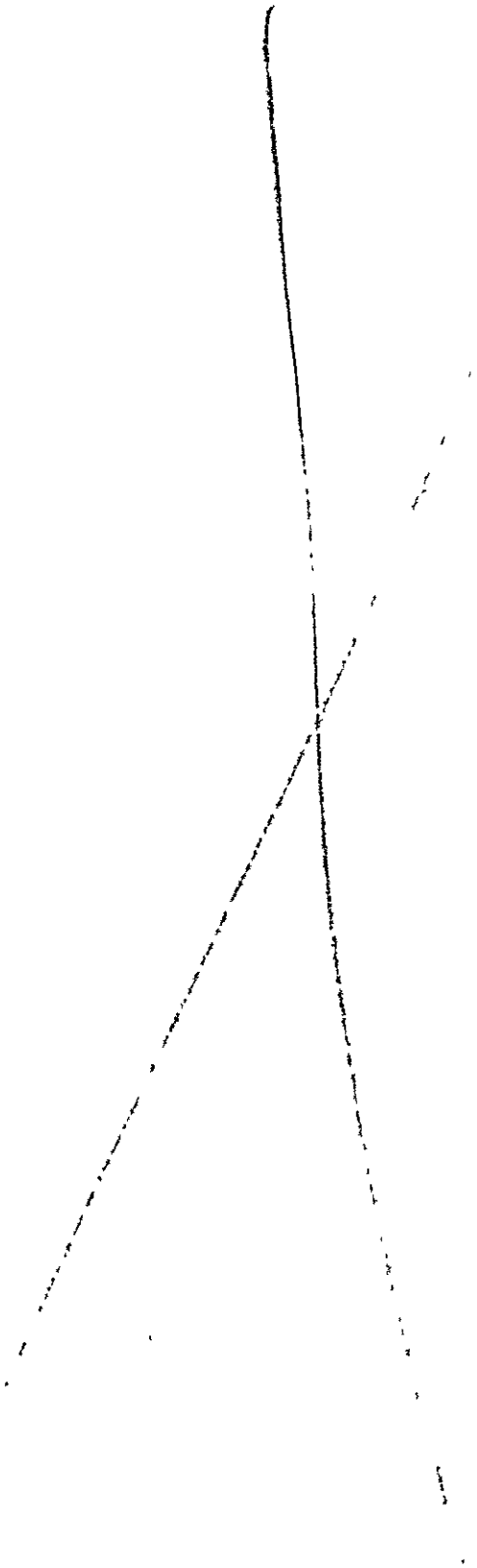

3. Compact Lug Design

Senior Investigator: D. B. Goetschel

a. Introduction

A critical aspect of many aerospace structural elements is the load transfer that takes place between the connecting lugs at the ends of the structure and the portions of the structure wherein the loads are well distributed if not uniform. An example is provided by the engine drag strut of the L-1011 aircraft (see Figure IV-A-3-1). Such lugs are highly loaded and have a very complex stress state (see Figure IV-A-3-2). Further, since they must mate with connecting parts, these lugs are usually designed within rather stringent dimensional envelope constraints. As compared to lugs which, as in the case of the L-1011 strut, are made from 200 ksi steel, meeting the geometric constraints even with a composite structural design making maximum use of unidirectional graphite-epoxy could prove to be a difficult task. This research is intended to solve the load/volume problem in favor of composites rather than either reverting to designs using 200 ksi steel lugs attached to a composite strut or forcing the dimensional constraints to be relaxed in a redesign of the mating parts.

b. Status

The design of lugs which are capable of L-1011 drag strut loads has been undertaken. Because a flat lay-up appears to

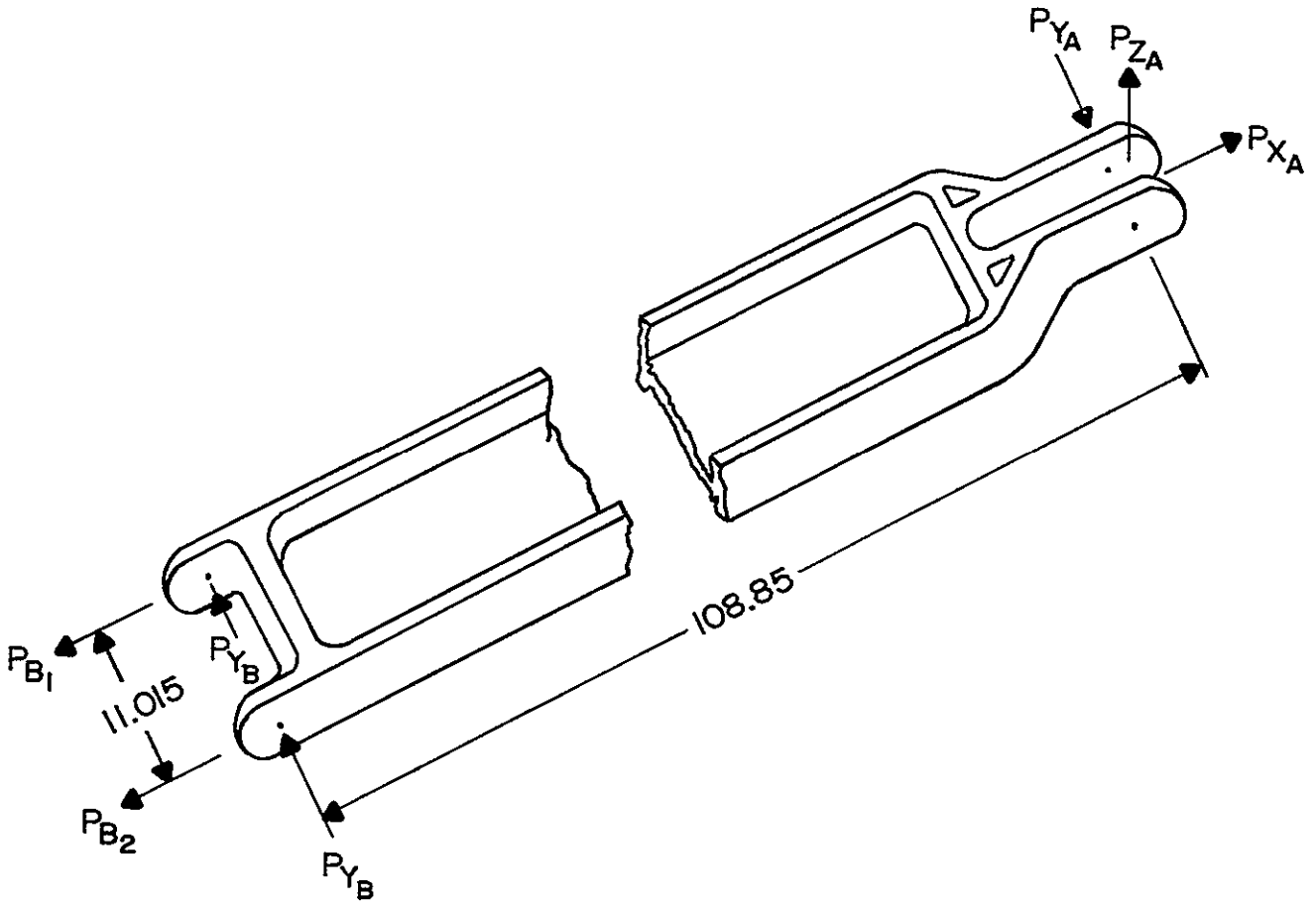

Figure IV-A-3-1.
Lockheed L-1011 Engine Drag Strut (Schematic)

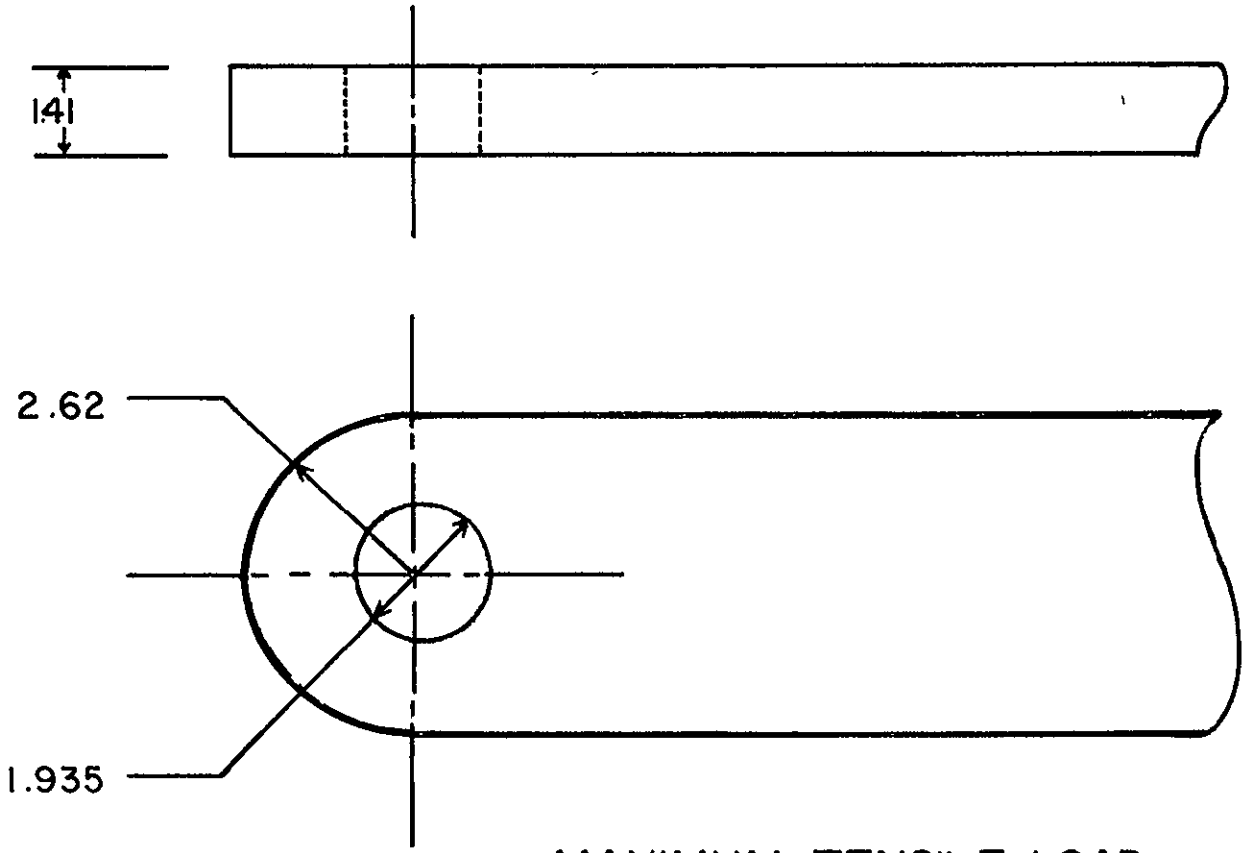

MAXIMUM TENSILE LOAD - 207.7 KIPS
MAXIMUM COMPRESSIVE LOAD - 236.8 KIPS
MAXIMUM LATERAL LOAD - 12.0 KIPS

DIMENSIONS IN INCHES

Figure IV-A-3-2. Lug Experiment: Full-Scale L-1011 Drag Strut

be the easiest and cheapest to manufacture when compared to other proposed designs, we decided, first, to try to use a flat, symmetric zero-plus-minus-angle-ply laminate whose lamina each consist of unidirectional graphite epoxy. Unidirectional graphite epoxy was selected because of its ready availability, reasonable cost and high strength in both tension and compression.

A zero-plus-minus-angle-ply lay-up has the potential of being optimized to resist the potential failure modes of bearing shear, compression or tension. The second decision was to concentrate initially on the tension design load, since it produces the most complex stress state with large compressive, shear and tensile stresses. If this design loading can be handled, then it should be relatively easy to handle the compression design load.

c. Progress During Report Period

An initial exploratory testing program was conducted by senior undergraduate student Anthony Staniorski to examine the behavior of the proposed lug design under tensile loads. To accomodate testing machine capacities and conserve on fabrication costs, quarter-scale model specimens, as compared to the L-1011 strut, were tested. Simple scaling of the ultimate design load requires the quarter-scale models to withstand 13 kips in static tension. This is well within the testing machine capacities.

Three specimens were made, each with a different lay-up. The material properties of the graphite-epoxy unidirectional tape used are listed in Table IV-A-3-1. The lay-ups were chosen somewhat arbitrarily but with the intent of generating various types of failure. The lay-ups and failure loads are listed in Table IV-A-3-2. In all cases, the failure mechanism was tensile failure in the net section through the pin hole. As can be seen, in comparison with the required strength of 13 kips, large improvements were needed.

In parallel with these tests, computer programs were written by senior undergraduate students William Dhimitri and Paul Adel which would facilitate the design of an optimum lay-up. As a first approximation, very simple failure criteria were used. It was assumed the lugs would fail in either pin bearing, pin shear-out or net tensile failure. For each condition an average stress state was calculated using simple free body diagrams. These average stresses were then multiplied by stress concentration factors chosen intuitively. The quadratic interaction criterion was applied to these stresses as a final step. These programs predicted that all the specimens would fail in either bearing or shear-out and that the specimens should have wide margins from tensile failure. Since the actual failure mode was, in fact, in tension, it was obvious that improved analysis and design modifications were called for.

TABLE IV-A-3-1

MATERIAL PROPERTIES OF GRAPHITE/EPOXY USED IN TESTING

Longitudinal Modulus	= E =	21,300 ksi
Transverse Modulus	= E =	1,400 ksi
Shear Modulus	= E =	930 ksi
Poissons Ratio	= ν =	.32
Ply Thickness	= h =	.005 inches
Longitudinal Tensile Strength	= X =	200 ksi
Longitudinal Compressive Strength	= X' =	170 ksi
Transverse Tensile Strength	= Y =	6 ksi
Transverse Compressive Strength	= Y' =	36 ksi
Shear Strength	= S =	10 ksi

TABLE IV-A-3-2

FAILURE LOADS OF LUG TEST SPECIMENS

Sample Number	Failure Load (kips)	Percent of Design
1	7.3	56
2	6.1	47
3	9.6	74

Design Ultimate Load = 13 kips

Two explanations and corrective actions were postulated for the unexpected weaknesses in tension. First, it was observed that at the sides of the hole, where high normal stresses are expected, there is a free edge with associated interlaminar stresses. To alleviate these interlaminar stresses, it was proposed to bond a thin bushing into the pin hole. This should provide some stress continuity from lamina to lamina at the otherwise free edge. The bushing was made of brass with a wall thickness of .015 inches. Second, it was suspected that the normal stress concentration factors at the sides of the hole were much greater than expected. Slots were suggested as shown in Figure IV-A-3-3 as one means to reduce this stress concentration. By channeling the load away from the hole, instead of requiring it to "flow" immediately behind the hole, the tendency for stresses to concentrate next to the hole should be reduced.

A second round of exploratory tests was performed to evaluate these design modifications. Some improvements were noticed, but the detailed data will not be reported here since variations of results between tests greater than the differences attributable to design changes appeared to be due to random causes. Multiple samples of each design and better consistency in specimen fabrication will be required to get more meaningful data.

The failure mode of the modified samples did, in general, tend to be pin shear-out, however, rather than net

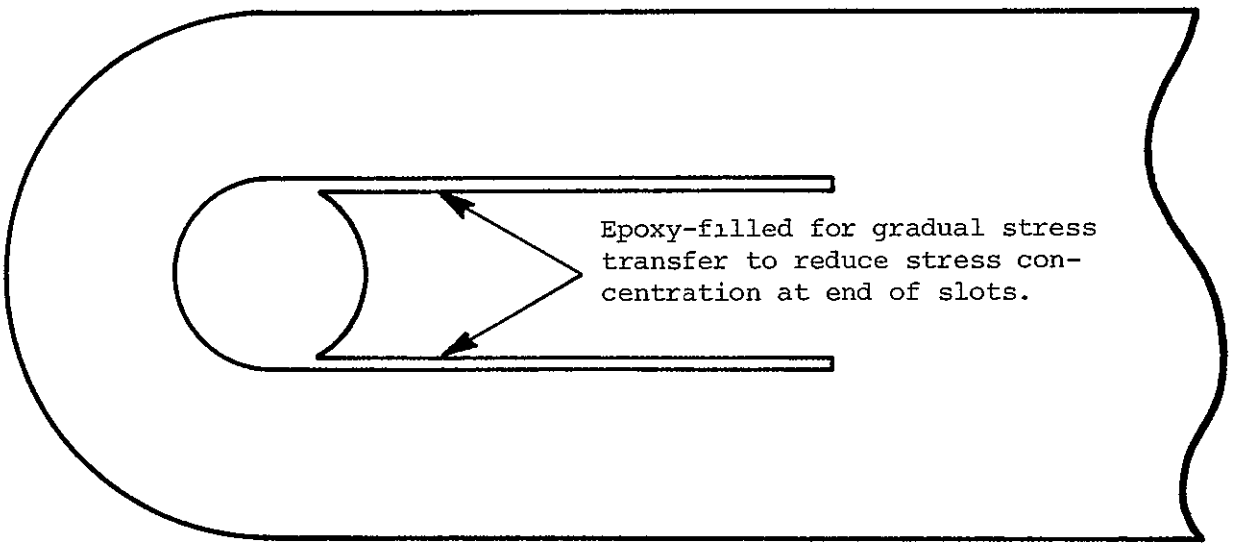

Figure IV-A-3-3

Placement of Slots for Stress Release

tension. Perhaps the most encouraging result was that one slotted specimen reached 90% of the ultimate design load, and there is no reason to believe that design is very close to optimum.

Finite element analysis was used to examine the tensile stress at the sides of the pin hole for both slotted and unslotted configurations. It was found that slots should reduce the tensile stresses next to the hole by thirty to forty percent. While this is a dramatic reduction, one would not expect to see a corresponding increase in lug strength, since other failure modes are likely to govern before the full improvement is realized. Other failure modes were not examined in the FEM analysis because an unreasonable amount of postprocessing of the results had to be done by hand.

FEM analyses were also used to examine the variations that changes in ply lay-up had on net tensile failure. Both the percentage and angle of the angle plies were varied. It was found that ply lay-up changes did dramatically alter the stress concentration next to the pin hole, but these alterations were roughly proportional to the variations in the lay-up's tensile strength. The ultimate result was that net tensile strength for the lug appears to be only a weak function of ply lay-up changes. Here again, other failure modes were not examined because of the large amount of hand processing of the data that was required.

d. Plans for Upcoming Period

The optimums that were found in the FEM analyses to date will be used as a guide in designing the next sequence of tests. The finite element capabilities, however, must be improved. Work will begin on automating the postprocessing needed to calculate composite material failure criteria so that all potential failure modes can be examined. Once the composite material failure criterion calculation is automated, various criteria will be tested for accuracy. It is important to have much more complete results of stress analysis to use as a guide in designing new tests.

All tests are being planned using larger numbers of samples to handle the statistical variations in strength that occur within a given configuration. In addition, more consistent fabrication methods will be developed.

IV-B SCALING EFFECTS IN TESTING COMPOSITE STRUCTURES

Senior Investigator: D. B. Goetschel

1. Introduction

It can be extremely valuable in terms of both time and money to be able to test small scale models when designing large structures. This is especially true for structures being designed in composite materials such as graphite epoxy, since the material itself is relatively expensive. As a first step in investigating scaling effects in design development testing of structures using composite materials, a study of scaling of simple tensile specimens was conducted. This study was primarily conducted by senior undergraduate student Scott Baxter.

2. Status

Two main effects were identified and hypothesized as being the mechanisms resulting in failure stress variations due to scaling. First, Weibull statistics are expected to be a major factor. These probability distributions are used in an attempt to estimate the effect that flaw distribution in a material has on the failure load of the specimen. The larger the specimen the greater the probability that flaws will influence the strength of the specimen, since with more material there is a greater chance of a critical grouping of flaws. Weibull statistics would, therefore, predict that larger specimens generally have lower nominal failure stresses.

Brittle materials such as composites are extremely susceptible to flaws at the microstructure level, so this effect should be relatively important for composites.

The effect of free edges on interlaminar stresses is expected to be another factor affecting scaling in these tensile tests. At a free edge there is a large concentration of interlaminar shear stresses. Thus, there is a "boundary layer" along a free edge that will reach failure stress first, as the laminate resists the load. The width of the "boundary layer" will be proportional primarily to the ply thickness. In a specimen with a smaller cross sectional width but equal laminate thickness, the "boundary layer" will be a greater percentage of the cross sectional area. The strength of the smaller specimen would, therefore, be reduced proportionally more than that of the larger specimen.

In any structure where edge-effects on strength are important, the full-sized structure will, in general, be designed with a ply stacking sequence that has a maximum mixing of the plies at different angles. Since prepreg composite materials generally aren't available in thicknesses less than those used for full-sized structures, ply thickness can't be scaled when making small-scale structures.

No other inherent scaling mecahnism has been identified in this study on tensile loading. There can always be differences in manufacturing and testing procedures that result

from specimen size differences. Every effort will be taken to minimize these effects in this test program. Presumably, similar care can be exercised when scale model tests are performed on real structures.

3. Progress During Report Period

For an initial test, dog-bone tensile specimens were made from graphite-epoxy with material properties as listed in Table IV-A-2-1. Specimens were constructed with three different ply lay-ups: $[0/30/-30]_{\alpha s}$, $[0/45/-45]_{\alpha s}$, and $[0/60/-60]_{\alpha s}$. These lay-ups were chosen because they seemed typical of practical lay-ups used in real structures. The different sized specimens were scaled in all three dimensions. The largest specimen sizes were limited by material costs and testing machine capacities. The smallest specimen sizes were limited by testing machine sensitivities and grip geometries. Also, with the above-listed lay-ups, the minimum thickness is that corresponding to six prepreg layers. Initially, specimens were made in three different sizes with $\alpha = 1$, 2 and 4 (6, 12 and 24 plies). A fourth, larger sized specimen was initially planned but was deleted from this beginning set of tests to save material costs. Larger specimens can be included in later test programs, once the reliability of the experimental procedure has been established. Three specimens were made for each size of each lay-up for a total of 27 specimens.

Figure IV-B-1 gives the dimensions for each of the specimen sizes in sequence. These dimensions provide for a safety factor of two for the shear stress incurred in the grips and a relatively gentle, five to one angle ratio in going from net section width to grip area width. Both of these proportions were judged to be sufficiently conservative to provide reliable tests results.

During testing it was discovered that the two smaller sizes could not be tested on the large Instron testing machine. A smaller Instron machine more suitable for testing the smaller sizes was found. It was not effective for testing the smallest size, however, because the size of the teeth on the grips caused too much damage to the specimen grip area, which was very thin (.030 inch). Results were thus obtained only for the middle two sizes (12 and 24 plies).

Calibration of the two Instron testing machines was necessary to insure accurate comparisons between the two specimen sizes. Calibration was performed with a proving ring. The smaller machine was accurately calibrated but the larger one was slightly off. To correct for the error in the large machine, corrections were applied to the measured loads to obtain "true loads". These corrections were a function of load and varied from -2% to +1%. Tables IV-B-1a and IV-B-1b contain the experimental results for the small and large specimens, respectively.

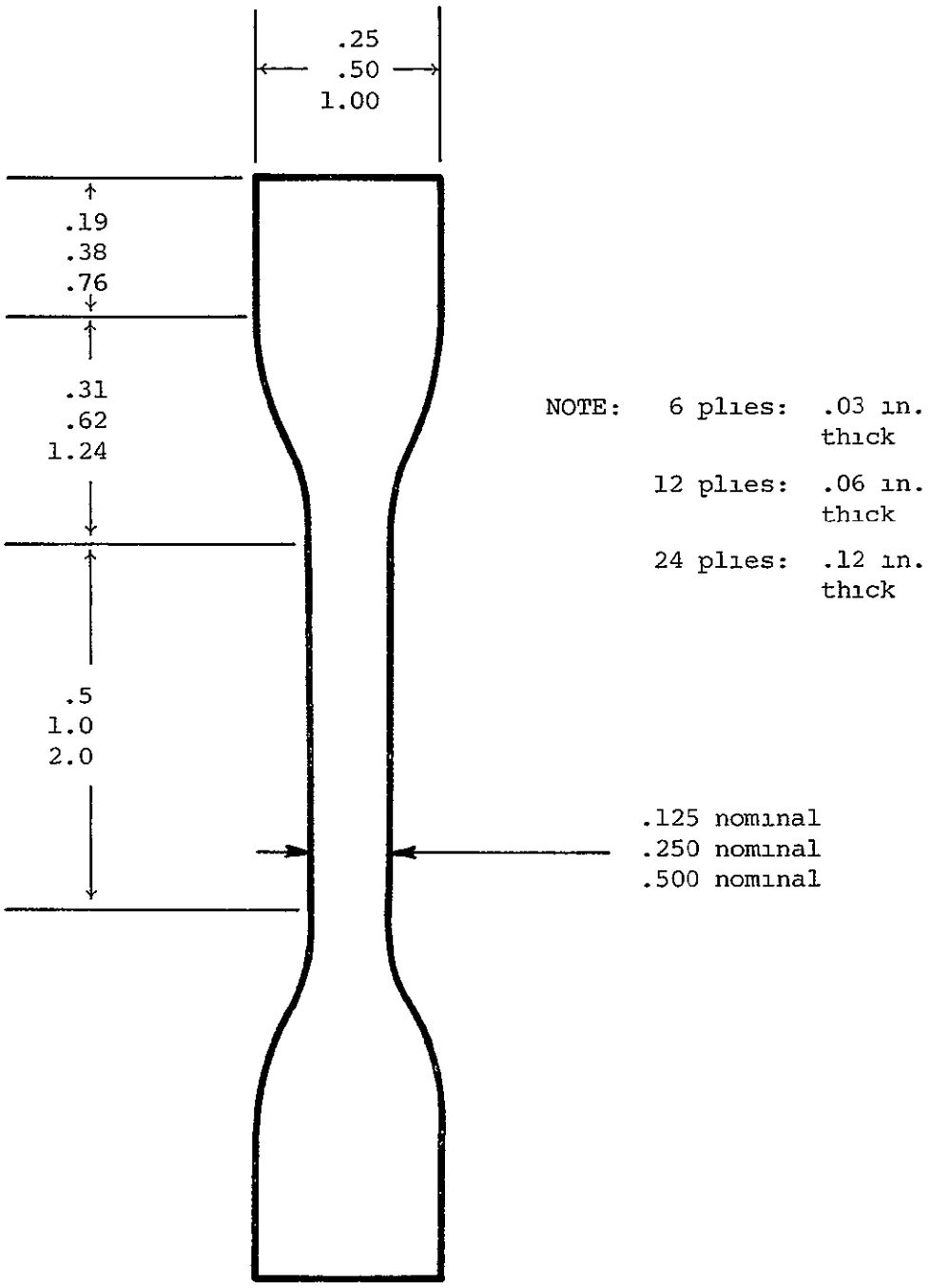

Figure IV-B-1

Dimensions for Three Specimen Sizes
(all dimensions in inches)

TABLE IV-B-1a

FAILURE DATA FOR THE 12-PLY SPECIMENS

Ply Angle (degrees)	Specimen Number	Neck Width (in.)	Area* (sq. in.)	Failure Load (lb.)	Failure Stress (ksi)
30	1	-------(damaged while testing)-----			
	2	0.285	0.0171	1987.0	116.2
	3	0.288	0.01728	2563.0	148.3
	average	0.2865	0.01719	------	132.26
45	1	0.254	0.01524	1400.0	91.9
	2	0.248	0.01488	1425.0	95.8
	3	0.253	0.01518	1600.0	105.4
	average	0.2517	0.01510	------	97.68
60	1	0.248	0.01488	1300.0	87.4
	2	0.253	0.01518	1325.0	87.3
	3	0.250	0.01500	1350.0	90.0
	average	0.2503	0.01502	------	88.22

TABLE IV-B-1b

FAILURE DATA FOR THE 24-PLY SPECIMENS

Ply Angle (degrees)	Specimen Number	Neck Width (in.)	Area* (sq. in.)	Failure Load (lb.)	Failure Stress (ksi)
30	1	-------(damaged while testing)-----			
	2	0.53	0.0636	7758.0	122.0
	3	0.52	0.0624	7946.0	127.3
	average	0.525	0.0630	------	124.7
45	1	0.47	0.0564	5281.0	93.6
	2	0.50	0.0600	5481.0	91.5
	3	0.58	0.0696	6233.0	89.6
	average	0.517	0.0620	------	91.56
60	1	0.50	0.0600	4450.0	74.2
	2	0.50	0.0600	5123.0	84.4
	3	0.53	0.0636	5385.0	84.7
	average	0.51	0.0612	------	81.41

*Test region cross section

a. Free Edge Effects

The magnitude of the interlaminar shear stress near the free edge of a laminate can grow to levels which cause large plastic deformations well before loads which can cause failures due to normal stresses. An inelastic solution is not readily available at this time, however, so an elastic solution was used to obtain an estimate of the effects of these free edge stresses.

Tang and Levy[1]* give an elastic solution for T_{zx}, the shear stress oriented parallel to the free edge:

$$T_{zx} = E_x^o \left(Q_{16} - \frac{Q_{12}Q_{26}}{Q22} \right) (\pi/2) \frac{\sin h(\pi\xi/2)}{\cos h(\pi\xi_b/2)} \sin(\pi\eta/2) \qquad (1)$$

where:

$$\xi = \frac{y}{h}, \quad \xi_b = \frac{b}{h}, \quad \eta = \frac{z}{h}, \quad h = \frac{ho}{2}$$

and

Q_{ij} are the off-axis elastic moduli.

This equation can be used to estimate the size of the boundary layer (i.e., the width of the region near the free edge of the laminate) that doesn't contribute to resisting axial forces. One measure of this might be the width for which T_{zx} exceeds 5 ksi. It is assumed that this is the shear stress at which plastic strains become significant. The second columns of Tables IV-B-2a and -2b give these values.

*Numbers in brackets in this section refer to the references which are listed on page 197.

TABLE IV-B-2a

WIDTH OF BOUNDARY LAYER FOR 12-PLY SPECIMENS

Ply Angle (degrees)	Width for T_{zx} Less Than 5 ksi (in.)	Estimated Boundary Layer Width (in.)
30	.00375	.01125
45	.00239	.00717
60	.00078	.00234

TABLE IV-B-2b

WIDTH OF BOUNDARY LAYER FOR 24-PLY SPECIMENS

Ply Angle (degrees)	Width for T_{zx} Less Than 5 ksi) (in.)	Estimated Boundary Layer Width (in.)
30	.0037	.0111
45	.0024	.0072
60	.00067	.00201

Since the large shear stresses predicted by the elastic analysis would never be achieved because of large plastic deformations, the actual boundary layer would be larger than these values. Lacking a more reliable non-linear analysis, physical intuition must be relied on to estimate the size of this increased boundary layer. For the time being, a multiplying factor of three has been chosen to approximate the size of the actual boundary layer. This estimate is contained in column three of Tables IV-B-2a and -2b. A reduced area (A_r) can now be calculated as

$$A_r = t(w - 2B_\ell) \tag{2}$$

where t is the laminate thickness, w is the average of the measured test section widths and B_ℓ is the boundary layer width. The nominal area is

$$A = tw \tag{3}$$

These free edge effects predict a ratio of failure stress due to scaling, of the small to large specimens equal to

$$\frac{\sigma_s}{\sigma_\ell} = \frac{(A_r/A)_s}{(A_r/A)_\ell} \tag{4}$$

Table IV-B-3 shows the predicted scaling effects due to free edge effects in terms of a ratio of the failure stresses. As can be seen, smaller specimens show a failure stress reduction of between one percent and four percent.

TABLE IV-B-3

PREDICTED FREE EDGE SCALING EFFECTS

Ply (degrees)	Small Specimens A_r (sq. in.)	Small Specimens $\frac{A_r}{A}$	Large Specimens A_r (sq. in.)	Large Specimens $\frac{A_r}{A}$	$\frac{\sigma_s}{\sigma_\ell}$
30	.01584	.9215	.06034	.9577	.9622
45	.01424	.9430	.06031	.9721	.9701
60	.01474	.9813	.06072	.9921	.9891

TABLE IV-B-4

PREDICTED WEIBULL SCALING EFFECTS

Ply Angle (degrees)	$\frac{(A_r)_\ell}{(A_r)_s}$	$\frac{\sigma_s}{\sigma_\ell}$
30	7.62	1.114
45	8.47	1.120
60	8.24	1.119

b. Weibull Statistical Effects

For brittle materials such as graphite-epoxy composites, the size effect on strength through flaw distribution is much larger than it is for more ductile materials. Since this size effect is due to variability of strength of the constituent material, the larger the scatter in these properties, the greater the effect. A flaw in a brittle material causes a stress concentration and the material is unable to flow plastically to relieve the stresses at these concentrations as a more ductile material does. Thus, it can be predicted that a smaller specimen will fail at a higher average stress since the probability of encountering a large imperfection grows as the volume of the specimen increases.

Basically, Weibull Theory [2,3,4,5] says that a specimen of volume, V, containing an even distribution of flaws throughout its volume has a probability of survival, S, when subjected to a stress, σ, equal to

$$S = \exp\left[- \int_V \left(\frac{\sigma}{\sigma_o}\right)^m dxdydz\right] \qquad (5)$$

where σ_o is the characteristic strength of the material and m is the Weibull Modulus, a measure of the variability of the material. When a large number of specimens are tested, this equation reduces to

$$S = \exp\left[- KV\left(\frac{\sigma}{\sigma_o}\right)\right]^m \qquad (6)$$

In this study, specimens of the same shape but different volumes are compared. Thus, the equation becomes

$$V_1\left(\frac{\sigma_1}{\sigma_o}\right) = V_2\left(\frac{\sigma_2}{\sigma_o}\right)^m \quad (7)$$

and rearranging gives

$$\frac{\sigma_1}{\sigma_2} = \left(\frac{V_2}{V_1}\right)^{1/m} \quad (8)$$

To calculate the Weibull Modulus, m, Equation (6) can be manipulated to become

$$\log\log\frac{1}{S} = m\log\sigma - (m\log\sigma_o - \log KV - \log\log e) \quad (9)$$

Thus, if $\log\frac{1}{S}$ is plotted versus σ_o on log-log paper, m is the slope of the straight line. To find S it is seen that S = 1 - F, where F is the probability of failure.

One equation used in Weibull Theory to calculate F is

$$F = \frac{j - 0.3}{n + 0.4} \quad (10)$$

where n is the total number of samples and j is the rank of the specimen.

These tests gave a value for m of 18.78 with a correlation of .98. In previous tests, m for graphite-epoxy has been found to be approximately 20, which is in very close agreement.

Table IV-B-4 shows the expected scaling effects due to Weibull flaw distributions as calculated using Equation (8)

and accounting for the reduced areas calculated from free edge effects. As can be seen, smaller specimens show a stress increase of about twelve percent.

c. Correlation of Theory and Experiment

Table IV-B-5 shows the predicted and measured scaling effects. The predicted values are based on the combined effect of free edge interlaminar stresses and Weibull statistics as noted in the preceding sections. These results indicate that smaller scale specimens would be expected to show a failure stress increase of between five percent and ten percent for a scaling factor of two. The predicted and measured values are in reasonably good agreement.

4. Plans for Upcoming Period

The postulated scaling mechanisms do appear to model the measured tensile loading behavior closely enough to allow scaled models to be used reliably when designing large structures subjected to pure tensile loading. In the coming period, an additional series of more accurately controlled tensile tests over a wider range of parameters will be performed to confirm these preliminary results. Attempts will be made to establish a non-linear analysis to predict the free edge interlaminar stresses more reliably.

Investigations of other types of structural behavior will be planned as regards scaling effects. It would be particularly important to concentrate on those structural

TABLE IV-B-5

COMPARISON OF PREDICTED TO MEASURED VALUES

Ply Angle (degrees)	Measured Failure Stress Ratios (σ_s/σ_ℓ)	Calculated Failure Stress Ratios (σ_s/σ_ℓ)	% Error
30	1.061	1.072	1.0
45	1.067	1.087	1.9
60	1.0835	1.107	2.2

elements that show larger effects due to scaling. A member of Rensselaer's Industrial Technical Advisory Committee indicated that very large effects had been found when making scale models of joints. We plan, therefore, to first investigate bonded double lap joints.

The failure data for different ply lay-ups were compared against several failure criteria. Strain in the fiber direction gave much better correlation than the other popular criteria, like quadratic stress interaction. This seems reasonable for these types of lay-ups with a significant number of plies in at least three widely spaced directions, since matrix failure should have little effect on overall structural failure in a single static test. It is planned to investigate failure criteria further.

5. References

1. Tang, S. and A. Levy, "A Boundary Layer Theory - Part II: Extension of Laminated Finite Strip", Journal of Composite Materials, Vol. 9, January 1975, 42-52.

2. Hitchon, J. W. and D. C. Phillips, "The Effect of Specimen Size on the Strength of CFRP", Composites, April 1978, 119-124.

3. Hitchon, J. W., W. H. McCausland and D. C. Phillips, "The Variability of Tensile Strength of Unidirectional Carbon Fiber Reinforced Plastics", AERE-R 8217, November 1975.

4. Braidon, P. M., "An Introduction to Weibull Statistics", AERE-R 7165, December 1975.

5. Weibull, W., "A Statistical Distribution Function of Wide Applicability", Journal of Applied Mechanics, Vol. 18, 1951, 293-297.

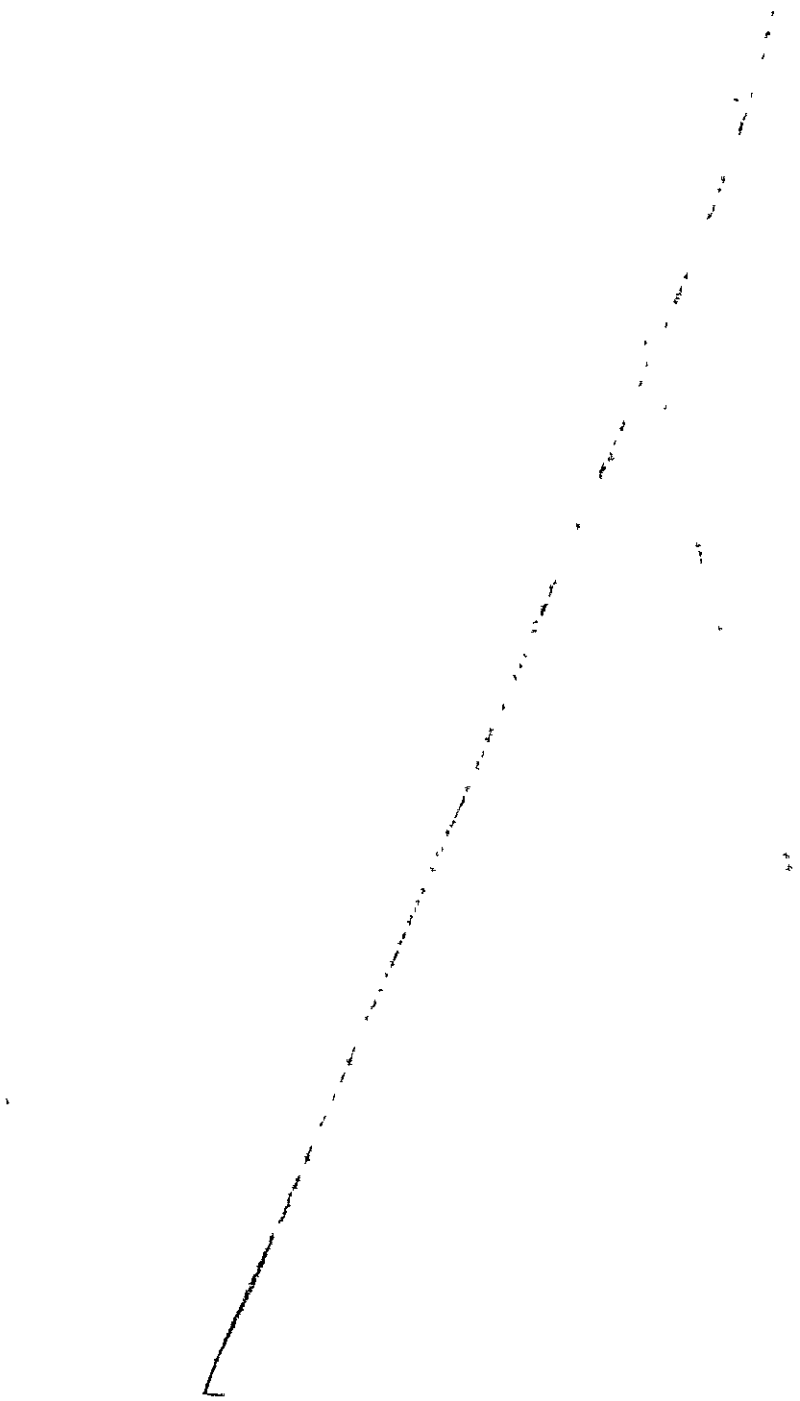

IV-C LOCAL BUCKLING OF COMPOSITE TUBES

Senior Investigator: D. B. Goetschel

1. Introduction

Because of their high unidirectional strength, continuous fiber composite materials are frequently used in thin-walled structures. When these types of structures are subjected to large compressive loads, such as is encountered on the L-1011 wing-mounted engine drag strut, for example, designing the member to be adequate for local buckling is very important.

2. Status

In the course of the preliminary design of a structure such as the L-1011 drag strut, it often will appear that the central portion of the strut can be relatively thin-walled. Local buckling, then, becomes a prime consideration. The best cross-sectional shape usually isn't obvious; I-beams or round, elliptical or rectangular tubes are all possibilities. The local buckling characteristics associated with these shapes could be the deciding factor in choosing among them. We concluded, based on results of a preliminary search, that the available equations are inadequate to the task of making that choice. To further investigate this, we decided to first concentrate on establishing the proper formulas for round tubes, in a form suitable for design purposes.

3. Progress During Report Period

This research is the work of graduate student Shu-Ping Chen. The earlier literature survey was extended to make an exhaustive collection of equations for predicting the local buckling of laminated, anisotropic round tubes. The papers perused are listed on pages 201 through 204.

A large number of theoretical studies were found in which various simplifying assumptions were made. Some investigators made use of empirical factors derived through correlations with experimental results to account for initial imperfections.

A test program was set up in order to make an initial screening of these various theories. Ten specimens were made from prepreg graphite-epoxy. They each had a two-inch inside diameter, a ten-inch length and were either three or four layers (.0165 or .022 inches) thick. These dimensions were chosen to eliminate Euler buckling, inelastic material response and prebuckling deformation as complicating factors. The lay-ups used all had zero degrees and plus-minus 30, 45 or 60 degree plies.

The buckling loads obtained in tests of these specimens were only 40 to 70 percent of those predicted by the various theories. Such large discrepencies can hardly be accepted in a design method. Since the theories being evaluated include a reduction factor to allow for initial imperfections, their prediction should have provided a reasonable lower bound to the test results.

4. Plans for Upcoming Period

It seems clear that there must have been something wrong with either the tests or the predictions to have such large discrepancies. Perhaps the equations used for the predictions have been empirically calibrated in a different region of the design space. The reduction in buckling load due to initial imperfections would be expected to be a function of the thickness to diameter ratio. Another possibility is that the initial imperfections in the specimens used in previous studies may have been unreasonably small compared to what would be expected in production parts. Alternatively, the initial imperfections in the current tests may have been unreasonably large. These possibilities as well as the possibility that other faults existed in the experimental procedure used here will have to be explored further. In addition, we hope to begin developing design equations for the other candidate cross-sections.

5. References

1. Almroth, B. O., A. M. C. Holmes and D. O. Brush, "An Experimental Study of Cylinders Under Axial Compression", Experimental Mechanics, 4, 1964, 263-270.

2. Almroth, B. O., "Postbuckling Behavior of Orthotropic Cylinders Under Axial Compression", Journal AIAA, Vol. 2, 1964, 1795-1799.

3. Almroth, B. O., A. B. Burns and E. V. Pittner, "Design Criteria for Axially Loaded Cylindrical Shells", J. Spacecraft, Vol. 7, 1969, 714-720.

4. Babcock, C. D., Jr., "Experiments in Shell Buckling", Thin Shell Structures, Y. C. Fung and E. E. Sechler, Eds., Prentice Hall, Englewood Cliffs, NJ, 1974

5. Batdorf, S. B., "A Simplified Method of Elastic Stability Analysis for Thin Cylindrical Shells", NACA Rept. No. 874, 1947.

6. Becker, H. and G. Gerard, "Elastic Stability of Orthotropic Shells", J. Aerospace Science, 29, 1962, 505-512.

7. Booton, M. and R. C. Tennyson, "Design Criteria for Elastic Buckling of a Circular Cylinder Under Combined Loads", International Colloquium on Stability of Structure, Stability of Structures Under Static and Dynamic Load, Washington, DC, 1977.

8. Brush, D. W. and B. O. Almroth, "Circular Cylindrical Shells", McGraw-Hill, NY, 1976, 142-189.

9. Budiansky, B. and J. W. Hutchinson, "Buckling of Circular Cylindrical Shells Under Axial Compression", Contributions to the Theory of Aircraft Structures, Rotterdam Press, 1971.

10. Burns, B., and B. O. Almroth, "Structural Optimization of Axially Compressed, Ring-Stringer Stiffened Cylinders", J. Spacecraft, Vol. 3, 1966, 19-25.

11. Bushnell, D., "Buckling of Shells - Pitfall for Designers", Journal AIAA, Vol. 19, 1981, 1183-1226.

12. Calcote, L. R., "The Analysis of Laminated Composite Structures", Van Nostran-Reinhold, Princeton, NJ, 1969.

13. Chang, C. M., "Acoustic Emission of Local Buckling of a Thin Graphite-Epoxy Tube" , M. Engr. Project, Dept. of Mechanical Engr., Aeronautical Engr. and Mechanics, Rensselaer Polytechnic Institute, Troy, NY, May 1982.

14. Chilver, A. H., "Elastic Stability of Structures", Stability, H. H. E. Leipholz, Ed., SM Study 6, U. of Waterloo, Waterloo, Canada, 1972.

15. Donnell, L. S., "A New Theory for the Buckling of Thin Cylinders Under Axial Compression and Bending", Trans. ASME 56, 1934, 795-806.

16. Dow, N. F. and W. Rosen, "Structural Efficiency of Orthotropic Cylindrical Shells Subjected to Axial Compression", Journal AIAA 4, 1966, 481-485.

17. Esslinger, M., "Postbuckling Behavior of Structures", Springer-Verlag, NY, 1975.

18. Esslinger, M. and B. Gerier, "Calculated-Postbuckling Loads as Lower Limits for Buckling Loads of Thin-Walled Circular Cylinders", Buckling of Structures, B. Budiansky, Ed., Spring-Verlag, NY, 1976.

19. Flugge, W., "Stress in Shells", 2nd ed., Springer, Berlin, 1973.

20. Gerard, G., "Elastic and Plastic Stability of Orthotropic Cylinders", NASA Note No. D-1510, Collected Papers on Instability of Shell Structures, 1962.

21. Greenberg, J. B. and Y. Stavsky, "Buckling and Vibration of Orthotropic Composite Cylindrical Shells", ACTA Mechanica 36, 1980, 15-29.

22. Hansen, J. S. and J. Roorda, "On a Probabilistic Stabilits Theory for Imperfection Sensitive Structures", Intl. J. of Solid Structures 10, 1974, 341-359.

23. Hansen, J. S., "Influence of General Imperfection in Axial Compression", J. of Solid Structures 11, 1975, 1223-1233.

24. Harper, J. G. and A. N. Palazetlo, "Buckling Analysis of Laminated Composite Circular Cylindrical Shells", SAE Trans. No. 790981, 1979.

25. Jones, R. M., "Buckling of Circular Cylindrical Shells with Multiple Orthotropic Layers and Eccentric Stiffeners", Journal AIAA, 6, 1968, 2301-2305.

26. Jones, R. M. and J. C. F. Hennemann, "Effect of Prebuckling Deformations on Buckling of Laminated Composite Circular Cylindrical Shells", Journal AIAA, 18, 1975, 110-115.

27. Kabanov, V. V., "Stability of an Anisotropic Circular Cylindrical Shell Under Compression and Internal Pressure", Soviet Aeronautics 10, 1967, 37-44.

28. Kempner, J. and Y. N. Chen, "Buckling and Initial Postbuckling of Oval Cylindrical Shells Under Combined Axial Compression and Bending", Trans. New York Academy of Science, 36, Series II, No. 2, 1974, 171-191.

29. Khot, N. S., "Buckling and Postbuckling Behavior of Composite Cylindrical Shells Under Axial Compression", Journal AIAA, 2, 1970, 229-235.

30. Mikisheva, V. I., "Optimal Winding of Filament-Wound Reinforced Plastic Shells Designed to Resist Buckling Under External Pressure or Axial Compression", Polymer Mechanics 4, 1967, 696-704.

31. Mysyk, D. A. and L. A. Shakimov, "Stability Analysis of Three-Layer Orthotropic Cylindrical Shells Under Axial Compression", Soviet Applied Mechanics 13, 1977, 1223-1226.

32. Roorda, J., "Equivalent Axisymmetric Imperfections in Axially Compressed Cylindrical Shells", U. of Waterloo, SMD Rept. No. 87, 1971.

33. Roorda, J. and J. S. Hansen, "Random Buckling Behavior in Axially Loaded Cylindrical Shells with Axisymmetric Imperfection", J. of Spacecraft and Rockets 9, 1972, 88-91.

34. Stein, M., "The Influence of Prebuckling Deformations and Stresses on the Buckling of Perfect Cylinders", NASA Tech. Note D-1510, 1962.

35. Structures Division, Air Force Flight Dynamics Laboratory, "Advanced Composite Design Guide", Sec. 2.1.5 and Sec. 2.2.2, Wright-Patterson Air Force Base, OH, 1973.

36. Sukhinin, S. N., V. I. Mikisheva and V. I. Smykov, "Experimental-Theoretical Studies of the Stability of Orthotropic Shells with a Filter in Axial Compression", Polymer Mechanics 3, 1978, 397-401.

37. Tennyson, R. C., D. B. Muggeridge and R. D. Caswell, "New Design Criteria for Predicting Buckling of Cylindrical Shells Under Axial Compression", J. of Spacecraft and Rockets 8, 1971, 1062-1067.

38. Thielemann, W. F., "New Developments in the Nonlinear Theories of the Buckling of Thin Cylindrical Shells", Aeronautics and Astronautics, Proc. of the Durand Centenial Conference, N. J. Hoff and W. G. Vincenti, Eds., Pergamon, Oxford, 1960, 76.

39. Timosenko, S. P. and J. M. Gere, "Theory of Elastic Stability", 3rd ed., McGraw-Hill, NY, 1961.

40. Tsai, J., "Effect of Heterogeneity on the Stability of Composite Cylindrical Shells Under Axial Compression", Journal AIAA, 4, 1966, 1058-1062.

41. Tsai, S., "Introduction to Composite Materials", Technomic, CT, 1980.

IV-D ACOUSTIC EMISSION OF LOCAL BUCKLING IN GRAPHITE TUBES

Senior Investigator: H. A. Scarton

1. Introduction

The use of acoustic emission (AE) testing for detailed analysis of failure scenarios in advance of ultimate failure has proven successful in delineating their mechanism of failure[1-5]*. Because of this capability, the AE technique is being used in the study of local buckling in slender prepreg graphite-epoxy circular cross section tubes, reported in Part IV-C of this report.

2. Status

This acoustic emission study, initiated during the current reporting period, was primarily performed by Mr. Chi-Min Chang[6], in support of the local buckling research of Mr. Shu-Ping Chen[7]. The major emphasis in this effort is to assist in assessing the degree of local buckling occurring in the specimens. Examples of local and Euler buckling modes appear in Figure IV-D-1**.

3. Progress During Report Period

a: Specimens and Test Set-Up

Ten specimens made of prepreg epoxy (1048 AE prepreg[8]) were used for acoustic emission testing. The first specimen

---

*Numbers in brackets in this section refer to the references which are listed on page 217.

**For the sake of clarity, figures in this part are placed at the end of its text, pages 219 through 243.

was constructed using four layers of 0.559 mm (0.022 in.) thickness. The remaining nine specimens were in three layers of 0.419 mm (0.0165 in.) thickness. All ply lay-ups used axially oriented layers, i.e., where fibers are aligned at 0°, along with balanced plies, with one of the following orientation pairs: ±30°, ±45° or ±60°. Table IV-D-1 shows the identification numbers used for the specimens.

In the initial testing of the first two tubes, failures occurred at the ends of the specimens. Each of the remaining specimens, therefore, was reinforced with glass epoxy material on both of the ends, as shown in Figure IV-D-2a. Figure IV-D-2b is a photograph of the nine three-layer specimens tested in this study. The one four-layer specimen, not shown, was tested without acoustic emission instrumentation.

Two AE sensors of the R15 type (resonant at 150 kHz), Physical Acoustic Corporation[9], were taped directly onto the specimens, using an appropriately curved "shoe" and high vacuum grease, 50A4084, from Automation Industries, Inc.[10] (see Figure IV-D-3). The AE signal was bandpass-filtered (100 ~ 300 kHz) with a preamplifier (PAC model 1220A). The total system amplification was maintained at 98 dB and a constant threshold voltage of 2V (after amplification) was used. The test dead time was set at 2 ms. Schematic diagrams of the experimental set-up are given in Figures IV-D-4 and -5.

TABLE IV-D-1

STACKING SEQUENCE OF THE NINE SPECIMENS

Specimen Tube Number	Stacking Sequence Outer-To-Inner Surface
1	$(-30°/0°/30°)_T$
2	$(30°/0°/-30°)_T$
3A	$(45°/0°/-45°)_T$
3B	$(-45°/0°/45°)_T$
3C	$(-45°/0°/45°)_T$
4A	$(45°/0°/-45°)_T$
4B	$(45°/0°/-45°)_T$
5	$(-60°/0°/60°)_T$
6	$(60°/0°/-60°)_T$

To assure proper alignment of specimens with the load axis of the MTS Tension/Torsion Servohydraulic System[11] (20,000 lbs. max. tensile or compressive load, 10,000 in.-lbs. max. torque) during the test, an alignment attachment was designed to be inserted in the top and bottom of the specimen.

Strain gages[12] were installed on Specimen No. 3C, as shown in Figure IV-D-2b. A strain gage, installed on an unloaded specimen, No. 4A, was used for temperature compensation. Instrumentation used in the test was a Data Logger model 2760 from the FX System Corporation[16].

The MTS machine[11] was tested for background noise under loaded conditions. In this test, the PAC 3400 System[9] was set for a total system amplification gain of 63 dB, with a constant threshold voltage of 2 V. Noise, in the range 38-45 dB, was measured; its probable source is the hydraulic system. This may be compared to a Pentel test* result of 95-97 dB.

To reduce the MTS machine noise reaching the sensors, AE isolators 1, 2 and 3 were installed at the test. Figure IV-D-4 shows this schematically. AE isolators 1 and 2 consisted of Vibrex Pad (1/4" thickness) produced by Vibrasciences Incorporated[13], and AE isolator 3 was an E. A. R. ISODAMP C-1002-12 (1/8" thickness) produced by E. A. R.

*Lead break occurred using five clicks on a 0.5 mm Pentel pencil held at 45° adjacent to the sensor.

Corporation[14,15]. By this means, the machine noise was reduced at the sensors to the 30-40 dB range.

b. Initial Test Results

The computer controlled tests were conducted with monotonically increasing stroke control conditions. A typical load stroke curve for tube number 3A is shown in Figure IV-D-6. It appears that the glass ends underwent load readjustment at points A and B (Note the increasing slope of the curves after events A and B.). Local buckling occurred at point C. Figure IV-D-7 shows strain versus time curves for tube 3C. (Note that the other example uses tube 3A.) Symmetry is in evidence during most of the test, verifying pure compressive loading conditions. For reasons of economy, tube 3C was the only specimen instrumented for strain measurement. The more interesting AE data occurred in tube 3A, which has a different time history.

The AE sensors indicated AE events all through the loading sequence. Discussion of these results is divided, here, into the following three sections.

i) Overall test time.
ii) The local buckling period.
iii) Other selected points and time periods.

i) Overall test time. From AE displays "Parametric (Load) Rate (i.e., Load Change per Division of Time) versus Time", as shown in Figure IV-D-8 for tube number 3A, three peaks of acoustic emission activity were found (point A at 40 sec.,

point B at 51 sec. and point C at 115.5 sec.)*. Similarly, event rate (events per tick), energy rate and count rate versus time, Figures IV-D-9 through 11, respectively, show much activity at these times. The first two peaks (A and B) were associated with two end effects which occurred during the delamination between the graphite/epoxy and the glass/epoxy tape reinforcement. The delamination (shown in Figure IV-D-2a) had been inspected after tube number 3A was tested.

Analysis of the amplitude distributions during these times (see Figures IV-D-12 through -18) reveals that many events occurred in the range 40-60 dB. Two peaks can be easily found, one at 45 dB, the other at 55 dB. Failure mechanisms cannot be assigned with confidence on the basis of the overall time period data record, since a number of different phenomenon occurred. It is necessary to compare amplitude distributions obtained with tube number 3A: (1) before the end-effect events occurred and (2) before local buckling occurred. Note that an increase in events at amplitudes around 40-60 dB coincided with delamination between

---

*Note that the PAC 3400 plotting system labels the horizontal time axis in 120 divisions or tick marks, with the numbers being written vertically, such as $\begin{matrix}1\\2\\0\end{matrix}$. This represents 120 ticks x 1.5 sec./tick = 180 seconds. Figure IV-D-8 shows only parametric rate data. Since an absolute calibration was not deemed necessary, only the temporal sequence of events is needed to provide insight into the actual time history. Rate data analysis, rather than cumulative data, is used, since this technique increases the sensitivity of the instrument to particular failure scenarios.

the two different materials at the ends. This is discussed further in Section iii, page 212.

ii) Local buckling period. The PAC 3400 has the capability of "labelling" data recorded within certain time periods. Data can then be recovered for analysis purposes from that aggregated without respect to time, by a technique called "time-filtering". This was done, in the Post Test Mode[9], for each tube so as to eliminate events which occurred at times associated with postbuckling behavior. For this reason, the events from between time ticks 85 and 120 (127.5 to 180 seconds) have been suppressed in the data discussed in this section.

It will be seen from the time-filtered display of "Event Rate versus Time" (Figure IV-D-19) or "Energy Rate versus Time" (Figure IV-D-20) that the event and energy rates are not at their highest levels at the final load drop point C, for tube number 3A. The end effects for that specimen had occurred before point C, and their energy rates are almost the same as those associated with point C. However, before point C, there is an event scenario associated with point D which has a still larger AE energy rate. In fact, when the precurser load drop point (point D in Figure IV-D-8) occurs, the material is seen to release the largest AE energy rate (see Figure IV-D-20). Point D might be explained as the onset of local buckling and the following load drop point C as

the point at which local buckling has been completed and its mode shape fully developed[7].

Analysis of mode shapes indicates that the number of pulses of rise time versus time may be twice the experimentally measured circumferential mode number N. For example, Figure IV-D-21 shows specimen 3A after testing; a mode number of three is in evidence. Figure IV-D-22[7] shows the identical post-test buckled shape under the action of an axial preload to demonstrate its deformed shape. Study of this shape for tube number 3A reveals that the circumferential mode number N is, in fact, 3. Analysis of the number of pulses of rise time rate versus time, as seen in Figures IV-D-23 and -24, between the time tick divisions 60 and 84 (90-126 seconds), is found to be approximately 6 or 2N (two times the circumferential mode number). Note that Figure IV-D-24 shows only the 90-126 second time intervals. The same conclusion was observed by studying data from the other tubes.

Plots of duration rate (Figure IV-D-25), amplitude rate (Figure IV-D-26) and count rate (Figure IV-D-27) versus time for specimen 3A also show the specific characteristics of local buckling.

iii) Other selected points and time periods. As has been mentioned previously, subsegments of AE data at any time can be filtered by the "post" and "exam" analysis of

software available on the PAC 3400[9]. For tube number 3A, the segments of interest for initial end effects occur at points A, at time tick 30 (45 seconds) and B, at time tick 35 (37.5 seconds); the local buckling period is a segment in the time tick range from 60-84 (90-126 seconds). Figures IV-D-28 and -29 show the display of Energy Rate versus Time and a Time-Filtered Amplitude Distribution for point A alone; Figures IV-D-30 and -31 for B alone; and Figures IV-D-32 and -33 for C alone. Figures IV-D-34 and -35 show the AE display for the local buckling segment between 60-74 ticks (90-111 seconds).

Recall that the AE amplitude range of delamination for composite materials such as glass/epoxy and graphite-epoxy can be in the range of 45-60 dB*, while fiber breakage occurs above 80 dB[3]. The same conclusions can be obtained from points B and C, as seen in Figures IV-D-30 through -33. Since Figure IV-D-33 shows an amplitude distribution in the range of 45-60 dB, the initiation of local buckling could be associated with debonding.

Figures IV-D-36 and -37 portray events which occurred at a maximum constant stroke. Analysis of these plots verified the visual observation that after local buckling occurred, intense fiber breakage (amplitudes above 80 dB) took place. Figure IV-D-37 depicts events which occurred early

*Attenuation with distance tests using Pentel-lead breaks were performed on the tube, and they showed less than a 5 dB drop in amplitude over the length of the specimen. This lends credence to arguments based on amplitude characteristics.

in the constant-hold stroke phase and shows only fiber breakage. Figure IV-D-38 shows the amplitude distribution when the stroke was held to maximum time; it would appear from this that more delamination then occurred.

Table IV-D-2 sumarizes results from the remainder of the specimens studied. Analogous conclusions were drawn by either analysis similar to that done for tube 3A or by interrupting the test prior to one of the above effects for visual inspection and appropriate AE analysis.

c. Preliminary Conclusions

Experience with AE analysis of specimens subject to debonding suggests that the major amplitude distribution during incipient local buckling is in the range associated with debonding (around 45-60 dB). Postbuckling behavior, on the other hand, seems associated with AE amplitude distributions typical of fiber breakage. It also seems possible that AE parameters such as energy rate, rise time rate, duration rate and count rate may have a numerical relation with the circumferential mode indices which describe the local buckling shapes of composite tubes. Taping the ends of specimens with the same material as they are made of promises to eliminate the end effect for the future tests.

4. Plans for Upcoming Period

A major study in unaxial tension-tension, tension-compression, biaxial tension-torsion low cycle fatigue and

TABLE IV-D-2

SUMMARY OF THE LOCAL BUCKLING TEST

Test Item	Buckling Load (lbs.)	Acoustic Emission (events)	Inspection After Test	Note Number[i]
1. Tube No. 1 $(-30°/0°/30°)_T$[ii]	1935	----	m = 1[iii] n = 4[iv]	(1)
2. Tube No. 2 $(30°/0°/-30°)_T$	1550	----	m = 1 n = 4	(1)
3. Tube No. 3A $(45°/0°/-45°)_T$	2095	1330	m = 1 n = 3	(2,3)
4. Tube No. 3B $(-45°/0°/45°)_T$	2605	843	m = 1 n = 4	(4)
5. Tube No. 3C $(-45°/0°/45°)_T$	2100	----	m = 1 n = 3	(5)
6. Tube No. 4A $(45°/0°/-45°)_T$	1690	----	m = 1 n = 3	(6)
7. Tube No. 4B $(45°/0°/-45°)_T$	1950	1664	m = 1 n = 3	(7)
8. Tube No. 5 $(-60°/0°/60°)_T$	2365	1246	m = 1 n = 3	(8)
9. Tube No. 6 $(60°/0°/-60°)_T$	2800	----	m = 1 n = 3	(9)

[i] See following page for notes

[ii] Stacking sequence, outer-to-inner surface

[iii] m = Number of axial half-waves for a displacement mode in a simply-supported shell

[iv] n = Number of circumferential waves as seen in Figure 4.2[15]

TABLE IV-D-2 (Continued)

Note Information:

(1) Tubes nos. 1 and 2 fractured at both ends. Therefore, each of the tubes was reinforced on both ends with filament (glass/epoxy) winding before testing, and Tubes 1 and 2 were not monitored with AE instrumentation. The test sequence is Nos. 3C, 6, 4A, 4B, 3A, 3B and 5.

(2) As shown in Figure IV-D-6, load drop points A and B are due to end effects caused by delamination between specimen and the end reinforcing material (glass/epoxy).

(3) Tube no. 3A has good AE results, for local buckling and end effects.

(4) Tube no. 3B has good AE results, for local buckling without end effects (the load-stroke diagram for this tube is shown in Figure IV-D-6.).

(5) Tube no. 3C failed rapidly under load control (500#f/min); after testing of this specimen, stroke control of the MTS machine was advised.

(6) Tube no. 4A lost AE signals due to misoperation of AE instruments.

(7) AE recording was stopped when local buckling noise from the test of tube no. 4B was heard.

(8) Tube no. 5 has good AE results for local buckling and end effects.

(9) AE recording was stopped just before the first end effect. No AE data for local buckling was obtained.

monotonic loading of cylindrical composite tubes is underway. We expect to be able to report results from these studies during the next project period.

5. References

1. Williams, J. H., Jr. and S. S. Lee, "Acoustic Emission Monitoring of Fiber Composite Materials and Structures", J. of Composite Materials, 12, 1978, 348.

2. Williams, J. H., Jr. and D. M. Egan, "Acoustic Emission Spectral Analysis of Fiber Composite Failure Mechanisms", Material Evaluation, 32, January 1979.

3. Otsuka, H. and H. A. Scarton, "Variation in Acoustic Emission Between Graphite and Glass-Epoxy Composites", J. of Composite Materials, 15, November 1981, 594.

4. Otsuka, H. and H. A. Scarton, "Acoustic Emission Testing of Composite Tensile Specimens", Composite Structural Materials Semiannual Report, September 1979 - April 1980.

5. Fowler, T. J., "Acoustic Emission Testing of Fiber Reinforced Plastics", ASCE Fall Convention and Exhibit, San Francisco, California, October 17-21, 1977.

6. Chang, Chi-Min, "Acoustic Emission of Local Buckling of a Thin Graphite Epoxy Tube", Masters Project, Department of Mechanical Engineering, Aeronautical Engineering and Mechanics, Rensselaer Polytechnic Institute, Troy, NY, 1981.

7. Chen, S. P., "The Local Buckling of Anisotropic Cylindrical Thin Walled Tubes Under a Compressive Load", Masters Project, Department of Mechanical Engineering, Aeronautical Engineering and Mechanics, Rensselaer Polytechnic Institute, Troy, NY, 1982.

8. Fiberite Corporation, "Advanced Composite Materials", Hy-E, 501 West Third Street, Winona, MN 55987.

9. Physical Acoustic Corporation, "General Principles of Acoustic Emission", Acoustic Emission Workshop, Physical Acoustic Corporation, P. O. Box 3135, 743 Alexander Road, Princeton, NJ 08540, 1978.

10. Automation Industries Incorporated, Sperry Division, 1000 Shelter Rock Road, Danbury, CT 06810.

11. MTS System Corporation, Box 24012, Minneapolis, MN 55424.

12. William T. Bean, Incorporated, 18915 Grand River Avenue, Detroit, MI 55424.

13. Vibrasciences Incorporated, New Haven, CT 06510.

14. E. A. R. Corporation, 7911 Zionsville Road, Indianapolis, IN 46218.

15. Scarton, H. A. and G. Bobal, Personal communication, Rensselaer Polytechnic Institute, Troy, NY, 1981.

16. FX System Corporation, B & F Instruments Division, P. O. Box 1818, Kingston, NY 12401.

6. Current Publications or Presentations by Professor Scarton on this Subject

"Variations in Acoustic Emission Between Graphite- and Glass-Epoxy Composites", with H. Otsuka.

Published in the Journal of Composite Materials, Vol. 15, November 1981, 591-597.

"Acoustic Emission in Composite Materials"

Presented at ASME Winter Meeting, Washington, DC, November 16-20, 1981 and Physical Acoustics Corporation, Montreal, Canada, January 5, 1982.

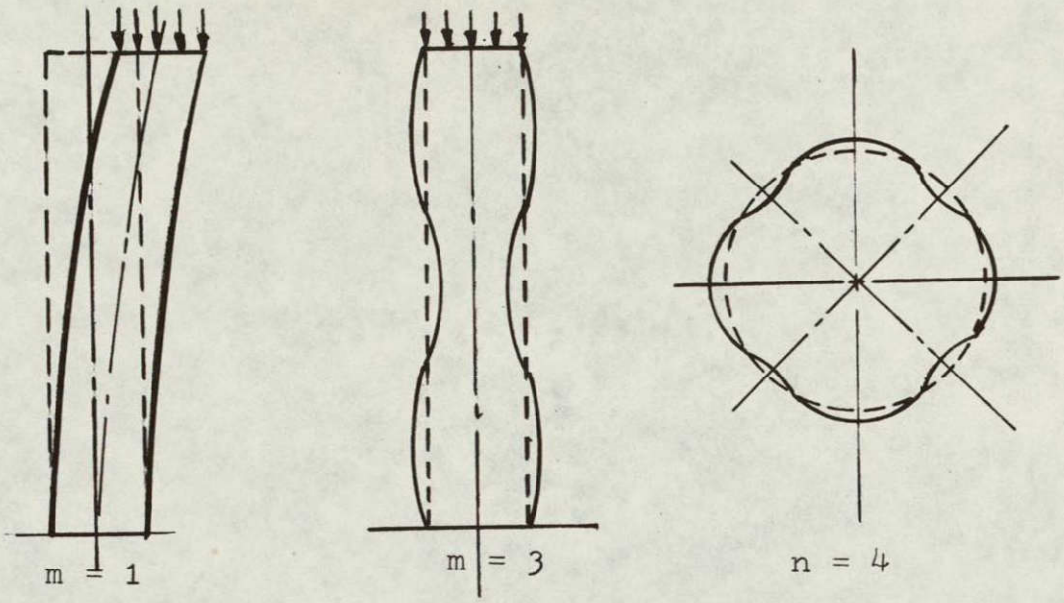

Euler Buckling | Local Buckling Axial | Local Buckling Circumferential

Local Buckling Type	Axial Mode	Circumferential Mode
Axisymmetrical Buckling	$m \geqslant 1$	$n = 0$
Nonsymmetrical (Asymmetrical, Unsymmetrical) Buckling	$m \geqslant 1$	$n \geqslant 1$

Figure IV-D-1. Buckling Mode Shapes [7]

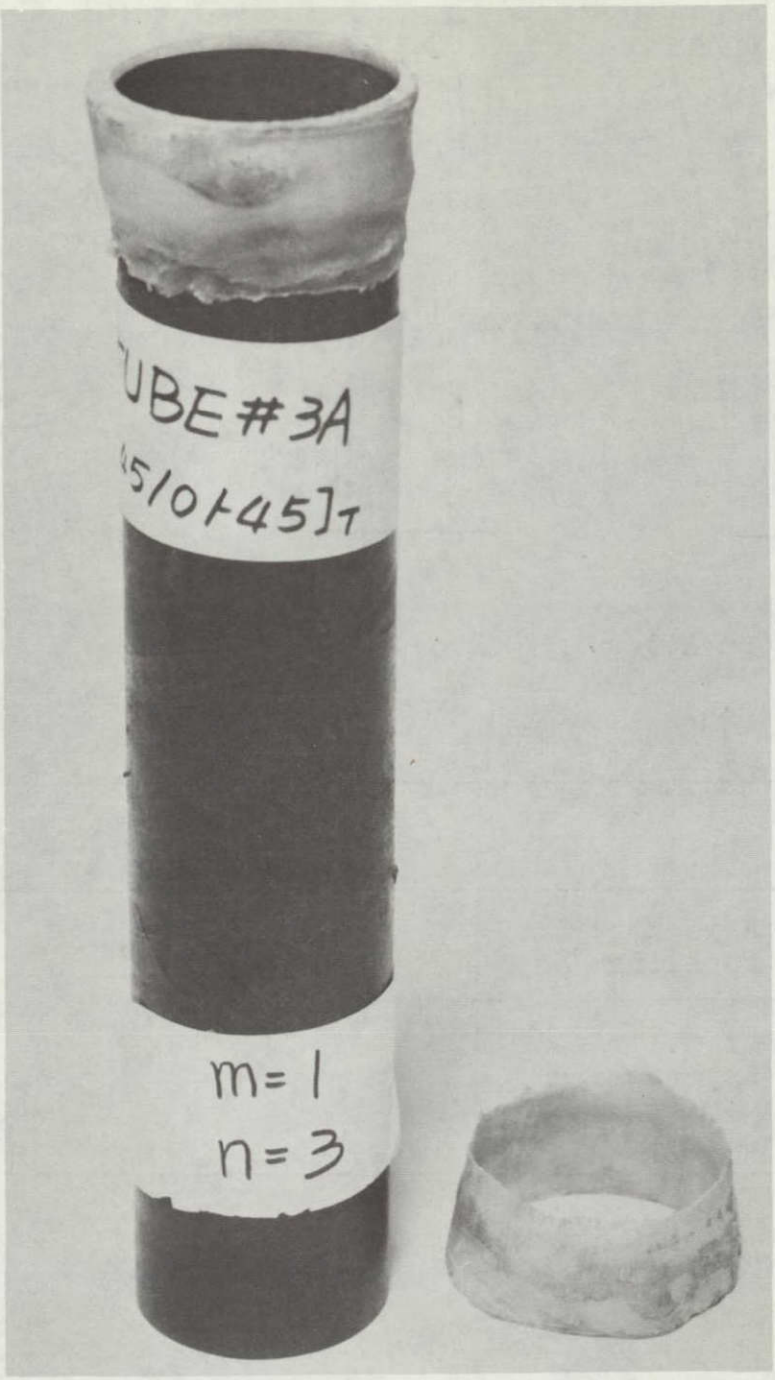

Figure IV-D-2a. Specimen Tube No. 3A with Reinforced Glass/Epoxy Ends

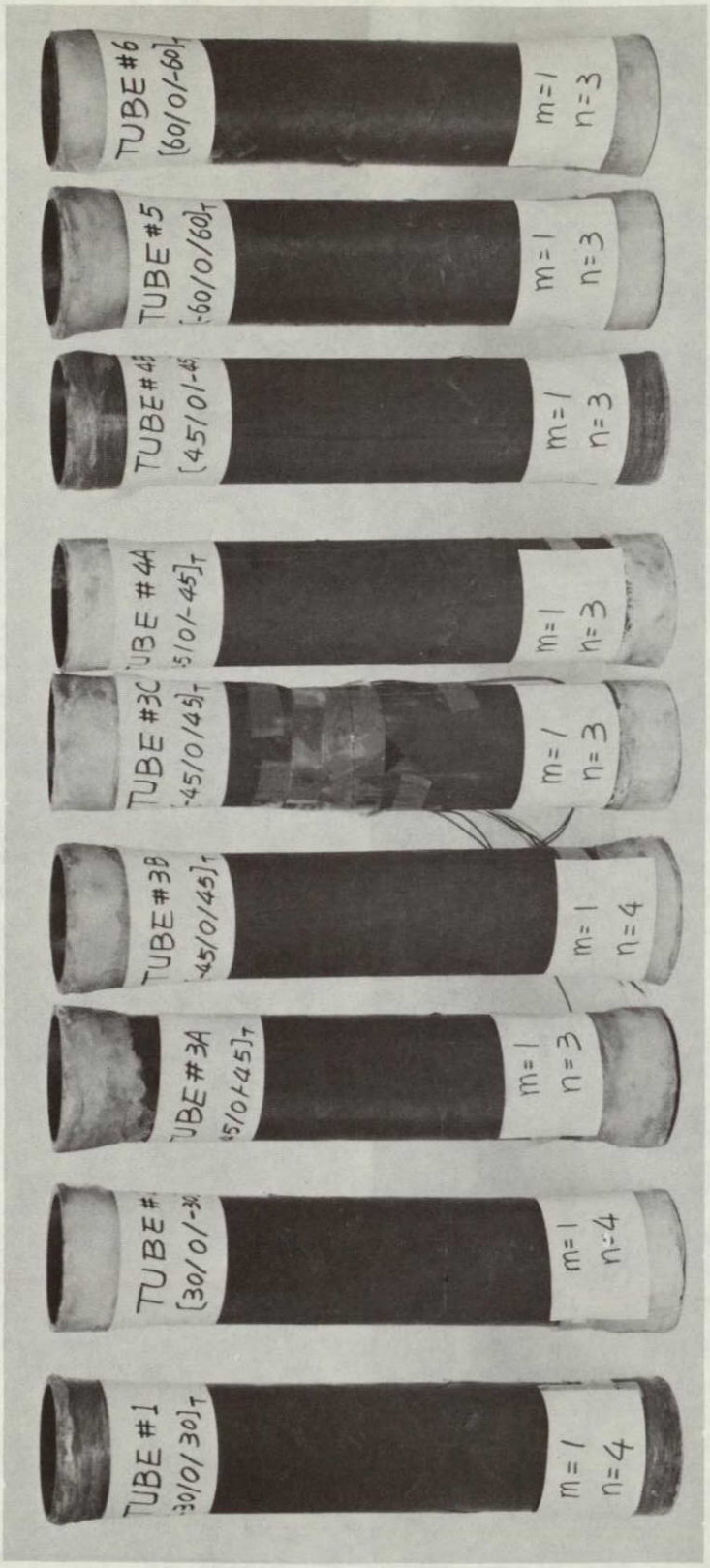

Figure IV-D-2b. Tubular Test Specimens with Glass/Epoxy End Reinforcements

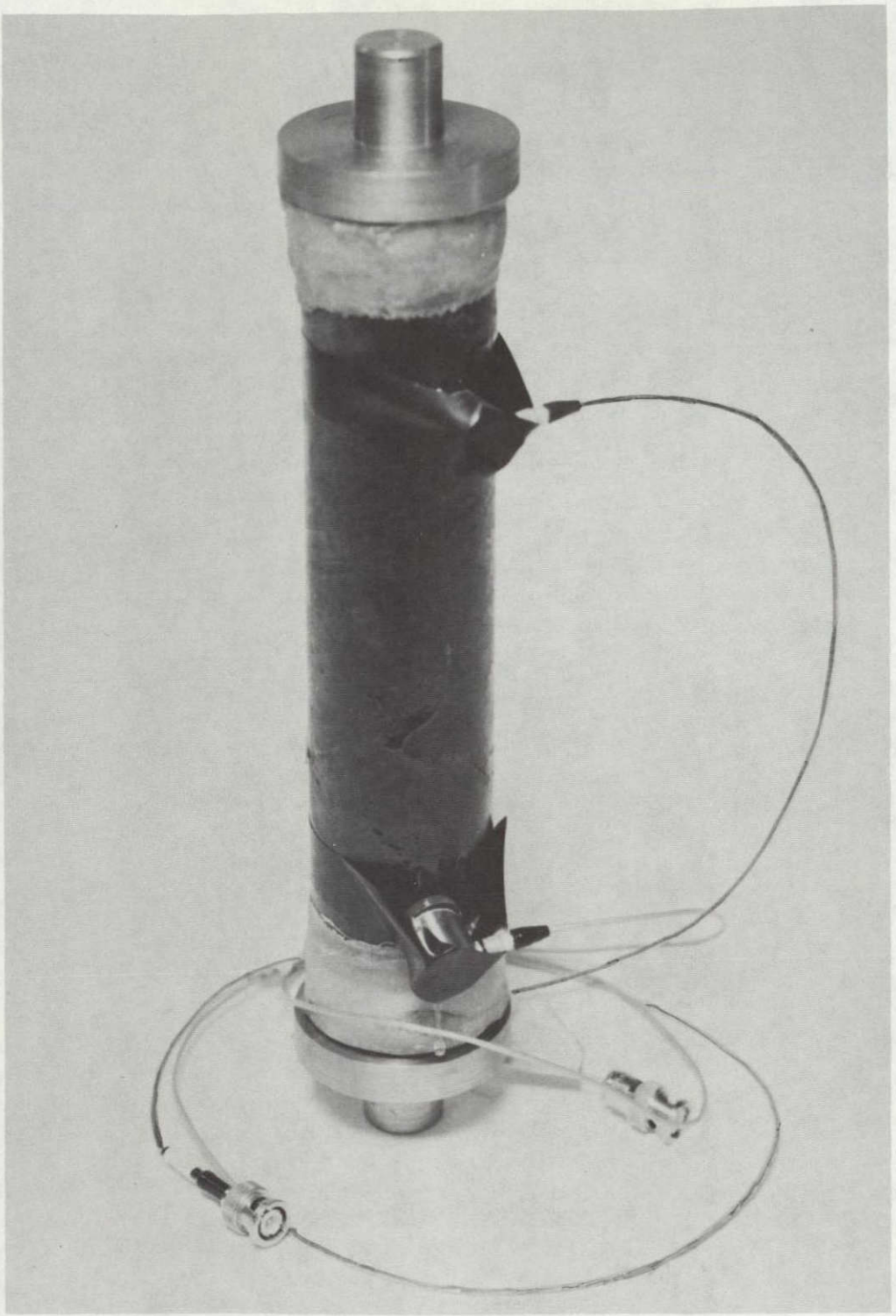

Figure IV-D-3. AE Sensors, AE Shoes, Alignment Attachment for Tube No. 3A

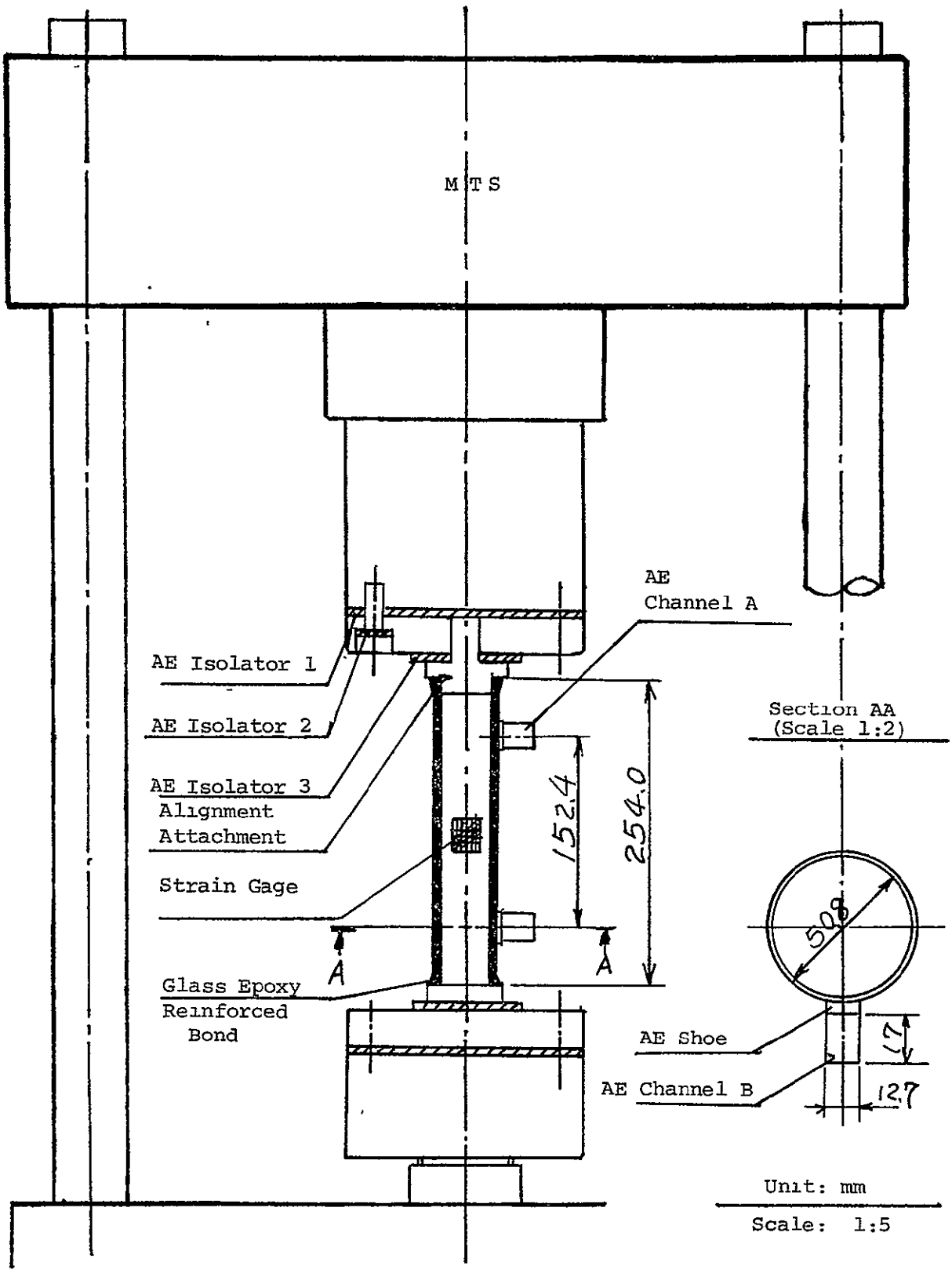

Figure IV-D-4. Schematic Diagram of Test Set-Up

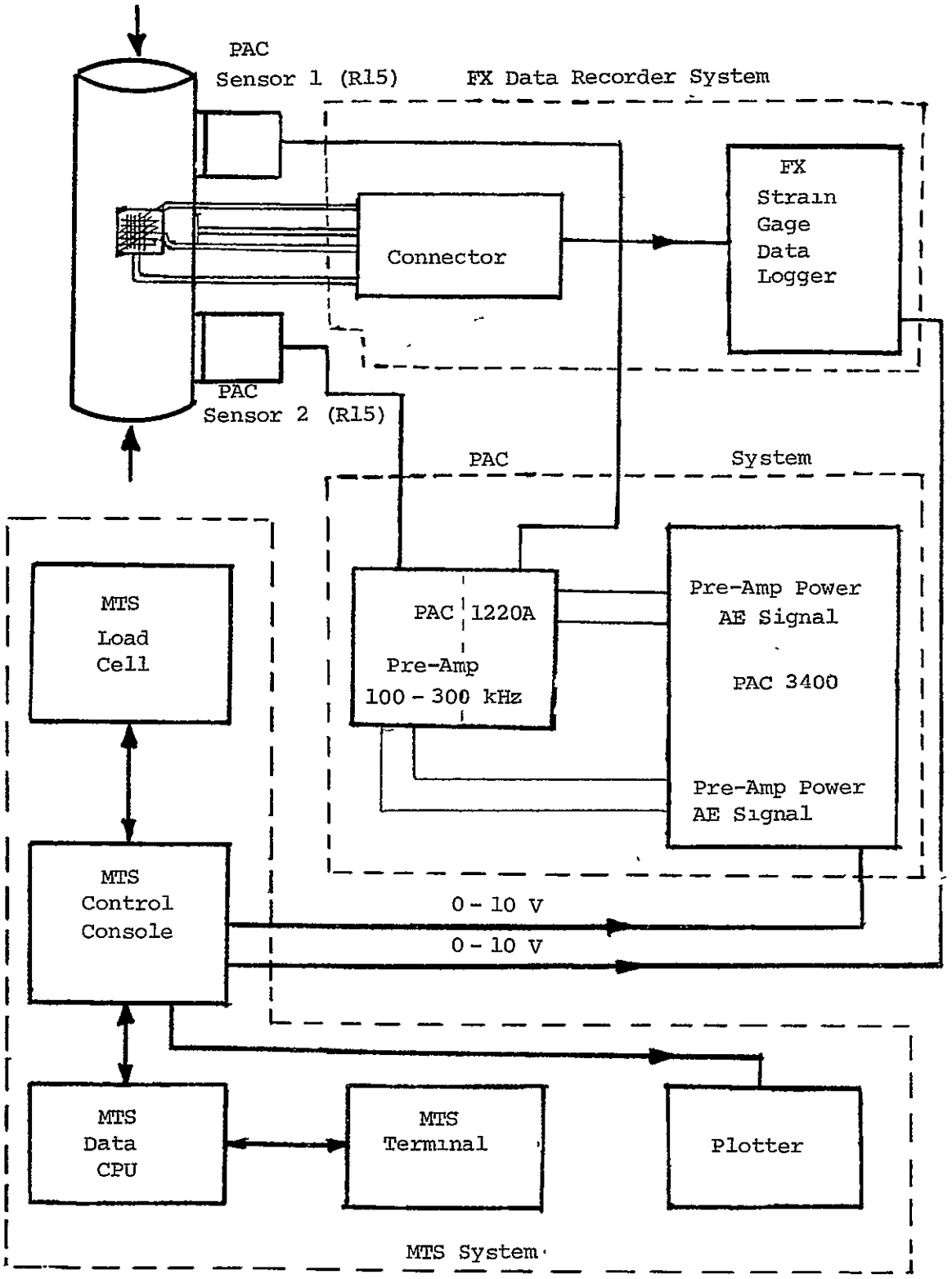

Figure IV-D-5. Schematic of the Set-Up for the Acoustic Emission System

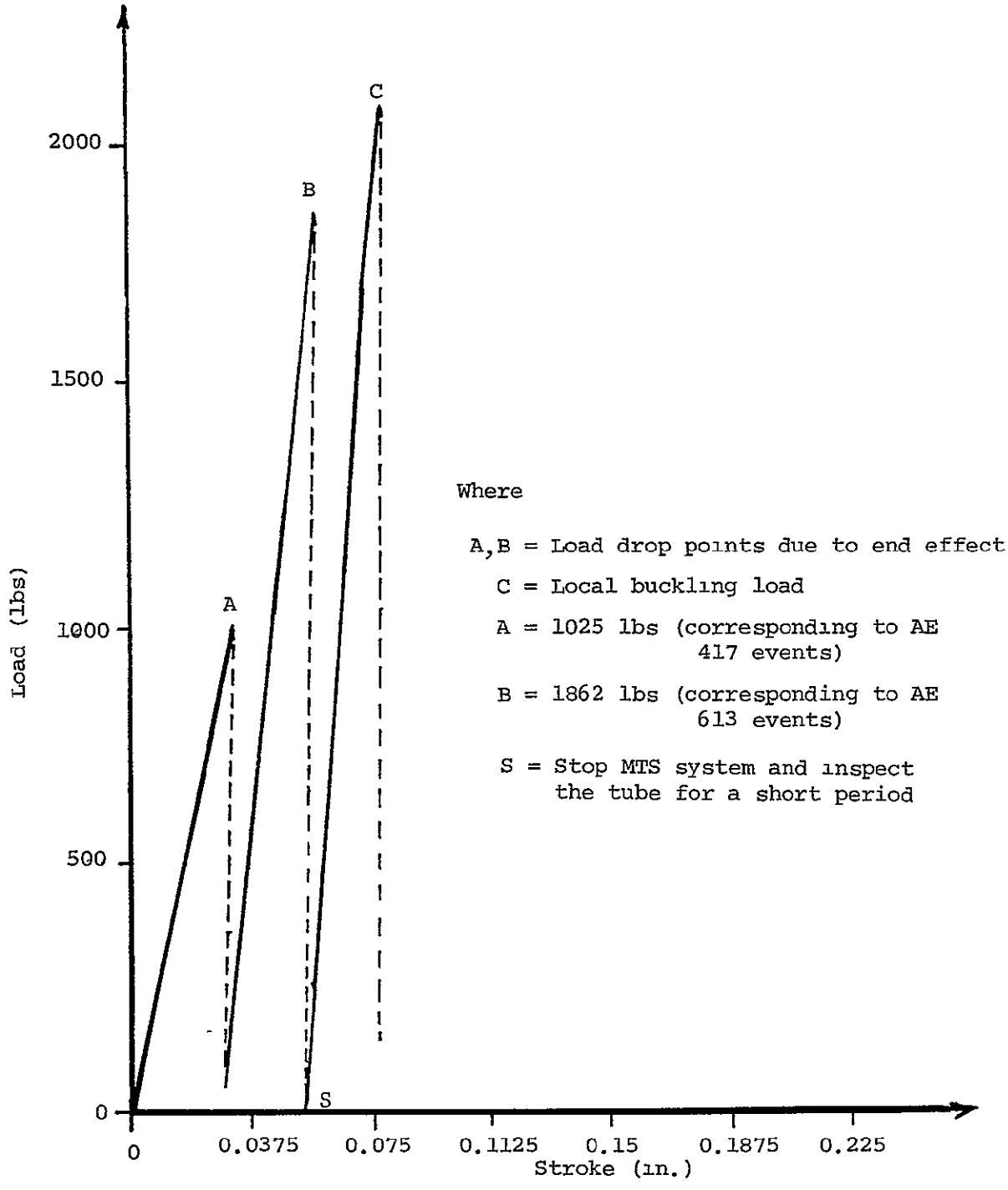

Figure IV-D-6. Load-Stroke Diagram of Tube No. 3A Graphite/Epoxy $(+45°/0°/-45°)_T$

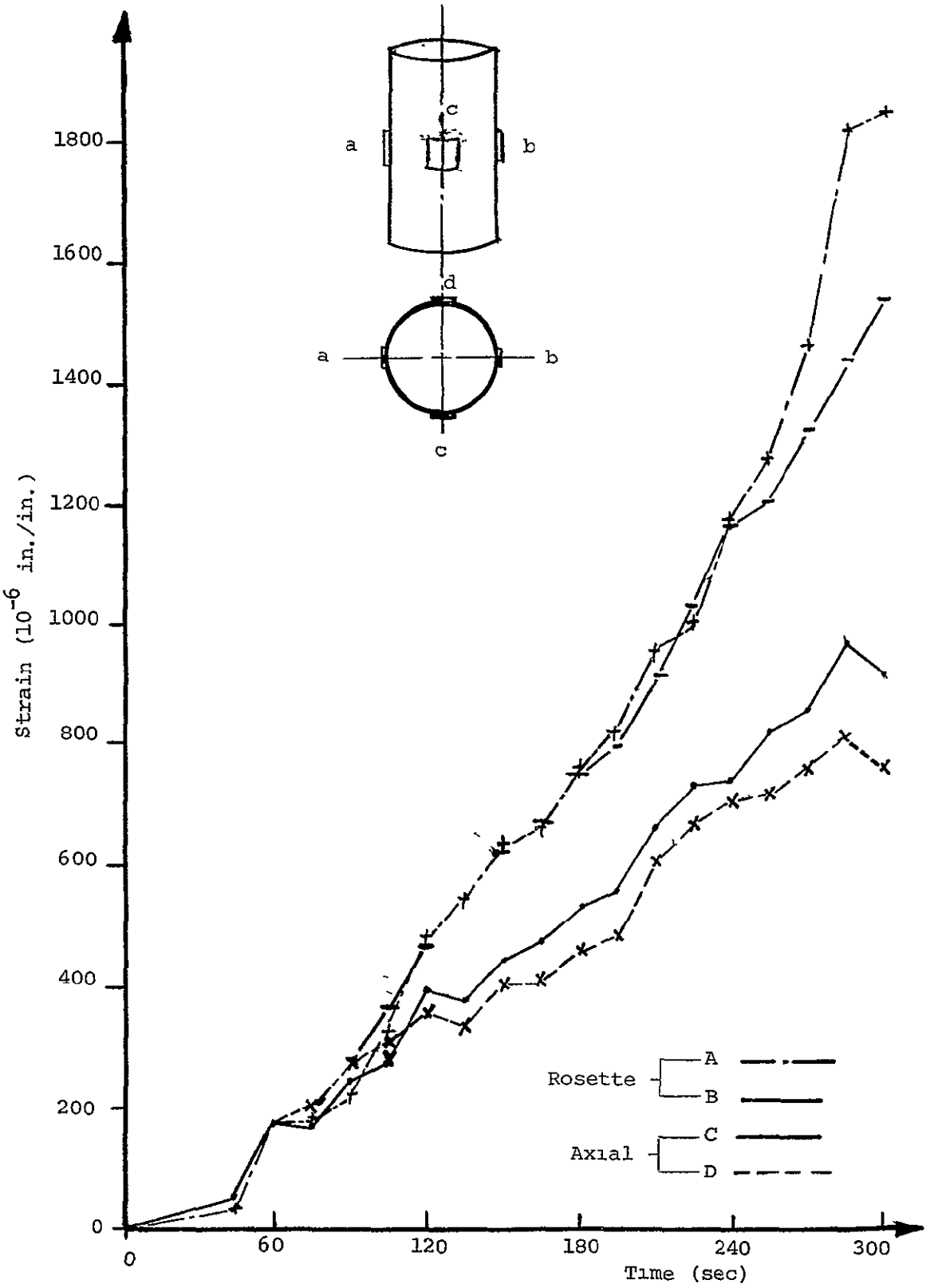

Figure IV-D-7. Curves of Strain vs. Time of Tube No. 3C

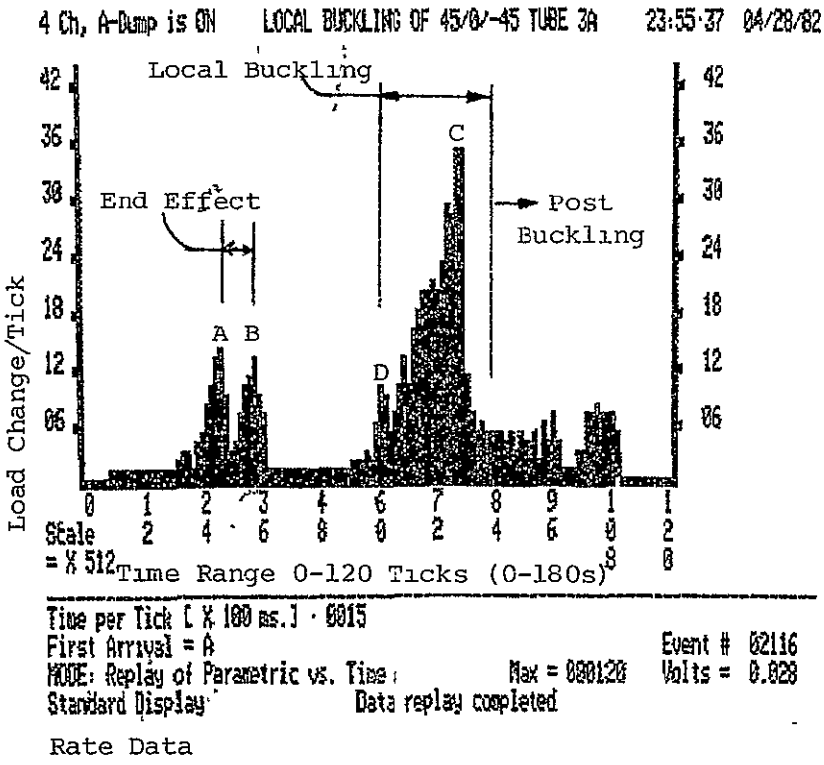

Figure IV-D-8. Parametric (Load) Change/Tick vs. Time for Tube No. 3A (Note the pause in stroke ramp at the 36th to the 50th tick mark for visual inspection of the specimen)

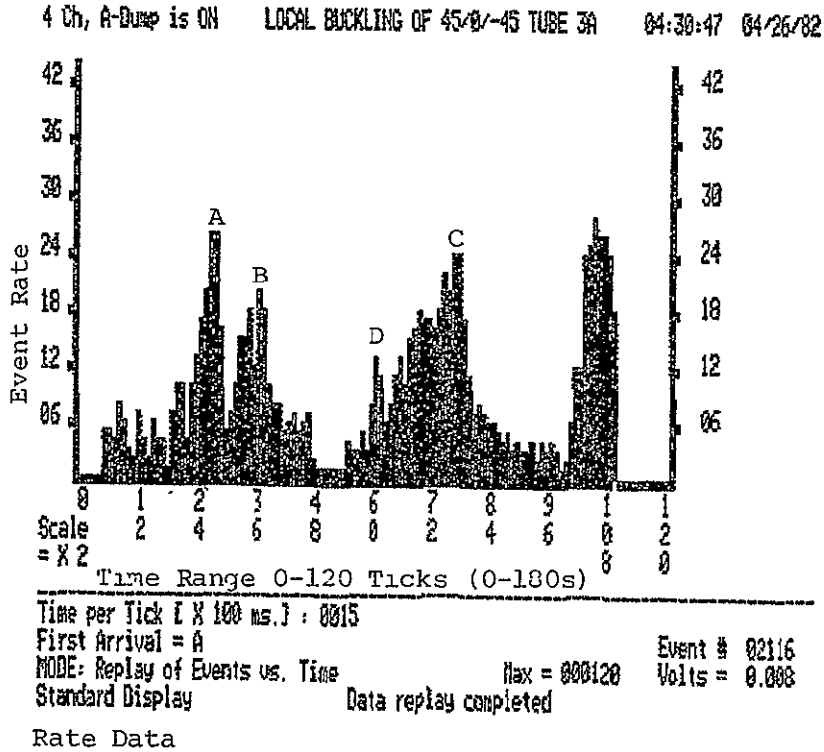

Figure IV-D-9. Event Rate vs. Time of the Whole Test for Tube No. 3A

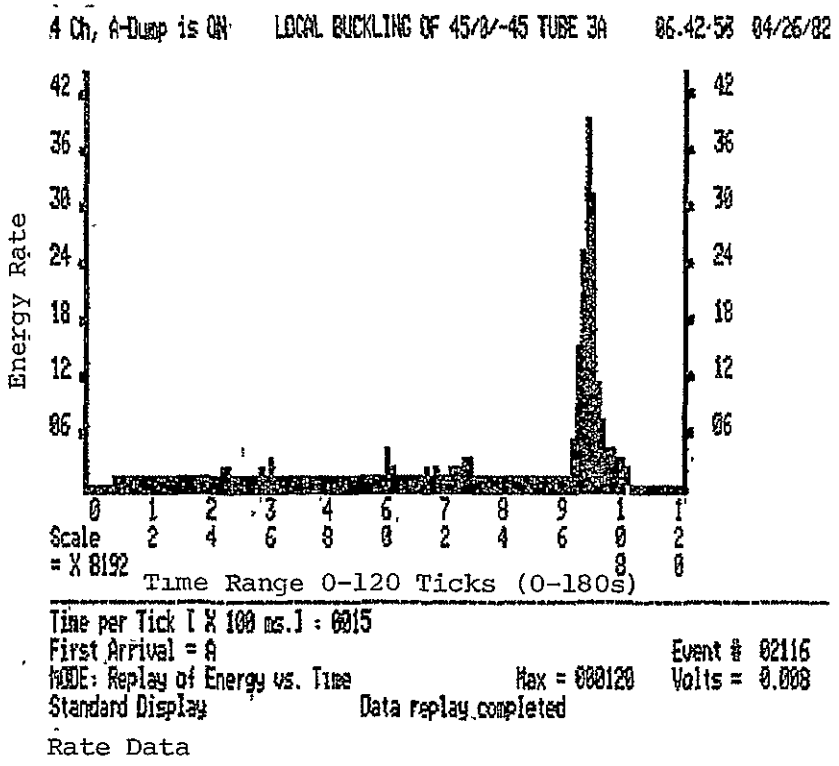

Figure IV-D-10. Energy Rate vs. Time of the Whole Test for Tube No. 3A

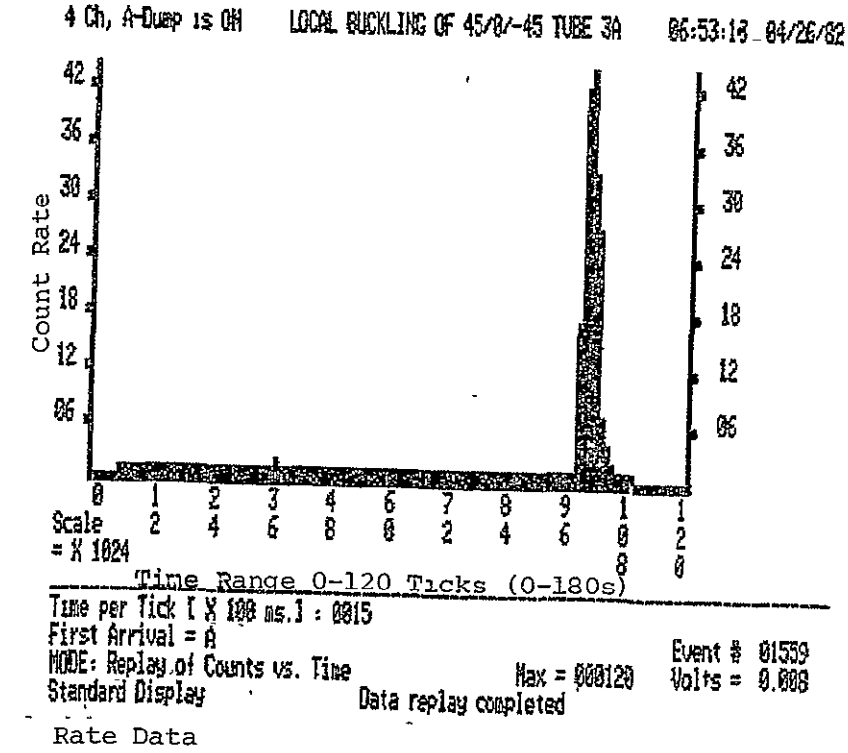

Figure IV-D-11. Count Rate vs. Time of the Whole Test for Tube No. 3A

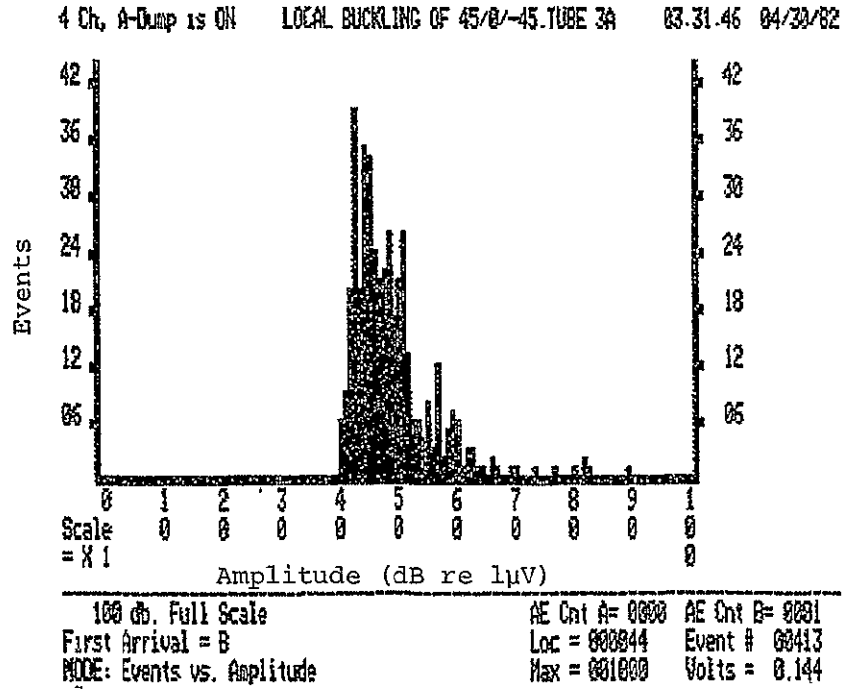

Figure IV-D-12. Amplitude Distribution for Tube No. 3A Before End Effect Point A

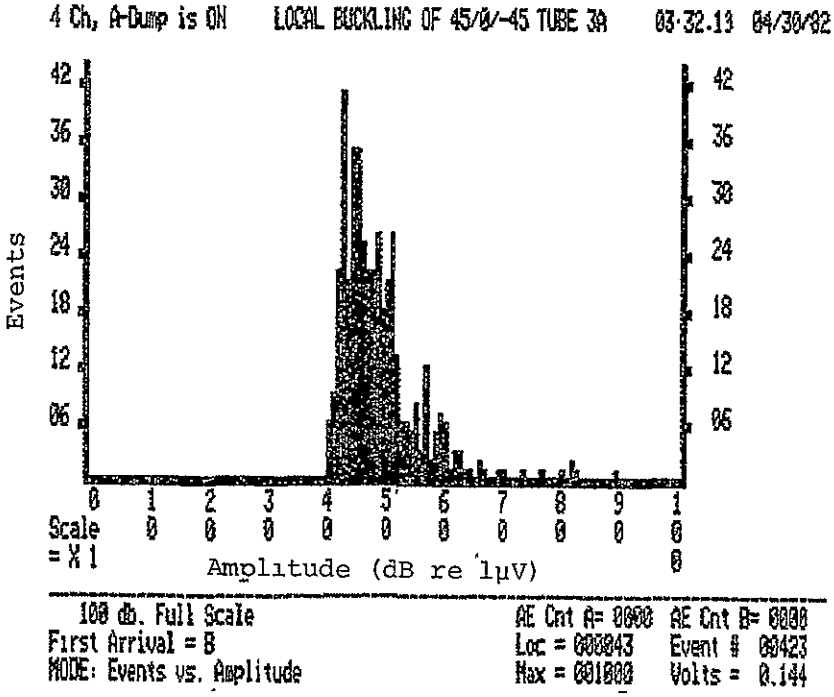

Figure IV-D-13. Amplitude Distribution for Tube No. 3A After End Effect Point A

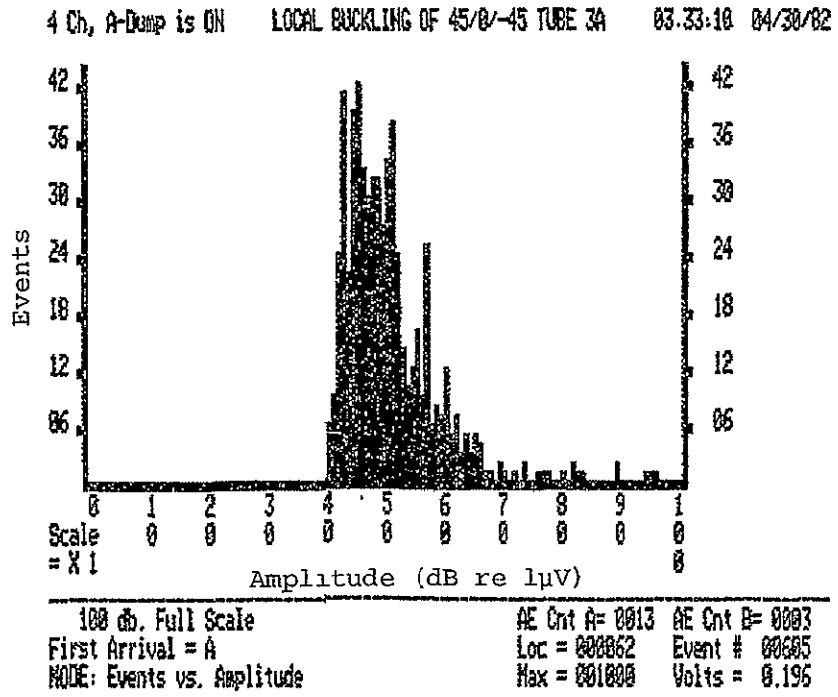

Figure IV-D-14. Amplitude Distribution for Tube No. 3A Before End Effect Point B

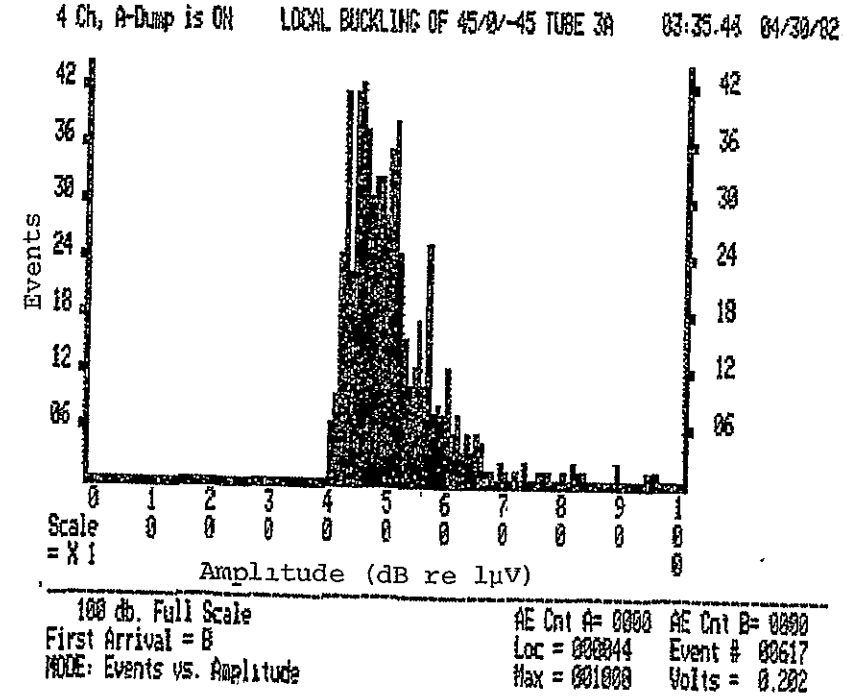

Figure IV-D-15. Amplitude Distribution for Tube No. 3A After End Effect Point B

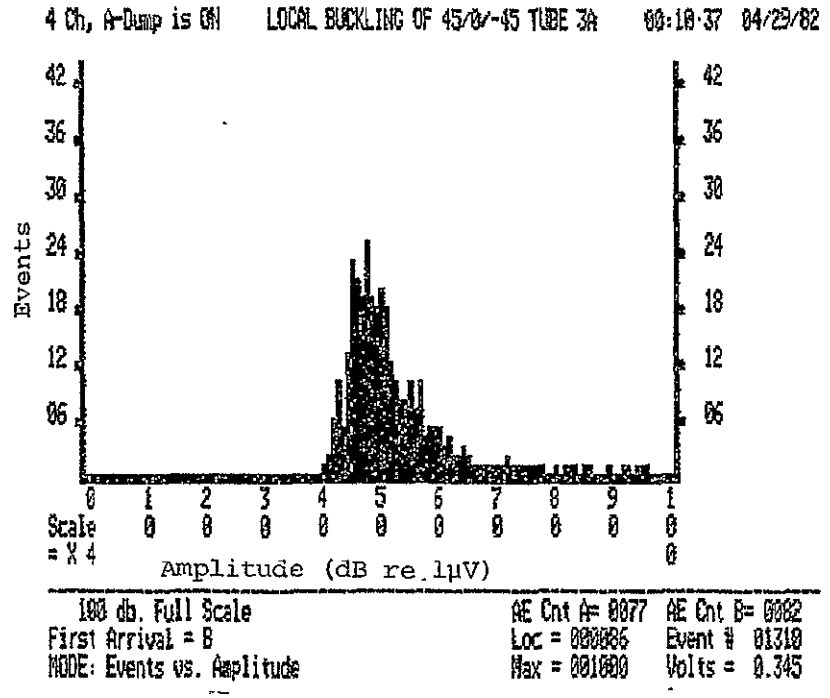

Figure IV-D-16. Amplitude Distribution for Tube No. 3A Before Local Buckling - Point C

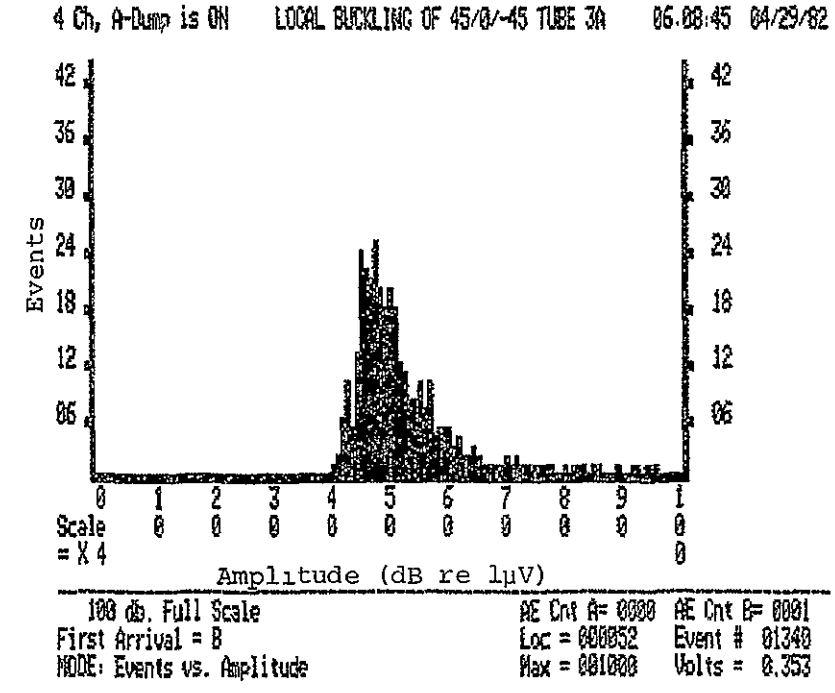

Figure IV-D-17. Amplitude Distribution for Tube No. 3A After Local Buckling - Point C

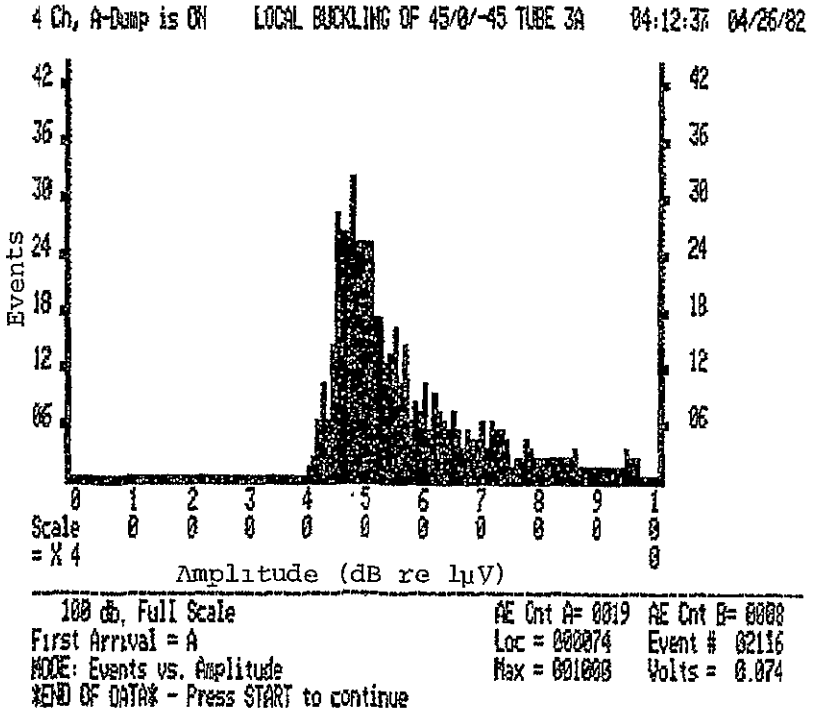

Figure IV-D-18. Amplitude Distribution for Tube No. 3A for the Whole Test

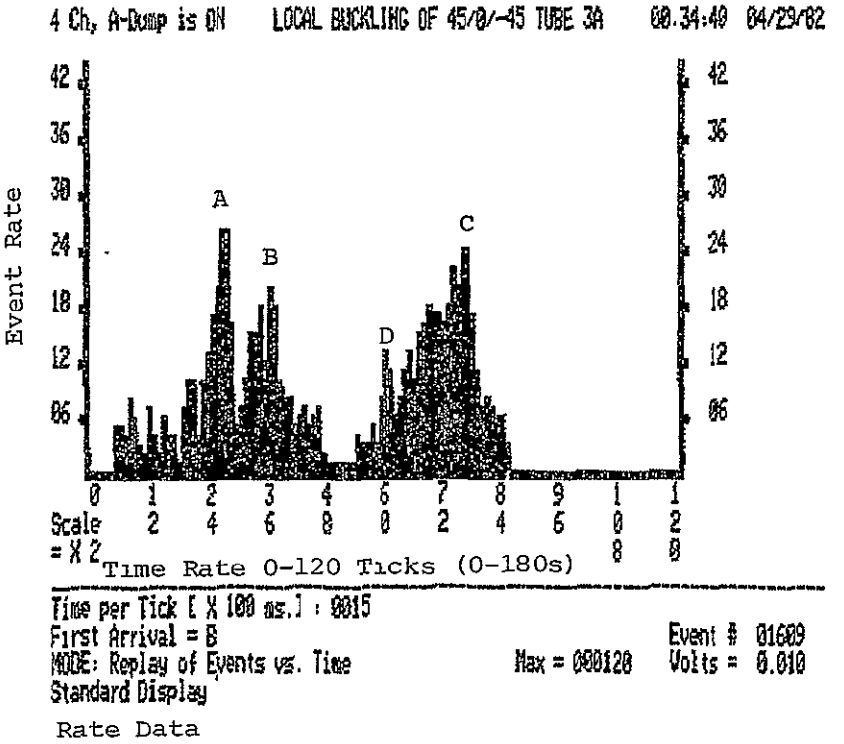

Figure IV-D-19. Event Rate vs. Time for Times Associated with Local Buckling of Tube No. 3A

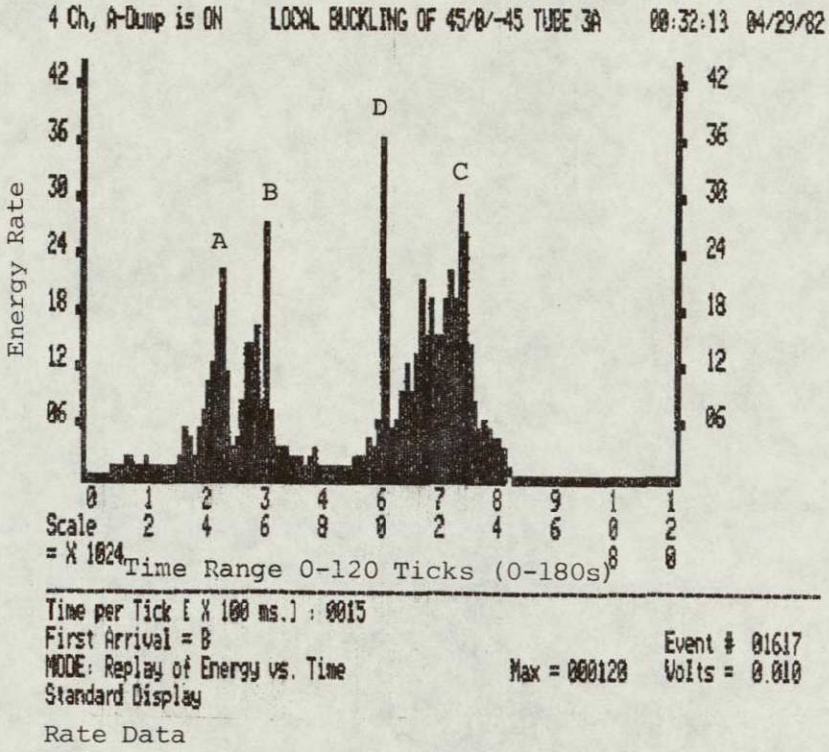

Figure IV-D-20. Energy Rate vs. Time of Local Buckling for Tube No. 3A

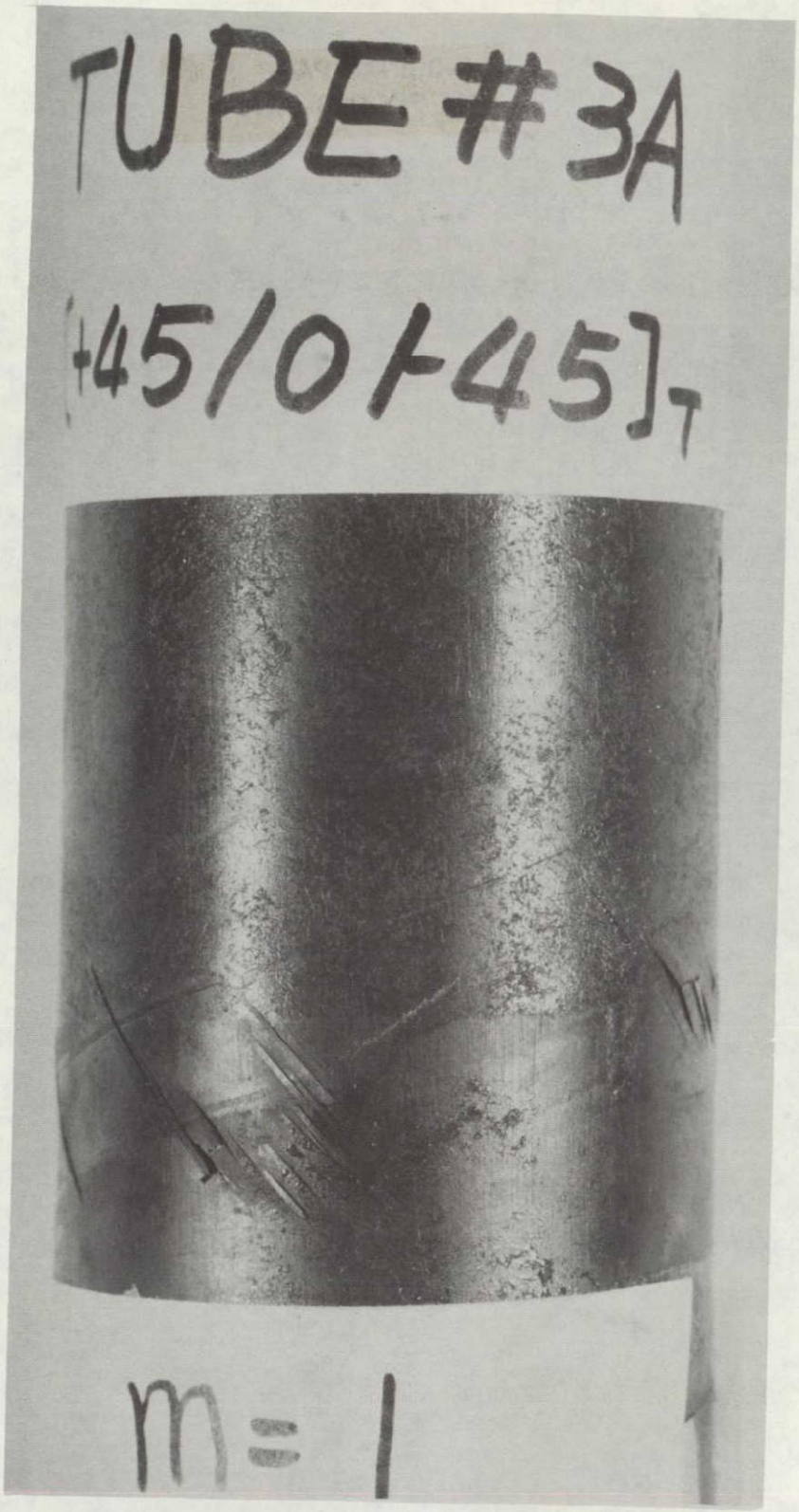

Figure IV-D-21. Posttest Photograph of Buckled Specimen 3A

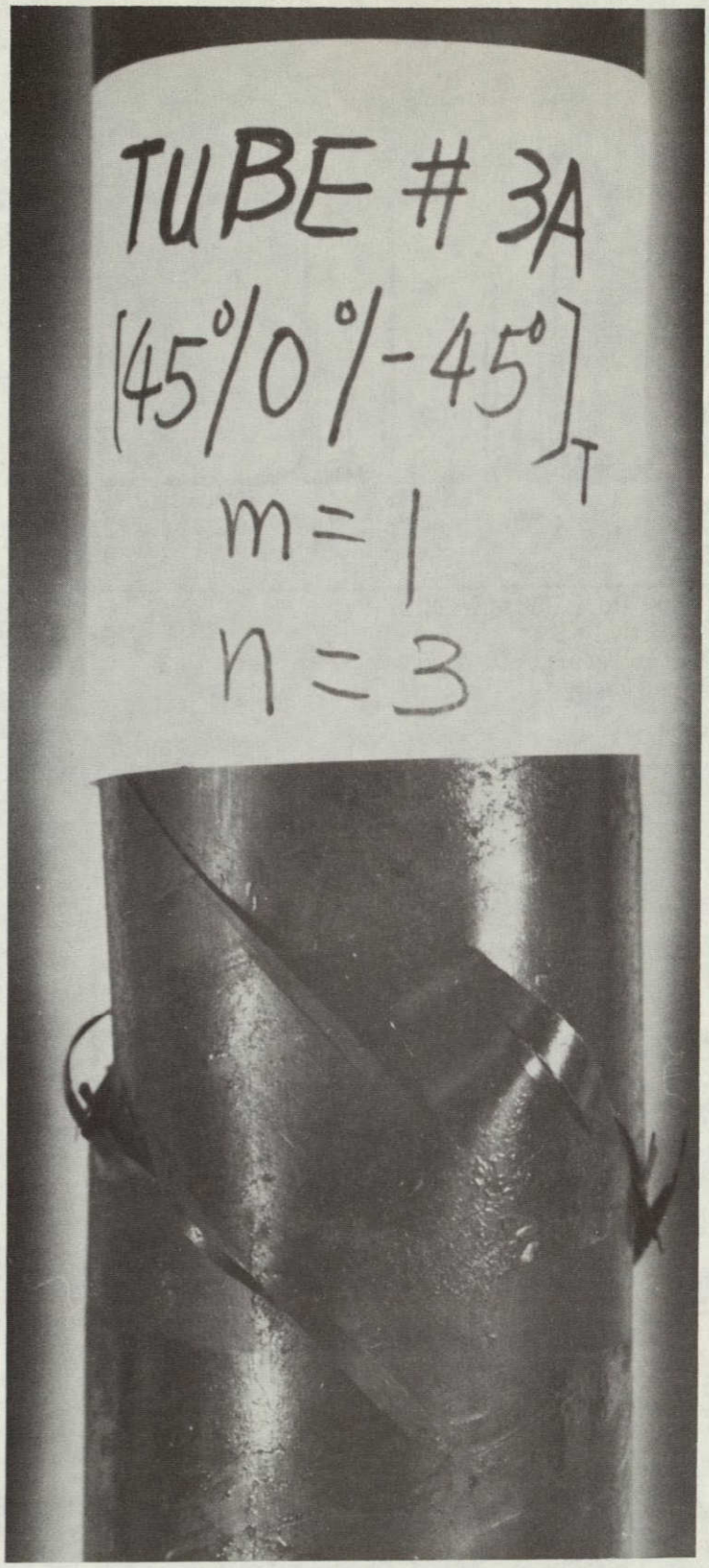

Figure IV-D-22. Additional Posttest Photograph of Buckled Specimen 3A Under Posttest Axial Preload Condition[7]

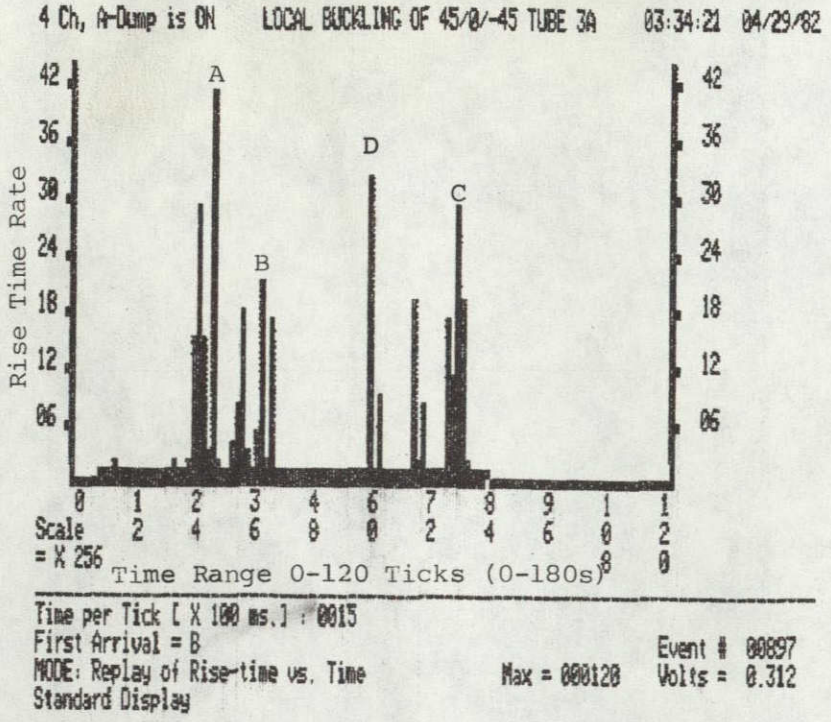

Figure IV-D-23. Rise Time Rate vs. Time of Local Buckling for Tube No. 3A

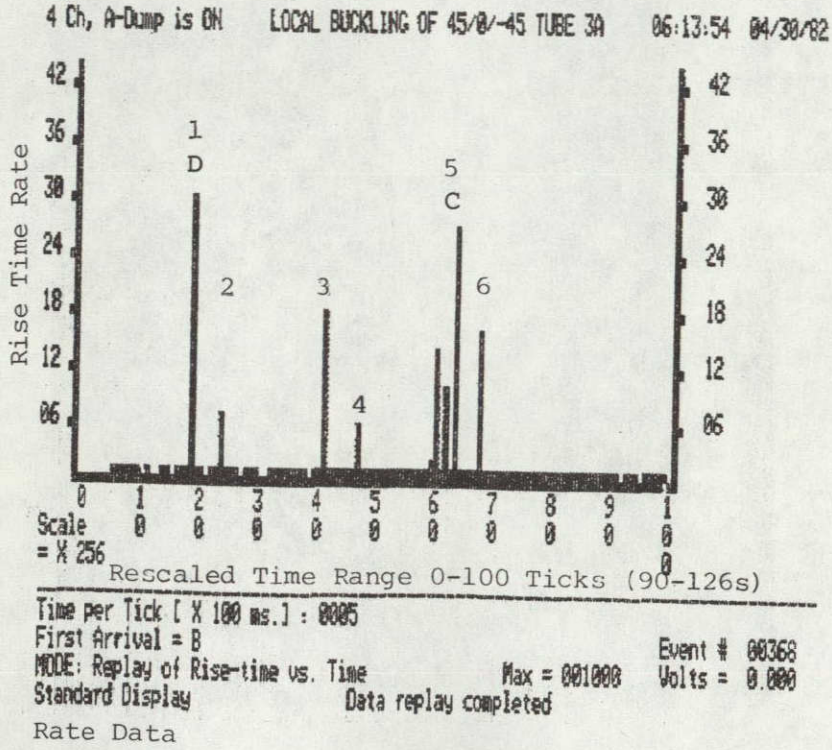

Figure IV-D-24. Rise Time Rate vs. Time of Local Buckling for Tube No. 3A (An amplified or rescaled time)

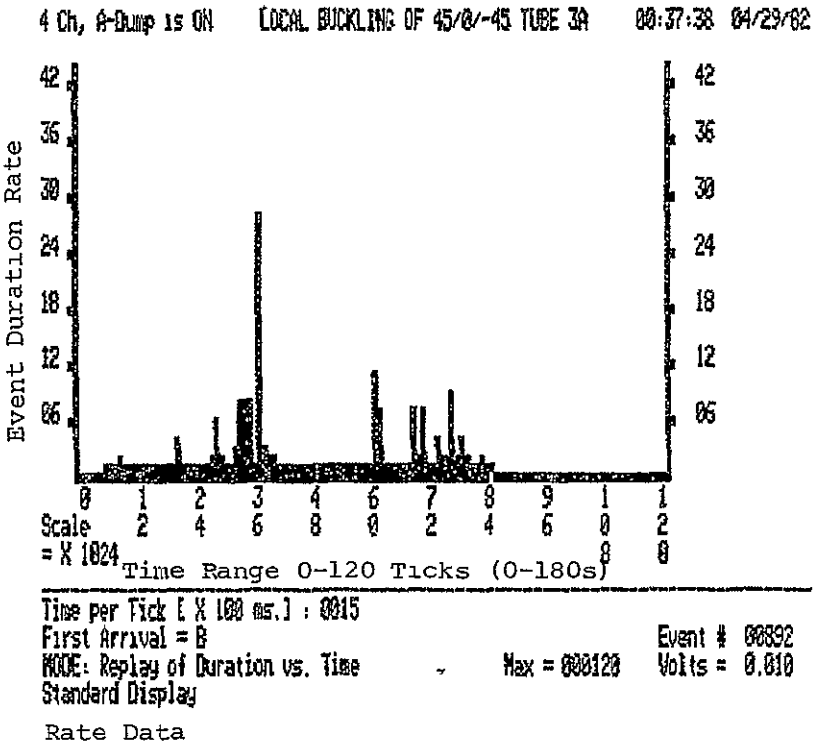

Figure IV-D-25. Duration Rate vs. Time of Local Buckling for Tube No. 3A

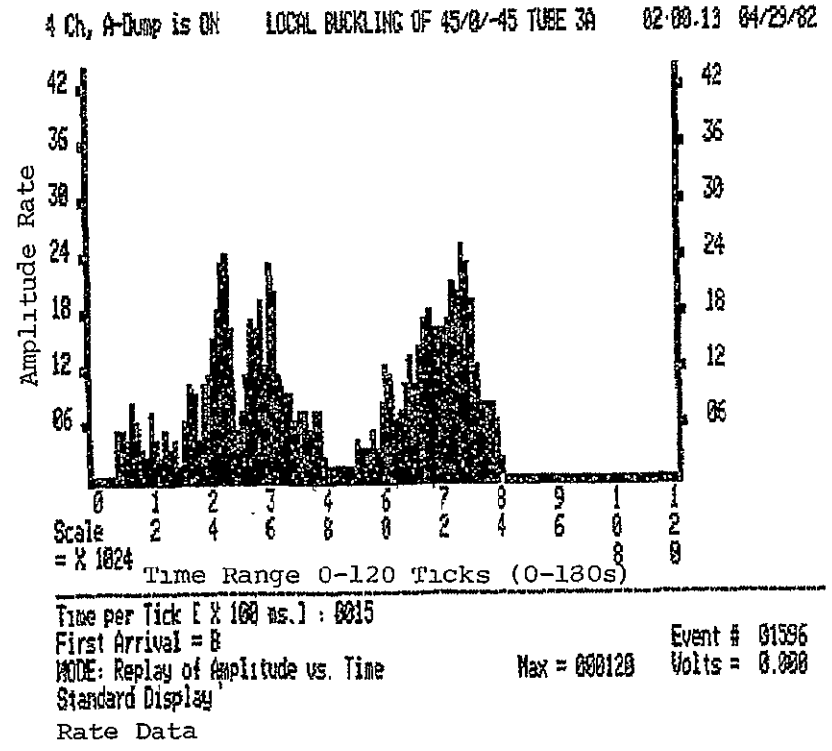

Figure IV-D-26. Amplitude Rate vs. Time of Local Buckling for Tube No. 3A

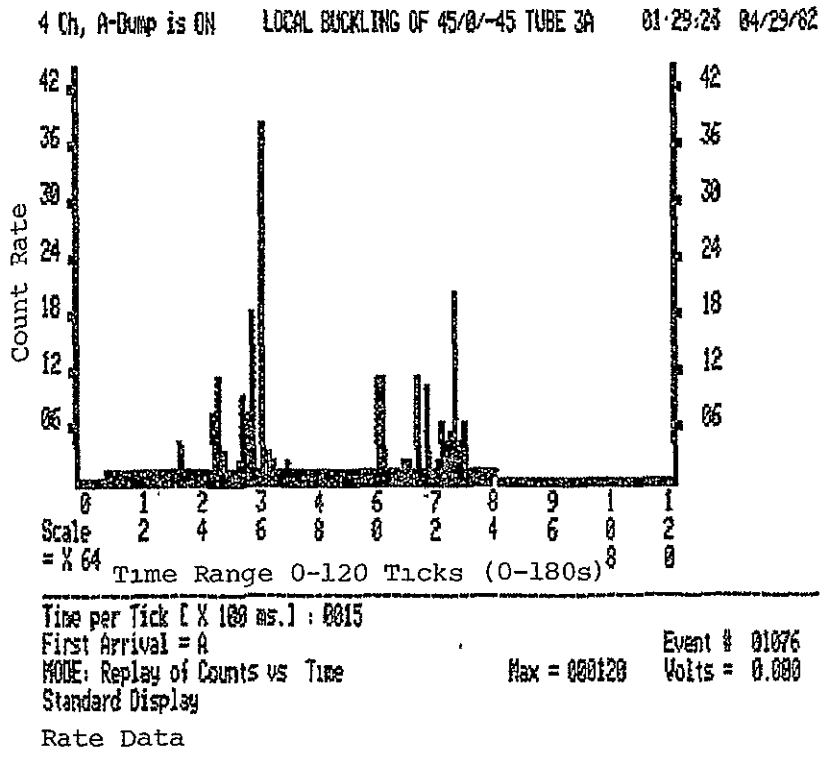

Figure IV-D-27. Count Rate vs. Time of Local Buckling for Tube No. 3A

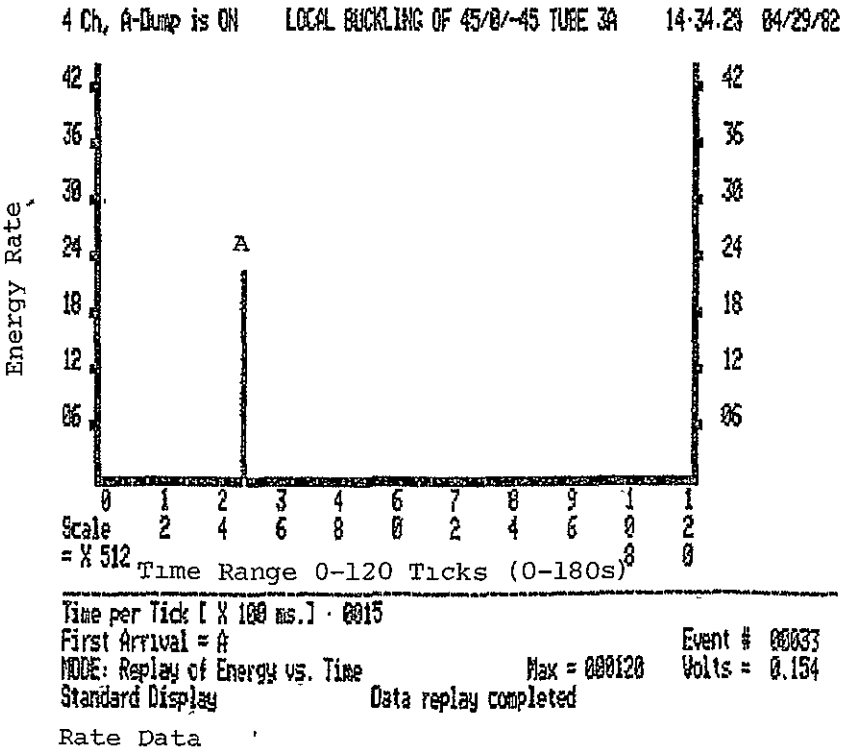

Figure IV-D-28. Energy Rate vs. Time of End Effect Only at Point A for Tube No. 3A

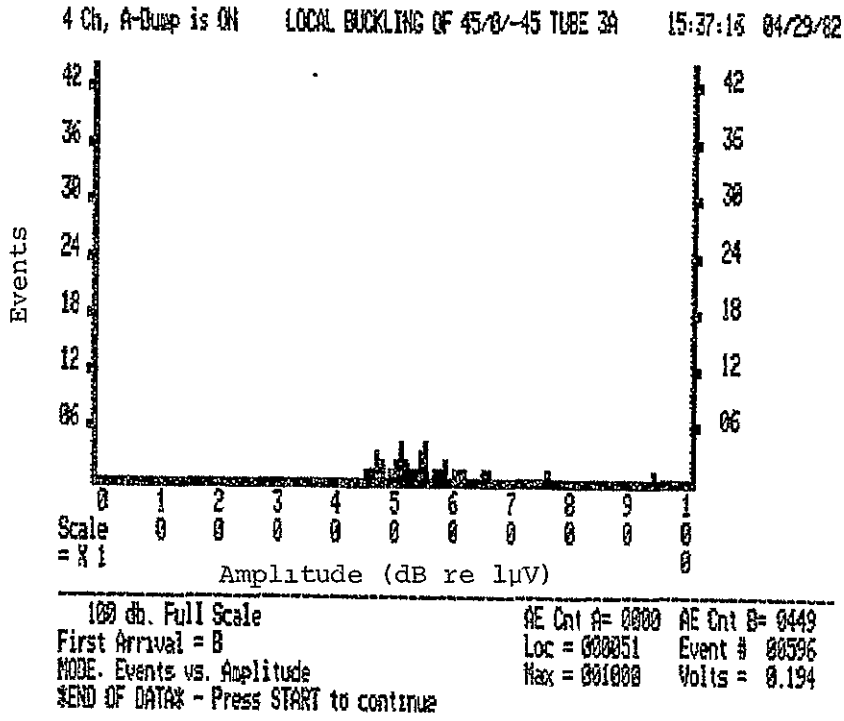

Figure IV-D-29. Amplitude Distribution of End Effect Only at Point A for Tube No. 3A

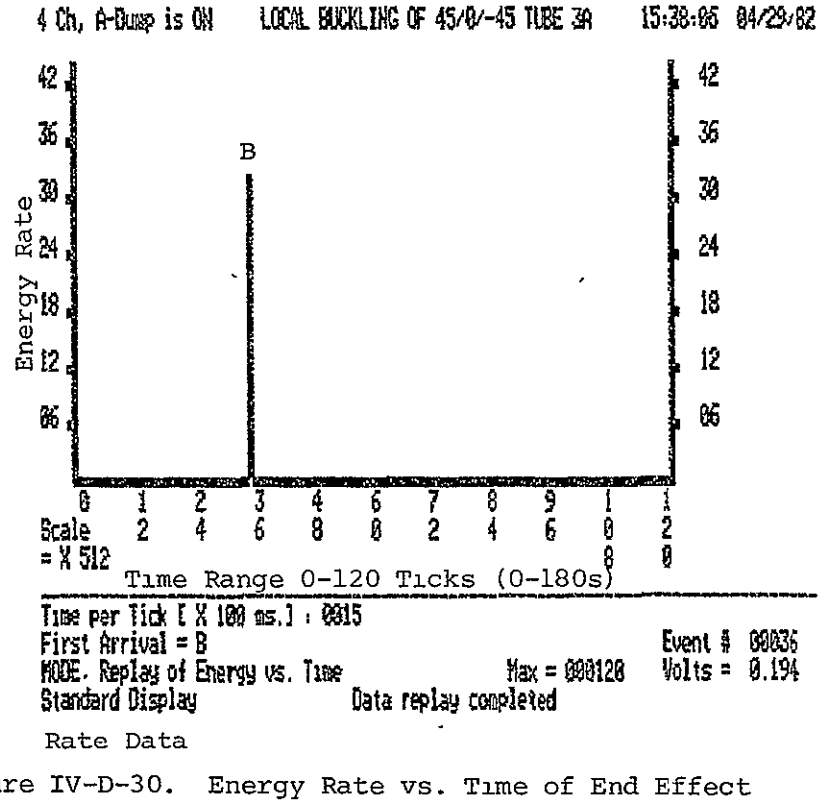

Figure IV-D-30. Energy Rate vs. Time of End Effect Only at Point B for Tube No. 3A

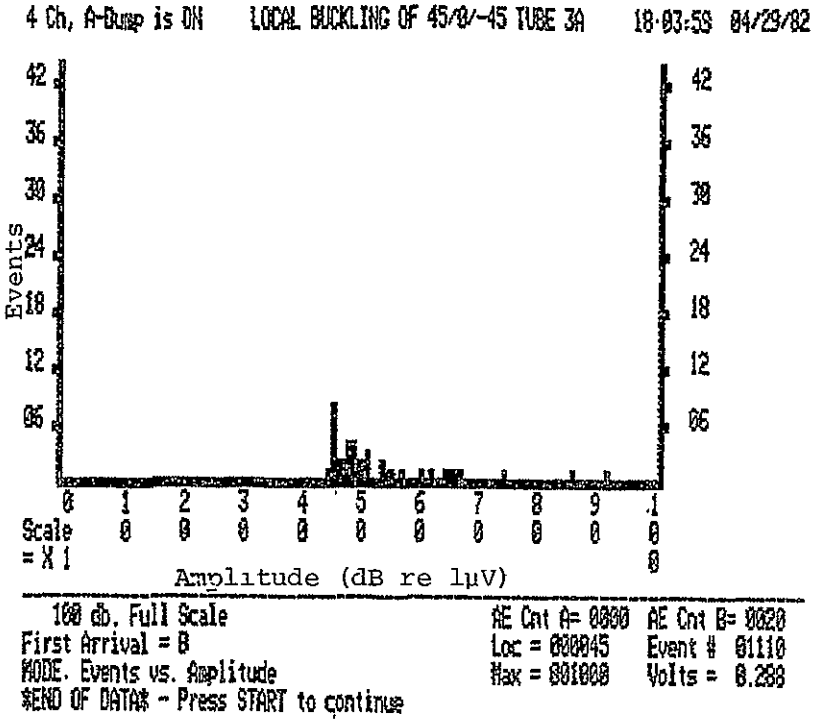

Figure IV-D-31. Amplitude Distribution of End Effect Only at Point B for Tube No. 3A

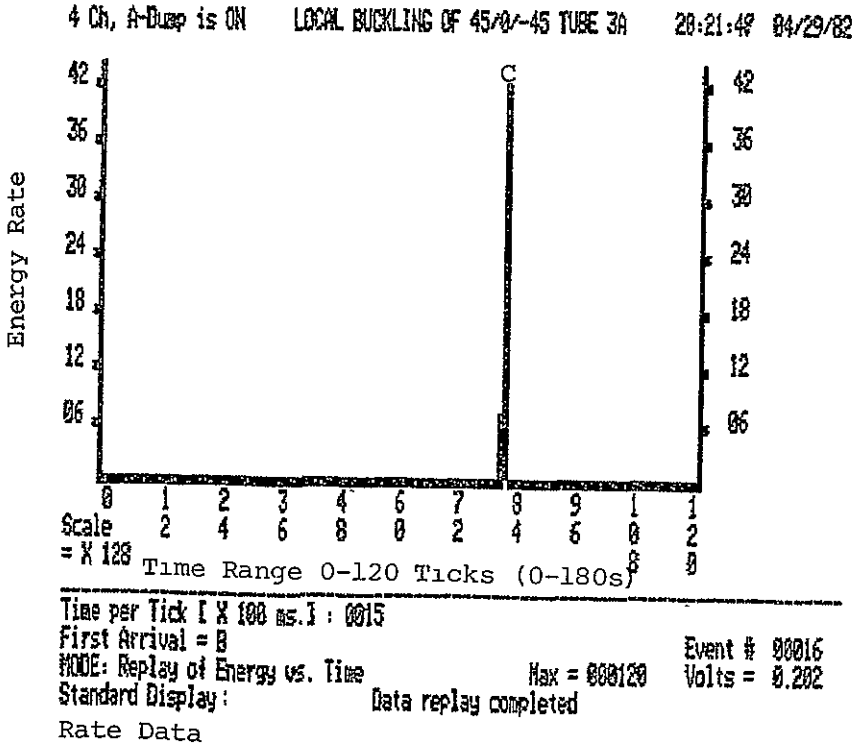

Figure IV-D-32. Energy Rate vs. Time of Local Buckling Only at Point C for Tube 3A

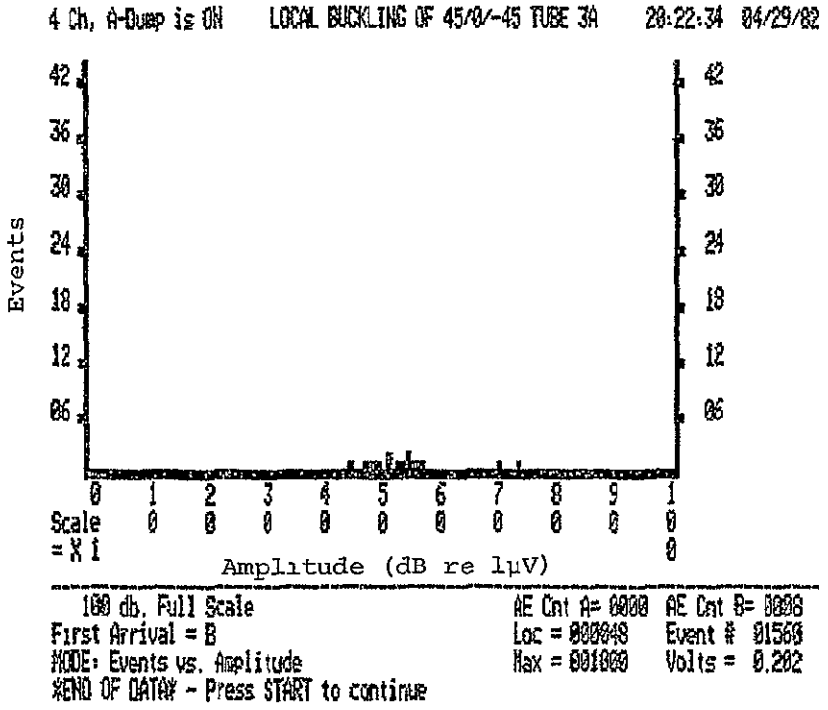

Figure IV-D-33. Amplitude Distribution of Local Buckling Only at End Point C for Tube No. 3A

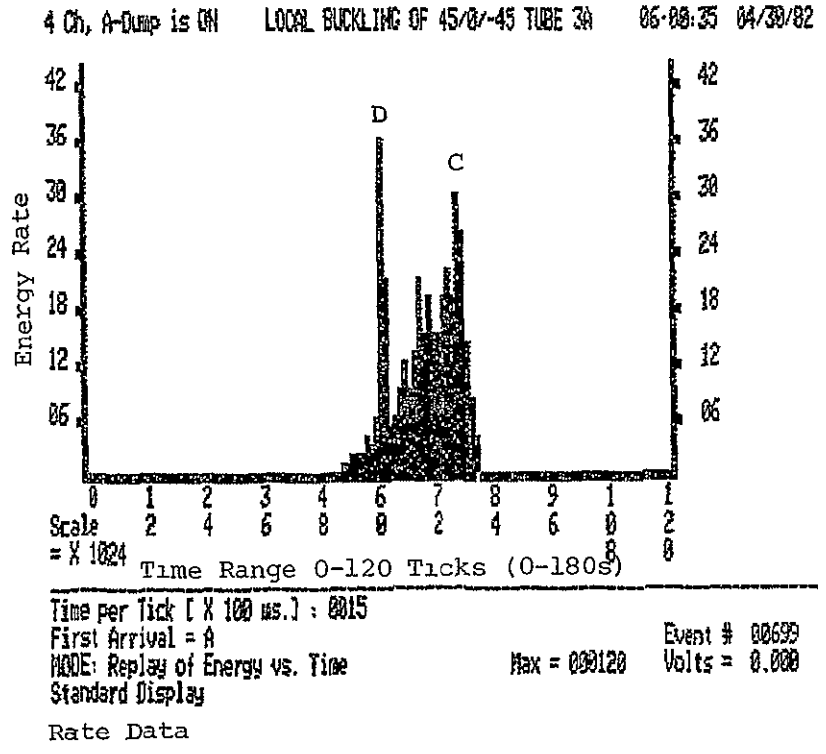

Figure IV-D-34. Energy Rate vs. Time for Only the Local Buckling Period for Tube No. 3A

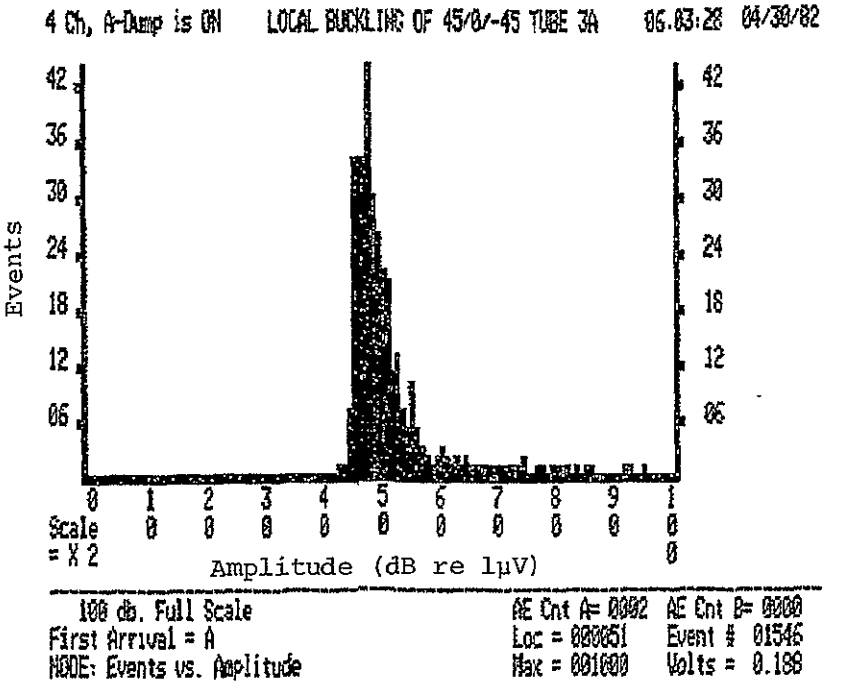

Figure IV-D-35. Amplitude Distribution for Only the Local Buckling Period for Tube No. 3A

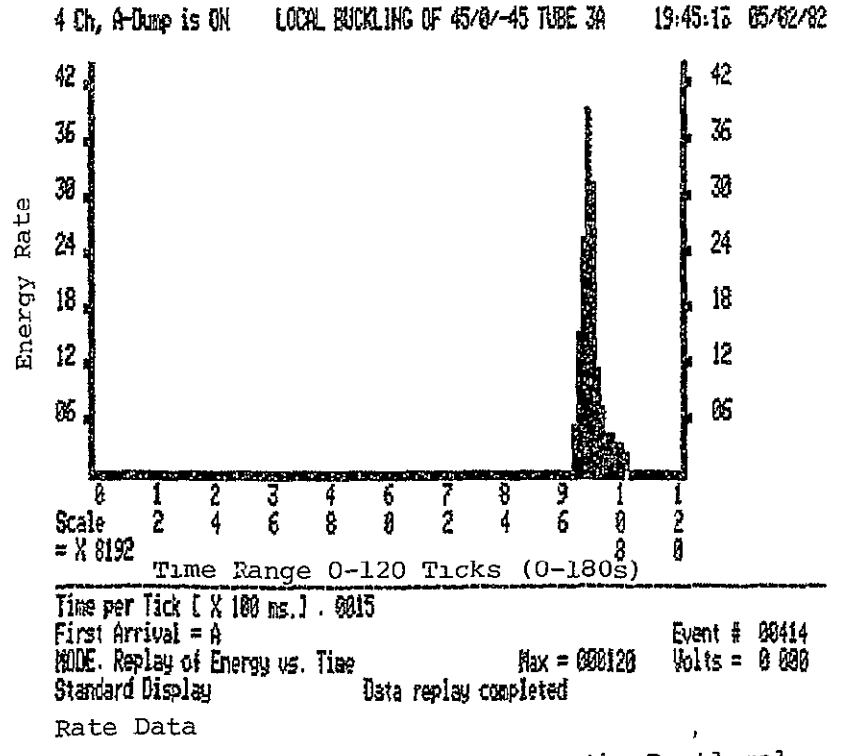

Figure IV-D-36. Energy Rate vs. Time in the Postlocal Buckling Period for Tube No. 3A

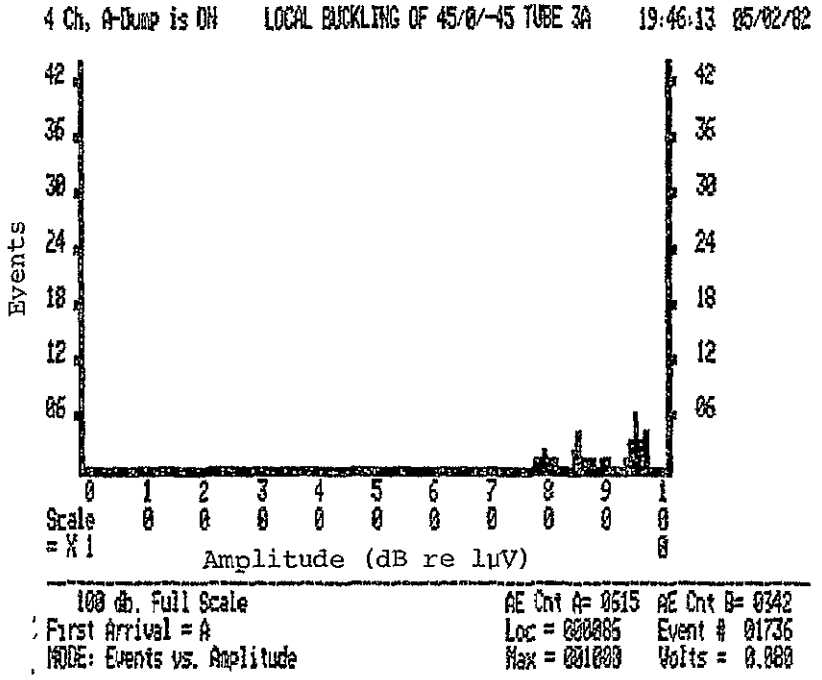

Figure IV-D-37. Amplitude Distribution in Early Portion of Postlocal Buckling Phase for Tube No. 3A

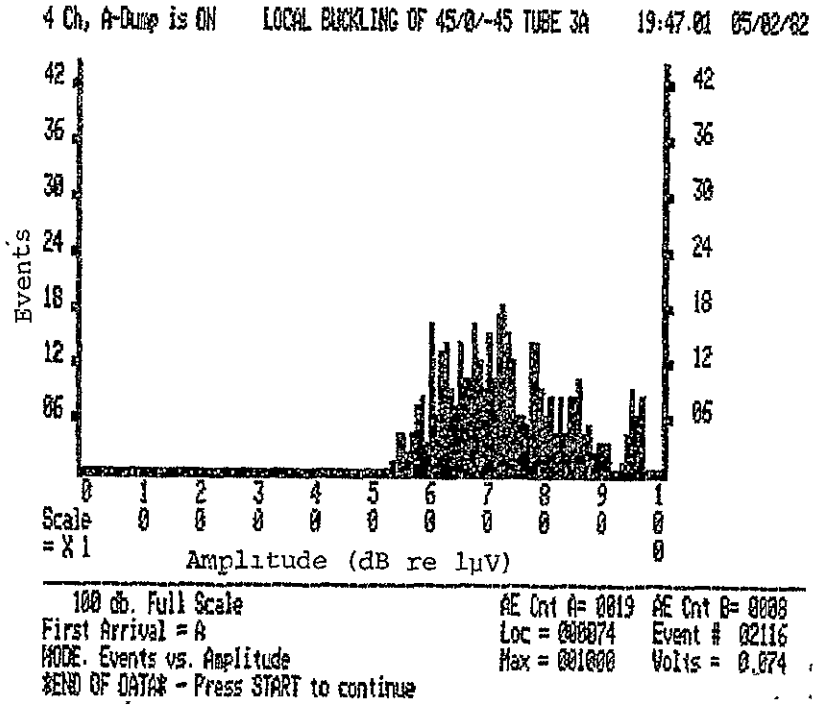

Figure IV-D-38. Amplitude Distribution for Total Period of Postlocal Buckling Phase for Tube No. 3A

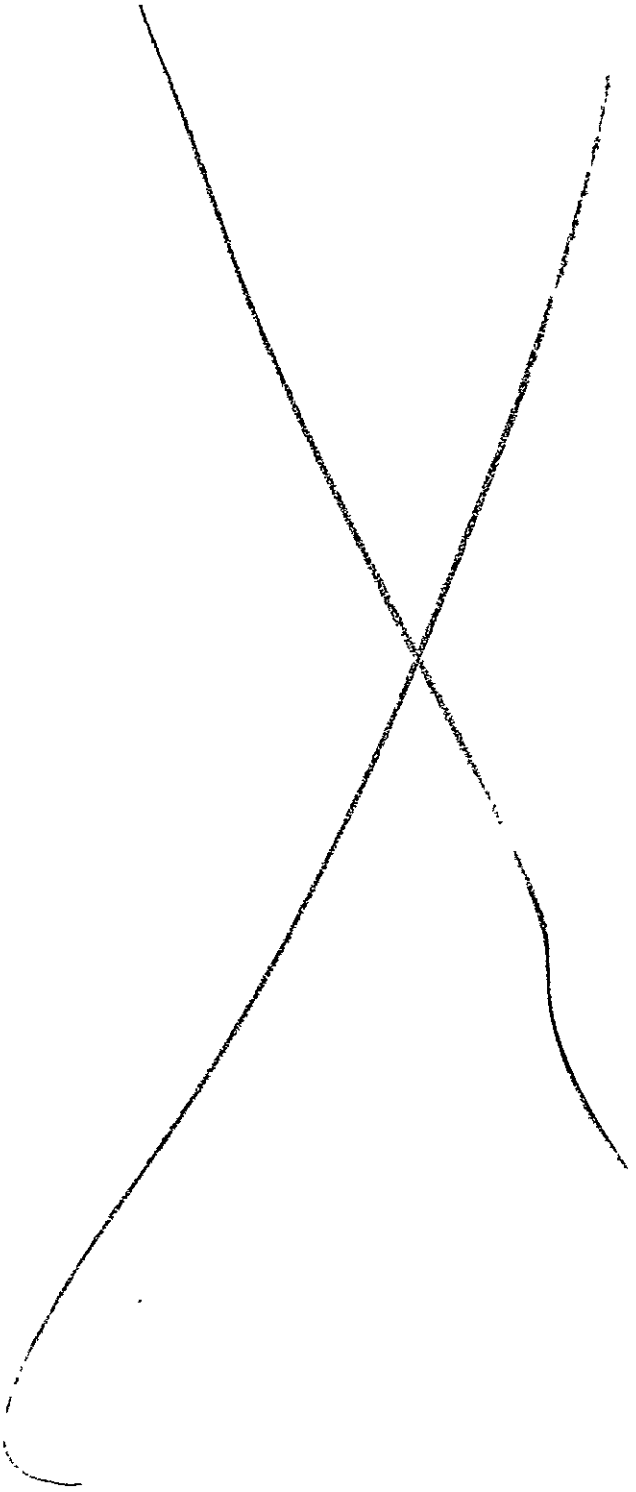

PART V
PROCESSING SCIENCE AND TECHNOLOGY

V-A INITIAL SAILPLANE PROJECT: RP-1

V-B SECOND SAILPLANE PROJECT: RP-2

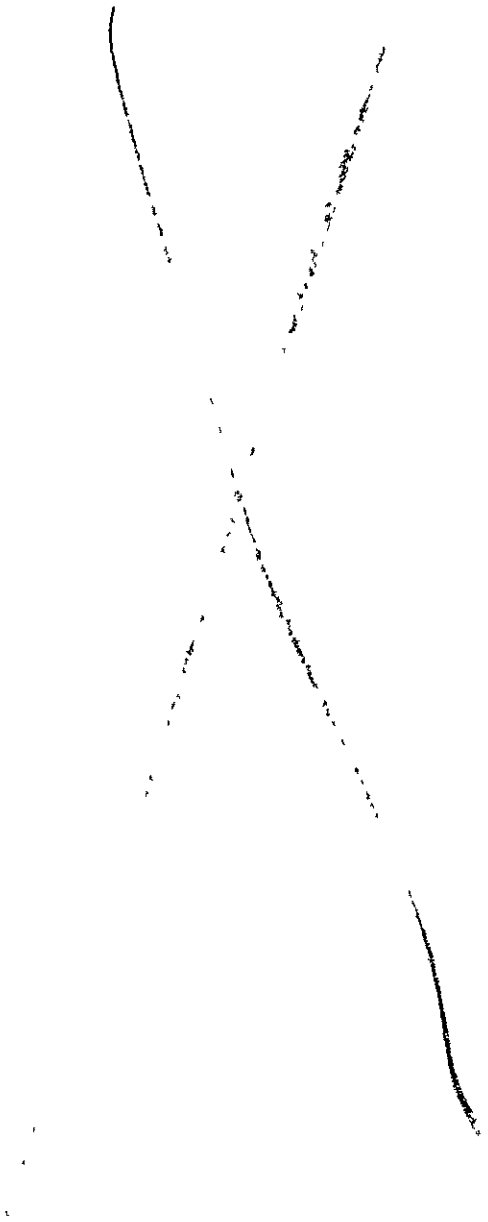

INTRODUCTION

The sailplane project involving design, fabrication and testing of advanced, full-scale, flight-worthy, all-composite aircraft was conceived as a highly productive way to conduct research on processing science and technology for low-cost aerospace structures. A series of innovative designs and processes has resulted from that research to date. It includes:

a) A simplified fabrication process without molds for accurate, smooth surface airfoils in wings and tail surfaces up to roughly twenty feet semispan,

b) Single sided, composite-foam "sandwich" structures which can be successfully joined to sub-structures to form ultralight-weight surfaces capable of carrying useful distributed loads,

c) Composite hinge configurations that are integrally bonded into airfoil contours to minimize peel-strength problems,

d) Proper mixtures of hardeners and experimental, especially low viscosity resins to achieve both minimum-depth bond and surfaces for ultralight - weight and acceptable strength, and

e) A technique for fabricating smooth-surfaced graphite/epoxy tubes of relatively small diameter, without the use of release agents or external molds, through the use of Teflon rods as mandrels.

The impetus toward innovation in processing science is being preserved in this project by undertaking continually more challenging structural functions in sailplane design. Further, research on problems within the disciplined context of actual manned flight testing is contributing to fundamental knowledge as regards monitoring and maintaining structural integrity of functioning, low-cost aerospace structures. These aspects are described in the following sections dealing with the first and second sailplane projects.

V-A INITIAL SAILPLANE PROJECT: THE RP-1

Senior Investigators: F. Bundy
R. J. Diefendorf
H. Hagerup

Flight tests through the summer of 1981 produced performance data for the 1981 configuration of the RP-1 showing best glide ratio equal to 11.3 and a minimum sink rate of 4.2 fps. This performance was sufficiently below design values that a drag clean-up program, involving light-weight secondary structure, was initiated. A two and one-half foot extension was added to the fuselage to improve airflow in the rear, between the two tail booms. The original design concept included a cockpit which was open below the pilot to permit operation in the foot-launch mode. This area has now been closed to insure that the induced drag of the wing corresponds to the full span, rather than half span. Fairings have also been provided around the supporting structure for the skid and around the wheel. We expect a twenty percent improvement in glide ratio to result from these modifications to the RP-1.

Before the RP-1 aircraft flies again, we are committed to performing the yearly proof-test to ensure that no structural degradation has occurred. This is anticipated to include both a repeat of past static tests and an additional test intended to investigate the failure condition on the RP-2 aircraft (see the following section, V-B) as it may

pertain to the RP-1. In addition, the first indication of possible strength degradation of typical structural elements used on the RP-1, and hidden from view, will be possible after the next reporting period. Five identical elements of this kind were tested in the Fall of '81, and five more will be tested prior to September 20, 1982.

Resumption of flight tests is scheduled for July, 1982.

V-B SECOND SAILPLANE PROJECT: THE RP-2

Senior Investigators: F. Bundy
R. J. Diefendorf
H. Hagerup
C. Muser

The completion of the structural framework of the fuselage and the finished empennage and wings of the RP-2 all-composite, high-performance, ultralight sailplane early last fall was followed by structural proof-tests of the wings and fuselage-wing connection. The fuselage was put upside down on an elevated platform. Once the wings were assembled on the fuselage, sandbags were used to load the structure. Deflections were measured at several stations along the wings. Preliminary loadings revealed the need for another transverse compression member in the fuselage framework at the forward part of the wing root rib. After this was installed, the structure was tested for the highest vertical bending to be encountered within the flight envelope. At that point, the maximum positive design load factor was 5.9. The sailplane successfully withstood this test without incident.

One week later the plane was tested for vertical bending and torsion combined. The magnitude of the load was the same as in the previous test, corresponding to the maximum design load point on the flight envelope, but the loading line was closer to the trailing edge to induce torsion. In this combined bending and torsion test, the center box of the wing connection failed catastrophically at 98 percent of design

load, causing serious damage to the wing connection itself, and also serious secondary damage to the outboard one-third of the wings, which were inadequately supported when the wing carry-through structure failed.

Immediately after this sobering test, a small task force was formed to investigate the possible sources for the unexpected failure of the structure. The failure was obviously not due to straightforward causes. The carry-through structure and associated fuselage design was devised so that the former would carry only bending in the vertical plane. The bending test was completed successfully, yet that same structure failed during a new test condition in which torsion was added. The task force consisted of three students; Keith Applewhite, Andrew Bertolazzi and Thomas de Mint. They were supervised and guided by Postdoctoral Associate Christoph Muser. The results of this investigatory group's efforts were summarized in a report submitted along with notes of all the calculations necessary to determine the cause of the structural failure.

The conclusion reached by the task force was that the cause of failure was the combined action of three separate loadings: vertical bending, torsion and horizontal bending. Horizontal bending moments were induced by a nose-down attitude of the sailplane on its platform. The severe implications of these combined loadings was not recognized earlier, because the load paths in the wing carry-through structure

were obscured by deflections whose magnitude had been underestimated. In other words, a load applied on the wings -- despite the intention of the designers to the contrary -- could take different paths through the fuselage depending on deformations and on how "tight" various fittings had been made.

Work in the fabrication laboratory pertaining to the RP-2 during the remainder of the present reporting period has been mainly concerned with (1) development of structural repair techniques, (2) wing connection failure analysis and redesign and (3) reconstruction of the damaged parts of the RP-2.

After evaluating all the damage done to the aircraft, it was decided to use all salvagable parts and to just replace the broken sections, rather than to rebuild a completely new set of wings. This had two advantages. First, costs could be kept at a minimum, and second, and perhaps most important, there would be the new challenge of repairing the primary structure of a light-weight composite wing.

The major areas which needed close attention could be singled out. The first one was the approach to splicing the capstrips of the I-beams used to carry vertical bending moments, on the one hand, and splicing the wing skins which carry horizontal bending and torsion, on the other hand. The second area was the wing-fuselage connection and carry-through structure which had to be redesigned to eliminate the design

faults revealed in the test-to-failure, within the limits imposed by the desire to salvage parts.

The capstrips of the I-beam are made of unidirectional graphite prepreg and are tapered towards the wingtip. At the splice locations, the capstrips are eight layers thick (0.04 in.), and the taper of the salvaged part of the capstrip restricted the allowable length of the splices to 40 cm (see Figure V-B-1). After studying the literature (see References on page 263), it was decided that the inboard and the newly built outboard section of the capstrips should have blunt ends which butt up against each other. On the top and bottom sides of the capstrips positioned in this way, reinforcements of the same material and with the same thickness as at the centerline of the capstrips should be used. The total length, the step-lengths and the manufacturing methods were arrived at in tests guided by approximate calculations. About twenty splice specimens were subjected to simple tension tests. Some specimens had reinforcements only 12 cm long, and some had nonuniform step-lengths. Some had step-ends which were arrowhead shaped in planform, others were straight and normal to the capstrip C_{L}. The splice designs selected for the extensive tests required by use in a flight vehicle had reinforcements 32 cm long, with straight ends, and a constant step-length of 4 cm. These specimens withstood a tensile load five times greater than the sparcap load present at the splice location under a design load factor of 5.9 g. It is important

Legend: 1 - Salvaged part of capstrip
2 - Reinforcements
3 - Rebuilt part of capstrip
4 - Room temperature cured glue line
(also untapered length of spar cap)

All material: unidirectional graphite prepreg.

(Drawing not in proportion)

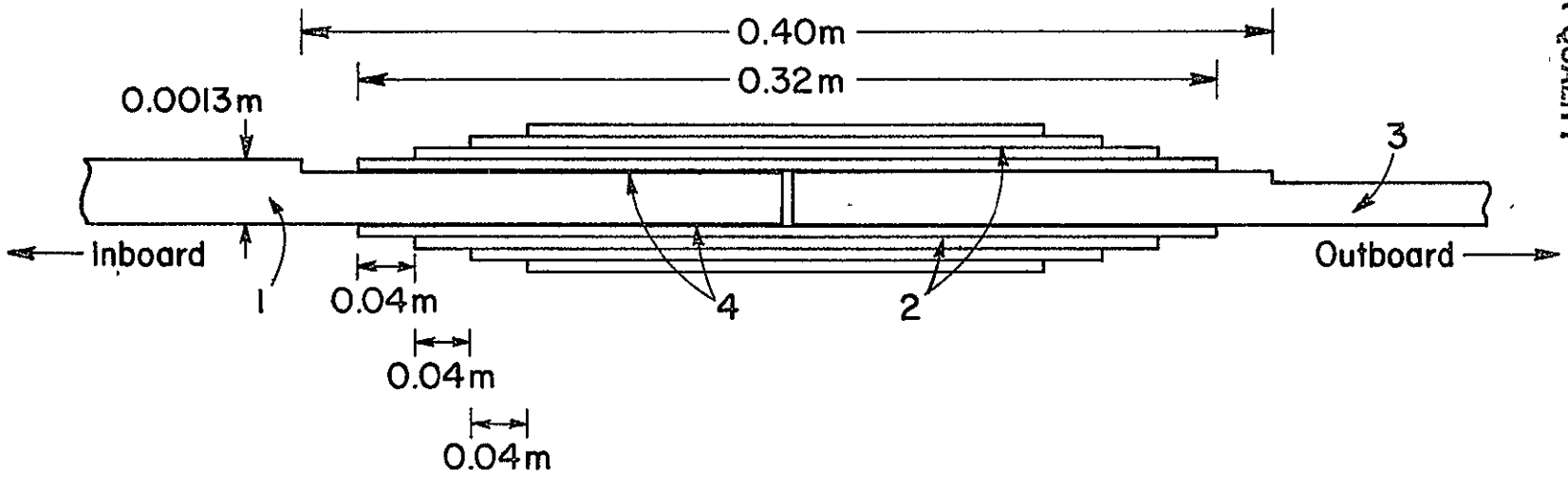

Figure V-B-1. Schematic of Spar Capstrip Splice

to recall that the governing design criteria for the wings is stiffness and not strength. In this regard, the spliced spar will actually be stiffer than the original.

An I-beam section of about 3 m length was built with spliced upper and lower capstrips. That beam was subjected to three times the bending moment experienced by the wings at 5.9 g, and no failure occurred. At this point, we are confident enough to plan to use this splicing technique -- which joins pressure vessel-cured parts together with a room-temperature-cured bond -- for the repair of the wings.

The failed carry-through structure design had several shortcomings. In principle, the two I-beams of the two wings were connected by means of a tight-fit sleeve. That is, one I-beam slid into a box-end built into the other I-beam (see Figure V-B-2). These two beams were prevented from disengaging, as a result of spanwise motion, by a safety pin. Short vertical shear pins or "studs", mounted in the root ribs, transferred both lift forces and torsion into the torque box of the fuselage. Horizontal bending moments caused by the components of lift and drag in the plane of the wing chord, were to be taken through these same pins, into the fuselage sides, and resisted in compression by the fuselage torque box at the aft set and by a compression strut between the front two torsion pins. Whether this horizontal moment was caused by forward or aft acting loads, the safety pin holding the wings together would always provide the tensile

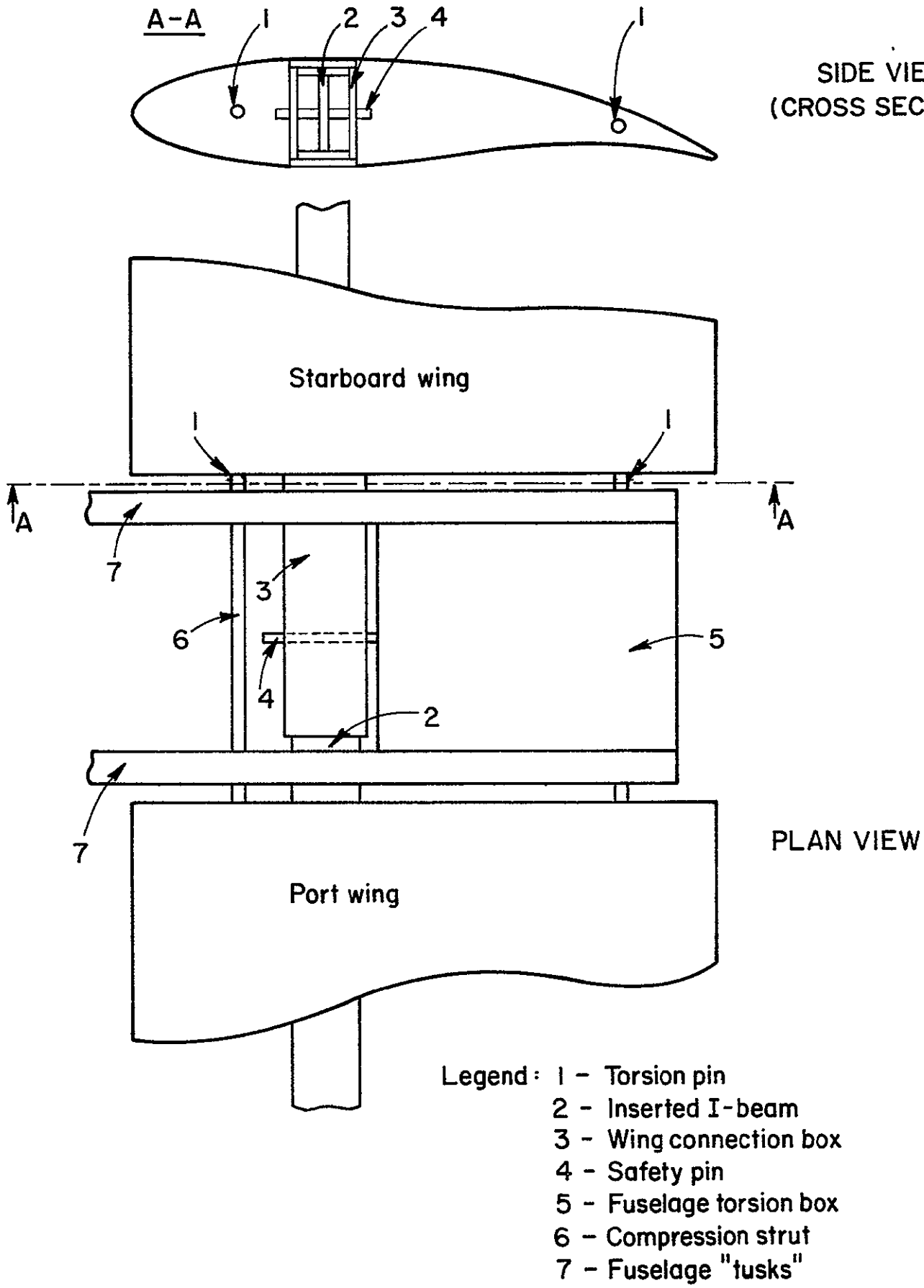

Figure V-B-2. Previous Design of Wing Carry-Through Structure

reaction. However, the elasticity of the fuselage and the safety pin made it possible for part of that horizontal moment to be transferred through the wing vertical bending carry-through structure's connection box. This additional stress concentration was most dangerous at point A of the open end of the box (see Figure V-B-3).

The redesign of the carry-through structure, conducted in this report period, took into account the fact that the capstrip sections to be used for the wing connection were of a given length and width and had only unidirectional fibers. There were similar salvage restrictions associated with the side of the fuselage and the positions of the torsion pins. The new wing connection design (Figure V-B-4) uses two steel bolts to transmit the vertical bending moment, which is the principal loading. These bolts connect the webs of the box of the one I-beam to the web of the other I-beam. This wing connection, however, is also designed to withstand the tension loads experienced from the horizontal moment. The same loads, but in compression, have to be taken by the compression strut between the front torsion pins. A careful redesign of that particular load path has been made. There is no longer any direct contact between the box at the end of one I-beam and the other I-beam. It is intended that the clearance at all points other than the two-bolt attachment will be sufficient that no unwanted loads will be carried by the spar connections, even in the presence of elastic deflections.

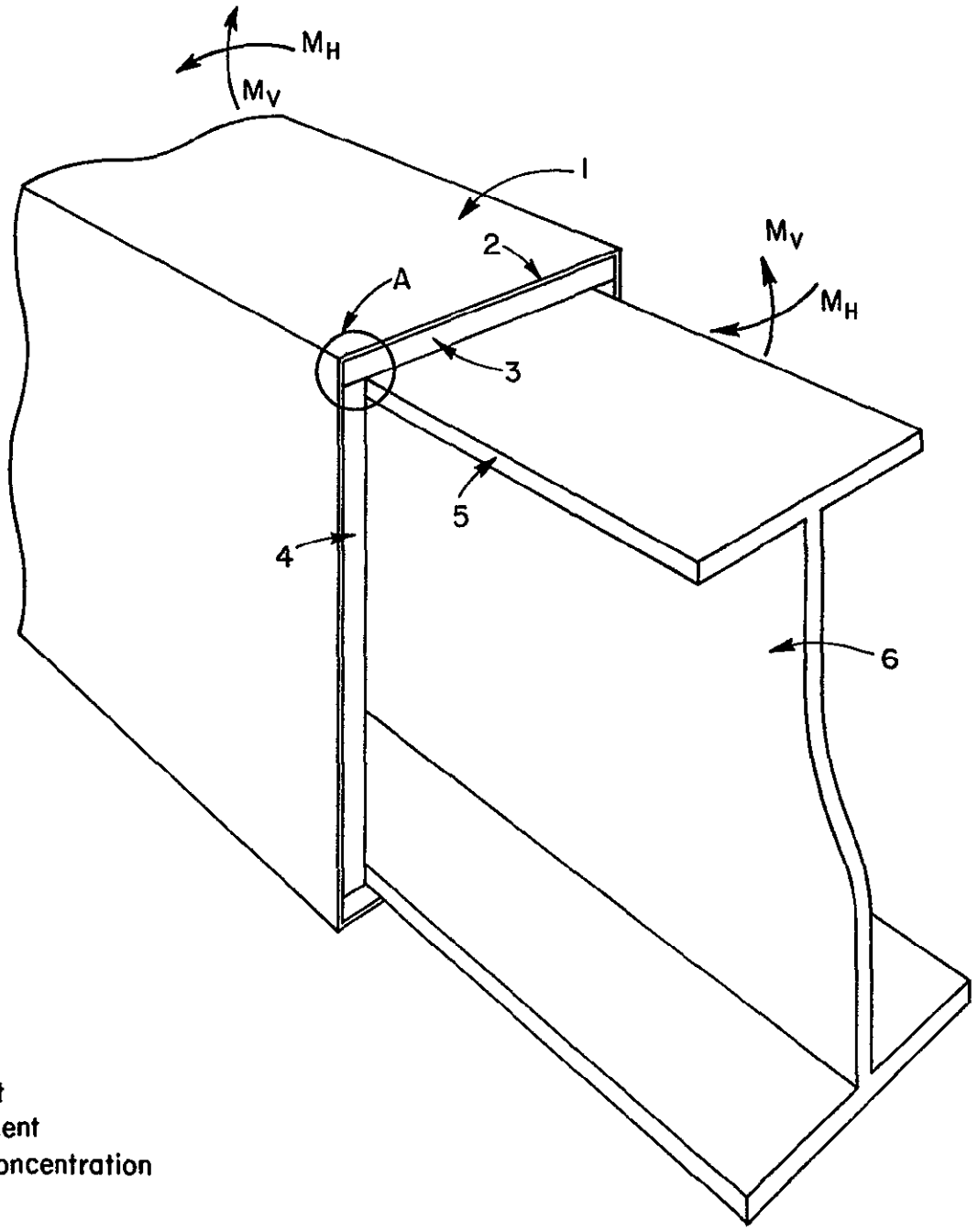

Legend: 1 – Wing connection box
2 – Graphite cloth wrap
3 – Capstrip of box
4 – Web of box
5 – Capstrip of I-beam
6 – Web of I-beam
M_V - Vertical bending moment
M_H - Horizontal bending moment
A – Point of highest stress concentration

Figure V-B-3. Wing Carry-Through Structure

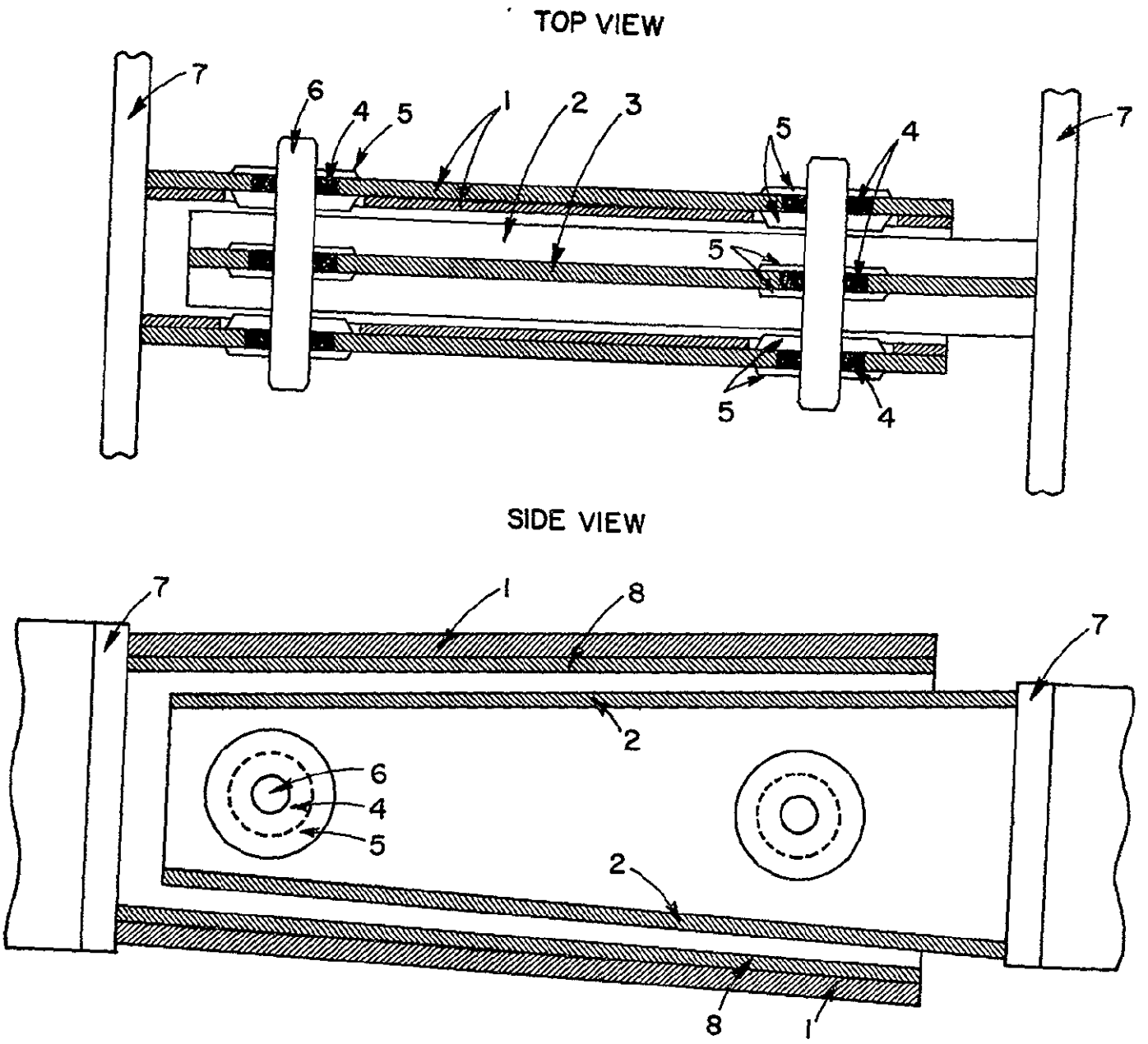

Legend: 1 – Web of wing connection box - G_r/E (prepreg. unidirectional tape)
2 – Capstrip of I-beam - G_r/E (prepreg. unidirectional tape)
3 – Web of I-beam
4 – Steel bushings
5 – Steel washers
6 – Steel pins
7 – Root ribs - G_r/E (fabric)
8 – Capstrip of wing connection box - G_r/E (prepreg. unidirectional tape)

Figure V-B-4. Modified Design of Wing Carry-Through Structure

Flat tensile specimens were tested to determine the number of layers required by the spar webs to transmit the loads transmitted to them by the bolts. These tests demonstrated that it is possible to transmit loads three times greater than the loads experience at 5.9 g and that failures, when they do occur, are in bearing. Steel bushings are used to prevent damage during assembly and disassembly. Steel washers are mounted on either side of the webs (not used for the tensile specimens) as an additional protective measure.

Presently, the two principal activities are repair of the wings and fabrication of the test spar for the new wing connection. The status of reconstruction is that the damaged outboard portions of the wings have been removed; the necessary replacement capstrips, shearwebs, stringers, ribs and panels have been fabricated; and assembly has begun. Local damage in one wing root, where the mainspar capstrips separated from the web for a distance of one and one-half inches into the left wing, has been excised and repaired, and a new root rib is being installed. Redesign of the center box of the wing connection also necessitated minor modification in the fuselage framework, which is in progress. Work is continuing, meanwhile, on the aerodynamic fairing of the fuselage framework and wing intersection, using RPI's graphics computer-aided-design capability.

We plan to have the assembled RP-2 aircraft retested in October, 1982. After that, the final assembly of the fuselage

can be carried out and the cockpit enclosure built.

In summary, a failure during structural proof-test has cost the RP-2 project six to eight months of time. An important and positive outcome, however, is that after successful flight operations with the RP-1 for two summers without significant structural damage, we have been required through this temporary setback on the RP-2 to concentrate on the important area of advanced composites structural repairs. The first flight of the RP-2 is anticipated now for the Summer of '83.

1. References

1. Goland, M. and E. Reissner, "The Stresses in Cemented Joints", Journal of Applied Mechanics, March 1944, A-17 to A-27.

2. Berg, K. R., "Problems in the Design of Joints and Attachments", Proc. 5th Symposium Naval Structural Mechanics 1967, Mechanics of Composite Materials, F. W. Wendt, H. Liebowitz and N. Perone, eds., Pergamon NY, 1970, 467-479.

3. Berg, K. R., "Analysis of Axial Stresses in a Multi-Ply Laminate Loaded in Shear on the Outer Ply", Whittaker Corporation, Narmco Research and Development Division, Technical note 67-TN-61, April 1967.

4. "Advanced Composites Design Guide", Advanced Development Division, Air Force Materials Laboratory, 3rd Edition, January 1973.

PART VI
COMPUTER SOFTWARE DEVELOPMENTS

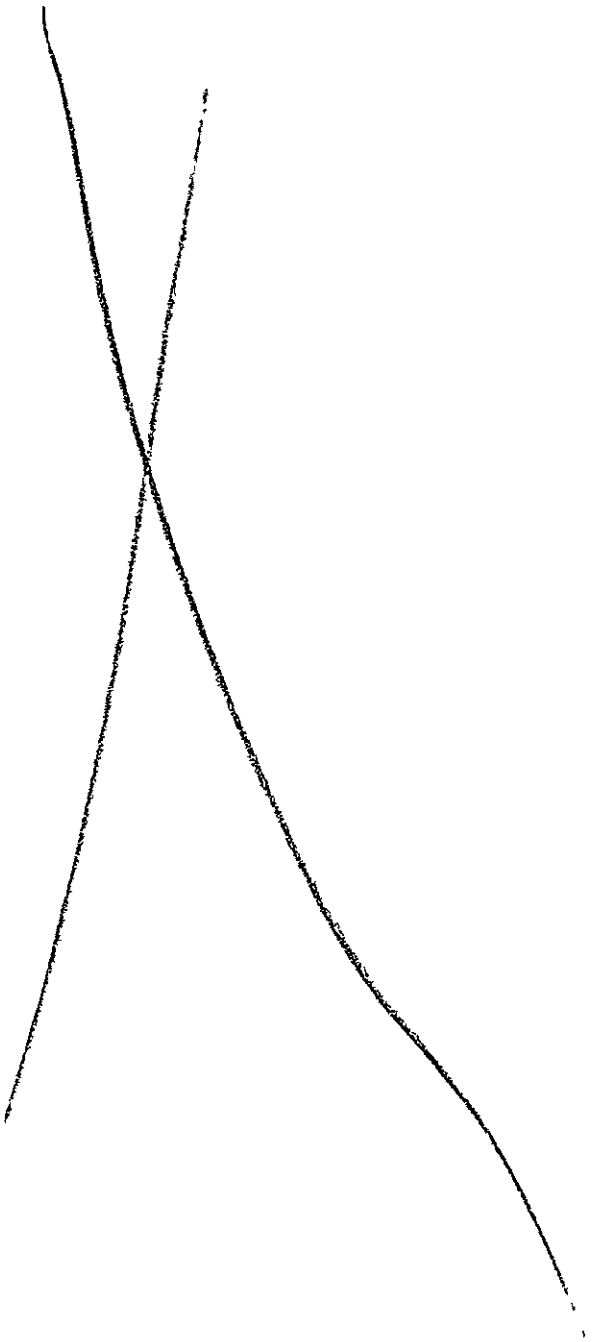

VI COMPUTER SOFTWARE DEVELOPMENTS

Senior Investigator: M. S. Shephard

1. Introduction

The objective of this portion of the project is to provide advanced and specialized computer "tools" for the analysis and design of composite structural elements and the study of structures-related phenomena in composite materials. The major thrust to date has been and will continue to be in the finite element area, with effort directed at implementing finite element analysis capabilities and developing interactive graphic preprocessing and postprocessing capabilities.

2. Status

The results achieved in this area of research during recent reporting periods have been used for the numerical analysis of moisture effects and the numerical investigation of the micromechanics of composite fracture discussed in Parts III-D and -E of this report. In addition, the POFES* system, which is available to the composites program, continues to be developed through student class projects and projects supported by the Graphics Center's Industrial Associates Group.

3. Progress During Report Period

Class projects with potential usefulness for the composites program include both specific analysis studies and

*POFES (People Oriented Finite Element Software) is RPI's finite element software system.

improvements to our general in-house analysis capabilities. Class composite analysis studies included:

1. "A Finite Element Analysis of a Graphite/Epoxy Aircraft Engine Drag Strut Lug", R. E. Walters.
2. "Composite Ring Stress Analysis", R. K. Phelan.
3. "The Natural Frequency and Mode Shape Investigation of an Octagonal, Orthotropic Sandwich Plate with the Finite Element Model Analysis", R. A. Valicenti.
4. "Finite Element Analysis of L-1011 Engine Drag Strut", F. Ogunlau.

Class Improvements to our general in-house analysis capabilities include:

1. an eigenvalue and eigen vector solution algorithm for natural frequency and mode shapes. This algorithm is based on the subspace iteration method[1]*.
2. a new triangular plate bending element based on discrete Kirhoff assumptions[2,3]. This element should prove very efficient for the analysis of composite plates and shells.

Although these class projects are limited in scope, they do serve to give the students involved additional insight into the numerical analysis of composites, they provide additional input into other portions of the project and/or they help improve our in-house facilities for the analysis of composite materials and structures.

---

*Numbers in brackets in this section refer to the references which are listed on page 277.

Projects of interest to the composites program supported out of the graphics center or elsewhere are discussed in the following subsections.

a. Three-Dimensional Preprocessor, Based on Extrusion Capabilities

The extrusion preprocessor allows for the definition and meshing of three-dimensional objects by first defining components with planar faces that are then extruded in the third dimension and patched to other, similarly-defined components. At this time only linear extrusion capabilities and some initial mesh generation capabilities have been implemented. The process of defining and meshing an object begins by establishing a three-dimensional planning grid (Figure VI-1) that delimits the object space. This grid is also used to help maintain numerical accuracy during curve definition. Next, the user defines planar faces and extrudes them to form components (Figure VI-2). Various extruded components are then interactively patched together (Figure VI-3) and passed on to the mesh generator where three-dimensional mesh patches are interactively created (Figure VI-4).

b. Shell Surface Program Redesign to Include Improved Modeling Capabilities

The shell preprocessor is being redesigned to allow for the improved representation of a wider class of surfaces and to improve the user interface. The basic curve type has been

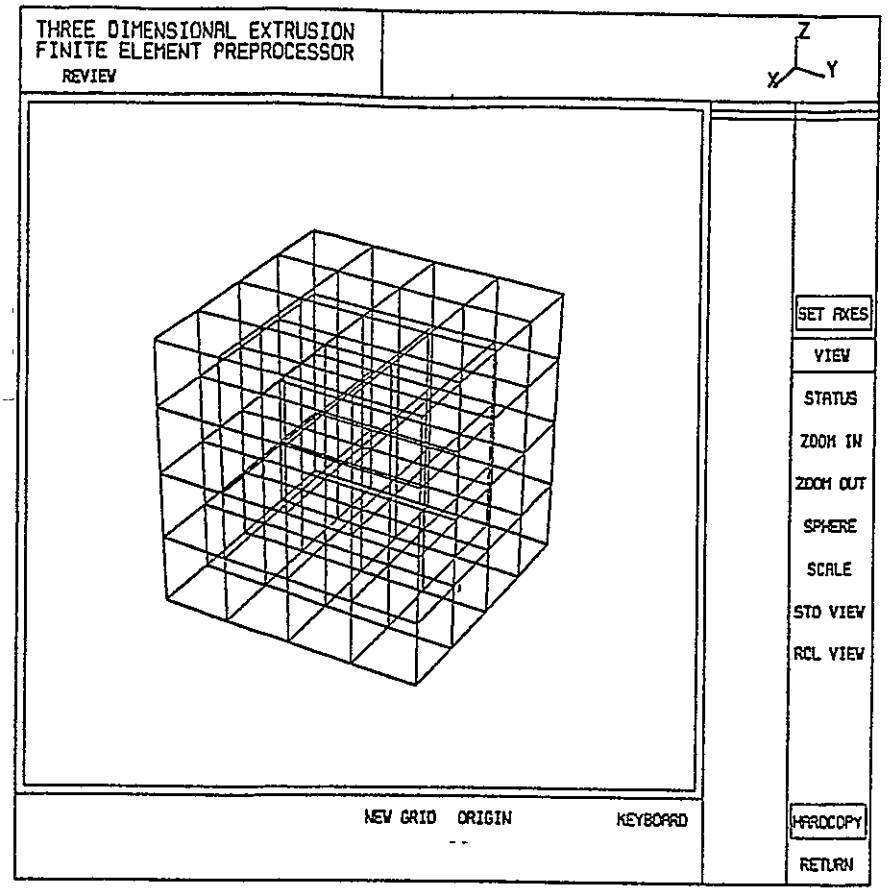

Figure VI-1. Three-Dimensional Planning Grid

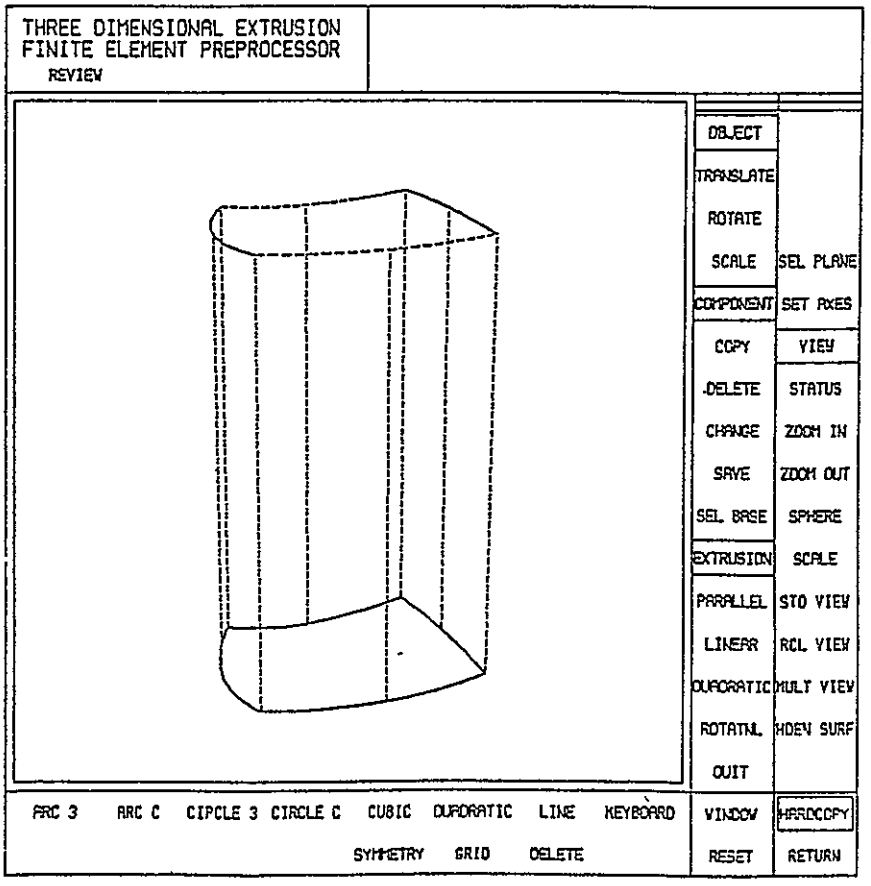

Figure VI-2. Extrusion of Planar Face

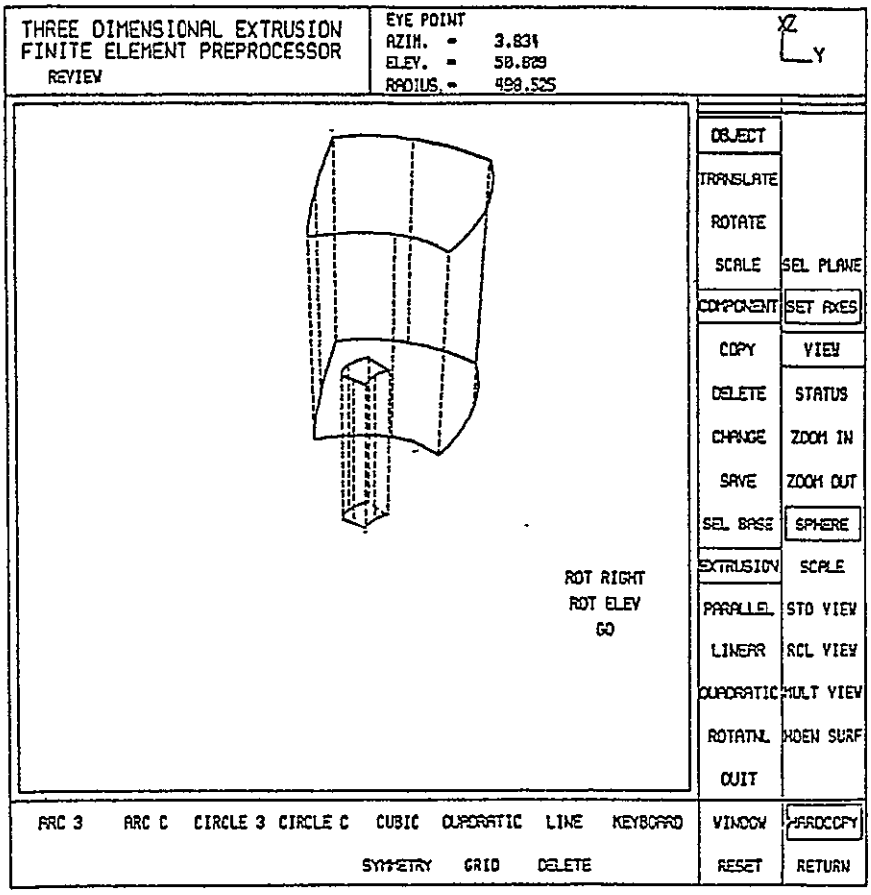

Figure VI-3. Patching of Component

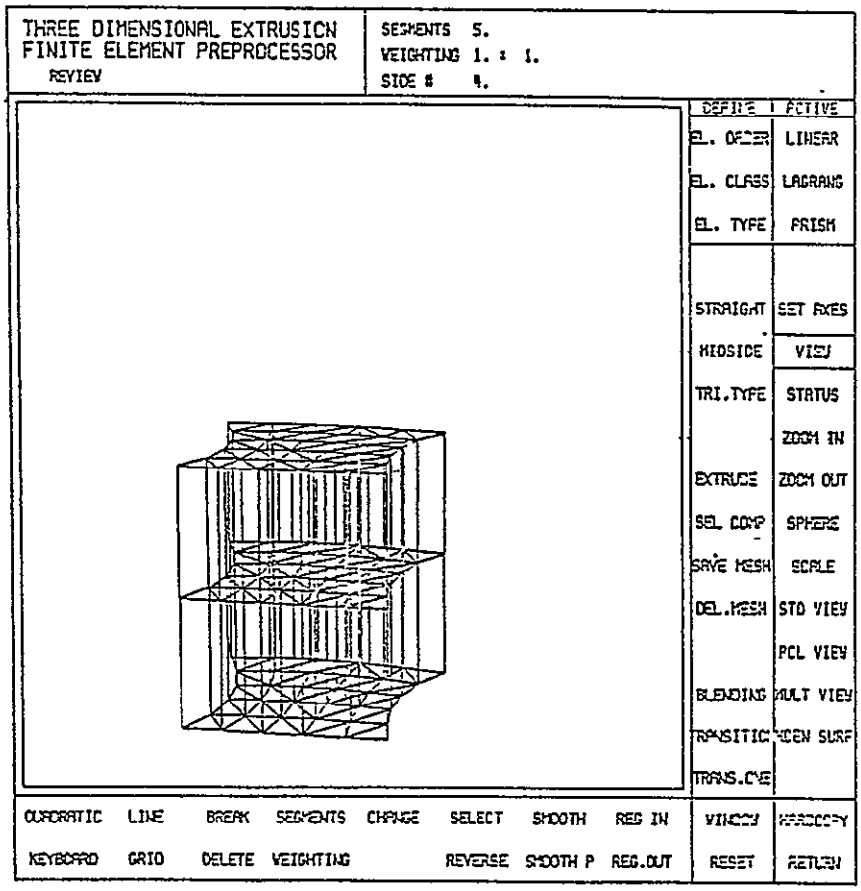

Figure VI-4. Three-Dimensional Component Mesh

changed to rational parametric cubics, which allow for error-free representation of all conic sections[4]. The use of rational parametric cubic surfaces is also planned. The user interface is being improved by the addition of new control/display features and the formalization of a menu hierarchy.

c. Three-Dimensional Postprocessor Development

An initial version of a three-dimensional postprocessor for deflected shapes has been developed. The program is designed for both static and dynamic analysis results, with the dynamic analysis results including both mode shapes and time-histories. Basic interactive operations include single and multiple view options, scale change, rotation, translation, windowing and sectioning. Figure VI-5 shows a multiple view display of a shell surface that has been sectioned by user-defined cutting planes.

d. Automatic Mesh Generator

A new approach to the automatic generation of two-dimensional finite element meshes has been developed. The method is referred to as the modified quadtree approach [5, 6] and appears to be extendable to three-dimensional problems through a modified octree method. The process begins with the interactive definition of the problem geom-

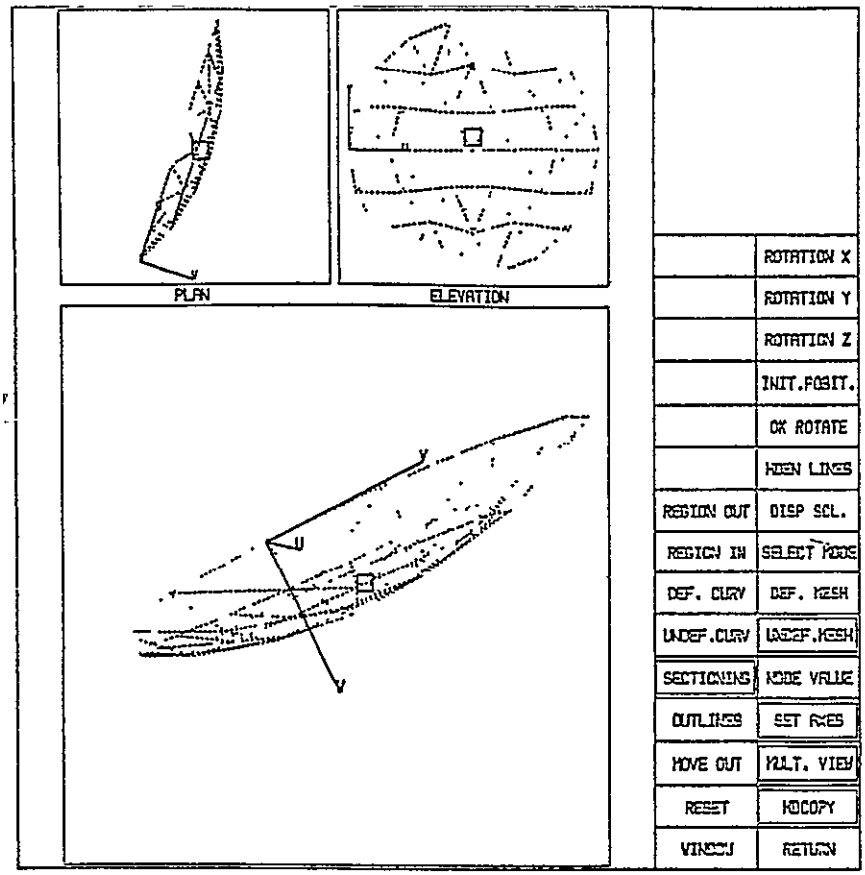

Figure VI-5. Multiple View Option in Three-Dimensional Postprocessor

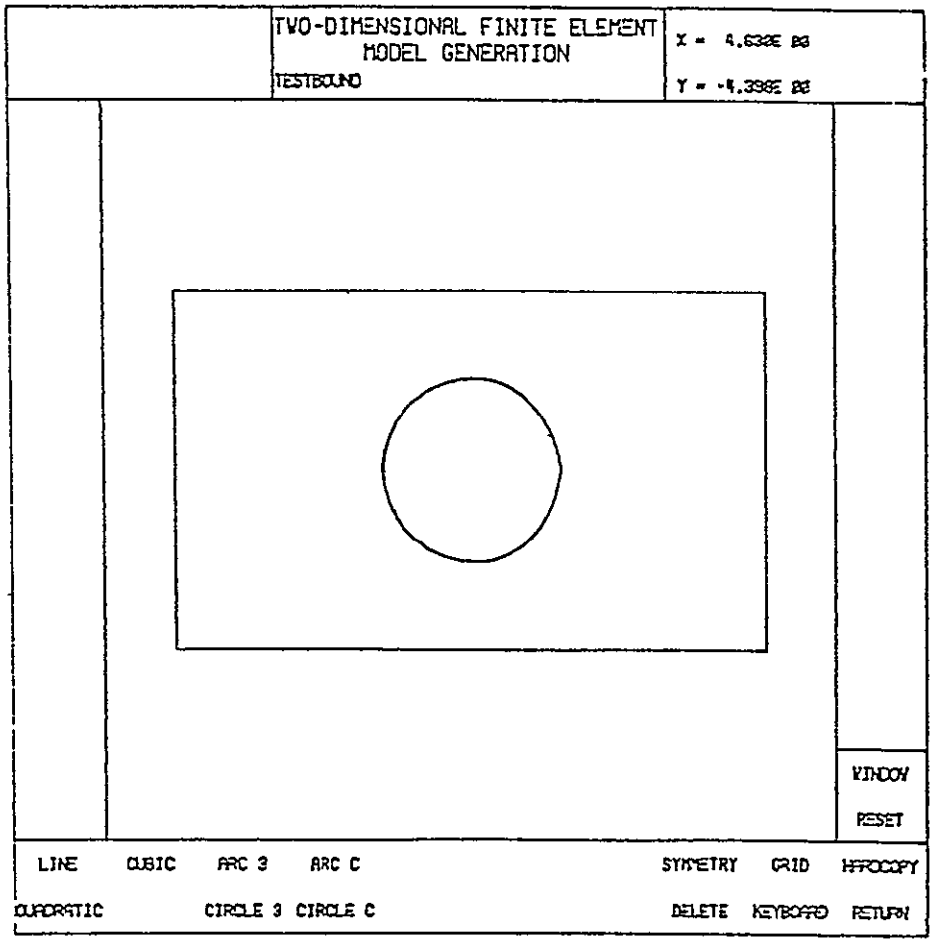

Figure VI-6. Boundary Curves for Plate with Hole

etry in terms of boundary curves. Figure VI-6 shows the curves used to define a plate with a hole in it. Curve tolerances are then defined interactively to produce desired mesh gradations. From this point the mesh is generated automatically. Automatic mesh generation proceeds by defining a modified quadtree (Figure VI-7) in an integer data space, then breaking the modified quadtree into a valid finite element mesh (Figure VI-8). The final steps involve, first, pulling the boundary nodes from their locations in the integer data space and moving them precisely to the geometric boundaries and, second, smoothing the internal node locations to improve the element aspect ratios. Figure VI-9 shows the final mesh for the plate with a hole in it, after pulling and smoothing. Figure VI-10 shows a mesh generated for a piston cross section, while Figure VI-11 shows a mesh generated for a typical bracket.

4. Plans for Upcoming Period

During the next reporting period, programming on the extrusion preprocessor and shell surface program will continue. As mentioned in the section in this report dealing with the numerical investigation of the micromechanics of composite fracture, Part III-E, the modified quadtree mesh-generating capability will be considered for use in the analysis method for following the process of crack propagation.

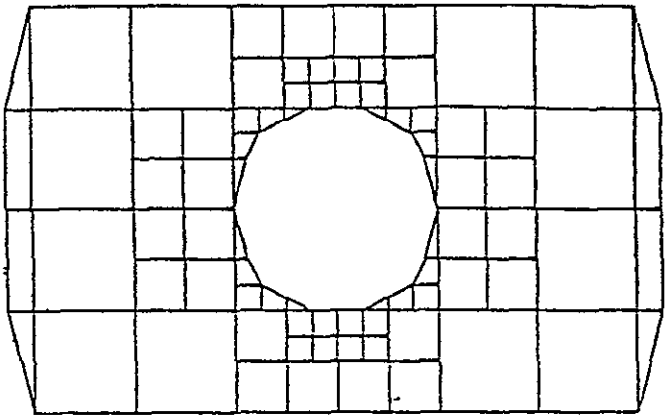

Figure VI-7. Modified Quadtree Representation

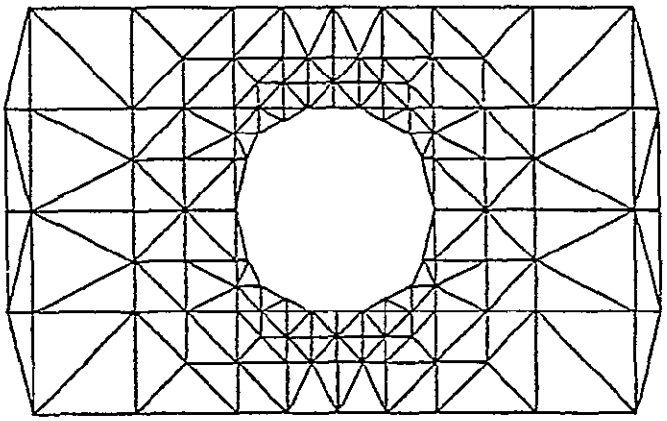

Figure VI-8. Integer Triangular Mesh

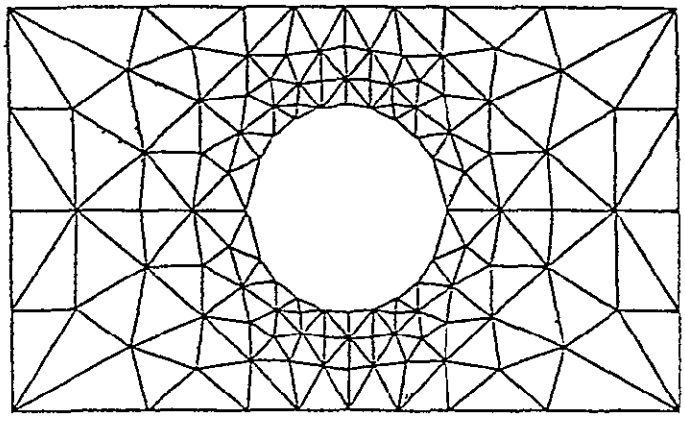

Figure VI-9. Final Triangular Mesh

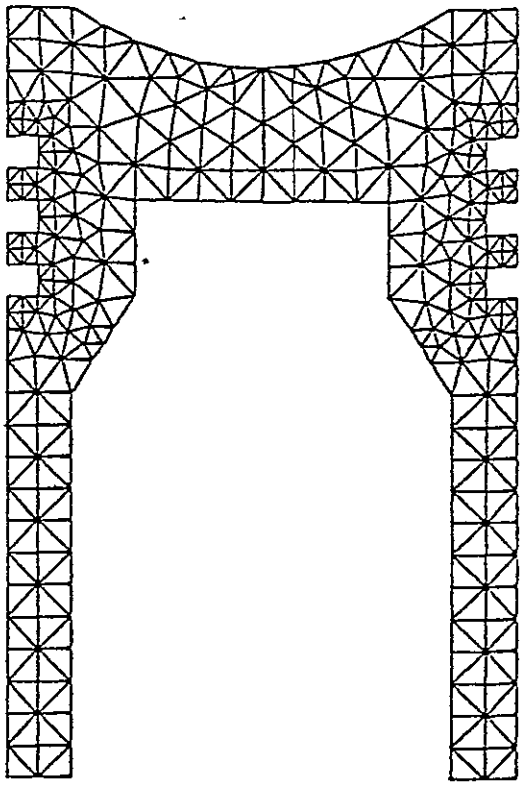

Figure VI-10. Piston Cross Section

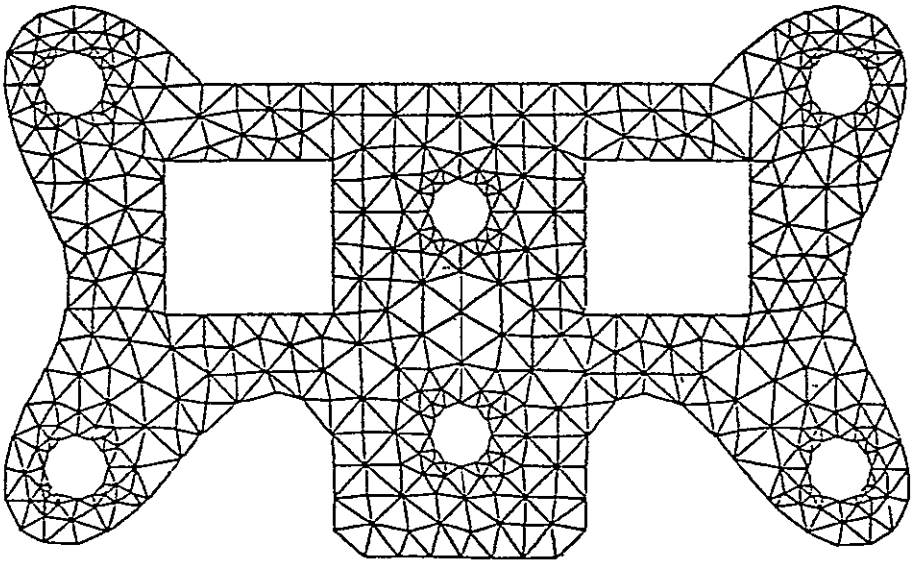

Figure VI-11. Bracket Example

5. References

1. Bathe, K. J. and E. L. Wilson, "Numerical Methods in Finite Element Analysis", Prentice-Hall, Inc., Englewood Cliffs, NJ, 1976, Chapter 12.

2. Botoz, J. T. and G. Phatt, "An Evaluation of Two Simple and Effective Triangular and Quadrilateral Plate Bending Elements", New and Future Developments in Commercial Finite Element Methods, J. Robinson, ed., 1981, 352-368.

3. Botoz, J. L., K. J. Bathe and L. W. Ho, "A Study of Three-Noded Triangular Plate Bending Elements", Int. J. Num. Meth. Engrg., Vol. 15, 1980, 1771-1812.

4. Faux, I. D. and M. J. Pratt, "Computational Geometry for Design and Manufacturing", Ellis Horwood Limited, Chichester, England, 1979, Chapters 5 and 6.

5. Yerry, M. A., "Modified Quadtrees for Finite Element Mesh Generation", M.S. Thesis, Rensselaer Polytechnic Institute, Troy, NY, May 1982.

6. Shephard, M. S. and M. A. Yerry, "An Approach to Automatic Finite Element Mesh Generation", To appear: Proc. 2nd Int. Computer Eng. Conference, ASME, August 1982.

6. Current Publications or Presentations by Professor Shephard on this Subject

"Computer Graphics in Civil Engineering at RPI"

Published in Computers and Education, Vol. 5, 1981, 219-227.

"Attribute Specification for Finite Element Models", with C. N. Tobias and T. J. Weidner.

Published in Computers & Graphics, Vol. 6, No. 2, 1982, 83-91.

"Interactive Finite Element Programs"

To be published in Proc. NCGA, June 1982.

"Academic Research in CAD/CAM"

Presented at the Nippon Univac Kaisha Seminar on Computer Assisted Design and Manufacturing, Carnegie Institute of Technology, October 20, 1981.

"Computer Graphics in Education and Research"

Presented at a seminar at Lehigh University, March 1, 1982

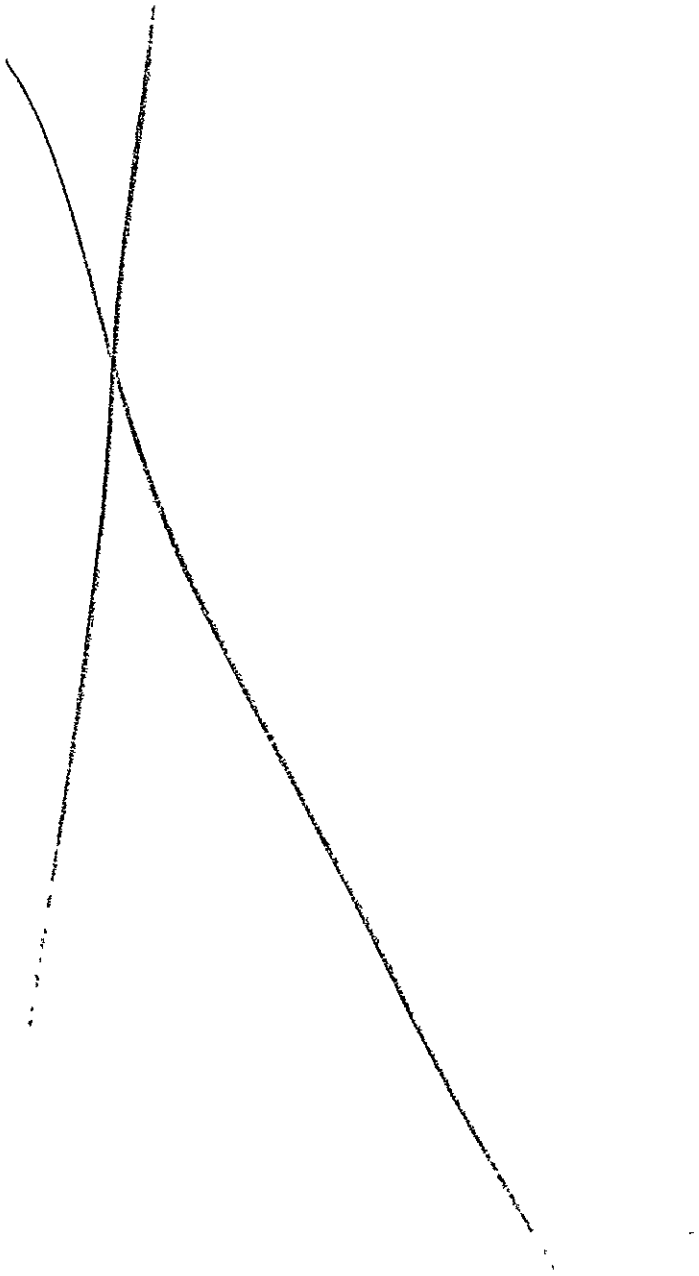

PART VII
TECHNICAL INTERCHANGE

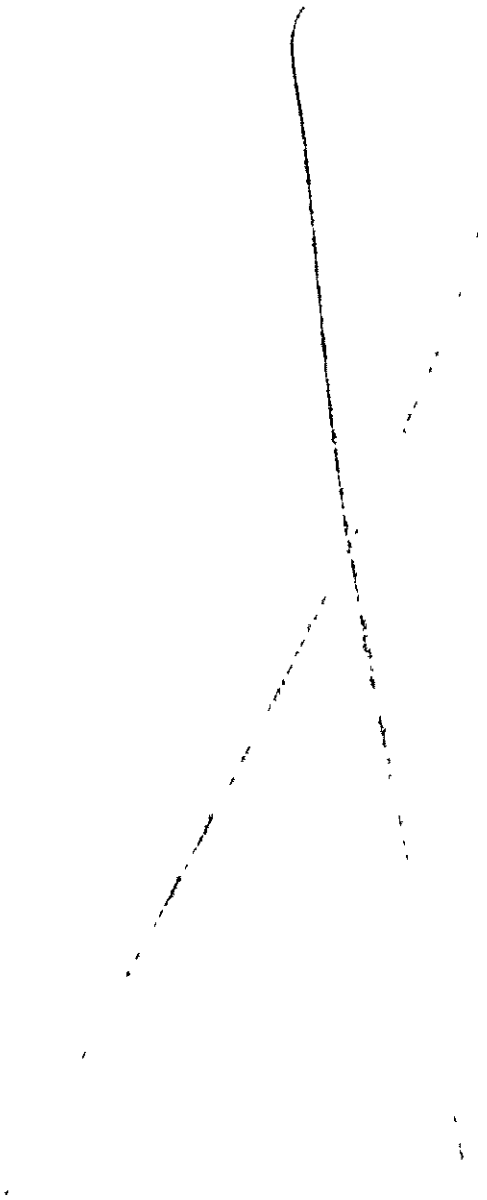

INTRODUCTION

Technical meetings, on- and off-campus, provide important opportunities for interchange of technical information. Because of the large number of composites meetings, a central catalog with all upcoming meetings is being maintained and distributed periodically. In this way we help to assure that a Rensselaer faculty/staff member can participate in important meetings. The calendar for this reporting period is shown in Table VII-1. Meetings attended by RPI composites program faculty/staff/students during the reporting period are shown in Table VII-2. Some meetings particularly relevant to composites, held on-campus with special speakers, are listed in Table VII-3. A list of composite-related visits to relevant organizations by RPI faculty/staff/students, with the purpose of each visit outlined, is presented in Table VII-4.

TABLE VII-1

CALENDAR OF COMPOSITES-RELATED MEETINGS

(September 30, 1981 through April 30, 1982)

1981

10/5-7	International Symposium on Aeroelasticity, Nuremberg, Fed. Rep. of Germany.
10/7	Symposium III - Design and Use of Kevlar in Aircraft, Los Angeles, CA. "Sponsored by DuPont."
10/9	Symposium III - Design and Use of Kevlar in Aircraft, Philadelphia, PA. "Sponsored by DuPont."
10/10-11	Annual Materials Science Seminar, Louisville, KY. "Sponsored by American Society of Metals."
10/12-15	3rd World Congress on Finite Element Methods, Los Angeles, CA.
10/13-15	13th National Technology Conference, Mt. Pocono, PA. "Sponsored by SAMPE."
10/19-22	International Symposium on Optimum Structural Design, Tucson, AZ.
10/20	Symposium on Producibility and Quality Assurance of Composite Materials, St. Louis, MO. "Sponsored by ASTM."
10/27	ASCE Annual Convention and Exposition, St. Louis, MO.
10/28-30	7th Annual Mechanics of Composites Review, Dayton, OH. "Sponsored by Air Force Wright Aeronautical Labs."
11/12-13	NASA Workshop on "High Temperature Nonlinear Constitutive Equations", Lewis Research Center, Cleveland, OH.
11/15-20	ASME Winter Annual Meeting, Washington, DC. "Sponsored by ASME,"
11/16-19	Composites Symposium on Fabrication, Design and Testing, Wilmington, DE. "Sponsored by SPE and SESA."
11/23-24	Annual Review of the Ceramic Materials Research Program on Brittle Material Design, Seattle, WA. "Sponsored by NASA and the University of Washington."
11/30-12/3	13th Annual Department of Defense Manufacturing Technology Conference, San Diego, CA. "Sponsored by Uniter States Department of Defense."

1981

12/7-9	V/STOL Conference, Palo Alto, CA. "Sponsored by AIAA."

1982

1/6	American Chemical Society and Society of Plastics Engineers, Albany, NY
1/11-13	20th Aerospace Sciences Meeting, Orlando, FL. "Sponsored by AIAA."
1/11-15	37th Annual Conference and Product Showcase of the SPI Reinforced Plastics/Composites Institute, Washington, DC. "Sponsored by the Society of the Plastics Industry, Inc."
1/18-22	Gordon Conference on Composite Materials, Ventura, CA.
3/2-5	Design Criteria for the Future of Flight Controls, Dayton, OH. "Sponsored by Flight Dynamics Lab."
3/9-10	Symposium on Long-Term Behavior of Composites, Williamsburg, VA. "Sponsored by ASTM."
3/22-26	Conference on Computers/Graphics in the Building Process, Washington, DC. "Sponsored by National Academy of Science and World Computer Graphics Association."
3/24-26	International Conference on Forward Swept Wing Aircraft, Bristol, U. K. "Sponsored by the University of Bristol."
3/29	International Conference on Deformation, Yield and Fracture of Polymers, Churchill College, Cambridge, England.
3/29-4/1	American Chemical Society Meeting, Las Vegas, NV.
4/7-9	11th Southeastern Mechanics Conference, Huntsville, AL.
4/28	ASTM Task Group E 24.04.09 Meeting on Crack Growth in Adhesive Joints, Philadelphia, PA.

TABLE VII-2

COMPOSITES-RELATED TECHNICAL MEETINGS ATTENDED OFF-CAMPUS

(September 30, 1981 through April 30, 1982)

1981

10/9 Symposium III - Design and Use of Kevlar in Aircraft (Prof. Diefendorf and Mr. Paedelt), Philadelphia, PA.

10/12-15 3rd World Congress on Finite Element Methods (Prof. Shephard), Los Angeles, CA.

Professor Shephard presented the paper, "The Finite Element Modeling Process - Will it be Automated".

10/27 ASCE Annual Convention and Exposition, (Prof. Shephard), St. Louis, MO.

Professor Shephard presented the paper, "Adaptive Element Analysis Accounting for Material Interfaces".

10/27-29 7th Annual Mechanics of Composites Review (Prof. Loewy), Dayton, OH.

Professor Loewy, Keynote Speaker, presented "Composites: Coming of Age".

11/12-13 NASA Workshop on "High Temperature Nonlinear Constitutive Equations" (Prof. Krempl), Cleveland, OH.

11/15-20 ASME Winter Meeting (Profs. Krempl and Scarton), Washington, DC.

Professor Scarton presented the paper, "Acoustic Emission in Composite Materials".

1982

1/6 ACS and Society of Plastics Engineers Meeting (Prof. Diefendorf), Albany, NY.

Professor Diefendorf presented the paper, "Aerospace Applications of Composite Materials".

1/18-22 Gordon Conference on Composite Materials (Prof. Diefendorf), Ventura, CA.

Professor Diefendorf presented the paper, "Residual Stresses in Carbon Fibers".

3/28-4/1 American Chemical Society Meeting (Prof. Diefendorf), Las Vegas, NV.

Professor Diefendorf presented the paper, "Interfaces and Liquid Crystalline Polymers".

3/29 International Conference on Deformation, Yield and Fracture of Polymers (Prof. Sternstein), Churchill College, Cambridge, England.

Professor Sternstein presented the paper, "Matrix Dominated Mechanical Properties of High Performance Composites".

4/7-9 11th Southeastern Mechanics Conference, Prof. Krempl), Huntsville, AL.

4/28 ASTM Task Group E 24.04.09 Meeting on Crack Growth in Adhesive Joints (Prof. Shephard), Philadelphia, PA.

TABLE VII-3

COMPOSITES-RELATED MEETINGS/TALKS HELD AT RPI

(September 30, 1981 through April 30, 1982)

Topic	Date	Speaker(s)
Composites Applications to Rotary Wing Aircraft	10/6/81	Erwin Durchlaub Boeing Vertol, Philadelphia
Kinking of Fibrous Composites	10/20/81	Bernard Budiansky Gordon McKay Professor of Structural Mechanics Harvard University
The Optical Method of Caustics as Applied to The Fracture of Ductile Materials	2/16/82	Ares J. Rosakis Division of Engineering Brown University
Design and Automated Manufacturing of Composite Airframe Structures	2/23/82	James O. Warren and David L. Smith McDonnell Douglas Corp.
Pulse Propagation in Composites Viewed as Interpenetrating Solid Continua	3/2/82	Matthew F. McCarthy Department of Engineering Science and Mechanics Virginia Polytechnic Institute and State University
Evidence for Crack Tip Controlled Stable Crack Growth	3/4/82	George Green General Electric R & D Center, on leave from Central Electricity Generating Board
Continuum Damage Mechanics (A Systematic Life Prediction Method)	3/9/82	F. A. Leckie Professor, University of Illinois
RPI Faculty Workshop on Instructional Computer Graphics	3/15/82	M. S. Shephard Assistant Professor of Civil Engineering Rensselaer Polytechnic Institute
Finite Element Modeling Design	3/24/82	M. S. Shephard Assistant Professor of Civil Engineering Rensselaer Polytechnic Institute

Fatigue Damage Mechanisms in Carbon Fiber Reinforced Plastics	4/2/82	Karl Schulte Research Associate Institut f. Werkstoff-Forschung, W. Germany
Fibrous Skins	4/6/82	S. A. Wainwright Professor, Duke University
An Analysis of the Influences of Time and Loading Rate on Crack	4/26/82	Mark M. Little Doctoral thesis disertation Department of Mechanical Engineering, Aeronautical Engineering and Mechanics
A Finite Element Time Integration Method for the Theory of Viscoplasticity Based on Infinitesimal Total Strain and Overstress	4/27/82	Robert M. Zirin Doctoral thesis dissertation Department of Mechanical Engineering, Aeronautical Engineering and Mechanics

TABLE VII-4

COMPOSITES-RELATED VISITS TO RELEVANT ORGANIZATIONS

by RPI Faculty/Staff/Students

(September 30, 1981 through April 30, 1982)

Visited	Date	By	Purpose
	1981		
Carnegie Institute of Technology, Pittsburgh, PA	10/20	Prof. M. S. Shephard	Presented at Nippon Univac Kaisha Seminar: "Academic Research in Cad/Cam"
Norton Company, Worchester, MA	10/22	Prof. R. J. Diefendorf	Presented talk: "Ceramic Composites"
General Electric Company, Saratoga, NY	10/28	Prof. R. J. Diefendorf	Presented talk: "Composite Materials"
Du Pont Pioneering Research Lab., Wilmington, DE	11/3	Prof. R. J. Diefendorf	Presented talk: "The Structure of Carbon Fibers and the Consequences on Performance"
Louisville, KY (S. P. E. Short Course)	11/4	Prof. S. S. Sternstein	Gave invited lecture: "Matrix Dominated Mechanical Properties of Composites"
Exxon Enterprises, Fountain Inn, SC	11/4-5	Prof. R. J. Diefendorf	Presented talk: "The Structure of Carbon Fibers and the Consequences on Performance
CIBA-Geigy Research Center, Tarrytown, NY	11/19	Prof. S. S. Sternstein	Presented talk: "Composites"
Naval Research Laboratory, Washington, DC	12/1	Prof. S. S. Sternstein	Presented talk: "Viscoelastic Characterization of Composites"
	1982		
Physical Acoustics Corporation, Montreal, Canada	1/5	Prof. H. Scarton	Presented talk: "Acoustic Emission in Composite Materials"

1982

UCLA, Los Angeles, CA	1/12-13	Prof. R. J. Diefendorf	Presented talk: "Composite Materials"
Aerospace Corporation, El Segundo, CA	1/14	Prof. R. J. Diefendorf	Presented talk: "Structure of Carbon Fibers and Consequences on Performance
Lehigh University, Bethlehem, PA	3/1	Prof. M. S. Shephard	Presented at seminar: "Computer Graphics in Education and Research"
General Motors Research Laboratory, Detroit, MI	3/8	Prof. M. S. Shephard	Presented talk: "Progress on Automated 3-D Mesh Generation"
Kent State, Kent, OH (Liquid Crystal Institute)	3/17	Prof. R. J. Diefendorf	Presented at seminar: "Discotic Liquid Crystals in Pitch"
Cornell University, Ithaca, NY (Program for Computer Graphics)	3/19	Prof. M. S. Shephard	Presented talk: "Automatic Finite Element Mesh Generation"
Du Pont Corporation, Wilmington, DE	4/18	Prof. R. G. Loewy	To Discuss Composites Program with Dr. A. Dhingra
Iowa State University, Ames, IA	4/21-22	Prof. M. S. Shephard	To attend: "Workshop on Computer-Aided Design in Education"

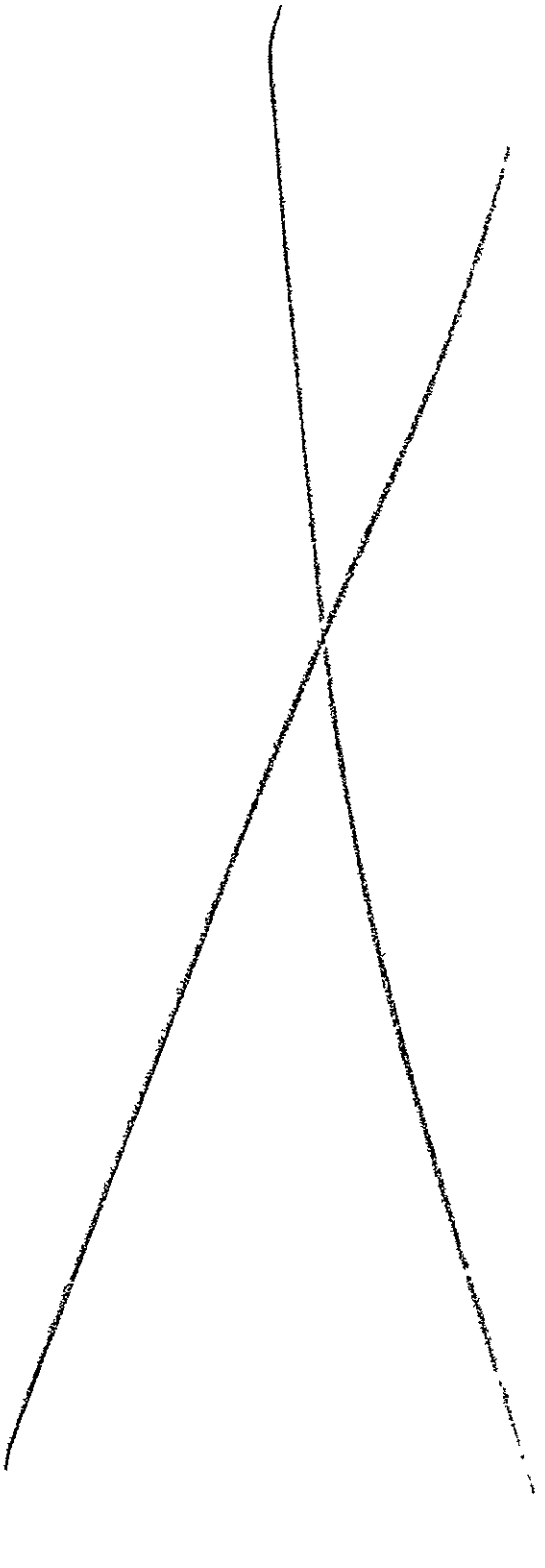

PART VIII

PERSONNEL

AUTHOR INDEX

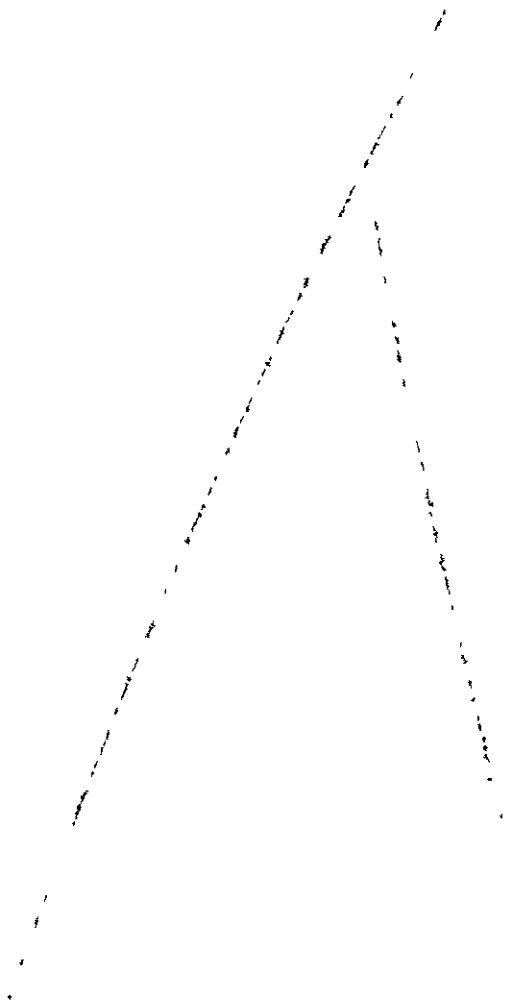

PERSONNEL

Co-Principal Investigators

Ansell, George S., Ph.D.	Dean, School of Engineering
Loewy, Robert G., Ph.D.	Institute Professor
Wiberley, Stephen E., Ph.D.	Professor of Chemistry

Senior Investigators

Brunelle, E. J., Jr., SC.D. (Aeroelastic and structural design and analysis, applied mechanics of composite structures)*	Associate Professor of Aeronautical Engineering
Bundy, F., Ph.D. (Physical chemistry and structures testing)*	Research Professor of Materials Engineering
Diefendorf[i], R. J., Ph.D. (Fabrication, resin matrix, fiber behavior, interfaces)*	Professor of Materials Engineering
Feeser[i], L. J., Ph.D. (Computer applications and graphics, computer aided design, optimization)*	Professor of Civil Engineering
Goetschel, D. B., Ph.D. (Structural analysis design and testing)*	Assistant Professor of Mechanical Engineering
Hagerup, H. J., Ph.D. (Aerodynamics, configuration, pilot accomodation, flight testing)*	Associate Professor of Aeronautical Engineering
Krempl, E., Dr.Ing. (Fatigue studies, failure criteria)*	Professor of Mechanics and Director of Cyclic Strain Laboratory
Scarton, H., Ph.D. (Acoustic emission NDE)*	Associate Professor of Mechanical Engineering and Mechanics

*Fields of Speciality

[i]Member of Budget Committee together with Co-Principal Investigators

Senior Investigators

Shephard, M. S., Ph.D. (Computer graphics, finite element methods)*	Associate Director, Center for Interactive Computer Graphics and Assistant Professor of Civil Engineering
Sternstein[i], S. S., Ph.D. (Failure analysis, matrix behavior, moisture effects)*	William Weightman Walker Professor of Polymer Engineering

Research Staff

Manager & Master Technician, Composites Laboratory

Paedelt, Volker

Research Associate

Muser, Christoph, Dr.Eng.

Graduate Assistants

Bobal, Gail, M.E.	Ogunlari, Fola, B.S.
Chang, Chi-Min, M.S.	Singh, Sachchida, B.S.
Chen, Chikuang, B.S.	Uzoh, Cyprian, B.S.
Chen, Kuang-jung, B.S.	Valicenti, Raymond, B.S.
Chen, Shu-ping, B.S.	Winckler, Steven, M.E.
Helmer, James, B.S.	Yehia, Nabil, M.S.
Lumban Tobing, Frida, M.S.	Yurgartis, Steven, M.S.
Niu, Tyan-Min, M.S.	

Undergraduate Assistants - Seniors

Adel, Paul	Chin, Hong
Applewhite, Keith	Cox, Mary
Baxter, Scott	DeTaranto, Francis
Bergman, Richard	Dhimitri, William
Bertolazzi, Andrew	Fairchild, Kendall
Bristol, Brian	Fisher, Steven

*Fields of Speciality

[i]Member of Budget Committee together with Co-Principal Investigators

Newmark, Glenn
Niederer, Melvin
Northrop, Steven
Staniorski, Anthony
Vaney, Philippe

Undergraduate Assistants - Juniors

Baucom, Allan
Benson, Robert
Burdett, John
Cioffoletti, Anthony
DeMint, Thomas
Ehrgott, Darhl
Ficarra, Fobert
Kirschenbaum, Susan
Koch, Stephen
Kuntsmann, Debra
Lafreniere, Suzanne
LeBlanc, James
Lundquist, Cheryl
Malusa, Stephen
Melendez, Hermenegildo
Powell, David
Quinlivan, Patrick
Sirkin, Stephen
Spinelli, Gregory
Taffinder, Douglas
Toomey, John
West, Jeffrey
White, Eric

Undergraduate Assistants - Sophomores

Tobiason, Scott
Goguen, Gary
Hsi, Ten-Li
Martin, Randall
Schroeder, Hans

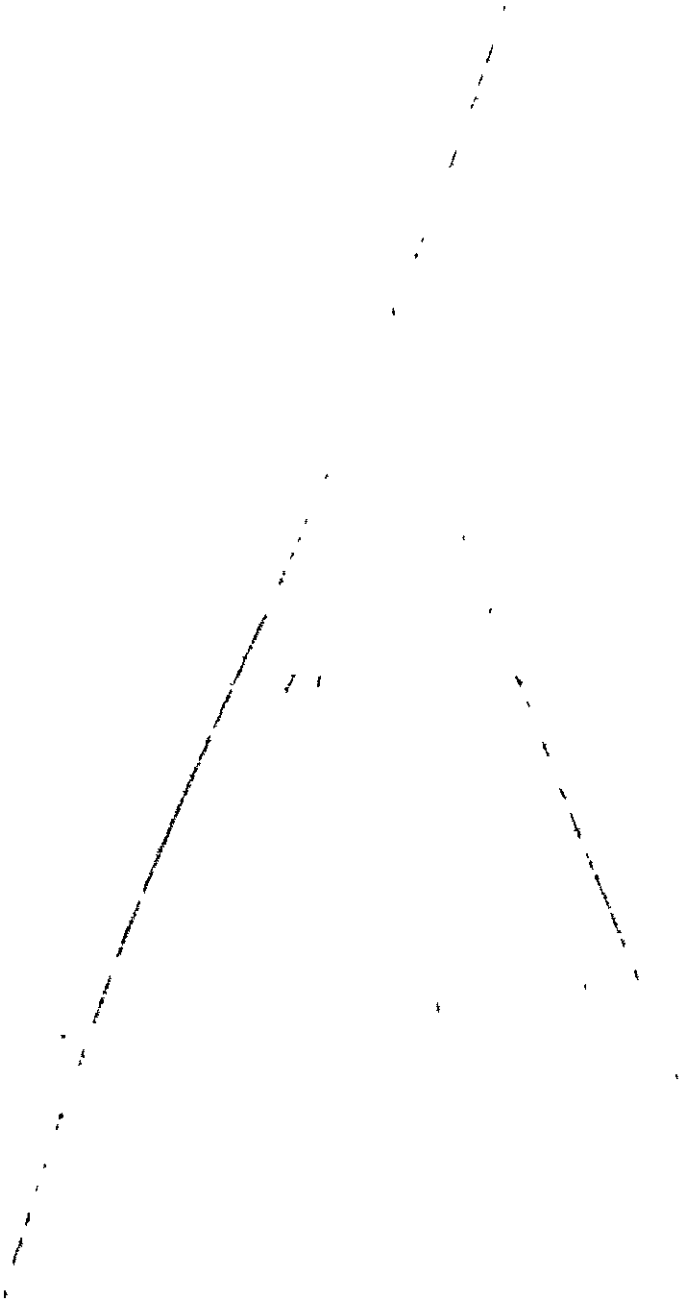

AUTHOR INDEX